

UC San Diego

UC San Diego Electronic Theses and Dissertations

Title

Optimization of Spark-Plasma Sintering Efficiency: Tailoring Material Structure and Advanced Tooling Design

Permalink

<https://escholarship.org/uc/item/8vv659gc>

Author

Giuntini, Diletta

Publication Date

2016

Peer reviewed|Thesis/dissertation

UNIVERSITY OF CALIFORNIA, SAN DIEGO

SAN DIEGO STATE UNIVERSITY

**Optimization of Spark-Plasma Sintering Efficiency:
Tailoring Material Structure and Advanced Tooling Design**

A dissertation submitted in partial satisfaction of the requirements
for the degree Doctor of Philosophy

in

Engineering Sciences (Mechanical and Aerospace Engineering)

by

Diletta Giuntini

Committee in charge:

San Diego State University

Professor Eugene A. Olevsky, Co-Chair
Professor Kaveh Akbari Hamed

University of California, San Diego

Professor Marc A. Meyers, Co-Chair
Professor J. Enrique Luco
Professor Vitali F. Nesterenko

2016

©

Diletta Giuntini, 2016

All rights reserved.

The Dissertation of Diletta Giuntini is approved, and it is acceptable in quality and form for publication on microfilm and electronically:

Co-Chair

Co-Chair

University of California, San Diego

San Diego State University

2016

Dedication

To my parents

Table of Contents

Signature Page.....	iii
Dedication.....	iv
Table of Contents.....	v
List of Symbols.....	vii
List of Figures.....	ix
List of Tables.....	xiv
Acknowledgements.....	xv
Vita.....	xviii
Abstract of the Dissertation.....	xx
Chapter 1	
Introduction: uniformity of materials consolidated by spark plasma sintering.....	1
1.1 Material structure topology during spark plasma sintering.....	3
1.2 Spark plasma sintering tooling setup and temperature.....	17
Chapter 2	
Research objectives: optimization of spark plasma sintering efficiency.....	24
Chapter 3	
Modeling of consolidation of hierarchical (agglomerated) porous structures with nonlinearity of the material's constitutive behavior.....	30
3.1. Semi-analytical modeling of hierarchical porous structures densification kinetics.....	30
3.1.1. Definition of hierarchical porous structures.....	30
3.1.2. Sintering kinetics of hierarchical porous structure.....	42
3.1.3. Sintering stress of homogeneous and hierarchical porous structures with nonlinear viscous constitutive behavior.....	55
3.1.4. Bulk modulus of homogeneous and hierarchical porous structures with nonlinear viscous constitutive behavior.....	66
3.1.5. Shear modulus of homogeneous and hierarchical porous structures with nonlinear viscous constitutive behavior.....	83
3.2. Optimization of the material structure based on strain-rate sensitivity.....	94
3.2.1. Strain-rate sensitivity and temperature.....	94
3.2.2. Optimization strategies.....	103

3.2.3. Multiscale FEM simulations of pore shape evolution during sinter-forging of hierarchical composites.....	130
Chapter 4	
Optimization of spark plasma sintering based on improved tooling setup.....	144
4.1. The role of the spark plasma sintering tooling geometry.....	144
4.2. Optimization of the radial temperature distributions by improved punch design.....	148
4.2.1. The radial thermal gradients issue.....	148
4.2.2. FEM reconstruction of the spark plasma sintering tooling setup.....	157
4.2.3. FEM and experimental implementation of the novel punch design....	169
4.2.4. FEM analysis of further developments for the novel punch design....	195
4.3. Optimization of the axial temperature distributions by improved spacers design.....	208
4.3.1. The top punch overheating issue.....	210
4.3.2. FEM-based optimization of the spark plasma sintering spacers design.....	217
Chapter 5	
Conclusions.....	233
5.1. Summary.....	233
5.2. Scientific and engineering novelty	238
References.....	240

List of Symbols

θ : total porosity	$\dot{\epsilon}$: strain rate tensor first invariant (volumetric shrinkage rate)
θ_S : small-size porosity	\dot{H} : macroscopic (biporous) volumetric shrinkage rate
θ_L : large-size porosity	$\dot{\gamma}$: strain rate tensor second invariant (shape change)
$\dot{\theta}_S$: small-size porosity shrinkage rate	$\dot{\gamma}_S$: strain rate tensor second invariant for fully dense material
$\dot{\theta}_L$: large-size porosity shrinkage rate	$\dot{\Gamma}$: macroscopic strain rate tensor second invariant
ρ : relative density	V_i : velocity vector
ρ_{th} : theoretical density	ψ : normalized bulk modulus associated with small pores
ρ_{eff} : effective density	φ : normalized shear modulus associated to small pores
r : radial coordinate	Ψ : normalized macroscopic bulk modulus
a : large pore radius	Φ : normalized macroscopic shear modulus
b : biporous study domain radius	δ_{ij} : Kronecker delta
r_{sp} : small pore radius	α : surface tension
r_{sd} : monoporous study domain radius	P_L : macroscopic sintering stress
\dot{r}_{sp} : small pore radius shrinkage rate	
\dot{a} : large pores radius shrinkage rate	
σ_{ij} : stress tensor	
p : stress tensor first invariant	
P : macroscopic (biporous) stress tensor first invariant	
τ : stress tensor second invariant	
$\dot{\epsilon}_{ij}$: strain rate tensor	
$\dot{\epsilon}'_{ij}$: strain rate tensor deviator	

P_{L_S} : sintering stress due to small pores	C_1, C_2 : transient creep material constants
$P_{L_{0_S}}$: surface sintering stress on small pores	t : time
$P_{L_{0_L}}$: surface sintering stress on large pores	t_s : normalized sintering time
P_{ext} : externally applied pressure	D : dissipative potential in porous material
k : sintering stresses ratio	D_S : dissipative potential in fully dense material
$\sigma(W)$: equivalent stress	$s(\theta)$: flow stresses ratio
W : equivalent strain rate	σ_{zf} : flow stress
A_m : creep coefficient	S_{comp} : compression strength
m : strain-rate sensitivity	S_{flex} : bending strength
A_n : Ashby's creep coefficient	σ_{el} : electrical conductivity
n : Ashby's creep exponent	C_p : heat capacity
A_0 : pre-exponential creep factor	k_T : thermal conductivity
Q_{PLC} : creep activation energy	ν_{rad} : emissivity
R : ideal gas constant	J : current density
T : temperature	V : voltage
T_m : melting temperature	r_{el} : electrical resistivity
σ_{ref} : Ashby's creep reference stress	$r_{el,c}^h$: horizontal electrical contact resistance
η_0 : viscosity	$r_{el,c}^v$: vertical electrical contact resistance
E : Young's modulus	
$A_{\bar{n}}$: transient creep coefficient	
\bar{n} : transient creep exponent	
\bar{K} : transient creep factor	

List of Figures

Figure 2.1 – Flow chart of the research objectives.....	29
Figure 3.1 – Agglomeration in a vanadium carbide powder.....	32
Figure 3.2 – Effects of agglomeration in loose powder and sintered materials.....	33
Figure 3.3 – Partially sintered agglomerated alumina	34
Figure 3.4 – Agglomeration in iron nanopowders and schematics of its effects.....	34
Figure 3.5 – Definition of the study domain representative of hierarchical porous structures.....	39
Figure 3.6 – Geometry and loading schematics acting on the biporous study domain.....	41
Figure 3.7 – Comparison between the present kinetics model ($m = 1$) and the one derived by Olevsky and Rein for linear viscous materials.....	55
Figure 3.8 – Zooming in to define the domain study for the monoporous context.....	59
Figure 3.9 – Geometry and loading schematics acting on the monoporous study domain.....	61
Figure 3.10 – Normalized bulk modulus expressions for monoporous materials and different values of the strain-rate sensitivity parameter.....	70
Figure 3.11 – Comparison between dilute and non-dilute normalized bulk modulus expressions.....	75
Figure 3.12 – Non-dilute normalized bulk modulus expressions for monoporous materials and different values of the strain-rate sensitivity parameter.....	79
Figure 3.13 – Normalized sintering stress expressions for monoporous materials and different values of the strain-rate sensitivity parameter.....	80
Figure 3.14 – Comparison of the densification kinetics model with experiments for alumina powder of different sizes.....	81
Figure 3.15 – Plot of the function s as a function of relative density with the corresponding experimental data.....	89
Figure 3.16 – Normalized shear modulus expressions for monoporous materials and different values of the strain-rate sensitivity parameter.....	92
Figure 3.17 – Strain-rate sensitivity evolution with temperature for copper.....	101

Figure 3.18 – Strain-rate sensitivity evolution with temperature for alumina.....	101
Figure 3.19 – Strain-rate sensitivity evolution with temperature for silicon nitride.....	102
Figure 3.20 – Strain-rate sensitivity dependence on temperature and stress for silicon nitride without and with activation energy correction.....	103
Figure 3.21 – Small and large size porosities evolution for initial small pores radius = 100 nm and initial large pores radius = 10 μm	110
Figure 3.22 – Small and large size pores radii evolution for initial small pores radius = 100 nm and initial large pores radius = 10 μm	111
Figure 3.23 – Small and large size porosities evolution for initial small pores radius = 1 μm and initial large pores radius = 5 μm	112
Figure 3.24 – Small and large size porosities evolution for initial small pores radius = 1 μm and initial large pores radius = 5 μm	113
Figure 3.25 – Impact of strain-rate sensitivity on the intersection between large and small-size porosity densification curves.....	114
Figure 3.26 – Densification curves for various initial porosities values.....	114
Figure 3.27 – Pores radii ratio evolution for different m values.....	115
Figure 3.28 – Comparison between the proposed kinetics model and experiments.....	117
Figure 3.29 – Optimization strategy based on shrinkage kinetics.....	119
Figure 3.30 – Shrinkage kinetics for the linear viscous case with 500 MPa applied pressure.....	121
Figure 3.31 – Shrinkage kinetics for the $m = 0.5$ case with 500 MPa applied pressure.....	122
Figure 3.32 – Shrinkage kinetics for the $m = 0.1$ case with 1 GPa applied pressure.....	123
Figure 3.33 – Shrinkage kinetics for the $m=0.1$ case with 1 GPa applied pressure and a narrow pores size gap.....	124
Figure 3.34 – Macroscopic bulk modulus in function of small and large size porosities.....	126
Figure 3.35 – Macroscopic shear modulus in function of small and large size porosities.....	127
Figure 3.36 – Macroscopic sintering stress in function of small and large size porosities.....	127

Figure 3.37 – Comparison between the present and Kuzmov-Shtern models for biporous materials.....	129
Figure 3.38 – Multiscale FEM domains definition.....	134
Figure 3.39 – FEM boundary value problem definition.....	136
Figure 3.40 – Correlations between FEM-implemented unit cell and experimental results.....	137
Figure 3.41 – FEM-derived deformation and porosity distributions of specimen and unit cell at the end of the isothermal holding.....	138
Figure 3.42 – FEM-derived evolutions of global porosity, large pores' size and aspect ratio for the 0, 3 and 5 MPa-applied pressure cases.....	139
Figure 3.43 – Comparison between experimental and FEM results.....	140
Figure 3.44 – Schematics of the material structure optimization strategies.....	142
Figure 4.1 – Spark plasma sintering tooling setup.....	145
Figure 4.2 – SPS tooling presenting the radial thermal gradients issue.....	153
Figure 4.3 – Temperature regime and temperature disparity among the two pyrometers in the conventional SPS setup.....	157
Figure 4.4 – Schematics of the setups utilized to study SPS contact resistance.....	163
Figure 4.5 – Fitting between experimental and numerical temperature profiles of pyrometers A and B.....	168
Figure 4.6 – Alternative punch designs: Holes and Rings.....	170
Figure 4.7 – Photographs of the experimentally-implemented Holes and Rings setups.....	172
Figure 4.8 – Temperature disparity among the two pyrometers for the conventional Full configuration and the experimentally-implemented Holes and Rings ones.....	173
Figure 4.9 – Percentage of alpha-phase content along the radial direction in the silicon nitride specimen for the three experimentally implemented configurations.....	176
Figure 4.10 – Density along the radial direction in the silicon nitride specimen for the three experimentally implemented configurations.....	176

Figure 4.11 – SEM images of the microstructure at the center and at the edge of the specimens obtained with the three experimentally-implemented configurations.....	177
Figure 4.12 – Temperature disparity for the FEM-implemented Holes configurations.....	180
Figure 4.13 – Temperature disparity for the FEM-implemented Rings configurations.....	181
Figure 4.14 – Temperature disparities at mid-holding for the Holes and Rings configurations.....	183
Figure 4.15 – Selection of the Rings configurations to be further investigated.....	184
Figure 4.16 – FEM- derived temperature profile and temperature disparity of the optimized 3 Rings configuration.....	186
Figure 4.17 – FEM-derived temperature distribution (°C) in the central radial cross-section for the Full and optimized 3 Rings configurations.....	186
Figure 4.18 – SPS setup with the optimized 3 Rings punch.....	188
Figure 4.19 – Comparison between the Full and optimized 3 Rings punches.....	189
Figure 4.20 – Experimental verification of the temperature disparity with the optimized 3 Rings configuration.....	190
Figure 4.21 – Axial displacement during experimental procedures with the Full and optimized 3 Rings configurations.....	190
Figure 4.22 – Geometrical parameters along the radial direction for the Constant Thickness and the Constant Distance configurations.....	196
Figure 4.23 – Temperature disparity for the Constant Thickness and Constant Distance configurations.....	198
Figure 4.24 – FEM-implemented Rings configurations with boron nitride coating deposited on the external ring.....	201
Figure 4.25 – FEM-derived temperature disparity for the BN-coated Rings configurations.....	204
Figure 4.26 – Optimized BN-coated Full punch configuration.....	206
Figure 4.27 – FEM-derived temperature distribution (°C) in the central radial cross-section for the conventional and optimized BN-coated Full configurations.....	207
Figure 4.28 – Spark Plasma Sintering (SPS) tooling manifesting the overheating problem.....	211

Figure 4.29 – Comparison between experimental and numerical temperature profiles.....	216
Figure 4.30 – Axial peak temperatures distribution (K) for the conventional tapered setup, with ideal and resistive contacts.....	217
Figure 4.31 – Conical transition replaced by 2 Disks, 3 Disks and 4 Disks configurations.....	219
Figure 4.32 – Peak temperature distributions (K) for two of the 2 Disks configurations.....	221
Figure 4.33 – Peak temperature distributions (K) for two of the 4 Disks configurations.....	221
Figure 4.34 – Peak temperature distributions (K) for two of the 2 Disks configurations with ideal contacts.....	224
Figure 4.35 – Peak temperature distributions (K) for two of the 4 Disks configurations with ideal contacts.....	224
Figure 4.36 – Temperature evolution in the top punch.....	225
Figure 4.37 – Peak temperature distribution—Height influence comparison for a 3 Disks configuration.....	226
Figure 4.38 – Temperature evolution—Effect of height variation.....	227
Figure 4.39 – Comparison of maximum (transient) temperature difference between top punch and specimen.....	229
Figure 5.1 – Conclusions summary.....	237

List of Tables

Table 3.1 – Expressions of normalized bulk modulus of a monoporous material compared in Figure 3.10.....	69
Table 3.2 – Expressions of normalized bulk modulus of a monoporous material compared in Figure 3.12.....	78
Table 3.3 – Expressions of normalized sintering stress of a monoporous material compared in Figure 3.13.....	78
Table 3.4 – Expressions of normalized shear modulus of a monoporous material compared in Figure 3.16.....	91
Table 3.5 – Summary of sintering kinetics, sintering stress and bulk and shear moduli expressions for monoporous and biporous materials.....	104
Table 4.1 – Tooling setup components for the radial gradients study.....	152
Table 4.2 – R7710 graphite properties.....	153
Table 4.3 – Silicon nitride properties.....	155
Table 4.4 – Cross-section areas and final densities of the experimentally-implemented alternative punch configurations.....	174
Table 4.5 – Hexagonal boron nitride properties.....	202
Table 4.6 – Tooling setup components for the axial gradients study.....	212
Table 4.7 – Isocarb 85 graphite properties.....	212
Table 4.8 – Alumina properties.....	214
Table 4.9 – Electric contact conductances.....	215

Acknowledgements

None of this work would have been possible without the guidance of Prof. Olevsky. He is the best advisor one could hope for – careful, caring, supportive, both tough and understanding, always available for his students. My co-advisor, Prof. Meyers, was also a constant source of inspiration, knowledge and encouragement. I need to thank my colleagues at the Powder Technology Laboratory: Xialu, José, Geuntak, Elisa, Wei, Yen-Shan, and all the former and current PhD, Master and visiting students and professors, who shared their experience and input with me. And thank you to Prof. Nesterenko, Prof. Luco and Prof. Akbari Hamed for honoring me by agreeing to be part of my doctoral committee.

None of this work would have been possible without all the people who made San Diego my home for five years. Lorenzo and Pietro, my Italian family in California. Farzaneh and Mehrdad, my Iranian family in California. The Awesome San Diegans.

None of this work would have been possible without my big Italian family. Jacopo, Eleonora, Mauro and Donatella, always there like siblings and parents. Leonardo, always there despite his disappearances, Abu, always there with his caustic wisdom, and Niccolò, always there despite. Le Gemelle Diverse, who keep me part of their life back home with tens of messages at each awakening. I Fratellini Qui e Quo, to whom I turn for every important decision (like Carbonare).

None of this work would have been possible without those invaluable people who helped me build a bridge between the two worlds. My parents in primis. Words cannot explain how much I admire, respect and love them. They gave me all I have. And my grandparents, uncle, aunts, Tosca, whose sweet unconditioned support feels even stronger from a ten thousand-km distance. Rachele, Virginia, Negin and Rose, best girlfriends forever for real. And, yet again, Joseph, hayete. Bala 7doud.

Parts of Chapter 3 have been published in the *International Journal of Refractory Metals and Hard Materials* (D. Giuntini, X. Wei, A.L. Maximenko, L. Wei, A.M. Ilyina, and E.A. Olevsky, “Initial Stage of Free Pressureless Spark-Plasma Sintering of Vanadium Carbide: Determination of Surface Diffusion Parameters,” *Int. J. Refract. Met. Hard Mater.*, 41, 2013). Other parts of Chapter 3 are in press in the *Journal of the American Ceramic Society* (D. Giuntini and E.A. Olevsky, “Sintering Stress for Materials with Nonlinear Viscous Rheology,” *Rapid Comm. J. Am. Ceram. Soc.*, accepted for publication) and prepared for publication in *Acta Materialia* (D. Giuntini and E.A. Olevsky, “Sintering Kinetics of Agglomerated Powders with Nonlinear Viscous Rheology,” *Acta Mater.*, prepared for publication). The dissertation author is the primary author of these publications. The results in the last paragraph of the same Chapter 3 are part of a work prepared for publication in *Acta Materialia* (H. Shang, D. Giuntini, E.A. Olevsky, and R.K. Bordia, “Pore Shape Evolution during Sinter-Forging of LSM-YSZ Composites,” *Acta Mater.*, prepared for publication).

Parts of Chapter 4 have been published in *Materials* (D. Giuntini, E.A. Olevsky, C. Garcia-Cardona, A.L. Maximenko, M.S. Yurlova, C.D. Haines, D.G. Martin, and D. Kapoor, “Localized Overheating Phenomena and Optimization of Spark-Plasma Sintering Tooling Design,” *Materials*, 6, 2013), in the *Journal of the Ceramic Society of Japan* (D. Giuntini, J. Raethel, M. Herrmann, A. Michaelis, C.D. Haines, and E.A. Olevsky, “Spark Plasma Sintering Novel Tooling Design: Temperature Uniformization during Consolidation of Silicon Nitride Powder,” *J. Ceram. Soc. Jpn.*, 124, 2016), and in the *Journal of the American Ceramic Society* (D. Giuntini, J. Raethel, M. Herrmann, A. Michaelis, and E.A. Olevsky, “Advancement of Tooling for Spark Plasma Sintering,” *J. Am. Ceram. Soc.*, 98, 2015). The dissertation author is the primary author of these publications. A part of the same Chapter 4 refers to work published in the *Journal of the American Ceramic Society*, of which the dissertation author was among the primary contributors (X. Wei, D. Giuntini, A.L.

Maximenko, C.D. Haines, and E.A. Olevsky, “Experimental Investigation of Electric Contact Resistance in Spark Plasma Sintering Tooling Setup,” J. Am. Ceram. Soc., 98, 2015).

Vita

- 2010 Bachelor of Science in Aerospace Engineering, University of Pisa, Italy.
- 2014 Master of Science in Aerospace Engineering (Aeronautical Engineering minor, Structures and Materials curriculum), University of Pisa, Italy.
- 2011-2016 Teaching Assistant, San Diego State University and University of California, San Diego.
- 2016 Research Assistant, San Diego State University and University of California, San Diego.
- 2016 Doctor of Philosophy in Engineering Sciences (Mechanical and Aerospace Engineering), University of California, San Diego and San Diego State University, USA.

Publications

- D. Giuntini, E.A. Olevsky, C. Garcia-Cardona, A.L. Maximenko, M.S. Yurlova, C.D. Haines, D.G. Martin, and D. Kapoor, "Localized Overheating Phenomena and Optimization of Spark-Plasma Sintering Tooling Design," *Materials*, 6 [7] 2612–2632 (2013).
- D. Giuntini, X. Wei, A.L. Maximenko, L. Wei, A.M. Ilyina, and E.A. Olevsky, "Initial Stage of Free Pressureless Spark-Plasma Sintering of Vanadium Carbide: Determination of Surface Diffusion Parameters," *Int. J. Refract. Met. Hard Mater.*, 41, 501–506 (2013).
- D. Giuntini, J. Raethel, M. Herrmann, A. Michaelis, and E.A. Olevsky, "Advancement of Tooling for Spark Plasma Sintering," *J. Am. Ceram. Soc.*, 98 [11] 3529-3537 (2015).
- X. Wei, D. Giuntini, A.L. Maximenko, C.D. Haines, and E.A. Olevsky, "Experimental Investigation of Electric Contact Resistance in Spark Plasma Sintering Tooling Setup," *J. Am. Ceram. Soc.*, 98 [11] 3553-3560 (2015).
- G. Lee, M.S. Yurlova, D. Giuntini, E.G. Grigoryev, J. McKittrick, and E.A. Olevsky, "Densification of Zirconium Nitride by Spark Plasma Sintering and High Voltage Electric Discharge Consolidation: A Comparative Analysis," *Ceram. Int.*, 41 [11] 14973-14987 (2015).
- D. Giuntini, J. Raethel, M. Herrmann, A. Michaelis, and E.A. Olevsky, "Spark Plasma Sintering Novel Tooling Design: Temperature Uniformization during Consolidation of Silicon Nitride Powder," *J. Ceram. Soc. Jpn.*, 124 [4] 403-414 (2016).

D. Giuntini, I.-W. Chen, and E.A. Olevsky, "Sintering Shape Distortions Controlled by Interface Roughness in Powder Composites," *Scripta Mater.*, 124, 38-41 (2016).

D. Giuntini and E.A. Olevsky, "Sintering Stress for Materials with Nonlinear Viscous Rheology," *Rapid Comm. J. Am. Ceram. Soc.*, accepted for publication.

E. Torresani, D. Giuntini, A. Molinari, and E.A. Olevsky, "Anisotropy of Mass Transfer during Sintering of Powder Materials with Pore-Grain Structure Orientation," *Acta Mater.*, prepared for publication.

D. Giuntini and E.A. Olevsky, "Sintering Kinetics of Agglomerated Powders with Nonlinear Viscous Rheology," *Acta Mater.*, prepared for publication.

H. Shang, D. Giuntini, A. Mohanram, E.A. Olevsky, R.K. Bordia, *et al.*, "Pore Shape Evolution during Sinter-Forging of LSM-YSZ Composites", *Acta Mater.*, prepared for publication.

D. Giuntini and E.A. Olevsky, "Optimization of Spark Plasma Sintering Tooling Design," *Advances in Powder Metallurgy & Particulate Materials, Proceedings of the Powder Metallurgy Conference 2015*, 09, 09-15.

Fields of Study

Major field: Engineering Sciences (Mechanical and Aerospace Engineering)

Studies in Sintering and Powder Technologies

Prof. E.A. Olevsky

Studies in Mechanical Behavior of Materials

Prof. E.A. Olevsky and Prof. M.A. Meyers

Abstract of the Dissertation

Optimization of Spark-Plasma Sintering Efficiency:
Tailoring Material Structure and Advanced Tooling Design

by

Diletta Giuntini

Doctor of Philosophy in Engineering Sciences (Mechanical and Aerospace Engineering)

University of California, San Diego, 2016

San Diego State University, 2016

Professor Eugene A. Olevsky, Co-Chair

Professor Marc A. Meyers, Co-Chair

The efficiency of Spark Plasma Sintering (SPS) is optimized by means of a temperature-based procedure. The correlations between temperature, porous material structure and tooling geometry are explored. The issue of agglomeration, cause of the formation of hierarchical porous structures in the powder compact, is addressed with an analytical and numerical approach. Densification kinetics, sintering stress, bulk and shear moduli of agglomerated compacts are modeled as functions of the hierarchy characterizing the porosity and the nonlinear viscous rheology of the material. The material nonlinearity is expressed by

the strain-rate sensitivity parameter, which in turn is dependent on temperature. An empirically-based explicit formulation of strain-rate sensitivity as a function of temperature is provided. A subsequent tuning of the strain-rate sensitivity allows the optimization of the thermal regime in order to obtain *in situ* de-agglomeration of the SPS specimen or the production of tailored material structures. In order to guarantee that the optimized thermal conditions are experienced by the entire specimen, we study the geometry of the SPS tooling setup. The tooling influence on temperature distributions is assessed in both the radial and the axial directions by means of a combined experimental and finite-element study. The phenomena underlying the presence of thermal gradients are individuated and controlled by tailoring the design of the tooling setup. Novel geometries are proposed for the components of the tooling, capable to annihilate the temperature disparities and thus complete the optimization of the SPS procedure. A comprehensive finite-element framework, in which both agglomerated powder compacts and tooling setup can be reconstructed and improved, is therefore developed.

Chapter 1

Introduction:

Uniformity of Materials Consolidated by Spark Plasma Sintering

Spark Plasma Sintering (SPS), also known as a low-voltage mode of Field-Assisted Sintering Techniques (FAST), is a powder consolidation technology that has been gaining growing attention in the last decades. Its distinguishing capabilities of densifying particulate materials within minutes instead of hours and with enhanced final chemical and mechanical properties are among the reasons lying behind such interest. The distinctions with respect to conventional sintering technologies do not consist solely in the application of an electric field, whose effects are still under controversial investigation and vary widely with the type of material considered, but extend to high heating rates and a consequent rapid volumetric heating of the entire powder specimen.¹⁻¹⁶ The specifications of a typical spark plasma sintering apparatus consist of low voltages (5-10 V) and high current (1-10kA), accompanied by heating rates up to 1000 °C/min and maximum attainable temperatures around 2400 °C (depending on the tooling material). The applicable loads range between 50 and 250 kN, again depending on the material of the tooling employed. Because of this combination of features SPS has been successfully employed to process a variety of different advanced materials, such as refractory metals and intermetallics, ultra-high temperature ceramics (UHTC), transparent polycrystalline ceramics, nano-structured materials, functionally graded materials (FGM), non-equilibrium materials, ceramic matrix composites, and many more.¹⁷

Even though largely applied in a variety of contexts, SPS still lacks deep understanding of these phenomena that render it so successful, and investigations on how to improve the procedure are needed. In the attempt of clarifying the role played by electric

fields in SPS, a new field-assisted sintering technique, flash sintering, was developed by Raj and coworkers.¹⁸⁻²² Here, by applying higher voltages to non-conducting ceramics without the aid of an external tooling, densification can be attained in a few seconds timeframe, thanks to thermal runaway phenomena, and possibly to the role played by atomistic defects. A significant amount of work has been conducted on the individuation of the onset of the flash phenomenon by Luo *et al.*, Pereira da Silva *et al.*, Chen *et al.*, and Todd *et al.*, but the mechanisms leading to densification in such reduced timeframes are still unclear.²³⁻³⁰ A hybrid between flash sintering and spark plasma sintering can be individuated in the high voltage electric discharge compaction (HVEDC), in which a specimen is inserted in an insulating die before applying high voltages (several kV) and pressures (greater than 100 MPa), leading to densification in a milliseconds timeframe.^{31, 32} In the area of FAST we can also consider microwave sintering, which enables a rapid volumetric heating and can be applicable to both ceramics and metals. Consolidation can be attained in timeframes that are somewhat in between conventional sintering and SPS.^{33, 34} All these field-assisted sintering techniques other than SPS involve, nevertheless, additional complex phenomena that go beyond the purposes of the present work. We will thus focus our attention on spark plasma sintering, better understood and widely employed in the materials processing community.

When studying spark plasma sintering optimization possibilities, several aspects can be considered, because of the "multi-physical" nature of the process itself, involving electric currents, heat transfer, solid and sometimes liquid mechanics, chemical reactions, phase transformations, and many more. The present work focuses on temperature-based optimization opportunities. The temperature parameter is already extremely wide in definition and implications. Both its temporal evolution and spatial distribution play a fundamental role during any SPS process. Additionally, its series of effects on the material system properties cannot be neglected. The analysis of temperature in SPS therefore needs to be initially

conducted from a basic point of view, in which temperature is considered as a major controlling parameter, and subsequently integrated into the complexity of the global SPS framework.

We can distinguish between temperature evolution in time, which is the sintering regime applied to the material that we aim at densifying, and its distribution in space, that can consider the only specimen or the entire SPS tooling setup employed in experimental procedures. The former allows the powder to undergo sintering, but also has substantial effects on the porous material structure. The latter controls the homogeneity of the final densified specimen, affects the overall tooling integrity and the procedure's safety, and can be controlled by means of the tooling geometry itself.

A temperature-based optimization procedure of SPS can, thus, proceed on two different levels, that also correspond to two different scales: material structure, which looks at the local morphology of the powder compact, and tooling design, which considers the entire SPS setup containing the specimen. We will first consider the former, and subsequently move to a larger scale and analyze the inter-relations between thermal distributions and tooling setup.

1.1 Material structure topology during spark plasma sintering

The material structure of a particulate medium can assume different meanings, and therefore the related studies on the optimization of SPS and other sintering techniques concern a variety of methodologies. In particular in the case of SPS, the high heating rates and the consequent fast processing time allow the development of strategies to address the issues of porosity non-uniformities in a particularly efficient way. This step is also specifically critical in SPS because of the recent shift of interest towards the consolidation of nanopowders.^{10, 35–43}

These kinds of particulate materials are extremely interesting for their high sinterability, which allows them to reach high final density values with excellent microstructural properties. Nanosized powders have led to the successful production of multi-functional ceramics, combining ultra-strength, hardness, translucency, transparency, or light-emission properties. In the field of multi-functional transparent and light-emitting nanoceramics, great progress has been attained lately by Garay *et al.*⁴⁴⁻⁵³ At the same time, nanopowders are very prone to the formation of hierarchical porous structures. Being spark plasma sintering claimed to guarantee the best outcomes in terms of nanopowders densification, the optimization of the porous material structure during this type of processing technique acquires a fundamental role for its successful application.

A first definition of porous material structure associates the hierarchical porous structure concept with bimodal or multimodal particle size distributions. The utilization of powder systems constituted by non-uniform powder particle sizes has been suggested since the early stages of conventional sintering in order to allow faster and more efficient densification. Studies similar to what conducted here, namely analyzing the densification kinetics of inhomogeneous powder mixtures, were conducted by Li *et al.*⁵⁴ and German *et al.*,⁵⁵ who both developed models for the consolidation of bimodal sized particle systems. The former considered hot isostatic pressing (HIP) of superalloys and, by assuming forces variation at the inter-particle contacts and considering the local deformations at such contacts, individuated densification rates for monomodal or bimodal particle systems. German *et al.* pointed out the significant improvements that bimodal powder systems allow in the green density of the specimens and developed expressions for the sintering kinetics of both sizes in order to allow predictions of the overall final density. This allowed the definition of optimization procedures for the particle size distributions, which were subsequently applied to experimental data on metals and ceramics. Even though such results were concerning

conventional sintering instead of SPS, they provided first attempts to optimize the powder consolidation regime by looking at the specimen's porous structure, and assessed the importance of the distributions of pore and particle sizes when aiming at obtaining uniform densification.

The same type of bimodal material structure was addressed by means of computer simulations, initially by Pan *et al.*⁵⁶ for spherical particles, and later by Cheng *et al.*⁵⁷ for cylindrical particles. Both determined shrinkage rates by considering the combined effect of grain boundary diffusion and surface diffusion and proposed optimization strategies. Recent works addressed the same problem with DEM techniques,⁵⁸ revealing that this type of bimodality affects all the stages of compaction in both metallic and ceramic particulates, and experimentally,⁵⁹ for tungsten, finally considering SPS instead of conventional sintering.

The study of multimodal powder sizes leads to the analysis of particle rearrangement during sintering. The analytical investigation of the role played by the disposition of particles in the powder compact was initiated by Petzow *et al.*,⁶⁰ who evidenced the importance of uniform arrangements to prevent localized stresses. Powder particle rearrangement has been frequently addressed by means of numerical simulations and discrete element methods. Leu *et al.* conducted a broad study of topological effects during sintering,⁶¹ individuating a univocal averaged densification rate for inhomogeneous material structures in both elastic and creep regimes. Kim *et al.* considered cold compaction,⁶² while DEM were utilized by Martin *et al.*, still for cold compaction,⁶³ and Henrich *et al.* for conventional sintering with a variety of loading conditions.⁶⁴ Both these last two analyses revealed the importance of material structure evolution and particle rearrangement, both in the pre-SPS cold compaction stage and in the sintering process itself, for the macroscopic properties of a porous medium.

The same denomination of multimodal material structures has been applied to composites too, whose behavior has been studied analytically, from a continuum perspective

for both hot isostatic pressing and spark plasma sintering,^{65, 66} and with combined experimental and numerical approaches for materials that have well-assessed characteristics when considered separately, such as copper and alumina.⁶⁷

A few more peculiar cases involved unconventional material structures in terms of powder particles shapes, such as compaction of hollow spheres.⁶⁸

Non-uniform material structures definitions that are closer to the ones that we will consider in the present work consist in inhomogeneous pores distributions. A comprehensive analytical model of the behavior of such a porous medium was proposed by Skorokhod *et al.*,⁶⁹ who applied a continuum approach to a domain characterized by different values of porosity fraction in separate zones. The pores size was instead uniform.

In spite of the classifications listed above, the inhomogeneous material structure that is the most typical and critical in sintering and especially SPS processes is agglomeration. Agglomeration phenomena and the consequent bimodal porous structures were first addressed by Rhodes and Lange,^{70, 71} and such topics are currently becoming progressively more relevant. The reason why this phenomenon has become progressively more significant is the above-mentioned widespread utilization of nanopowders, for whose consolidation spark plasma sintering is particularly suitable. Since these extremely fine powders are rapidly monopolizing the SPS applications field, and because of their very high tendency to agglomerate, the issue of hierarchical porous structures due to agglomeration has become of central importance in the analysis and optimization of SPS efficiency.

Powder agglomeration is the consequence of weak interactions among particles before compaction, leading to the formation of hierarchical porous structures. The hierarchy consists in the presence of multiple porosity sizes, typically small pores inside the agglomerates and larger ones among them (bimodal). Namely, weak forces, such as Van der Waals phenomena, tend to form agglomerates inside the loose powder, areas in which the particles are kept at

close distances, while large inter-agglomerate pores are left in the adjacent zones. Such hierarchical porous structures significantly hamper densification. The small size intra-agglomerate pores tend to sinter faster, so that the agglomerated areas become fully dense while large inter-agglomerate pores are still undergoing consolidation. Once the agglomerates have reached full density, large pores become difficult to eliminate, while in the dense areas grain growth starts happening. Thus, hierarchical porous structures lead to non-negligible amounts of residual voids and inhomogenous microstructure of the final product.⁷²⁻⁷⁵

The agglomeration problem has been experimentally detected in any type of material. Empirical strategies to prevent or solve the issue have been attempted.^{76, 77} In certain cases the addition of opportune agents prevents the formation of porosity hierarchies.^{78, 79} It has been shown that agglomeration also serves as obstacle in the production of transparent materials, such as YAG systems,⁸⁰ and a solution was found in the utilization of lyophilized YAG gels. Other approaches consisted in applying suitable pre-sintering powder treatments, typically milling and annealing.^{81, 82}

We have mentioned that the risk of formation of hierarchical porous structures increases when dealing with nanosized powders, which present new challenges in terms of agglomeration prevention and elimination. Complex mechanochemical processing is necessary to prevent it and a careful optimization of the milling and chemical agents addition route is required.⁸³ The problem becomes even more significant in nanocomposites. Schmid *et al.* shown that in alumina/silicon carbide nanocomposites the agglomerates of SiC were causing the stabilization of big pores.⁸⁴ In alumina/copper composites the alumina particulates present agglomeration problems both in hot pressing and spark plasma sintering.⁸⁵ In nanocomposites of carbon nanotubes and copper porosity tends to increase because of the nanotubes tendency to agglomerate.⁸⁶ Severe agglomeration issues are encountered in metal composites, but in certain specific cases they can be reduced with the tuned addition of

reinforcements, such as fullerenes.⁸⁷ It is worth mentioning that in some situations agglomeration is appositely produced to in-situ control the sintering process. This is usually the case in reactive sintering, and an example of successful application was offered by Cabouro *et al.*,⁸⁸ who created agglomerates in a MoSi₂ powder by high-energy planetary ball-milling. Tailored biporous structures have also become interesting for the energy sector, and specifically for the production of fuel cells components with maximized gas absorption capabilities.⁸⁹⁻⁹¹

These procedures are extremely specific and cannot be generalized to become more comprehensive guidelines. There is also a lack of investigations on how to eliminate agglomerates *in situ* instead of by means of preventive treatments. Pre-SPS processing can indeed be made vain by the subsequent necessary manipulation of the powder before the effective beginning of the sintering process. Anselmi-Tamburini *et al.* are among the few who addressed the hierarchical porous structure issue from this viewpoint.⁹² They were able to process nanopowders of zirconia, pure ceria and samaria-doped ceria by SPS and reach elevated final densities notwithstanding the presence of agglomeration. They achieved this result thanks to the application of extremely high pressures, up to 1 GPa, which caused particle rearrangement and agglomerates destruction in the initial stages of the process, and plastic or superplastic deformation in the subsequent steps. Such approach is effective, but limited in applications, since not any SPS device and tooling setup allows the utilization of these high pressure values.

Purely experimental approaches therefore present several limitations, since they tend to provide local empirical solutions to a problem that requires a more generic understanding. An exception consists in an experimental study by Ada *et al.* on agglomerated alumina that aimed at deriving the sintering kinetics parameters as functions of temperature.⁹³ This aspect is of particular importance, since we will show in the present work how significant the role

played by temperature in the reorganization of a hierarchical porous structure can be. Notice that in this case conventional sintering was the object of the study, while the analogous procedure has not been attempted for spark plasma sintering yet, even though the high heating rates of the latter offer promising opportunities of process optimization. Nevertheless, in the work by Ada *et al.* the kinetics studies concern the neck growth rate, and not the overall porosity evolution, which we will address in this work. Also, only intra-agglomerates kinetics were considered, due to the extremely elevated agglomeration content, around 80%.

Another more rigorous approach to the study of agglomeration was conducted by Liu *et al.* for zirconia powders, in which a quantification of the phenomenon was defined by means of the size ratio of sedimentationally-measured particles and primary particles.⁷⁷ Their results confirmed the strong influence of pore size hierarchy on both the green density and the sintering process, and in particular they evidenced that the presence of agglomerates enhances localized densification.

Among the most recent works, the investigation by Lichtner *et al.* is of particular interest, since they explored the characteristics of hierarchical porous structures by creating porosities with tailored morphology and geometry, thanks to a sequence of freeze-casting and partial sintering. It emerged that different mechanisms govern the shrinkage of large and small pores, where large and small sizes are defined relatively to the grain size of the material under consideration. Diffusion or shift of entire grains inside the voids can occur, depending on the dimensions of the pores and on the load applied.⁸⁹

It is thus evident that a more thorough analysis of agglomeration phenomena in sintering is necessary, namely by developing analytical models and numerical simulations of such hierarchical porous structures. At the same time, an experimental reference framework is necessary in order to conduct a reliable investigation. The present study will mainly refer to the most recent work of Lee *et al.*,⁹⁴ who reinvigorated the experimental investigation on

agglomerations issues by proposing a refined approach to powder de-agglomeration in the context of powder injection molding. By controlling the interface volume of agglomerates, they were able to enhance material transport, and analyze the densification process and microstructure evolution. Note that the case of SPS is even more critical than any other powder consolidation technique when dealing with agglomerated structures. The characteristic short processing time presents both advantages and disadvantages in the treatment of hierarchically porous materials. The disadvantages lay in the fact that such process rapidity, if the SPS regime is not appropriately tuned, and the powder shows the presence of agglomerates, can “crystallize” this hierarchy of the porosity and maintain the consequent non-uniformities in the final densified specimen. This combines with the high tendency of SPS-typical nanosized powders to form agglomerates. We, thus, need to exploit the advantageous side of the short processing times, by optimizing the holding temperature in order to obtain *in situ* de-agglomeration and prevent previous material rearrangements thanks to the high heating rates that only SPS can achieve. In order to do so, a necessary preliminary step of the study consists in modeling the behavior of inhomogeneous porous material structures.

While the presence of hierarchical porous structures and the related issues were individuated and addressed experimentally, some purely analytical and numerical studies arose, attempting to model these material structures and to make prediction on their evolution during sintering regimes. A first approach was suggested by Scherer, who developed a "cylindrical" model to simulate a porous medium.⁹⁵ It consisted of a net made of dense tubes with the porosity being constituted by the voids left by the net. This implies that the porosity is open, namely all interconnected and in communication with the external environment, and that therefore we are dealing with the initial stages of sintering, when pores are not isolated yet. By applying his analysis to a linear viscous biporous domain, *i.e.* with two sizes of pores

involved, he proved that large size pores are extremely difficult to remove. More interestingly, he also considered the domain from a macroscopic point of view, and individuated the effective elastic constants and densification kinetics for a medium containing two distinct types of porosities.

This latter aspect, the individuation of effective parameters by switching from a local scale to a global perspective, is of high interest when dealing with hierarchical porous structures, and was investigated by other authors in the following years. Kadushnikov and Skorokhod developed computer simulations in which they distinguished and reconstructed both the micro-scale, the local contacts among particles, and the macro-scale, the overall behavior of the agglomerated powder material.^{96,97} They investigated on the different mechanisms influencing densification kinetics and derived global parameters as functions of agglomeration. Since they did not use a continuum approach, the material parameters on which they focused were the mean coordination number and contact extent among particles. Analogously, but with an analytical study instead of numerical, Liu and German proceeded to emphasize the importance of mean nearest distance among the particles in agglomerated powder systems.⁹⁸

More recently, DEM simulations have been employed with similar purposes.^{99,100} In both cases, nevertheless, only cold compaction was analyzed, so that their results can provide valuable insight only on the pre-sintering route used to produce green specimens. In particular, Martin *et al.* conducted a comprehensive study in which the agglomerates presence was simulated by introducing additional interparticle contact forces. They studied the strength of agglomerates under compression, individually and globally during pressing in a rigid die. A notable influence of agglomerates crushability, morphology and rearrangement of densification emerged.

Perrin *et al.* combined analytical and numerical approaches in the study of the evolution of a biporous domain under hydrostatic tension.¹⁰¹ They introduced a convenient domain constituted by a hollow porous sphere, and treated the porous layer with Gurson's model,¹⁰² while the central hole was simulating the large porosity. Again, it emerged that large pores tend to not collapse or even grow, because of the coalescence of small pores adjacent to the large one with this large void itself. Gurson is the author of one of the principal theories on the plastic deformation of porous media, in which he defined yield criteria and flow rules for ductile materials containing voids.

Most of the models described above consider conventional sintering techniques, since they were developed in years in which spark plasma sintering was not well known and assessed as it is starting to be now. Indeed, these same works are limited to the description of the evolution of powders during the consolidation process, but they lack the proposal of strategies in order to improve the porous material structure, which is a possibility that non-SPS technologies do not offer. They, nevertheless, provide a valuable insight in the role played by agglomeration during densification, and inspirational suggestions on how to proceed to the modeling stages, also for SPS.

When aiming at optimizing the porous material structure by eliminating agglomeration *in situ*, and in particular during the SPS holding time, a fundamental step consists in the derivation of the densification kinetics of the two types of porosity present in the domain. The most significant works in this direction were conducted by means of the continuum theory of sintering. Olevsky and Rein were the first to investigate on the kinetics evolution with time for large size porosity and small size porosity separately, together with the global one. They derived analytical expressions for the porosities changes with time for a linear viscous material, but did not reformulate the porous material properties as a function of the hierarchical structure.¹⁰³ The subsequent works expanded their analysis, by deriving the

biporous material's mechanical properties, still for a linear viscous case, and utilizing numerical methods for the application of their results to a variety of loading schematics and external constraints.¹⁰⁴⁻¹⁰⁶ It was found that hot isostatic pressing leads to the fastest densification rates, while the process is slower in sintering in a rigid die, and even slower in sinterforging.¹⁰⁷ Large and small pores revealed to be very sensitive to the enforced constraints and loading paths, and this offered the possibility of optimizing both these parameters in order to control the two porosities kinetics, even though the most common case consisted in the faster densification of small pores with respect to the large size ones, as confirmed experimentally. Some disadvantages of this approach lie in the chance of having local increases in porosity and material instability. It also arose, by using a mean square strain rates-based analysis of the solid phase, which also allows the generalization to the macroscopic scale, that it is possible to have non-zero energy dissipation even in absence of macroscopic strains when agglomeration is present. This implies that collapse and growth of both types of pores are simultaneously possible, explaining the extreme instability and uncontrollability of hierarchical porous structures when spark plasma sintering technologies are not taken into consideration.¹⁰⁸

The abovementioned studies of hierarchical porous material structures are all based on a continuum approach. The porous material is considered as a continuum, whose mechanical properties are corrected in order to take into account the effects of the voids. The continuum theory of sintering was developed by Skorokhod, Olevsky and others.¹⁰⁹⁻¹¹³ The related publications proposed a constitutive equation for sintering processes, now well assessed in the literature, for linear and non-linear viscous materials, together with applications to a variety of case studies. The development of a continuum theory of sintering requires that the main mechanical properties of the domain considered are adjusted in order to take into account the presence of the pores. The first study that individuated the elastic constants of porous

materials was conducted by Mackenzie,¹¹⁴ and many others followed. Another fundamental parameter during sintering processes is the sintering stress, a consequence of the Laplace pressure that tends to minimize the free surface in the medium and thus to cause the shrinkage of a sintering specimen. Shuttleworth was among the first to theorize sintering stress and to individuate appropriate quantitative expressions.¹¹⁵ Sintering stress is a fundamental parameter of the theory of sintering, both with a continuum and with a particle approach. A large number of studies were therefore dedicated to the analysis of this parameter during the initial developments of sintering science.^{116–132} In later stages these investigations decreased in number, because of the dominating use of external pressures which values such that sintering stresses became negligible (hot pressing, sinter-forging, or spark plasma sintering of micro-sized powders). Most recently, nevertheless, the advent of nanopowders made this parameter non-negligible, as sintering stress is inversely proportional to the particle size.^{133–137} A fundamental contributor to the definition of sintering stress was Wakai, who proposed methods for the calculation of this parameter in a variety of contexts.^{138,139}

The great majority of the works on hierarchical porous structures conducted until now do not consider all these aspects simultaneously, and in the few cases in which they did, the material considered was assumed to be endowed with a linear viscous rheology. Such assumption eases the problem of individuating biporous materials' properties and kinetics, but cannot be considered applicable to a wide variety of case studies. A linear viscous behavior of the solid material in a sintering specimen is typical of amorphous materials, or of crystalline materials sintered in absence of external loads, where mass transfer through diffusion mechanisms is predominant.^{140–143} This implies that in the typical sintering and SPS processes, which generally deal with crystalline materials and employ external pressures to favor densification while hampering the undesired grain growth, the rheology of the material will be nonlinear viscous.

A nonlinear viscous behavior can be described as the creeping of the material due to the high temperatures and static loads to which it is subjected. The presence of creep has been assessed experimentally for most of the materials treated in spark plasma sintering and conventional sintering, for both metals and ceramics.^{144,145} Cannon and Langdon devoted a broad review publication, in two parts, in which he summarized the available experimental data and reported the existing models for the creep of ceramics, proving that even this kind of materials, characterized by brittleness, could present significant creep phenomena.^{146,147}

The deformation under creep of porous materials has often been studied starting from the solution of creep problems in opportune domains, typically spheres and cylinders presenting an internal hole. Simple analytical solutions or more complex ones are available in the literature,^{148–150} and they were used as sources of data on stresses and strain rates in the studies of sintering for the derivation of densification kinetics of a porous nonlinear viscous material. Comprehensive analytical models were developed by Kuhn and McMeeking for the case of open porosity,¹⁵¹ and by several other authors for closed porosity.^{73, 145, 152–161} More details of these works will be given later (Chapter 3), but it is already worth mentioning that they consist in analytical and numerical investigations on the power-law creep of monoporous media, thus not including the hierarchy characteristic of the porous structures that are the object of the present study. Their importance in the present context lies in providing valuable inspiration for the broadening of the problem to agglomeration's analyses and a series of useful comparisons for the model that we will develop, when we assume that the large inter-agglomerates pores disappear. The first and one of the most significant works in this direction was conducted by Wilkinson and Ashby,¹⁵² who derived densification kinetics for a porous material with nonlinear viscous rheology in all the stages of sintering. Their analysis was subsequently expanded by considering more complex loading conditions than the initial hot isostatic pressing, and formulating expressions for bulk and shear moduli that would take into

account both the presence of porosity and the power-law creep behavior characterizing the skeleton of the powder specimen.¹⁵⁵ Another fundamental model for the compression of powder materials with viscoplastic rheology was proposed by Carroll, Holt and Nesterenko. They considered dynamic loading conditions and the dependence of the powder material's viscosity and yield stress on temperature. Their results showed how the hollow sphere approximation is valid also for large amounts of voids, and that the temperature dependence of the mechanical characteristics of the powder leads to a good agreement with experimental results.¹⁶²⁻¹⁶⁴

All the proposed approaches dealt with the nonlinearity of the material as a set component of the process. What we aim at doing in the present study is connecting such nonlinearity with the treatment of hierarchical porous structures. While the previously conducted works considered either agglomerated structures with linear viscous rheology or non-agglomerated structures with nonlinear behavior, here we develop a semi-analytical approach to identify the densification kinetics, mechanical properties and sintering stress of a hierarchical porous structure characterized by a power-law creep rheology.

This is the where the optimization of the material structure becomes possible: the strain-rate sensitivity characterizing the type of creep that the material is undergoing is a temperature-dependent parameter. Even though it is well known that strain-rate sensitivity, the indicator of the nonlinearity of a creeping material, is not constant with temperature,¹⁶⁵ the literature lacks investigations about such a dependency. Norton points it out,¹⁶⁶ Follansbee *et al.* proposed an expression of strain-rate sensitivity as a function of the material's mechanical properties, dislocations, activation energy, applied stress and temperature.¹⁶⁷ Another expression, empirical, was proposed by Schindler *et al.*, for whom strain-rate sensitivity was a linear function of temperature, at least in a specific range of this parameter.^{168, 169} These are mainly empirical formulations, with validity restricted to the specific material system utilized

and hardly generalizable. Even less explored are the optimization approaches of the sintering material's structure based on temperature, with the only exception being, to the best of our knowledge, a work by Olevsky and Molinari analyzing the problems of instability in the early stages of compaction, for both free sintering and hot isostatic pressing, and developing an optimization procedure for the sintering route able to control such undesired effects.¹⁷⁰ Being spark plasma sintering a relatively new technology, an analogous type of optimization, aimed at eliminating agglomeration *in situ* and supported by the high temperatures and heating rates that only this technology can achieve, has not been conducted yet and will be the main topic of our study. An efficient de-agglomeration stage is vital in order to achieve the best possible outcomes in terms of uniformity of the sample's density and microstructure, and therefore to attain optimal mechanical properties in the entirety of the final products.

Once developed a theoretical framework in which the main features of the biporous material are expressed as a function of the strain-rate sensitivity, by simply assuming this parameter as piecewise constant for the various levels of temperature considered, we will perform our *in situ* elimination of agglomerates thanks to a suitably optimized thermal route. Spark plasma sintering makes this possible thanks to its intrinsically high heating rates, which do not allow for material reorganization and pre-holding densification at non-optimized temperatures. Chapter 3 will consider this temperature-based modeling and optimization of hierarchical porous material structures.

1.2 Spark plasma sintering tooling setup and temperature

As anticipated at the beginning of this introduction, for spark plasma sintering it is not enough to perform an optimization of the temperature regime. In order to guarantee that such regime is effectively experienced by the overall powder specimen, one needs to ensure that the

thermal spatial distribution within the specimen is uniform. Such a step is not trivial in spark plasma sintering. The flow of current through the SPS setup, to which the temperature distribution is entangled, can follow several paths, depending on the powder system that is being consolidated and the geometry of the tooling setup. Since the first parameter cannot be altered if not slightly, by means of dopants and additives aimed at enhancing densification more than homogenizing it, a thermal distribution optimization needs to be based on the latter.

The presence of an articulated tooling setup, made of several components assembled around the powder specimen, is unavoidable in SPS, but at the same time this creates severe temperature gradients issues. The larger the size of the setup, the more significant such inhomogeneities become.¹⁷¹⁻¹⁷⁵ Depending on the electrical resistivity of the powder relative to the tooling material's one, the current will flow through the powder compact or around it, thus creating localized overheating at the center or at the edge of the specimen, depending if we are dealing with a conductor or an insulator. Significant localized overheating phenomena can also appear in zones further from the specimen, therefore not hampering the densified product's properties directly, but endangering the integrity of the tooling and the safety of the process, together with creating undesired energy wastes. A non-optimized SPS tooling setup is, therefore, the origin of a series of problems during experimental procedures, ranging from non-uniform density and microstructure in the densified specimen to serious damages of the tooling and the entire device.

Since these thermal gradients are very intense even within the powder specimen itself, it is immediate to infer that a thermal route optimization cannot be applied successfully unless such disparities are annihilated. A material structure optimization cannot be considered complete without a temperature distributions optimization, which can only rely on a redesign of the geometry such that it is guaranteed that the entirety of the specimen will experience the selected temperature profile.

Even though the fundamental role played by the SPS tooling geometry has been broadly assessed, among the approximately 700 yearly publications addressing current-assisted sintering techniques, only a few works investigated on the role played by the tooling setup characteristics and on the relative possibility of optimization, treated with experimental approaches, numerical modeling or a combination of both. Such studies analyzed the consequences of modifying the constituent material,¹⁷⁶⁻¹⁸⁰ the geometrical design of the components,^{171, 172, 181} the manufacturing machine's combination with characterization technologies,^{182, 183} or the scalability of the process.^{184, 185} Being this last aspect of fundamental importance in the understanding of how thermo-electrical phenomena distribute within the powder specimen and the entire setup, since an increase in the characteristic dimensions unfailingly causes the development of augmenting internal temperature gradients, it is rather surprising that so far non-uniformities have been assessed only for small sample diameters.¹⁸⁶

Some more specific analysis were operated in order to customize the die shape for the production of complexly shaped axial symmetrical parts and of functionally graded materials,¹⁸⁷ evidencing how extensive and versatile SPS-tooling optimization procedures can be. More efforts are needed in order to attain satisfactory results in terms of reproducible production of bulky parts with homogeneous property distributions, suitable for industrial production.¹⁸⁸

When considering the SPS or FAST equipment, certain distinctions have been individuated and defined, in the context of comprehensive reviews of the various methodologies and patents released since the introduction of these electrically-assisted densification technologies.^{31, 189, 190}

Even in this variety of approaches, an analysis fully dedicated to the optimization of the tooling design in order to mitigate thermal gradients has not appeared yet. A setup optimization process needs to follow a thorough analysis of the conventional configurations'

conditions, in which the influencing factors can be pointed out, classified and investigated. Therefore a preliminary study of the internal temperature distributions needs to be performed as a first step.

The SPS devices present intrinsic difficulties in measuring the sample actual temperatures, since the process happens in a closed chamber and in vacuum conditions. The temperatures can be measured only at specific points, usually by means of a single probe (thermocouple or pyrometer), or by two separate ones in the best case scenario. After a few experimental approaches to the temperature distributions' reconstruction,^{191–193} numerical tools have revealed to be particularly effective in compensating for this lack of experimental data.^{194, 195} Finite element models have been developed, capable to simulate the electrical and thermal evolutions of the specimen and tooling components during SPS procedures.^{47, 186, 196–}

201

These were the first attempts to the building of temperature and current mapping methods by means of numerical simulations, and involved only the respective electricity and heat transfer simulations. Nevertheless, in order to faithfully recreate the experimental conditions, fully coupled models, combining electrical currents, heat transfer, mechanics and densification kinetics, need to be implemented. The complex interconnected phenomena happening during a SPS procedure require the simultaneous combination of all these physics to consider a numerical framework reliable. A variety of studies have addressed this issue, providing indispensable information on the inherent mechanisms of such innovative densification techniques.^{202–213}

Thermal gradients in the axial and in the radial cross-section planes of the SPS setup have usually been addressed separately. This study aims at mitigating both. A broader section (Chapter 4) will be dedicated to the radial temperature disparities, since these are the ones that generate the most significant non-uniformities in the specimen, and thus their annihilation is

an immediate requirement for the completion of our material structure optimization study. We do not want to neglect the axial inhomogeneities either, which will be considered in the same Chapter 4. Axial thermal disparities have resulted to be even more intense than the radial ones, and can directly hamper the specimen's evolution for when the aspect ratio between the height and the diameter of the powder compact is close to 1. They also have a high potential for tooling damaging.

We have, thus, shown how broad and interrelated the temperature-related aspects of SPS optimization can be. The aspects that need to be considered when aiming at uniformizing the conditions experienced by the powder compact, and therefore its morphology, range from the distribution and size of the pores to the geometry of the tooling setup. This implies that the problem can be addressed at multiple scales. Multi-scale approaches are indeed showing their high potential for advanced materials processing, and particularly for spark plasma sintering.^{214, 215}

We can look at the so-called meso-scale, the one relative to the porous material structure. At this level the problems related to agglomeration phenomena have been experimentally evidenced by a variety of authors, and modeled, analytically or numerically, by a few, but never for SPS, which is the technology in which these issues are most influential. The important role played by the strain-rate sensitivity for the densification kinetics of hierarchical porous structures has barely been identified in the literature, in which this nonlinearity parameter has been taken into consideration only for materials in which porosity is assumed to be uniform in size and distribution. The temperature dependence of this same strain-rate sensitivity has also been investigated in a very limited fashion. We, therefore, aim at compensating for this lack of analyses on hierarchical porous structures in materials with nonlinear viscous rheology (that is the most common situation in SPS) by connecting all these aspects. A semi-analytical model will be developed throughout Chapter 3. We will not only

derive the densification kinetics of the various types of porosities contained in an agglomerated powder, but we will also evaluate the effects of the compresence of multiple pore sizes on the overall mechanical properties of the specimen. By defining parameters such as bulk modulus, shear modulus and sintering stress - which until now have only been investigated for non-hierarchical structures and linear viscous rheologies - for the more comprehensive and reality-adherent case of nonlinear viscous materials presenting agglomeration, we will also be empower our modeling framework with a macro-scale perspective that looks at the entire specimen. We will therefore have a variety of tools allowing us to individuate the most suitable SPS processing temperatures such that strain-rate sensitivity reaches values that can lead to *in situ* powder de-agglomeration. Multi-scale FEM modeling of biporous structures will also be addressed.

An even larger scale can be reached in this field of temperature-based optimization of spark plasma sintering, since we need to look at the entire tooling setup in order to understand how thermal effects distribute within the specimens. The fundamental influence of the tooling geometry on the formation of significant temperature gradients within the SPS setup has been recently the object of a large number of studies, which, nevertheless, fail to investigate on the physical phenomena underlying such mechanisms and to propose improvement strategies. Chapter 4 will be dedicated to this larger scale of the temperature optimization study. Thermal gradients will be thoroughly analyzed by means of an extensive experimental and numerical campaign, until the main factors affecting temperature distributions in SPS are individuated. We will finally apply the acquired knowledge into the redesign of the geometry of certain tooling components able to uniformize the temperatures within the entire tooling and specimen assembly.

The combination of thermal route and thermal distribution improvements results in a spark plasma sintering efficiency optimization capable of guaranteeing the best outcomes in

terms of specimen's uniformity and mechanical characteristics. Such results are reached with an investigation that includes the development of a novel analytical model for hierarchical porous structures with nonlinear viscous rheology and of a FEM framework for the reconstruction of any SPS procedure.

Chapter 2

Research Objectives:

Optimization of Spark Plasma Sintering Efficiency

In the previous chapter we have provided an overview of the several aspects involved in the study of how to optimize Spark Plasma Sintering (SPS) efficiency with temperature as the main parameter. We have explained that the SPS temperature regime and distribution both play fundamental roles in the characteristics of the final densified product. The thermal route impacts the uniformity of the porous material structure, while the temperature spatial distribution is strongly dependent on the geometry of the employed tooling.

We can therefore identify two major research objectives for the present work:

1. Material structure optimization;
2. Temperature uniformization within SPS specimen and tooling.

The two objectives are subsequent to each other. Namely, material structure optimization relies on the selection of the ideal thermal route for SPS procedures, which thus needs to be uniformly experienced by the entirety of the processed powder specimens (while keeping the SPS tooling setup in safe conditions by avoiding overheating issues).

The first objective can, in turn, be subdivided into two sub-categories, depending on what type of final result one is interested in achieving:

1. Material structure optimization
 - a. In situ de-agglomeration (porous structure uniformization);
 - b. Production of tailored hierarchically porous structures.

Each objective has a corresponding major research task, namely:

Objective 1. Ideal SPS thermal routine selection;

Objective 2. Improved tooling geometry design.

as we have pointed out how the thermal routine controls the material structure evolution and the tooling geometry influences the temperature distribution within the SPS setup.

For Objective 1, we will also explore collateral factors that need to be tuned, together with the thermal routine, in order to be able to achieve de-agglomeration during processing. Specifically, we will focus on the role played by the initial porous material structure, namely the relative dimensions of agglomerates and powder particles (or, equivalently, small and large voids), which have a direct influence on the shrinkage kinetics of a porous specimen.

The associated research tasks need to take into account the main features of nanopowders undergoing spark plasma sintering processing.

A realistic porous material structure subjected to spark plasma sintering is characterized by the presence of agglomerates and in most cases by a nonlinear viscous rheology. The formation of hierarchical porous structures is due to the growingly widespread utilization of nanopowders, for which SPS is considered to be particularly suitable, but that also tend to undergo non-negligible agglomeration phenomena. A nonlinear viscous rheology is characteristic of the processing of crystalline materials at high temperatures with the application of external loads, which is the case in most of the SPS applications. A lack of comprehensive analyses has been revealed during the associated literature review, thus we aim here at creating an analytical framework to describe material structures presenting both these aspects. We will describe hierarchical porous structures by means of a simplified spatial domain and we will derive expressions of the main mechanical characteristics.

The research tasks associated with the first research objective therefore consist in the development of analytical expressions for:

- Densification kinetics of the different types of porosities;
- Bulk and shear moduli;
- Sintering stress.

Since we will consider a power-law creep behavior of the solid material, all the parameters listed above will be dependent on the material's nonlinearity, which is expressed by the strain-rate sensitivity parameter. Being strain-rate sensitivity a function of temperature, by opportunely tuning the SPS temperature route we will be able to mitigate the undesired consequences of agglomeration. Specifically, we aim at individuating the optimal holding temperature, which is the highest temperature reached during the consolidation process, and corresponds to the stage in which most of the specimen's shrinkage happens and the microstructural characteristics are defined. A specific value of strain-rate sensitivity will correspond to this optimal temperature value. A fourth research task necessary to accomplish the first research objective thus consists in:

- Individuation of the correlation between strain-rate sensitivity and temperature.

The power of SPS in this context relies on the high heating rates that this technique allows, such that the optimal holding temperature is reached in very short times (few minutes), and that the reorganization of the material structure typical of heating ramps in conventional sintering is here prevented.

The obtained material properties for biporous structures will also enable the formulation of a multi-scale FEM-based modeling framework. Simulations can be

implemented to reconstruct the simultaneous evolution of entire specimen and the various types of porosities. This numerical tool will become valuable for both de-agglomeration and design of tailored hierarchical porous structures. The last research task associated with the material structure optimization research objective is then:

- Implementation of a multi-scale FEM simulation platform for densification processes.

We have subsequently noted that for this thermal route optimization to be successful, we need to ensure that the temperatures are uniformly distributed throughout the entire specimen. This is the second research objective.

The non-triviality of this aspect in the context of SPS has been assessed by a variety of authors. We will therefore complete our study by developing a strategy to homogenize temperatures within the powder compact and even in the rest of the tooling setup.

The necessity, typical of SPS, to locate the powder compact into an articulated tooling setup is the cause of a complex distribution of the flow of current through the tooling itself, and consequently of the heat generated by Joule effect. The geometry of this tooling greatly affects the conditions experienced by the powder compact. Some studies have explored the consequences of changing the dimensions, and more rarely the design, of the various components of the tooling assembly, but a lot still needs to be done to understand the underlying mechanisms behind thermal gradients and how to control them in a convenient way.

The thermal gradients that appear during SPS can be distinguished based on the cross-section they interest, *i.e.* radial thermal gradients, in particular in the central cross-section of the specimen, and axial thermal gradients, which involve all the tooling components.

We aim at developing optimal tooling redesign strategies capable of annihilating the specimen's non-uniformities and guaranteeing the safety of the SPS device and process. We want to propose novel tooling designs of simple realization that exploit the knowledge gained from the temperature distribution analysis. We will do so with an extensive campaign of finite-element simulations and with the appropriate experimental verification.

The research tasks corresponding to the second research objective are thus found in the following sequence of steps:

- Experimental individuation of temperature non-uniformities;
- Development of a multi-physics FEM framework involving both specimen and tooling;
- Punch redesign for radial thermal gradients mitigation;
- Transition redesign for axial thermal gradients mitigation.

The meaning of the above-listed tooling components will be clarified in the following sections.

We, finally, plan to integrate the two developed aspects of SPS optimization in a multi-scale and multi-physics modeling framework in which predictions on densification uniformity and tailored material structures can be obtained, and again experimentally verified.

The following flow chart identifies the present work's research objectives, the associated research tasks, and the relative interconnections.

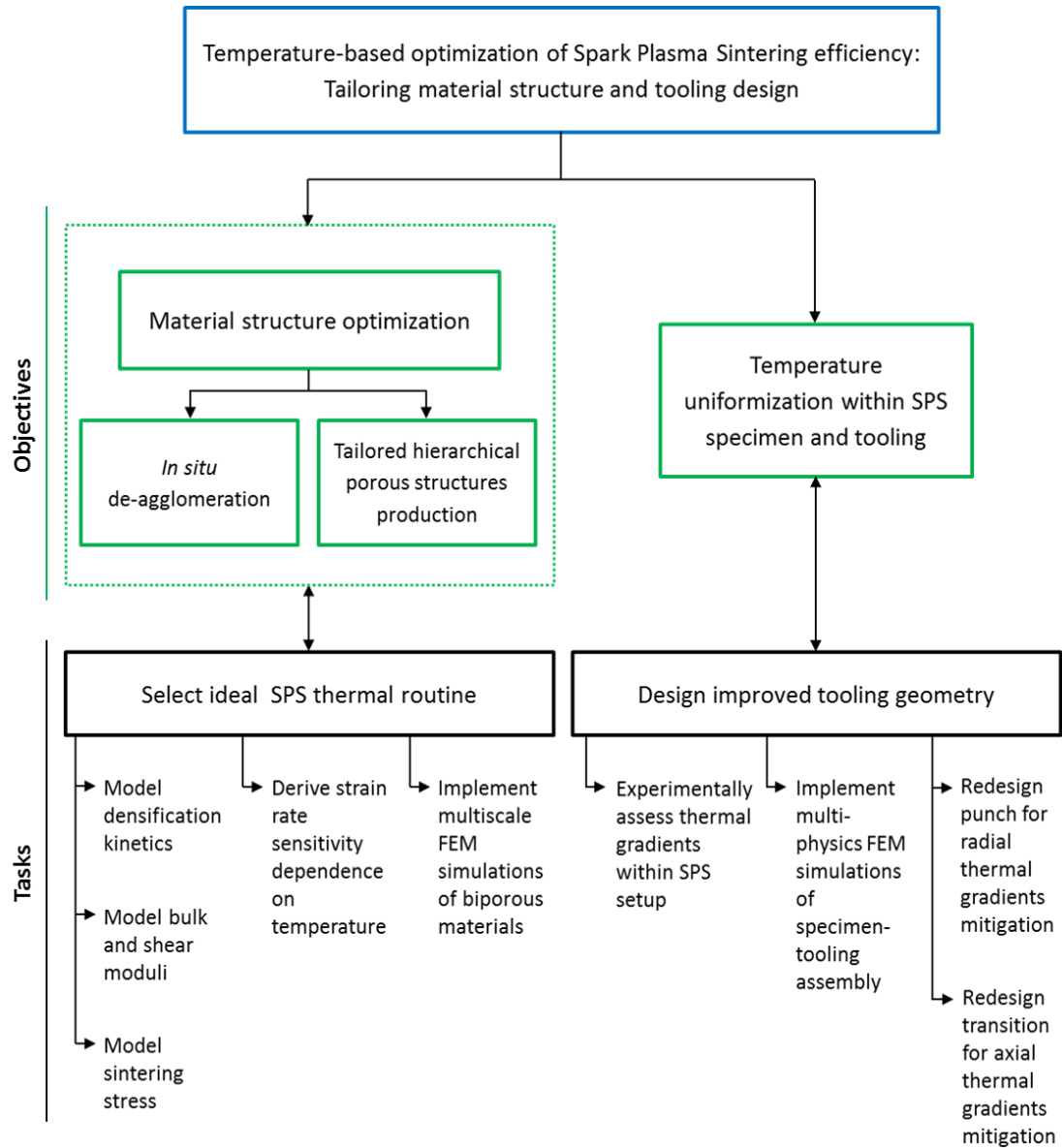


Figure 2.1 – Flow chart of the research objectives.

Chapter 3

Modeling of Consolidation of Hierarchical (Agglomerated) Porous Structures with Nonlinearity of the Material's Constitutive Behavior

3.1 Semi-analytical modeling of hierarchical porous structures densification kinetics

3.1.1 Definition of hierarchical porous structures

As introduced in the previous chapters, an optimization of the spark plasma sintering process based on the role played by the temperature can be conducted on different levels. While an improvement in the spatial temperature distribution is to be performed by means of an improved tooling design (Chapter 4),¹⁷³⁻¹⁷⁵ a very important aspect lies in the temperature regime to be applied. The role played by the latter does not consist merely in the selection of the most suitable values of heating rate and holding temperature in order to allow densification to happen. The temperature regime has a more indirect, but certainly non-negligible, influence on the evolution of the porous structure of the specimen at the so called “meso-scale”.

There is a sort of “loop” effect between the SPS material structure and temperature uniformization. The powder material structure controls how temperature is distributed within the specimen itself, such that material structure homogenization implies temperature uniformization. This, in turn, leads to controlled and homogeneous pore and grain structure evolution. Such a feedback effect is what the proposed spark plasma sintering optimization relies on.

In a powder compact, three scales can be individuated. The macro-scale considers the entire specimen, and deals with its global shrinkage and other macroscopic characteristics. The micro-scale goes down to the level of the grains constituting the single powder particles, and it is the aspect we refer to when analyzing grain growth and local defects, such as vacancies and dislocations. The meso-scale is introduced because of the powders' natural tendency to form inhomogeneous porous structures since the stages antecedent to sintering itself, and it is roughly comparable to the particle size, or slightly larger. It is at the meso-scale that hierarchical porous structures are identified. Such non-uniform configurations of the loose powder morphology are due to weak interactions among the particles, mainly Van der Waals forces tending to attract the powder particles towards each other. These interactions are responsible for the formation of groups of agglomerated powder particles, another definition of hierarchical porous structures.

Figure 3.1 depicts a typical agglomeration phenomenon, in the loose powder (top) and after partial densification (bottom). These images were obtained during a study on the consolidation of vanadium carbide by means of conventional sintering and SPS.⁷² Even though the focus of the study was on the neck growth kinetics and on the individuation of the VC's surface diffusion parameters, some interesting side aspects appeared. Conventional sintering resulted to be not capable of processing vanadium carbide, since, even after long exposures to supposedly optimal temperatures, the sintered specimen appeared to have started densification only at the center, while the outer area was extremely crumbly. Spark plasma sintering provided better outcomes, but agglomeration issues arose, as the bottom part of the same figure shows.

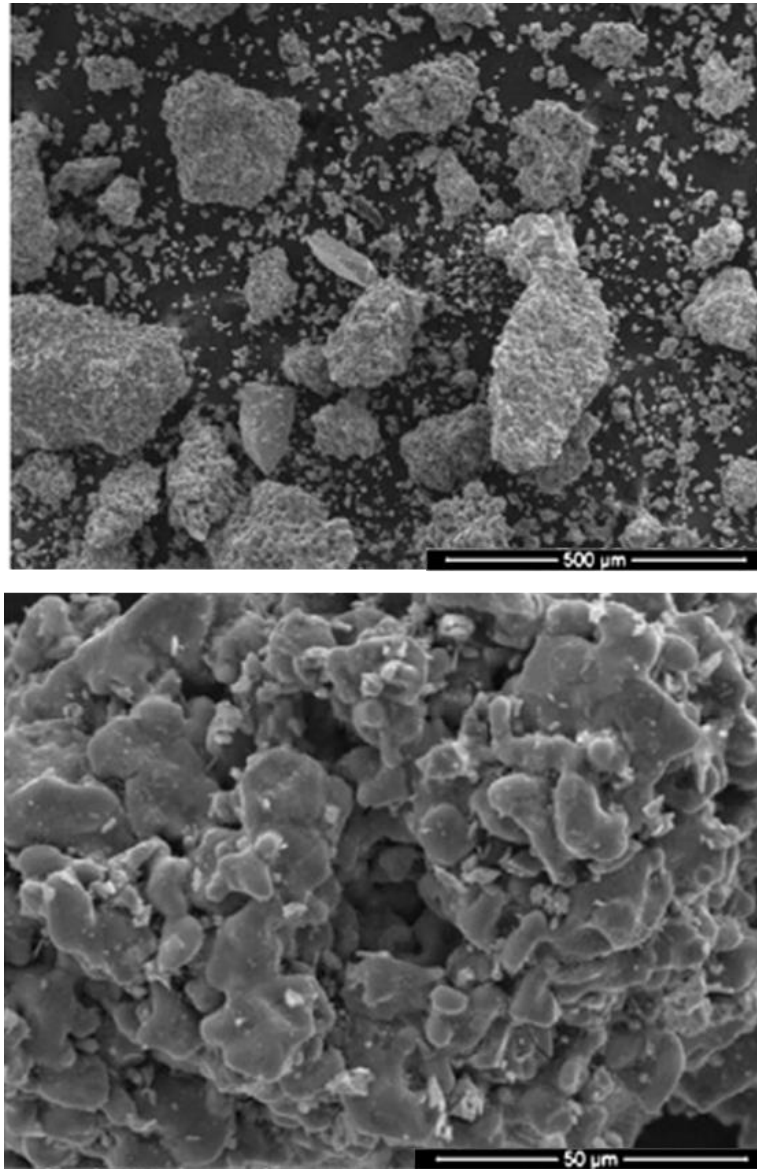


Figure 3.1 – Agglomeration in a vanadium carbide powder: loose powder (top) and after spark plasma sintering (bottom).
(Giuntini *et al.*, *Int. J. Refract. Met. Hard Mater.*, 2013)⁷²

Agglomerates are fragile unions of powder particles, but the proximity that the involved particles experience is a cause for intra-agglomerates preferential densification. If the agglomerates are not removed prior to the application of raising temperatures, they will tend to undergo a faster sintering process with respect to the looser adjacent powder, characterized by larger distances among the particles and therefore hampered diffusion phenomena. Agglomerated areas can therefore reach quasi-full density while the neighboring areas are still at the initial consolidation stages. Once such localized and uneven densification is attained, the specimen's meso-scale morphology will consist in a number of “stones”, namely fully dense zones, hard to deform and surrounded by a highly porous matrix, whose voids' elimination will now be extremely complex. Figure 3.2, Figure 3.3 and Figure 3.4 show further examples of this phenomenon. The preferential densification within the agglomerates is evident. Figure 3.4 highlights how relevant agglomeration becomes in the case of nano-sized powders, and depicts the respective schematics.

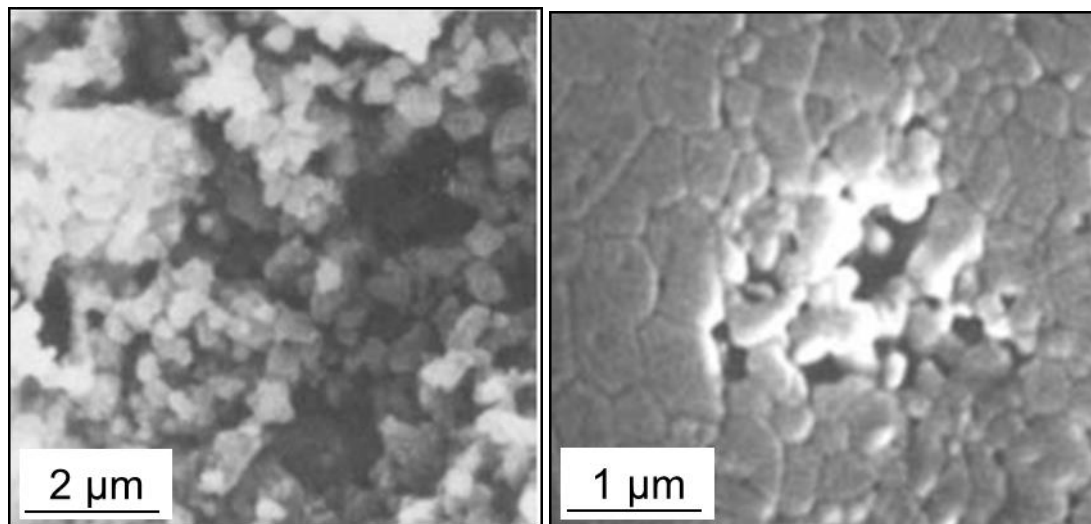


Figure 3.2 – Effects of agglomeration in loose powder and sintered materials.
(Sacks M. D. and Pask J. A., *J. Am. Ceram. Soc.*,1982)²¹⁶

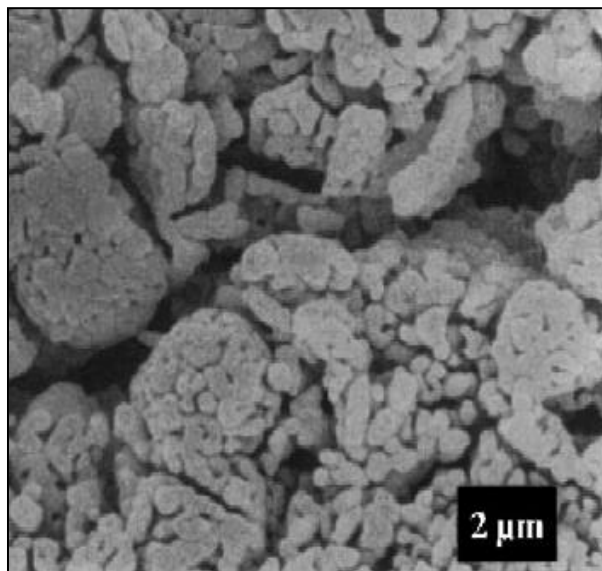


Figure 3.3 – Partially sintered agglomerated alumina.
 (Ada K. et al., *Powder Tech.*, 2006)⁹³

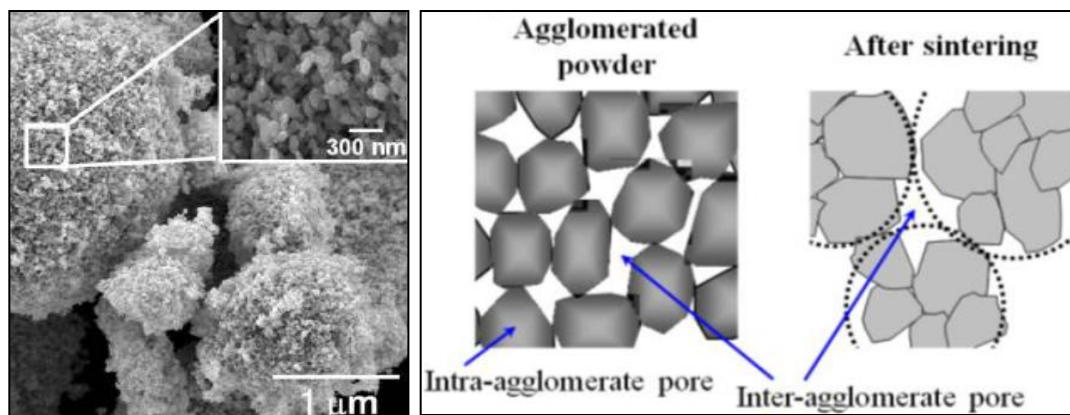


Figure 3.4 – Agglomeration in iron nanopowders and schematics of its effects.
 (Lee J.S. et al., *Materials*, 2013)⁹⁴

At this point it is clear how agglomeration is a phenomenon that greatly damages sintering processes, leading to strong non-uniformities in density and grain size in the final product. Once the agglomerated areas have reached full density, indeed, grain growth phenomena will start occurring locally, while the same phenomena are prevented from occurring in the still porous proximities. The inhomogeneities due to hierarchical porous structures are comparable to the ones caused by uneven temperature distributions or localized stresses due to differential shrinkage (processing of composites), and therefore deserve a careful analysis.

Both the prevention and the elimination of agglomerates are difficult tasks to perform. Such difficulty becomes more significant when reducing the size of powder particles from the micrometer to the nanometer order of magnitude. Nanopowders are gaining growing attention in the spark plasma sintering field, because of the improved density and microstructure properties that they allow the final product to attain, together with their intrinsic capability of enhancing consolidation thanks to the large available free surface area, whose minimization is the driving force for sintering. Their use is becoming widespread for the production of advanced ceramics, such as high surface area components used in supercapacitors, rechargeable batteries and gas absorbers. At the same time, nanopowders are obviously more prone to be subjected to agglomeration phenomena.

Whatever the particles size is, nevertheless, directly impeding the formation of hierarchical porous structures is a delicate and sometimes even unfeasible step. Even though the employment of apposite additives or of optimized mixing and milling procedures as pre-sintering steps has shown successful applications, the handling of the powder subsequent to these steps, such as its simple relocation or the preparation of the green sample, can significantly reduce the just obtained beneficial effects by leading to the creation of new hierarchical structures.

We, therefore, chose to address the problem at a different stage of the SPS process: we considered *in situ* de-agglomeration. Here is where the importance of the temperature regime in optimizing SPS efficiency lies. De-agglomeration operated during the consolidation process itself relies on the applied pressure and, mainly, temperatures. It has been shown, as anticipated in the introductory chapter, that the pressures necessary for *in situ* removal of pores hierarchy are of the GPa order of magnitude, which are values hard to attain in conventional SPS devices.⁹² Temperatures offer a more technologically feasible option.

A crystalline material, especially if sintered with the aid of an external pressure, presents a nonlinear viscous rheology during sintering. In such a case, the behavior of the skeleton (the solid portion of a porous domain) is described by means of the power-law creep behavior, which can be expressed as follows

$$\sigma(W) = A_m W^m \quad (3.1)$$

where σ is an equivalent stress (Pa), W an equivalent strain rate (1/s), m the strain-rate sensitivity (1) and A_m a factor with an Arrhenius-type dependence on the activation energy for power-law creep (Pa·s^m). The subscript m has been added in order to distinguish it from the A utilized in the most common creep equations, such as Ashby's model,²¹⁷ where strain rate is given as a function of stress, and not vice versa. We will denote this most common factor with A_n , since the corresponding creep law is usually given as

$$\dot{\epsilon} = A_n \sigma^n \quad (3.2)$$

Here the strain rate has been indicated by $\dot{\epsilon}$ instead of W because such power-law creep equation, in its most general form, does not necessarily consider porous materials. It is also immediate to see that

$$A_m = \frac{1}{(A_n)^m} \quad (3.3)$$

and

$$m = \frac{1}{n} \quad (3.4)$$

which are useful relationships, since in the literature one can generally find tabulated the values of A_n and n for a variety of materials.

By observing this formulas, we immediately see that when $n = 1$ the linear viscous case is represented, while when $n \rightarrow \infty$ we are ideally in a regime of perfect plasticity. It follows that

$$0 < m < 1$$

with $m = 0$ being the perfectly plastic case, and $m = 1$ the linear viscous one.

The meaning of equivalent stress and equivalent strain rate of equation (3.1) are relative to the continuum theory of sintering¹¹³ and will be clarified in detail later.

As for now it is important to emphasize that the possibility of optimizing the SPS efficiency by means of an opportune holding temperature lies in the role played by the strain-rate sensitivity m . Even though it has almost always been treated as a constant value, mainly for simplicity's sake and lack of experimental data, there is a general agreement on recognizing that strain-rate sensitivity changes with temperature.¹⁶⁵ Such dependence is not of immediate determination, but a good approximation can be defined by analyzing it as piecewise constant, suitable to the individuation of the optimal holding temperature. The empirical models proposed in the literature for the description of creep phenomena can also be employed, together with the available data, to find the relation between strain-rate sensitivity and the soaking temperature chosen for the powder consolidation process. The latter is the approach selected for the present work, described in detail in section 3.2. Thanks to the high heating rates typical of SPS, we will be able to reach the optimized holding temperature values

in an extremely rapid fashion, therefore preventing undesired effects of material structure reorganization during the heating ramp.

We will show how m , which is also an index of the nonlinearity of the material's viscous behavior, influences all the main parameters of sintering, namely its kinetics and the properties of a porous material. More specifically, we will derive densification equations, sintering stress, bulk and shear moduli for a hierarchical porous structure with nonlinear viscous constitutive behavior, and consequently identify how a change of strain-rate sensitivity (caused by a change in temperature) can positively affect spark plasma sintering. A dependence on temperature is found in A_m too, since

$$A_n = A_0 \exp\left(-\frac{Q_{PLC}}{RT}\right) \quad (3.5)$$

where A_0 is a pre-exponential factor depending on the material considered ($1/\text{s}/\text{Pa}^n$), Q_{PLC} the activation energy for power-law creep (J/K/mol) and R the Boltzmann constant (J/K/mol). A_m will also be taken into account in order to optimize the SPS thermal regime. A comparative study on the influence of both A_m and m will be conducted in order to identify the power-law creep parameter which has the strongest impact on the consolidation of hierarchical porous structures, and on such comparison the structural optimization procedure will be based.

In order to address the densification kinetics problem, a suitable domain describing hierarchical porous structures needs to be defined. One can first consider a typical morphology at the meso-scale of a green specimen. Since agglomerates consist in powder particles kept at a closer distance with respect to the neighboring ones, it is reasonable to assume that the pores inside an agglomerate will be of smaller size than the inter-agglomerates ones. We can therefore describe a green specimen as a biporous structure, with small size intra-agglomerates porosity and a large size inter-agglomerates one. We will denote the former as θ_S and the latter as θ_L , while the overall porosity will be simply called θ . By porosity, in general, we

indicate the volume fraction of the domain considered that is occupied by voids, and it is therefore a dimensionless parameter.

Figure 3.5 provides the schematics employed for the identification of the study domain. We imagine considering a large, inter-agglomerate pore, surrounded by agglomerates that are themselves porous with small internal voids. We approximate the large pore as spherical, and we take a concentric spherical layer of agglomerated material to complete the domain. We therefore have a large central spherical void surrounded by a concentric porous spherical shell. The geometry of the domain is fully defined by the two radii a and b , a being the internal radius (large pore radius) and b being the external radius of the entire domain.

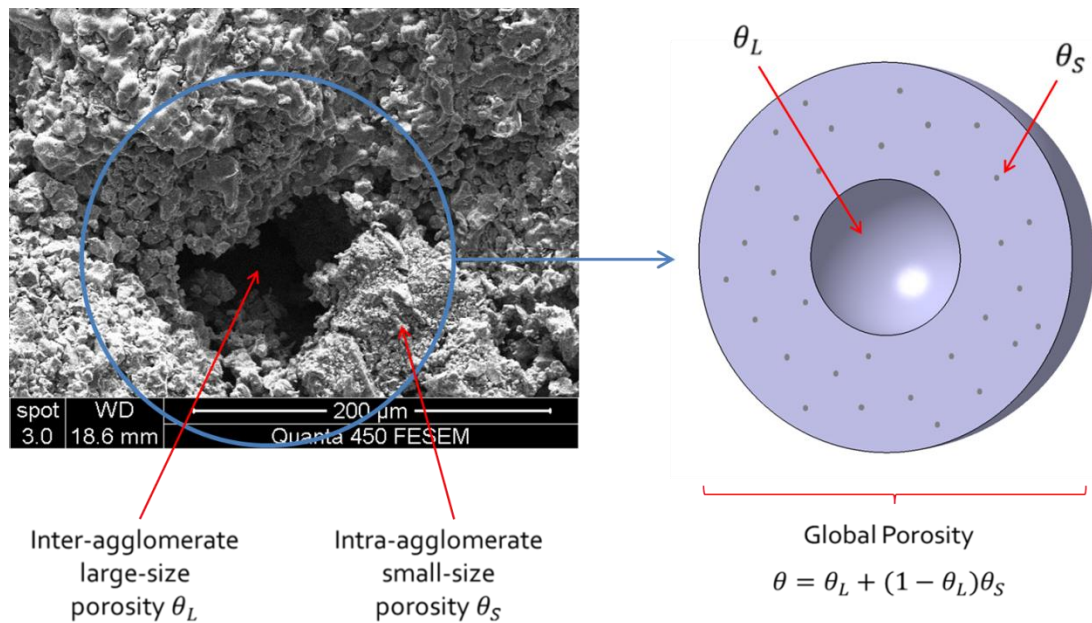


Figure 3.5 – Definition of the study domain representative of hierarchical porous structures.

While the small size porosity θ_S will be directly treated with the continuum theory of sintering,¹¹³ and consequently embedded in the external layer as an intrinsic material property,

large size and total porosities can be easily defined through geometrical considerations. θ_L is the ratio of the volume occupied by the large central hole divided by the entire domain's one, and θ is calculated as the sum of the two volume fractions (small and large voids).

It follows that

$$\theta_L = \left(\frac{a}{b}\right)^3 \quad (3.6)$$

and

$$\theta = \theta_L + (1 - \theta_L)\theta_S \quad (3.7)$$

We will consider the process of spark plasma sintering assisted by an externally applied pressure operating on our domain. We assume the spherical biporous layer to be located in the middle of a specimen characterized by the repetition of such type of hierarchical structure, so that it is reasonable to also consider the domain as subjected to a hydrostatic compression at its outer border, which we will call P_{ext} , as Figure 3.6 shows. The same Figure 3.6 also shows that at the internal boundary of the shell a load is applied, called P_{L0L} . This is the surface sintering stress due to the surface tension, which is the force responsible for the voids progressive shrinkage and ultimate disappearance.

We will dedicate a section of the present chapter to the sintering stress definition for a hierarchical porous structure endowed with nonlinear viscous constitutive behavior. Here we will limit to clarify the notation utilized. P_L is the general denomination chosen for sintering stress, since the stress caused by surface tension is often called Laplace pressure. We distinguish between P_L , a body stress characteristic of a porous body undergoing sintering (and therefore shrinkage), and P_{L0} , the surface stress acting at the boundary of a single void and leading to its closure. The former is the result of averaging the effects of all the pores present in a material and trying to minimize their free surface area, when enough energy is

provided in the form of temperature. The latter is directly proportional to the surface tension of the material considered, and inversely proportional to the pore characteristic size.

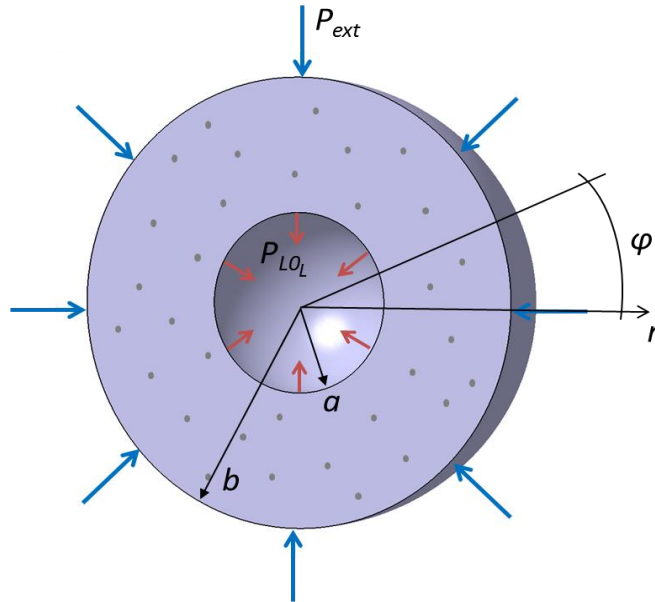


Figure 3.6 – Geometry and loading schematics acting on the biporous study domain.

In the case of spherical pores, the factor of proportionality has been found to be 3 (while it would be 2 for cylindrical pores).¹¹¹ The subscripts S and L will generally always be indicating if we refer to small or large size porosity.

Thus, P_{L0_L} is the surface sintering stress acting on the large pore, which is

$$P_{L0_L} = \frac{3\alpha}{r_p} = \frac{3\alpha}{a} \quad (3.8)$$

with α surface tension of the material considered (J/m^2) and r_p radius of the pore (m), in this case equivalent to the large pore radius a .

3.1.2 Sintering kinetics of hierarchical porous structures

The final aim of our study consists in optimizing the SPS outcomes in terms of density and microstructure uniformization (or, alternatively, building tailored porous structures). In a biporous domain, a necessary condition to attain such homogeneity consists in eliminating the porosity “duality” itself, by reducing the size of the large pores until it reaches the typical dimensions of the small ones. It is crucial that the large porosity shrinkage occurs at a faster pace than the small porosity one, in order to avoid the formation of preferentially densified areas (the abovementioned “stones”) and their undesired consequences. We aim at designing temperature regimes that allow a quick densification of large size porosity, such that, once θ_L becomes comparable in size to θ_S , the spark plasma sintering will be applied to a homogeneous, monoporous powder compact, as ideal consolidation conditions require.

Thus, we need to analyze how sintering kinetics evolve during SPS in the case of a hierarchical porous structure. Namely, we search for two equations capable to describe the densification rates of the two porosities as functions of the applied load, material properties and temperature regime, indirectly involved by the power-law creep parameters, and especially by the strain-rate sensitivity.²¹⁸

In synthesis:

$$\dot{\theta}_S = f(\theta_S, \theta_L, P_{ext}, A_m, \alpha, m)$$

$$\dot{\theta}_L = g(\theta_S, \theta_L, P_{ext}, A_m, \alpha, m)$$

When plotting large and small size porosities with respect to time, we investigate on how to reach the ideal condition of having the two curves not crossing each other, at least until the very end of the SPS regime. We, indeed, reasonably assume to have an initial large size porosity value $\theta_L(t = 0) = \theta_{L_0}$ that is lower than the small size porosity one $\theta_S(t = 0) = \theta_{S_0}$, and therefore the uniformization of the porosity size translates in a progressive reduction

of the central void volume while θ_S has not reached zero yet. On the contrary, if the two curves crossed each other, this would be indication of the agglomerates having reached full density while the large inter-agglomerate pore is still undergoing the shrinkage process.

To derive the two functions f and g the continuum theory of sintering is applied to our biporous domain.¹¹³ By applying the appropriate boundary conditions to the sintering characteristic equations, we can obtain the kinetics of θ_S , and therefore derive the evolution θ_L by means of geometrical considerations.

The constitutive equation of the porous material behavior during sintering is

$$\sigma_{ij} = \frac{\sigma(W)}{W} \left[\varphi \dot{\varepsilon}_{ij} + \left(\psi - \frac{\varphi}{3} \right) \dot{\varepsilon} \delta_{ij} \right] + P_{L_S} \delta_{ij} \quad (3.9)$$

in which σ_{ij} is the stress tensor (Pa), $\dot{\varepsilon}_{ij}$ the strain rate tensor (1/s), $\dot{\varepsilon}$ the first strain rate tensor invariant, namely the trace of the tensor (1/s), φ the normalized shear modulus (1), ψ the normalized bulk modulus (1), δ_{ij} the Kronecker delta, P_{L_S} the volumetric sintering stress due to the presence of small pores in the matrix (Pa).

While, as anticipated in the previous paragraphs, the surface sintering stress, tending to cause the closure of the pore to which it is applied, is purely a function of surface tension and pore size, the volumetric sintering stress is an averaged parameter that comes into play when considering a material endowed with a very high number of pores, which we decide to treat as a continuum. If we have a porous matrix that contains a distribution of small pores, which we will assume to be isotropically distributed, the application of a continuum theory requires that the properties of the bulk (fully dense) material constituting the layer are appropriately modified in order to embed the effects of the pores on the overall material domain. This translates in deriving suitable formulations for bulk and shear moduli (that indeed here are functions of porosity), and in adding to the main equation a term that accounts for the tendency of the porous material to shrink. Such term is the sintering stress, which is

expressed as the surface sintering stress associated with a small pore multiplied by a function h of the porosity that we are including in our continuum, as

$$P_{L_S} = \frac{3\alpha}{r_{sp}} h(\theta_S) \quad (3.10)$$

We will show in the next sections of this chapter how h can be individuated and how the expression of the sintering stress is altered when dealing with a hierarchical porous structure. It is worth mentioning now that the surface sintering stress is generally well approximated as independent of temperature, since it has been found experimentally and for a variety of materials that the changes in surface tension with temperature can be considered negligible in the SPS context (while obviously porosity is evolving with temperature).²¹⁹ The study of P_L that we will propose later will nevertheless include an indirect correlation with the thermal conditions experienced by the sintering sample, because we will search for an expression that considers the sintering stress dependence on the material's nonlinear rheology, namely on the strain-rate sensitivity m . Being m a function of temperature, the volumetric sintering stress will start playing a role in the optimization of the temperature regime to be applied in order to eliminate agglomeration. The more common assumption of P_L being independent on temperature holds only as long as the material power-law creep behavior is not considered as a significant contribution, or as long as we take the strain-rate sensitivity as a constant value. Thus, we aim at individuating more precise expressions for the sintering stress, paying particular attention at its variations when switching from a homogeneous monoporous powder compact to a hierarchical porous structure as the one described by our domain (Figure 3.5).

Finally, the equivalent stress and strain rate $\sigma(W)$ (Pa) and W (1/s), are the two parameters that take into account the contribution of the skeleton, which is the fully dense material located in the external porous spherical layer. In the case of a crystalline material

being deformed at high temperatures with the aid of an externally applied load, the skeleton deforms following a power-law creep behavior.

The equivalent stress $\sigma(W)$ is thus expressed as a function of the equivalent strain rate as reported in equation (3.1), and W is written as

$$W = \sqrt{\frac{\psi \dot{\epsilon}^2 + \varphi \dot{\gamma}^2}{1 - \theta_S}} \quad (3.11)$$

where the only still undefined parameter is $\dot{\gamma}$, the second invariant of the strain rate tensor (1/s), associated with the domain's change of shape and expressed as a function of the deviatoric part of the tensor $\dot{\epsilon}'_{ij}$ as

$$\dot{\gamma} = \sqrt{\dot{\epsilon}'_{ij} \dot{\epsilon}'_{ij}} \quad (3.12)$$

Before proceeding with our derivations, it is important to underline here that the sintering constitutive equation has been written only in terms of the small size porosity, θ_S . All the parameters, such as W and P_{L_S} , even the ones that have not been defined yet, φ and ψ , do not include the large size porosity. This can be better understood by looking at our domain definition again. We have a porous spherical matrix surrounding a concentric large hole. The porous spherical matrix contains the small pores, in an extremely high number and whose distribution is unknown, but assumed to be widespread enough to render the overall matrix isotropic. Such is the condition that allows the treatment of a porous domain as a continuum. The large size porosity, on the other hand, is represented by a single central void, whose sintering will coincide with its progressive volume shrinkage due to the external load and to the shrinkage of the surrounding matrix. Therefore, the continuum theory of sintering is solely applied to the external layer, endowed with the small size porosity, while the large porosity change will be evaluated geometrically, thanks to the derivation of the velocities of the internal and external boundaries of the domain (at a and b).

Once defined all the parameters and clarified this point, we can proceed to substitute the power-law creep law in the constitutive equation, which becomes

$$\sigma_{ij} = A_m W^{m-1} \left[\varphi \dot{\varepsilon}_{ij} + \left(\psi - \frac{\varphi}{3} \right) \dot{\varepsilon} \delta_{ij} \right] + P_{LS} \delta_{ij} \quad (3.13)$$

Note that we have only substituted $\sigma(W)$ and W , while we have left open the formulations for φ , ψ and P_{LS} . Even though in the literature many models have been proposed for the normalized moduli and the sintering stress, only a small number of them consider the case of nonlinear viscous rheology,^{155, 156, 160} even less the case of agglomerated (hierarchical) structures,¹⁰⁴ and none of them the combination of both effects. These parameters will therefore be individuated in the following paragraphs and only finally included in our densification kinetics formulations.

The boundary conditions for our domain (Figure 3.6) are

$$\sigma_r|_a = -P_{L0L} \quad (3.14)$$

$$\sigma_r|_b = -P_{ext} \quad (3.15)$$

The strain rate tensor first and second invariants, in spherical coordinates and taking into account the symmetries, become respectively

$$\dot{\varepsilon} = \dot{\varepsilon}_r + 2\dot{\varepsilon}_\varphi \quad (3.16)$$

and

$$\dot{\gamma} = \sqrt{\frac{2}{3}} |\dot{\varepsilon}_r - \dot{\varepsilon}_\varphi| \quad (3.17)$$

with the strain rate radial and tangential components, again considering the symmetries, expressed as a function of the radial velocity V_r (m/s) only

$$\dot{\varepsilon}_r = \frac{\partial V_r}{\partial r} \quad (3.18)$$

$$\dot{\varepsilon}_\varphi = \frac{V_r}{r} \quad (3.19)$$

Thus what we need is V_r . In order to derive it we can notice the following

$$\frac{\partial V_r}{\partial r} + 2 \frac{V_r}{r} = \dot{\epsilon} \quad (3.20)$$

and also that

$$\frac{\partial V_r}{\partial r} + 2 \frac{V_r}{r} = \frac{1}{r^2} \frac{\partial}{\partial r} (r^2 V_r) \quad (3.21)$$

so that

$$\frac{\partial}{\partial r} (r^2 V_r) = \dot{\epsilon} r^2 \quad (3.22)$$

from which, assuming that $\dot{\epsilon}$ is constant with the radius r , we obtain

$$V_r = \frac{1}{3} \dot{\epsilon} r + \frac{C}{r^2} \quad (3.23)$$

In order to find C , we can employ the so-called sintering similitude equation, which is an equation that relates stress and strain rate invariants by means of the bulk and shear moduli:

$$\psi \frac{\dot{\epsilon}}{p - P_{LS}} = \varphi \frac{\dot{\gamma}}{\tau} \quad (3.24)$$

The similitude condition applied to the continuum theory of sintering arises from an analogy with the theory of plasticity. In the theory of plasticity we find an association rule between stress and strain fields. Its most common version is the similitude condition, according to which the stress and the deformation tensors are organized in an analogous fashion. This propagates to the invariants, leading to an expression that relates the ratios between first and second stress and strain invariants, with the appropriate proportionality coefficients. In the context of plasticity, these coefficients are constants, the plastic multipliers; while here we have the normalized bulk and shear moduli, functions of porosity, and strain rates instead of strains. Note that we also correct the first stress invariant, p , by subtracting the compressive hydrostatic contribution of the sintering stress.

In our spherical domain, writing the tensors invariants in terms of their components and substituting in (3.24), the similitude condition becomes

$$\psi \frac{\dot{\epsilon}}{\frac{\sigma_r + 2\sigma_\varphi}{3} - P_{L_S}} = \varphi \frac{\dot{\epsilon}_r - \dot{\epsilon}_\varphi}{\sigma_r - \sigma_\varphi} \quad (3.25)$$

where the various components denominations are self-explaining.

Rearranging and substituting our expressions for the strain rates, we get

$$\sigma_r - \sigma_\varphi = \frac{\varphi}{\psi} \frac{(-3C/r^3)}{\dot{\epsilon}} \left(\frac{\sigma_r + 2\sigma_\varphi}{3} - P_{L_S} \right) \quad (3.26)$$

Now, in order to find C , we apply the boundary condition at $r = a$, i.e. the large pore sintering stress acting on the internal boundary of the porous layer.

We find that C is

$$C = \dot{\epsilon} a^3 \frac{\psi}{\varphi} \frac{P_{L_{0L}}}{P_{L_{0L}} + 3P_{L_S}} \quad (3.27)$$

Therefore the radial velocity is expressed as

$$V_r = \frac{1}{3} \dot{\epsilon} r + \dot{\epsilon} \frac{a^3 \psi}{r^2 \varphi} \frac{P_{L_{0L}}}{P_{L_{0L}} + 3P_{L_S}} \quad (3.28)$$

and consequently the radial and tangential strain rates become

$$\dot{\epsilon}_r = \frac{1}{3} \dot{\epsilon} - 2\dot{\epsilon} \frac{a^3 \psi}{r^3 \varphi} \frac{P_{L_{0L}}}{P_{L_{0L}} + 3P_{L_S}} \quad (3.29)$$

$$\dot{\epsilon}_\varphi = \frac{1}{3} \dot{\epsilon} + \dot{\epsilon} \frac{a^3 \psi}{r^3 \varphi} \frac{P_{L_{0L}}}{P_{L_{0L}} + 3P_{L_S}} \quad (3.30)$$

From now on, for simplicity of notation and derivations, we will denote the sintering stresses ratio as follows

$$k = \frac{P_{L_{0L}}}{P_{L_{0L}} + 3P_{L_S}} \quad (3.31)$$

By substituting the obtained strain rates expressions in the constitutive equation, and rearranging, we arrive at the following formulation for the radial stress component σ_r

$$\sigma_r = A_m \dot{\epsilon}^m (1 - \theta_S)^{\frac{1-m}{2}} \psi^{\frac{m+1}{2}} \left(6k^2 \frac{a^6 \psi}{r^6 \varphi} + 1 \right)^{\frac{m-1}{2}} \left(1 - 2k \frac{a^3}{r^3} \right) + P_{LS} \quad (3.32)$$

At this point, with the aim of obtaining the small size porosity kinetics, we can utilize the indissolubility condition.

Reminding that $\dot{\epsilon}$ is the change in volume of the porous shell, and that θ_S is the volume fraction occupied by small pores in that same shell, conservation of mass imposes

$$\dot{\epsilon} = \frac{\dot{\theta}_S}{1 - \theta_S} \quad (3.33)$$

so that the expression for the radial stress becomes

$$\sigma_r = A_m \left(\frac{\dot{\theta}_S}{1 - \theta_S} \right)^m (1 - \theta_S)^{\frac{1-m}{2}} \psi^{\frac{m+1}{2}} \left(6k^2 \frac{a^6 \psi}{r^6 \varphi} + 1 \right)^{\frac{m-1}{2}} \left(1 - 2k \frac{a^3}{r^3} \right) + P_{LS} \quad (3.34)$$

We can now impose the remaining boundary condition for σ_r , at $r = b$. By doing that and remembering the definition of the large size porosity θ_L , we get

$$-P_{ext} = A_m \dot{\theta}_S^m \frac{(\theta_S - 1)^{1-m}}{(1 - \theta_S)^{\frac{m+1}{2}}} \psi^{\frac{m+1}{2}} \left(6k^2 \theta_L^2 \frac{\psi}{\varphi} + 1 \right)^{\frac{m-1}{2}} (1 - 2k\theta_L) + P_{LS} \quad (3.35)$$

and rearranging we finally derive the densification rate of the small size porosity, as

$$\dot{\theta}_S = \left[\frac{P_{ext} + P_{LS}}{A_m (2k\theta_L - 1)} \left(6k^2 \theta_L^2 \frac{\psi}{\varphi} + 1 \right)^{\frac{1-m}{2}} \left(\frac{1 - \theta_S}{\psi} \right)^{\frac{m+1}{2}} (\theta_S - 1)^{m-1} \right]^{\frac{1}{m}} \quad (3.36)$$

We can now proceed to the derivation of the large size porosity evolution, namely to the individuation of an expression for $\dot{\theta}_L$. Because of the reasons explained above, $\dot{\theta}_L$ can be individuated by means of simple geometrical considerations, such as

$$\dot{\theta}_L = \frac{d(a^3/b^3)}{dt} = \frac{3a^2 da}{b^3 dt} - \frac{3a^3 db}{b^4 dt} \quad (3.37)$$

with

$$\frac{da}{dt} = V_r|_a = \dot{e}a \left(\frac{1}{3} + k \frac{\psi}{\varphi} \right) \quad (3.38)$$

$$\frac{db}{dt} = V_r|_b = \dot{e}b \left(\frac{1}{3} + k\theta_L \frac{\psi}{\varphi} \right) \quad (3.39)$$

Substituting the boundary radial velocities in the $\dot{\theta}_L$ expression we obtain

$$\dot{\theta}_L = -3k\theta_L(1 - \theta_L) \frac{\psi}{\varphi} \frac{\dot{\theta}_S}{1 - \theta_S} \quad (3.40)$$

and ultimately

$$\dot{\theta}_L = -3k\theta_L \left(\frac{1 - \theta_L}{1 - \theta_S} \right) \frac{\psi}{\varphi} \left[\frac{P_{ext} + P_{L_S}}{A_m(2k\theta_L - 1)} \left(6k^2\theta_L^2 \frac{\psi}{\varphi} + 1 \right)^{\frac{1-m}{2}} \left(\frac{1 - \theta_S}{\psi} \right)^{\frac{m+1}{2}} (\theta_S - 1)^{m-1} \right]^{\frac{1}{m}} \quad (3.41)$$

Equations (3.36) and (3.41) provide the sintering kinetics of a biporous material. They need to be solved numerically, for instance with a Runge-Kutta (4,5) scheme, so that we can get the curves of θ_S and θ_L versus time. This is the only not purely analytical step in this section of our optimization study, which therefore has to be more correctly addressed as semi-analytical. As an aside, notice that, on the other hand, Section 3.2 will be mostly numerical, with the wide employment of finite element methods, and such will also be a substantial part of Chapter 4.

Together with the kinetics of the two porosities volume fractions, it is interesting to also monitor the evolution of the pores size with time.

The shrinkage rate of a small pore can be expressed as¹⁰³

$$\dot{r}_{sp} = r_{sp} \frac{\dot{\theta}_S}{3\theta_S(1 - \theta_S)} \quad (3.42)$$

which can be easily derived if we consider a spherical domain with a central small pore, as shown in Figure 3.8 of the following sections.

The shrinkage rate of a large pore is immediately inferred from the radial velocity field in our domain as given above. Considering the large pore's surface, $r = a$, we retrieve equation (3.38), such that, with the necessary substitutions

$$\dot{a} = a \left(\frac{1}{3} - k \frac{\psi}{\varphi} \right) \frac{\dot{\theta}_S}{1 - \theta_S} \quad (3.43)$$

The evolutions of small and large size porosities (volume fractions and radii) are given as a function of strain-rate sensitivity, material properties and externally applied load. Again, the temperature dependence is well expressed by the presence of m and A_m in our equations. We begin to notice now why we are focusing our temperature-based optimization on m and not on A_m . Indeed, A_m appears in both kinetics expressions in an analogous way, which implies that a change in its value plays a parallel role in both the evolution of small and large pores. This means that the densification curves will shift, but no significant changes will occur in terms of their behavior with respect to each other, such as the time at which they intersect.

Note also that all the other involved parameters, sintering stress and moduli, have been left explicitly mentioned in both equations. The reason behind this temporary choice is that, instead of using formulations provided by previous studies, we are interested in deriving our own expressions for all these parameters, expressions that need to take into account both the nonlinearity of the skeleton's viscosity and the hierarchical character of the meso-scale porous structure.

In the following sections we will, therefore, proceed to the derivation of our own P_{LS} , ψ and φ expressions. We will find such parameters for both the monoporous and the biporous case. The former is what we need to examine in order to find formulas to plug into the densification equations that we have just found, since, again, the matrix mechanics require that we consider the volumetric sintering stress and moduli relative to the small size porosity only

(therefore a monoporous context). The latter is an extension of the study that is needed if we want to shift from the meso-scale to the macro-scale. Finding sintering stress, bulk and shear moduli of a biporous structure corresponds to individuating the global macroscopic mechanical properties of a powder characterized by non-negligible phenomena of agglomeration. Individuating the properties of a biporous domain allows us to replace our domain composed by a spherical porous layer with an internal large void, with a homogenous and isotropic spherical domain, whose mechanical characteristics will already be taking into account the internal presence of two porosity sizes, and therefore the effect of the agglomerates.

The explicit densification kinetics equations for the two porosities, (3.36) and (3.41), for the pores sizes, (3.42) and (3.43), and the macroscopic sintering stress and moduli, therefore, provide a complete framework for the analysis of the hierarchical porous structures behavior.

The densification equations are an indispensable resource of information about how the shrinkage of the two types of porosities evolves with time, and most interestingly on how strain-rate sensitivity (and therefore the thermal regime) can control the consolidation process by enhancing the size reduction of the large inter-agglomerates pores while allowing only a slower disappearance of the small intra-agglomerates ones (Section 3.2.1).

The macroscopic properties and sintering stress of a biporous structure provide the possibility of treating the SPS specimen by the sole macroscopic perspective, and therefore evaluating its sintering globally, by looking at the entire specimen, without any need of modeling its internal morphology. Such expressions will also be a very valuable tool for the finite-element reconstruction of the SPS of a powder compact with an internal distribution of agglomerates, since the knowledge of the macroscopic mechanical properties prevents us from needing to simulate a complex multiscale framework in which both the meso-scale and the

macro-scale aspects need to be simultaneously considered during the computations (Section 3.2.2).

In Section 3.2 we will explore this latter aspect and the general FEM modeling of a hierarchical porous structure under SPS conditions, but first we will proceed to the individuation of the various sintering stresses (Section 3.1.3), bulk moduli (Section 3.1.4) and shear moduli (Section 3.1.5).

To conclude the biporous structures' sintering kinetics section, it is worth mentioning that a more elegant "time definition" can be utilized in the porosity evolution equations, which is the specific time of sintering. By specific time of sintering we mean a normalized time expression that varies depending on the rheology of the material and that allows a more effective comparison among different cases because of its normalized nature.

In our case, which is power-law creep with non-negligible sintering stress acting on the pores' surfaces, it can be written as

$$t_s = \left(\frac{P_{ext} + P_{L0S}}{A_m} \right)^{\frac{1}{m}} t \quad (3.42)$$

By replacing the time derivatives of equations (3.36) and (3.41) with the derivatives with respect to this specific time of sintering, we obtain

$$\frac{d\theta_S}{dt_s} = \left[\frac{\left(1 + \frac{P_{LS}}{P_{ext}}\right)}{\left(1 + \frac{P_{L0S}}{P_{ext}}\right)} \left(6k^2\theta_L^2 \frac{\psi}{\varphi} + 1\right)^{\frac{1-m}{2}} \frac{(\theta_S - 1)^{m-1}}{(2k\theta_L - 1)} \left(\frac{1 - \theta_S}{\psi}\right)^{\frac{m+1}{2}} \right]^{\frac{1}{m}} \quad (3.43)$$

$$\frac{d\theta_L}{dt_s} = -3k\theta_L \frac{1 - \theta_L}{1 - \theta_S} \frac{\psi}{\varphi} \left[\frac{\left(1 + \frac{P_{LS}}{P_{ext}}\right)}{\left(1 + \frac{P_{L0S}}{P_{ext}}\right)} \left(6k^2\theta_L^2 \frac{\psi}{\varphi} + 1\right)^{\frac{1-m}{2}} \frac{(\theta_S - 1)^{m-1}}{(2k\theta_L - 1)} \left(\frac{1 - \theta_S}{\psi}\right)^{\frac{m+1}{2}} \right]^{\frac{1}{m}} \quad (3.44)$$

It is also interesting to compare our results with what has been done in 1995 by Olevsky and Rein¹⁰³ for an analogous spherical biporous domain with linear viscous constitutive properties of the skeleton.

They reported the following kinetics equations

$$\dot{\theta}_S = \frac{P_{L0S}}{\eta_0} \frac{(1 - \theta_S)^3 \left[1 + \left(\frac{P_{L0L}}{P_{L0S}} - 1 \right) \theta_L \right]}{2\psi(\theta_L - 1)} \quad (3.45)$$

$$\dot{\theta}_L = -\frac{P_{L0S}}{\eta_0} \frac{3(1 - \theta_S)^2}{4\varphi} \frac{P_{L0L}}{P_{L0S}} \theta_L \quad (3.46)$$

As a difference with respect to what we did, they used expressions for ψ , φ and P_{LS} present in the literature, which explains why they have a factor P_{L0S} in the equations. The expressions are the ones derived by Skorokhod,¹¹¹ given here:

$$\psi = \frac{2(1 - \theta_S)^3}{3\theta_S} \quad \varphi = (1 - \theta_S)^2 \quad P_{LS} = P_{L0S} (1 - \theta_S)^2 \quad (3.47)$$

The constant value η_0 is the viscosity of the skeleton, which can be related to our A_m by considering the power-law creep equation (3.1) with $m = 1$ (linear viscous case), and comparing it to the $\sigma(W)$ expression for the linear viscous rheology, which is

$$\sigma(W) = 2\eta_0 W \quad (3.48)$$

It is therefore immediate to see that $A_m = 2\eta_0$.

By applying the opportune substitutions and rearrangements, and momentarily borrowing the Skorokhod's expressions, our consolidation equations for the two porosities when $m = 1$ end up being almost coincident with the Olevsky-Rein outcomes, therefore confirming the reliability of the individuated expressions. Figure 3.7 shows this comparison.

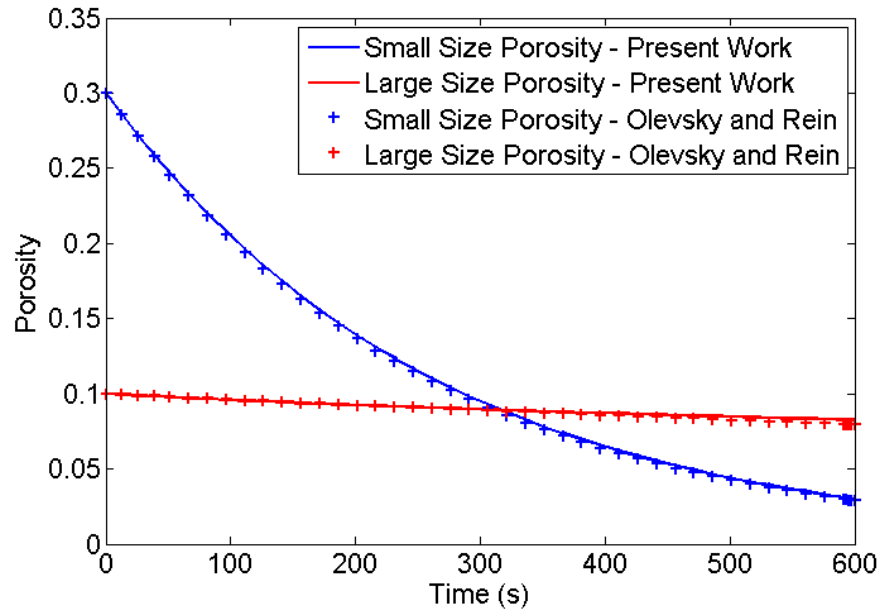


Figure 3.7 – Comparison between the present kinetics model ($m = 1$) and the one derived by Olevsky and Rein for linear viscous materials.

3.1.3 Sintering stress of homogeneous and hierarchical porous structures with nonlinear viscous constitutive behavior

We now proceed to the individuation of the first of the porosity-dependent parameters that we still have to define: sintering stress.

For both this parameter and the bulk and shear moduli, we will not only find the needed expressions for the small size porosity, but we will extend the analysis to the biporous case, in order to obtain also the macro-scale versions.

From the considerations made in the previous sections of this chapter, we can distinguish four categories in which the sintering stress can be classified, based on the meso-scale porous structure and on the rheology of the dense material constituting the skeleton:

1. Linear viscous material, monoporous structure;
2. Linear viscous material, biporous structure;
3. Nonlinear viscous material, monoporous structure;
4. Nonlinear viscous material, biporous structure,

where monoporous is synonym of homogeneous porosity size (absence of agglomeration) and biporous is synonym of hierarchical (presence of agglomeration). Previous studies mainly considered the first category only,¹³⁸ while for the prosecution of our work we are interested in the two last ones.

Since sintering stress accounts for the tendency of a porous material to minimize its free surface area, it is defined as the variation of free surface energy per unit mass with respect to the specific volume of the considered domain, and it is thus formulated as

$$P_L = \frac{dF_S}{d\vartheta} \quad (3.49)$$

with F_S free surface energy (J/kg) and ϑ specific volume (m^3/kg).

The sintering stress can thus be calculated by means of statistical and thermodynamic considerations according to this definition, as done by Skorokhod,¹¹¹ who theorized a general formulation for sintering stress, in the case of spherical voids, as

$$P_L = \frac{3\alpha}{r_p} (1 - \theta)^2 \quad (3.50)$$

It is evident that this solution was computed for a monoporous specimen. Skorokhod's sintering stress has revealed to predict experimental results quite well, but we are currently

interested in analyzing how its expression diversifies when dealing with more complex conditions, like nonlinear rheology and hierarchy of porosity.

Another approach can therefore be attempted, based on mechanics instead of thermodynamics. We can select a suitable domain (somewhat analogous to the one chosen for the densification kinetics study) and derive the sintering stress by solving the relative boundary value problem and taking into consideration the dissipative potential of the porous material. This strategy has been utilized in 1999 by Olevsky and Molinari in the case of a monoporous domain with a linear viscous behavior of the skeleton.¹⁷⁰ Their result is here reported, and we will follow an analogous procedure in order to derive the sintering stress for the nonlinear viscous biporous case.

An important notation choice needs to be evidenced here. Since our interest in this portion of the study is focused on the optimization of the material structure when hierarchical porosities are present, we have based our denominations on the assumption that two types of pores are present, distinct because of their size. Specifically, we have defined θ_S and θ_L , and we have reserved the simple notation θ for the global porosity, which includes both sizes. Since θ is commonly used to denote porosity in most of the sintering studies, usually dealing with only one type of pores, confusion can be generated.

In order to avoid misunderstandings, we will therefore denominate the porosity of every monoporous study as θ_S , and not θ . Such choice is based on the fact that, in the present work, the parameters of monoporous structures are of interest because they need to be inserted in the kinetics equations derived in 3.1.2, which, as explained before, are founded on the use of the sintering constitutive equation for the external shell, where only small pores are present.

Now that this point has been clarified, it will be immediate to understand why we report the Olevsky-Molinari result in the following form

$$P_{L_S} = \frac{3}{2} P_{L_{0S}} \sqrt{\frac{3}{2} \psi \frac{\theta_S}{1 - \theta_S}} \quad (3.51)$$

where again we avoided substituting ψ with an expression from the literature, while we are waiting to derive the bulk modulus for a monoporous material in the following section.

Notice that even though we will restrict our derivations of the bulk and shear moduli to the nonlinear viscous case, it is sufficient to impose $m = 1$ in the obtained equations to collapse the solution to the linear viscous case, as done in the end of the previous section in order to verify that our kinetics solution could be brought back to the Olevsky-Rein one for a linear viscous biporous specimen.

We will now proceed to derive the expression of P_{L_S} for a homogeneously porous material with nonlinear constitutive characteristics. The previous formulation for the corresponding linear viscous case will be a useful verification of the validity of our result.

Since we are considering a monoporous structure, with no trace of agglomeration phenomena, the domain to be employed for our derivations will still be a spherical layer of material with a concentric spherical hole, but this time the layer will be fully dense. As Figure 3.7 shows, we are zooming in inside the matrix of our previous biporous domain, and restricting our attention to a little spherical shell of fully dense skeleton material surrounding a small pore.

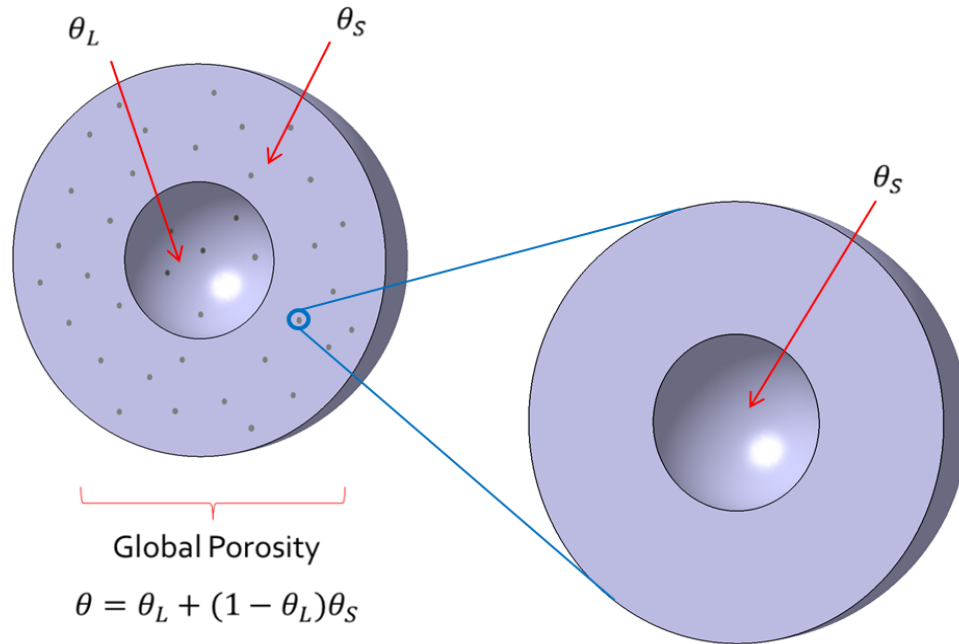


Figure 3.8 – Zooming in to define the domain study for the monoporous context.

As a rule of thumb to roughly estimate what scales we are considering in the two cases, one needs to think that an average agglomerate size is 10 μm , while a nanopowder particle size ranges in the 10-100 nm order of magnitude. It is reasonable, also based on experimental data,⁷² to evaluate the large inter-agglomerates pores average size as slightly lower with respect to the agglomerate size itself. This implies that with this shift in domain from biporous to monoporous we are moving to a scale about one or two orders of magnitude lower. It is nevertheless important to point out that such shift does not lead us into what we previously defined as micro-scale, since each nanopowder particle is itself crystalline, and therefore in order to reach the average grain size we need to move to lower scales.

Pointing out that our focus is on nanopowders is of particular importance in the context of sintering stress investigations. Generally, when conducting pressure-assisted sintering of crystalline materials, neglecting the impact of the sintering stress with respect to

the external loads has proven to be a more than acceptable approximation. But this ceases to be true if we employ powders with particles characteristic dimension below the micron level, such as the nanopowders that are becoming progressively more common in the SPS technologies field. An explanation can be found by looking at the dependence of sintering stress on the size of the pore on which it acts. It is an inverse proportionality, which means that if the pores radius is of the nanometer order, P_L can attain values of several MPa, thus not anymore negligible with respect to the externally applied pressures, which in spark plasma sintering processes are typically some tens of MPa. The importance of sintering stress in the nanopowders context explains why we chose to dedicate a detailed analysis to this parameter even if we are generally assuming the application of external loads during the SPS route.

A convenient approach to individuate the sintering stress from the solution of a simple boundary value problem consists in utilizing dissipative potentials definitions and identities, as we report here.

Since dissipative potentials, for both a fully dense and a porous material, are expressed as functions of strain rates, the first step needs to be the individuation of radial and tangential strain rates in the domain represented in Figure 3.7. We are dealing with a spherical shell that is creeping under the action of radial loads. An analogous problem has already been solved by Finnie first and Ashby later,^{148, 152} with slightly different boundary conditions.

In our case, an appropriate loading condition of the dense spherical shell, able to provide the sintering stress, consists in applying the sintering stress itself at the internal boundary of the shell (or, equivalently, the surface of a small pore) and leaving the external boundary free of loads, as shown in Figure 3.8. Note that we have changed the denomination of the radii not to ingenerate confusion: r_{sp} (radius of the small pore) is the internal radius; r_{sd} (radius of the small domain) is the external one.

Strain rates for these geometry and loading conditions are calculated and result to be

$$\dot{\epsilon}_r = A_n \frac{(r_{sp} r_{sd})^3}{(r_{sd}^{3m} - r_{sp}^{3m})^{\frac{1}{m}}} \left[\frac{3m}{2} P_{L0s} \right]^{\frac{1}{m}} \frac{1}{r^3} \quad (3.52)$$

$$\dot{\epsilon}_\varphi = -\frac{A_n}{2} \frac{(r_{sp} r_{sd})^3}{(r_{sd}^{3m} - r_{sp}^{3m})^{\frac{1}{m}}} \left[\frac{3m}{2} P_{L0s} \right]^{\frac{1}{m}} \frac{1}{r^3} \quad (3.53)$$

Being the strain rate tensor second invariant for this specific geometry defined as in the previous domain case, we find

$$\dot{\gamma}_s = \sqrt{\frac{3}{2}} A_n \frac{(r_{sp} r_{sd})^3}{(r_{sd}^{3m} - r_{sp}^{3m})^{\frac{1}{m}}} \left[\frac{3m}{2} P_{L0s} \right]^{\frac{1}{m}} \frac{1}{r^3} \quad (3.54)$$

where we have added the subscript s to underline that in the present case it is only the fully dense skeleton that is constituting the shell.

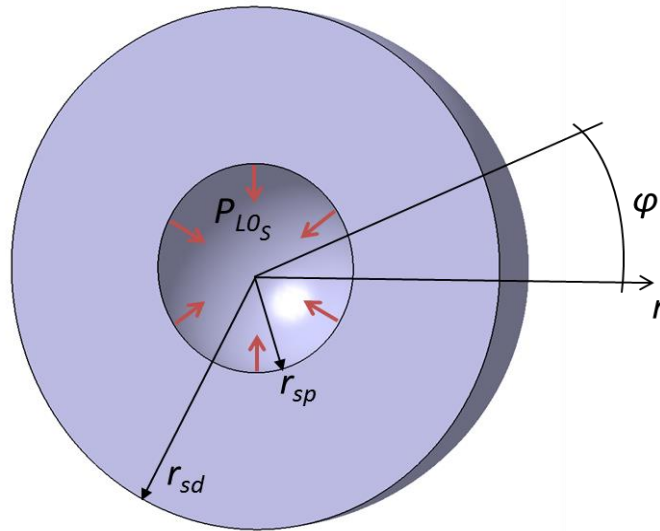


Figure 3.9 – Geometry and loading schematics acting on the monoporous study domain.

We define now the dissipation potential of a porous medium as D and the dissipation potential of the skeleton as D_S . The following identity holds, usually addressed as Hill's identity

$$D = (1 - \theta_S) \langle D_S \rangle \quad (3.55)$$

in which $\langle D_S \rangle$ indicates the volume average over the domain of the skeleton potential, which, for a nonlinear viscous material is defined as¹¹³

$$D_S = \frac{A_m}{m+1} \dot{\gamma}_s^{m+1} \quad (3.56)$$

By substituting the expression for $\dot{\gamma}_s$ found above and averaging over the shell volume, we have

$$\langle D_S \rangle = \frac{A_m}{m+1} \left\{ \sqrt{\frac{3}{2}} A_n \frac{(r_{sp} r_{sd})^3}{(r_{sd}^{3m} - r_{sp}^{3m})^{\frac{1}{m}}} \left[\frac{3m}{2} P_{L0_S} \right]^{\frac{1}{m}} \right\}^{m+1} \frac{3 \int_{r_{sp}}^{r_{sd}} r^{-3m-1} dr}{r_{sd}^3 - r_{sp}^3} \quad (3.57)$$

and therefore

$$\langle D_S \rangle = \frac{A_m A_n^{m+1}}{m(m+1)} \left[\left(\frac{3}{2} \right)^{\frac{m+2}{2}} m P_{L0_S} \right]^{\frac{m+1}{m}} \frac{r_{sp}^3}{(1 - \theta_S)(r_{sd}^{3m} - r_{sp}^{3m})^{\frac{1}{m}}} \quad (3.58)$$

The dissipative potential of a porous nonlinear viscous material is, on the other hand, defined as

$$D = \frac{A_m}{m+1} (1 - \theta_S) W^{m+1} \quad (3.59)$$

It is important to notice that D is here considering our domain from a macroscopic point of view, since in this specific case the porous medium is constituted by the overall shell-void union. In the previous section, instead, the sintering constitutive equation and all its parameters were only applied to the porous shell, without including the large internal pore.

Evidencing this distinction is of fundamental importance in order to understand why in the present case we can express the equivalent strain rate W as follows

$$W = \sqrt{\frac{\psi}{1 - \theta_S}} |\dot{\epsilon}| \quad (3.60)$$

that is with an expression that does not include $\dot{\gamma}$.

From a macroscopic perspective, a hydrostatically compressed sphere does not undergo any change of shape, which is the physical phenomenon that $\dot{\gamma}$ represents. In section 3.1.2, nevertheless, equating the second strain rate tensor invariant to zero would not have been legitimate, because in that case the equivalent strain rate is only referred to the shell, and is thus not looking at the overall biporous domain as a whole macroscopic entity.

At this point, the following equation, an immediate consequence of the sintering constitutive equation opportunely applied to calculate the stress invariants, comes into play

$$p = A_m W^{m-1} \psi \dot{\epsilon} + P_{L_S} \quad (3.61)$$

where p is the first stress tensor invariant, $\sigma_{kk}/3$.

Again in this macroscopic evaluation context, and in the absence of applied loads, $p = 0$, and therefore we obtain

$$W = \left(\frac{P_{L_S}}{A_m \sqrt{\psi(1 - \theta_S)}} \right)^{\frac{1}{m}} \quad (3.62)$$

We now have all the necessary parameters to be embedded in the Hill's identity.

By doing so and rearranging in order to isolate P_{L_S} we finally get an equation for the sintering stress of a monoporous nonlinear viscous material, as

$$P_{L_S} = \left(\frac{3}{2} \right)^{\frac{m+2}{2}} P_{L_0 S} \sqrt{\psi} \left[\frac{m \theta_S^m}{1 - \theta_S^m} (1 - \theta_S)^{\frac{1-m}{2}} \right]^{\frac{1}{m+1}} \quad (3.63)$$

This is what we need to insert in the densification kinetics equations obtained in the previous section.

If we impose $m = 1$, corresponding to a linear viscous rheology, we immediately verify that (3.63) results to be coincident with (3.51), the Olevsky-Molinari outcome that was individuated starting from the solution of an similar boundary value problem, but with the direct treatment of the material as linear viscous, and therefore using the analogy of such constitutive behavior with the elasticity regime.

We now proceed to the individuation of case number 4 in the classification at the beginning of this section: nonlinear viscous biporous material. We shift our attention from the meso-scale to the macro-scale, or, better, we provide a first tool to allow ourselves to do so. We are, indeed, calculating the first global property of a hierarchical porous structure, the macroscopic sintering stress P_L (no subscript is here used for coherence with the porosity notation). The remaining required parameters, *i.e.* macroscopic bulk and shear moduli, will be derived in the following paragraphs, together with their monoporous counterparts and following the same line of reasoning laid out in this section.

We will proceed in an analogous way as in the previous case of absence of agglomeration, but this time we consider the biporous domain that we utilized for the kinetics derivations (Figure 3.5).

An essential premise to the macroscopic derivations is the obtainment of the indissolubility equation in terms of the two porosities, or, equivalently, the macroscopic shrinkage rate, \dot{H} . Every macroscopic property will be indicated as the capitalized version of the analogous parameter at the meso-scale, such as Ψ for the normalized bulk modulus and Φ for the normalized shear modulus.

Following the usual definition, \dot{H} is

$$\dot{H} = \frac{\dot{\theta}}{1 - \theta} \quad (3.64)$$

Recovering the initial definition of the total porosity in terms of the small size and large size pores contributions, we can calculate the overall porosity evolution with time as

$$\begin{aligned}\dot{\theta} &= \frac{d}{dt}[\theta_L + (1 - \theta_L)\theta_S] = \dot{\theta}_L(1 - \theta_S) + \dot{\theta}_S(1 - \theta_L) = \\ &= \dot{\theta}_S(1 - \theta_L) \left(1 + 3k\theta_L \frac{\psi}{\varphi}\right)\end{aligned}\quad (3.65)$$

where $\dot{\theta}_S$ is the one derived in section 3.1.2, reported as (3.36).

Thus the global shrinkage rate results to be

$$\dot{H} = \frac{\dot{\theta}}{(1 - \theta_S)(1 - \theta_L)} = \frac{\dot{\theta}_S}{(1 - \theta_S)} \left(1 + 3k\theta_L \frac{\psi}{\varphi}\right)\quad (3.66)$$

Note that an analogous result can be reached if we consider that $\dot{E} = 3V_r|_b/b$.

We can now employ the macroscopic counterpart of (3.61), with the same considerations to be applied to the equivalent strain rate W , so that we have

$$P - P_L = A_m W^{m-1} \Psi \dot{H} = \frac{A_m |\dot{H}|^m}{(1 - \theta)^{\frac{m-1}{2}}} \Psi^{\frac{m+1}{2}}\quad (3.67)$$

with Ψ the macroscopic normalized bulk modulus, as anticipated.

As in the non-hierarchical case, the sintering stress can be individuated by assuming loading conditions in which no external pressure is applied, from which we derive

$$P_L = \frac{A_m \dot{H}^m}{(1 - \theta)^{\frac{m-1}{2}}} \Psi^{\frac{m+1}{2}}\quad (3.68)$$

By substituting the \dot{E} of (3.66), we have

$$P_L = \frac{A_m \Psi^{\frac{m+1}{2}}}{(1 - \theta)^{\frac{m-1}{2}}} \frac{\dot{\theta}_S}{(1 - \theta_S)} \left(1 + 3k\theta_L \frac{\psi}{\varphi}\right)\quad (3.69)$$

This is the sintering stress of a hierarchical porous structure characterized by the presence of small and large size pores. Further simplification is possible, but we will postpone the final rearrangements to when the appropriate expressions for Ψ , ψ and φ will have been

obtained. At this point of the study, indeed, we want to gain the maximum possible accuracy in our formulations, and therefore we want to consider the influence of the material nonlinearity on bulk and shear moduli too.

3.1.4 Bulk modulus of homogeneous and hierarchical porous structures with nonlinear viscous constitutive behavior

In the continuum theory of sintering, the material's main mechanical properties, bulk and shear moduli, become functions of porosity too, together with being dependent on the viscosity of the skeleton. This step allows considering the porous medium as homogeneous and isotropic, with the effect of the voids being included in the opportunely corrected moduli formulations. The literature provides certain general expressions, or some more specific formulations for a linear viscous biporous medium or for a nonlinear viscous monoporous.^{104, 155, 160} We hereby aim at obtaining an even more comprehensive result, *i.e.* the two moduli for a hierarchical porous structure whose skeleton's material exhibits a nonlinear constitutive behavior. It is worth remembering the intrinsic inclusiveness of such formulation, since one can easily retrieve the linear viscosity or homogeneous porosity cases by imposing $m = 1$ or $\theta_L = 0$, respectively.

Nevertheless, because of the choices operated while setting up the present analysis, we found useful to start our derivations from the nonlinear viscous monoporous case, such that we could immediately find an expression to plug into the kinetics equations derived in 3.1.2.

The previous paragraph's considerations, therefore, since we are rendering the individuations of ψ and Ψ separate and independent on each other, will anyways provide an interesting verification tool for checking that Ψ goes back to ψ when we set the large size

porosity to be zero. Analogous steps will be performed for the shear moduli φ and Φ in section 3.1.5.

For both the monoporous and biporous cases, a derivation procedure in line with what done for the sintering stress can be applied.

The baseline consists in the same equation (3.61), here reported for convenience

$$p = AW^{m-1}\psi\dot{\epsilon} + P_{L_S}$$

We start with the monoporous study, for which the same fully dense spherical layer domain of Figure 3.9 is employed.

While in the sintering stress analysis context we had to consider the condition of absence of externally applied loads, here we will do the opposite, by assuming that we are applying pressures on the external boundary that are significant enough for us to neglect the sintering stress, at least temporarily, and even for nanopowders.

By doing this and substituting in the previous equation the expression for the equivalent strain rate that does not include the change of shape term (since we are still loading the domain with a hydrostatic pressure), we find

$$P_{ext} = A_m \psi^{\frac{m+1}{2}} |\dot{\epsilon}|^m (1 - \theta_S)^{\frac{1-m}{2}} \quad (3.70)$$

Note that here it is θ_S that has to be analyzed from a geometrical viewpoint, because we have zoomed in at the meso-scale until we have individuated a single small size pore surrounded by a layer of fully dense material (Figure 3.9).

Accordingly, expressions for porosity and consolidation kinetics, necessary in order to obtain $\dot{\epsilon}$ for the present case, are calculated starting from

$$\theta_S = \left(\frac{r_{sp}}{r_{sd}} \right)^3 \quad (3.71)$$

Being $\dot{\epsilon} = \frac{\dot{\theta}_S}{1-\theta_S}$, we need to derive $\dot{\theta}_S$ in the following manner, analogous to what done previously for the large size porosity

$$\dot{\theta}_S = \frac{3r_{sp}^2}{r_{sd}^3} V_r|_{r_{sp}} - \frac{3r_{sp}^3}{r_{sd}^4} V_r|_{r_{sd}} \quad (3.72)$$

The radial velocity field during the power-law creep of a fully dense sphere with a central void is the same utilized in 3.1.3 to obtain the strain rates for the sintering stress of a non-agglomerated and nonlinear viscous material, and it is written as

$$V_r = -\frac{A_n}{2} \frac{(r_{sp}r_{sd})^3}{(r_{sd}^{3m} - r_{sp}^{3m})^{\frac{1}{m}}} \left(\frac{3}{2} mP_{ext}\right)^{\frac{1}{m}} \frac{1}{r^2} \quad (3.73)$$

From this we derive

$$|\dot{\epsilon}| = \frac{3A_n}{2} \left(\frac{3}{2} mP_{ext}\right)^{\frac{1}{m}} \frac{r_{sp}^3}{(r_{sd}^{3m} - r_{sp}^{3m})^{\frac{1}{m}}} \quad (3.74)$$

which is greater than zero, therefore we can remove the absolute value. After rearranging, replacing A_n with A_m^{-n} and elevating to the power m , we get

$$\dot{\epsilon}^m = \left(\frac{3}{2}\right)^m \frac{mP_{ext}}{A_m} \frac{\theta_S^m}{1-\theta_S^m} \quad (3.75)$$

From (3.70) we can finally obtain the bulk modulus of a monoporous nonlinear viscous material as

$$\psi = \frac{4}{9} \left[\frac{1-\theta_S^m}{m\theta_S^m} (1-\theta_S)^{\frac{m-1}{2}} \right]^{\frac{2}{m+1}} \quad (3.76)$$

A first, immediate, verification of the outcome's reliability is, again, conducted by imposing $m = 1$ and noticing that the solution collapses to a classic result of the theory of sintering, individuated by Mackenzie and Shuttleworth for a linear viscous material.^{113, 114}

It is also interesting to compare this formulation of ψ with others from the literature for the creep of crystalline materials containing isolated spherical voids. The main models are

the ones theorized by Sofronis and McMeeking, who individuated both bulk and shear modulus starting from their definitions of stress and strain potentials, in turn obtained via finite-element methods applied to the collapse of an isolated pore in a nonlinear viscous medium,¹⁵⁵ and Geindreau and Bouvard, who also worked in the nonlinear framework but employed a semi-experimental approach.¹⁶⁰

Figure 3.10 compares these two models with our results and with the more general Skorokhod's expression, which is relative to the linear viscous case and is derived by means of the elasticity analogy and the differential self-consistent approach.¹¹³ All the three formulations are given in the following Table 3.1.

Another important aspect is that the derived ψ respects the expected trends when the porosity fraction reaches 0% and 100%. In case of absence of porosity, the material becomes incompressible, and therefore the bulk modulus tends to infinity. Obviously, the opposite case translates in the bulk modulus tending asymptotically to zero (infinite compressibility due to the "disappearance" of the material).

Table 3.1 – Expressions of normalized bulk modulus of a monoporous material compared in Figure 3.10.

	Present Work	Skorokhod
ψ	$\left[\left(\frac{2}{3} \right)^m \frac{(1 - \theta_S)^{(m-1)/2} (1 - \theta_S^m)}{m \theta_S^m} \right]^{\frac{2}{(m+1)}}$	$\frac{2(1 - \theta_S)^3}{3\theta_S}$
	Geindreau, Doremus and Bouvard	Sofronis and Mcmeeking
ψ	$0.601 \left(\frac{0.43 - \theta_S}{\theta_S} \right)^{1.168}$	$\frac{4}{9} \left[\frac{3(1 - \theta_S^m)}{m \theta_S^m} \right]^{\frac{2}{(m+1)}}$

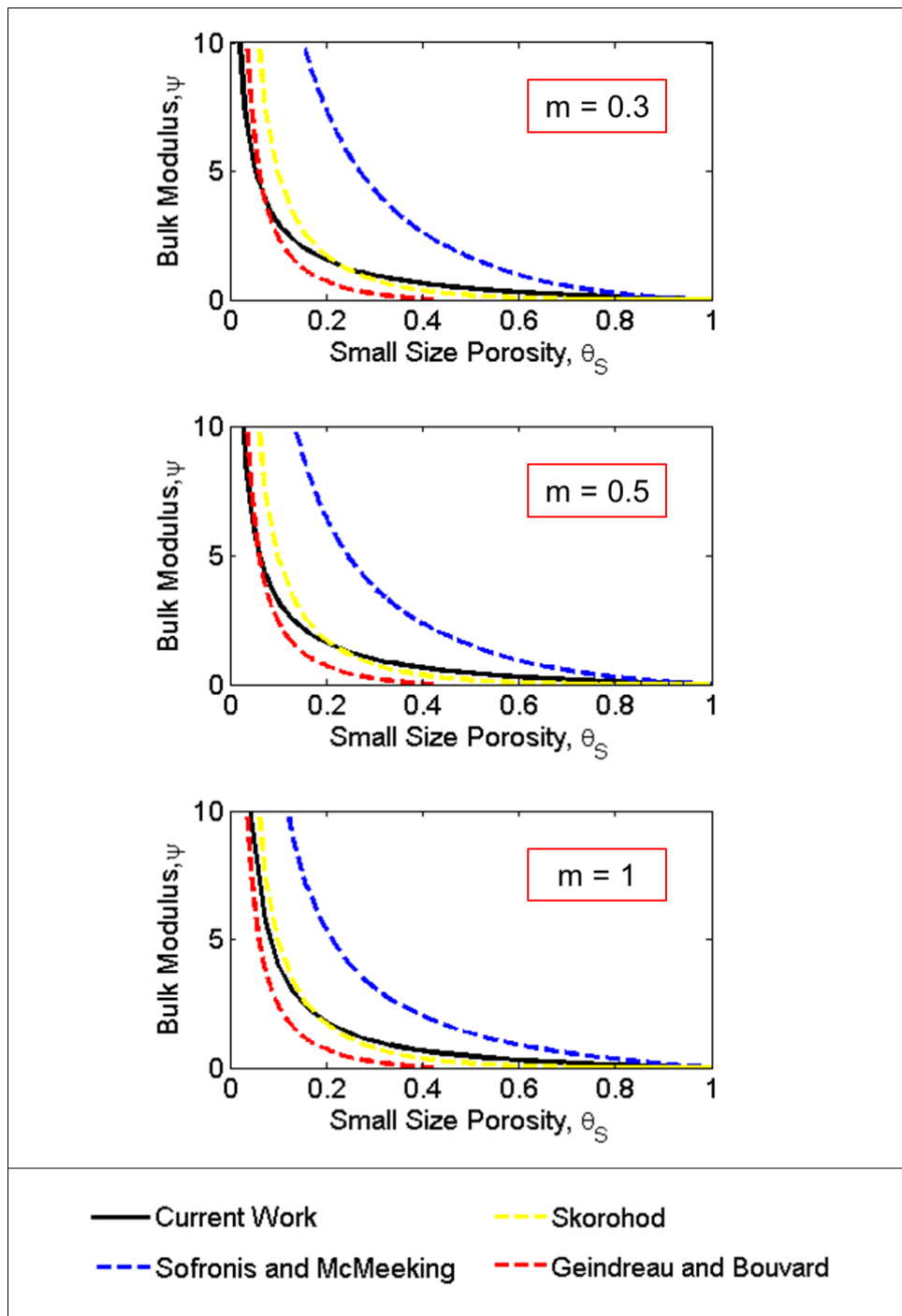


Figure 3.10 – Normalized bulk modulus expressions for monoporous materials and different values of the strain-rate sensitivity parameter.

We now shift again our attention to the main issue of this part of our optimization study, namely hierarchical porous structures. We need to individuate Ψ , the macroscopic normalized bulk modulus of a nonlinear viscous material containing agglomerates, and consequently two distinct porosity sizes. The importance of this parameter, together with its shear counterpart, does not only lie in the sake of completeness of our modeling framework. One has to keep in mind that our final aim is optimizing spark plasma sintering efficiency, and in this chapter we are attempting to do so by improving the temperature regime to which a biporous specimen is subjected. Having the thermal route a direct influence on the variations of strain-rate sensitivity m , when we find fundamental material properties, such as the bulk and shear moduli, as a function of this m (together with porosities) we are empowering our model with the possibility of predicting the indirect effects of temperature on these mechanical properties too, without even involving the kinetics equations, as Section 3.2 will show.

Analogously to what seen in the preceding sections, a hierarchical porous structure is successfully reproduced by a domain constituted by a porous spherical shell surrounded a concentric large void of much larger size. Therefore we are again employing the domain sketched in Figure 3.6, and considering it from a macroscopic perspective, as done in every case for the sintering stress and bulk modulus analyses.

Recalling that the macroscopic shrinkage rate results to be

$$\dot{H} = \frac{\dot{\theta}}{1 - \theta} = \frac{\dot{\theta}}{(1 - \theta_S)(1 - \theta_L)} = \frac{\dot{\theta}_S}{(1 - \theta_S)} \left(1 + 3k\theta_L \frac{\psi}{\varphi} \right) \quad (3.66)$$

and that equation (3.61) for the macroscopic viewpoint is expressed as

$$P - P_L = A_m W^{m-1} \Psi \dot{H} = \frac{A_m \dot{H}^m}{(1 - \theta)^{\frac{m-1}{2}}} \Psi^{\frac{m+1}{2}} \quad (3.67)$$

The individuation of the “biporous” bulk modulus immediately follows from imposing $P_L = 0$ and performing the necessary substitutions, so that we finally get

$$\Psi = \psi \frac{(1 - \theta_L)^{\frac{m-1}{m+1}}}{\left(1 - 3k\theta_L \frac{\psi}{\varphi}\right)^{\frac{2m}{m+1}}} \quad (3.77)$$

The choice of not substituting the “monoporous” ψ with its proper expression was aiming at simply checking that the agglomeration-inclusive case collapses to the one without any hierarchy of the pore structure, and, indeed, when $\theta_L = 0$ we see immediately that $\Psi = \psi$.

We also have an explicit dependence on a parameter that has not been derived yet: the shear modulus for a monoporous nonlinear viscous material, φ , which is the object of the following section.

Recall that, at the end of section 3.1.3, we had left the global (macroscopic for a biporous domain) sintering stress as a generic function of this Ψ whose calculation we have just finished to accomplish. We repeat it here for convenience

$$P_L = \frac{A_m \Psi^{\frac{m+1}{2}}}{(1 - \theta)^{\frac{m-1}{2}}} \frac{\dot{\theta}_S}{(1 - \theta_S)} \left(1 + 3k\theta_L \frac{\psi}{\varphi}\right) \quad (3.69)$$

Now we can replace $\dot{\theta}_S$ and Ψ with their respective expressions, until we obtain

$$P_L = \frac{P_{L_S}}{1 - 2k\theta_L} \left(6k^2\theta_L^2 \frac{\psi}{\varphi} + 1\right)^{\frac{1-m}{2}} \quad (3.78)$$

The decision of not replacing P_{L_S} with its own formulation is motivated by the same considerations made for Ψ and ψ . Here too we find that $P_L = P_{L_S}$ if $\theta_L = 0$.

For the linear viscous biporous case, on the other hand, we obtain that

$$P_L = \frac{P_{L_S}}{1 - 2k\theta_L} \quad (3.79)$$

Before we proceed to the analogous derivations for the shear modulus, some further refinements of our results can be made.²²⁰

Derivations based on the domain depicted in Figure 3.6 are representative of the material surrounding a void in a medium that contains isolated pores, such that the influence of the neighboring voids can be considered negligible. This is the so-called dilute case, and its applicability is limited to amounts of porosity below 5-10%, while typical initial values of porosity for any sintering process are around 35-40% volume fractions. The dilute case is appropriate only for the last stage of sintering, when the open porosity (interconnected net of voids communicating with the specimen's external surface) has disappeared and we are left with closed porosity only. Thus, some extra steps are required in order to guarantee the applicability of our model to domains containing arbitrary amounts of porosity, and therefore at the entirety of the SPS process.

We choose to proceed to this type of refinement only for the monoporous case, because of practical reasons when it comes to actual experimental procedures. Typically, the values of initial small size porosity range between 30-40% of the sample's volume, while large inter-agglomerates voids do not usually occupy more than 10% of the volume. The dilute case is thus still considered suitable for the treatment of large pores.

For the analysis of non-dilute monoporous cases, we will employ a first-order iterative procedure consisting in the following steps. We will start with the generic expression of the sintering stress proposed by Skorokhod, based on energy considerations and thus independent of the skeleton rheology, and at the same time valid for arbitrary values of pores content. By means of this expression and the sintering constitutive equation, opportunely written, we will obtain the normalized bulk modulus of the porous material, as a function of porosity and strain-rate sensitivity, which in turn will be including the effects of the surrounding pores on our domain. Finally, thanks to this "macroscopic" (non-dilute) form of the bulk modulus, and

by means of the above-mentioned dissipation potentials and the Hill's identity correlating them, we will derive the sintering stress for a porous medium characterized by a nonlinear viscous rheology of the skeleton and an arbitrary volume fraction occupied by voids.

The expressions that we will use have already been introduced in the present and previous sections, but will be here reported for the reader's convenience.

The starting point of the iterative procedure is a zero order approximation of the sintering stress as theorized by Skorokhod, formula (3.50):

$$P_{L_S} = P_{L_0_S}(1 - \theta_S)^2 \quad (3.50)$$

which has the advantage of being applicable to non-dilute cases, but does not take into account the influence of strain-rate sensitivity.

We also know that, directly from the sintering constitutive equation in absence of external loads, we have

$$P_{L_S} = A_m W^{m-1} \psi |\dot{e}| \quad (3.61)$$

which becomes

$$P_{L_S} = A_m (1 - \theta_S)^{\frac{1-m}{2}} \psi^{\frac{m+1}{2}} |\dot{e}|^m \quad (3.80)$$

This is the relationship that we use for the first step of our iterative procedure. Given P_{L_S} from (3.50) and \dot{e} from (3.75), here reported

$$\dot{e}^m = \left(\frac{3}{2}\right)^m \frac{m P_{ext}}{A_m} \frac{\theta_S^m}{1 - \theta_S^m} \quad (3.75)$$

we obtain an expression for the normalized bulk modulus of a material containing an arbitrary amount of voids that takes into account the skeleton's rheology, as

$$\psi = \left[\left(\frac{2}{3}\right)^m \frac{(1 - \theta_S)^{(m+3)/2} (1 - \theta_S^m)}{m \theta_S^m} \right]^{\frac{2}{m+1}} \quad (3.81)$$

where the effects of the overall material's compressibility due to the fact that our Figure 3.9 unit cell is surrounded by a porous medium, are provided by utilizing the Skorokhod's expression as zero-order approximation of the sintering stress.

It is worth pointing out that if we consider the linear case, by imposing $m = 1$, this expression for the bulk modulus is reduced to the one individuated by Skorokhod for a linear viscous material, even if through a different derivation path.

Figure 3.11 compares the dilute expression obtained above (3.76) with this non-dilute one (3.81). As expected, the non-dilute case predicts values of bulk modulus lower than in the dilute case, since the latter does not take into account the effects of the neighboring pores. This distinction is particularly noticeable for porosity values ranging between 10% and 50%, which are the typical amounts present in a sintering specimen before the final (closed porosity) stage is reached.

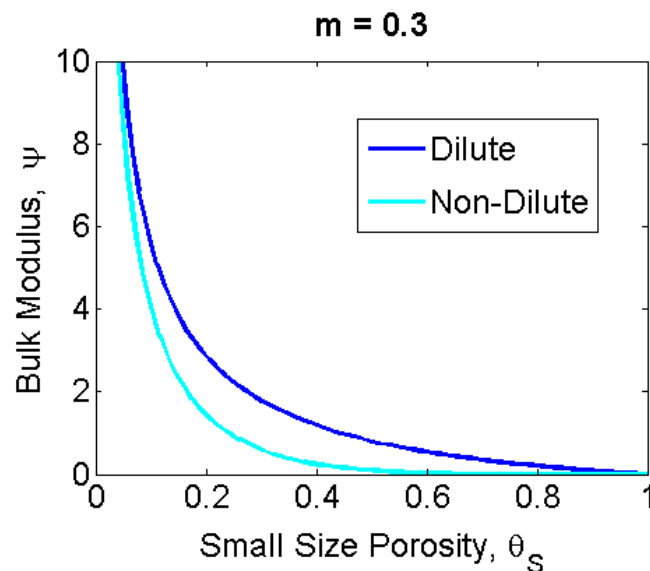


Figure 3.11 – Comparison between dilute and non-dilute normalized bulk modulus expressions.

For the second step of the iterative procedure, we employ the Hill's identity^{113, 221}

$$D = (1 - \theta_S) \langle D_S \rangle \quad (3.55)$$

Where the term on the left-hand side, D , *i.e.* the dissipation potential for the entire porous domain, results from the combination of (3.59) and (3.62), as

$$D = \frac{A_m}{m+1} (1 - \theta_S) \left(\frac{P_L}{A_m \sqrt{\psi(1 - \theta_S)}} \right)^{\frac{m+1}{m}} \quad (3.82)$$

and for the right-hand side we need the previously calculated expression of dissipation potential for the solid shell only, which is

$$\langle D_S \rangle = \frac{A_m A_n^{m+1}}{m(m+1)} \left[\left(\frac{3}{2} \right)^{\frac{m+2}{2}} m P_{L0S} \right]^{\frac{m+1}{m}} \frac{r_{sp}^3}{(1 - \theta_S)(r_{sd}^{3m} - r_{sp}^{3m})^{\frac{1}{m}}} \quad (3.58)$$

The substitution of (3.82) and (3.58) in (3.55) leads to a simple expression for P_{LS} , as follows

$$P_{LS} = P_{L0S} (1 - \theta_S)^{2/(m+1)} \quad (3.83)$$

Note that if we impose $m = 1$ we immediately verify that this newly derived expression results to be coincident with the Olevsky-Molinari outcome for the linear viscous case.¹⁷⁰

To the best of our knowledge, this is the first sintering stress expression that includes a dependence on the strain-rate sensitivity parameter, and furthermore is applicable to arbitrary amounts of porosity.

As pointed out above, the increasingly widespread use of nanosized powders has imposed to acknowledge the importance of role played by the sintering stress during densification. In this context, the classic results derived for a material characterized by a linear viscous rheology become too rough of an approximation. The dependence on the strain-rate sensitivity allows for a direct connection between the driving force of sintering and the

mechanism underlying the creep phenomena that are responsible for densification during hot deformation of crystalline materials. Furthermore, the proposed expression for sintering stress is also applicable to powder compacts containing arbitrary amounts of pores, which for sintering typically range between volume fractions of 0 and 40%, thanks to how our iterative derivation procedure was organized. Most commonly, the studies of sintering parameters in a nonlinear framework are limited to the dilute case, and are therefore applicable only to the final stages of sintering, when porosity is lower than 10%, or require complex averaging procedures to move from this local scale to a macroscopic solution.^{222–225} All the above considerations apply to the normalized bulk modulus too, for which certain models have been proposed in the literature, but again mainly valid for small porosity amounts only.¹⁵⁵

Figure 3.12 and Table 3.2 provide comparison plots of our model with other cases present in the literature (Table 1). Figure 3.12 compares the ψ that we have derived with expressions obtained by other authors through different procedures, for various values of m . We plot the same expressions proposed by Skorokhod, Sofronis and McMeeking, and Geindreau and Bouvard,^{113,155,160} and additionally the work of Ponte Castaneda and Willis. The latter is the most interesting comparison, since they used variational principles to obtain a non-dilute (self-consistent approximation) and strain-rate sensitivity-dependent expression of the bulk modulus.²²³ Indeed, the two respective curves are remarkably close to each other. It is interesting to notice that the main distinction between our result and the one by Sofronis and McMeeking consists in the factor $(1 - \theta)^{(m+3)/2}$, which arises from our iterative approach and is responsible for the generalization from local to macroscopic case. We can see that the work by Sofronis and McMeeking overestimates the bulk modulus with respect to the present case, in accordance with the fact that the former neglects the influence of neighboring pores, while we include it in our treatment. As expected, as m approaches 1, the curve relative to the present work gets closer to the one relative to Skorokhod's result.

Figure 3.13 and Table 3.3 present the analogous comparison for P_{LS} , again for several values of strain-rate sensitivity. In Figure 3.13 we can see that the present solution is located in between the models of Skorokhod and Olevsky and Molinari, approaching the former when m tends to 0 and the latter m goes to 1. Scherer proposed a microstructural model for the linear viscous case,²²⁶ while Bouvard and McMeeking focused on the early stages of sintering by analyzing inter-particle necks evolution during diffusion-controlled creep.²²⁷

Table 3.2 – Expressions of normalized bulk modulus of a monoporous material compared in Figure 3.12.

	Present Work	Skorokhod	Sofronis and Mcmeeking
ψ	$\left[\left(\frac{2}{3} \right)^m \frac{(1 - \theta_s)^{(m+3)/2} (1 - \theta_s^m)}{m \theta_s^m} \right]^{\frac{2}{(m+1)}}$	$\frac{2(1 - \theta_s)^3}{3\theta_s}$	$\frac{4}{9} \left[\frac{3(1 - \theta_s^m)}{m \theta_s^m} \right]^{\frac{2}{(m+1)}}$
	Geindreau, Doremus and Bouvard	Ponte Castaneda and Willis	
ψ	$0.601 \left(\frac{0.43 - \theta_s}{\theta_s} \right)^{1.168}$	$\frac{(m + 1)(1 - \theta_s)^{2-m}}{2\theta_s} \left(\frac{1 - 2\theta_s}{1 - \theta_s/3} \right)^m$	

Table 3.3 – Expressions of normalized sintering stress of a monoporous material compared in Figure 3.13.

	Present Work	Skorokhod	Olevsky and Molinari	Scherer	Bouvard and Mcmeeking
$\frac{P_L}{P_{L0}}$	$(1 - \theta_s)^{\frac{2}{(m+1)}}$	$(1 - \theta_s)^2$	$(1 - \theta_s)$	$\frac{\sqrt{(1 - \theta_s)/[\pi(1 + 2\theta_s)]}}{(\sqrt{[\pi(1 + 2\theta_s)]/(1 - \theta_s)} - 8\sqrt{2}/(3\pi))^{2/3}}$	$(1 - \theta_s)^{\frac{5}{3}}$

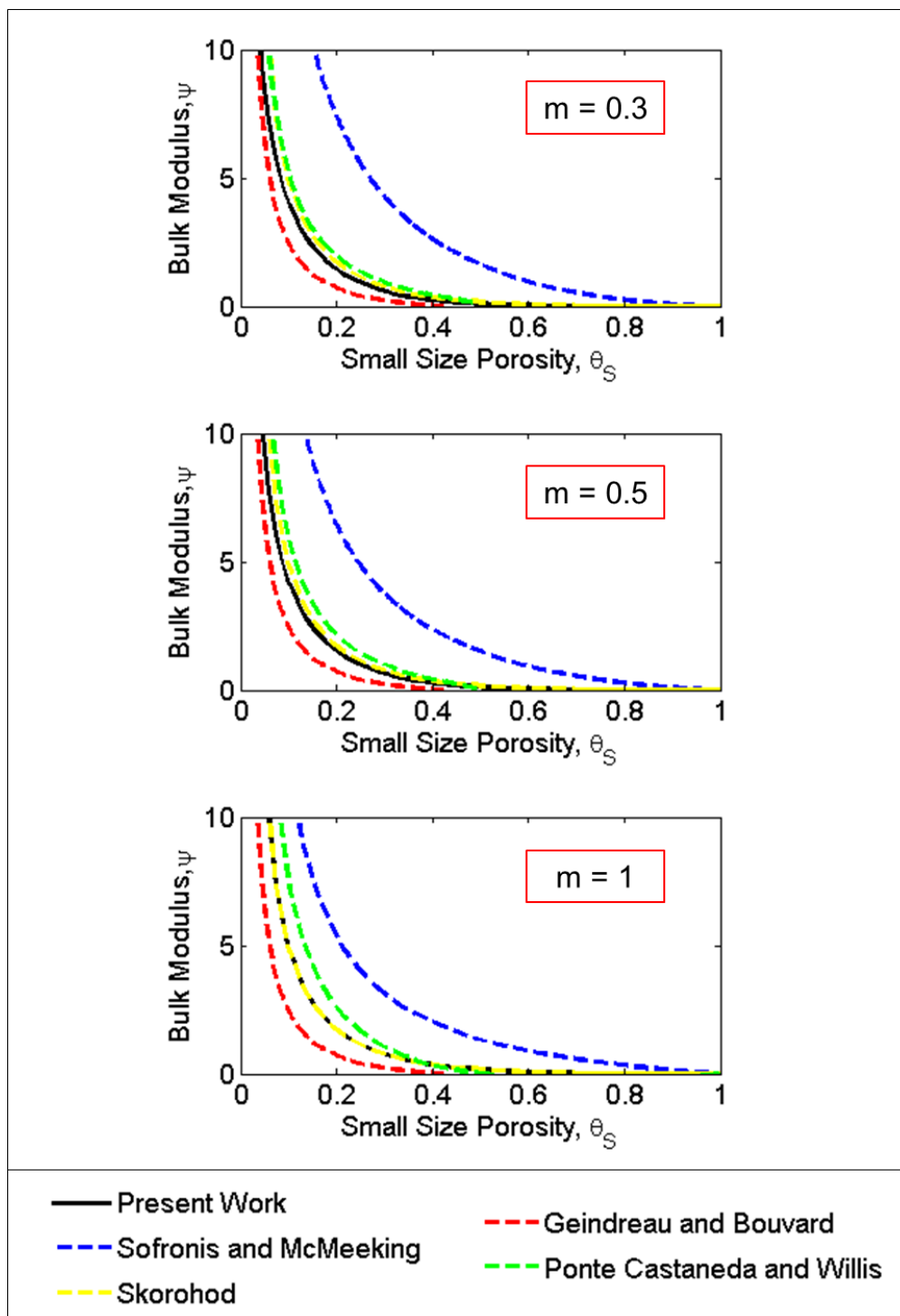


Figure 3.12 – Non-dilute normalized bulk modulus expressions for monoporous materials and different values of the strain-rate sensitivity parameter.

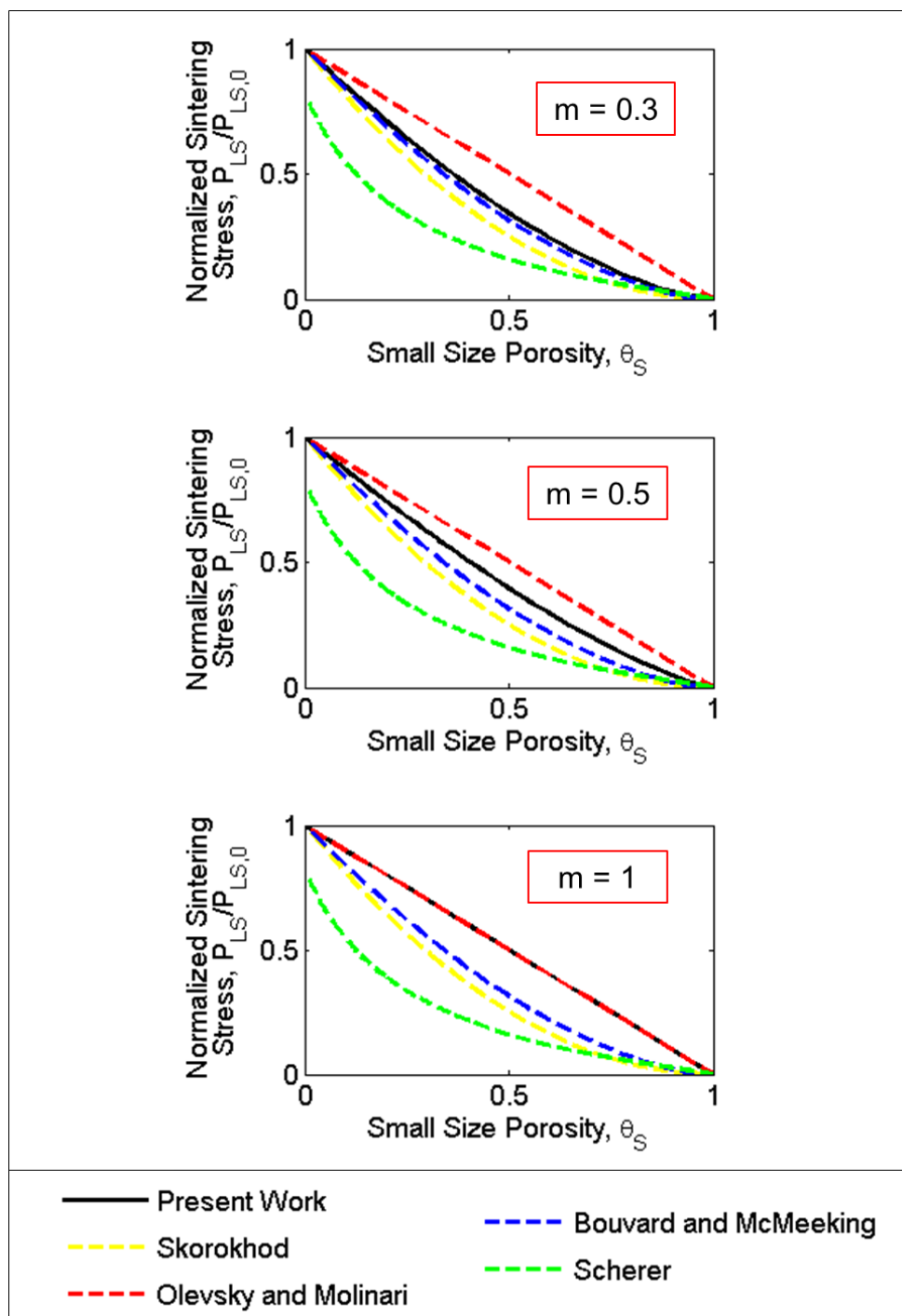


Figure 3.13 - Normalized sintering stress expressions for monoporous materials and different values of the strain-rate sensitivity parameter.

Finally, we can derive the evolution equation for the time evolution of small size porosity, combining (3.75), (3.80), (3.81), (3.83) and remembering the definition of normalized sintering time (3.42), as

$$\frac{d\theta_s}{dt_s} = \frac{3}{2} \left(\frac{m}{1 - \theta_s^m} \right)^{1/m} \theta_s (1 - \theta_s)^{(m-1)/(m+1)} \quad (3.84)$$

Note that this expression differs from the result obtained by Wilkinson and Ashby¹⁵² (developed for hot isostatic pressing but also applicable to the free sintering case) only for the power of the factor $(1 - \theta_s)$, which therefore represents the extension from the local solution to the non-dilute case. Figure 3.14 shows how this model fits experimental data relative to alumina processing. We considered free sintering of two different powder sizes of alumina, 300 and 25 nm, and, since such sizes are small enough to render the sintering stress contribution significant also when external loads of several MPa are applied, we also added data of sinter-forging with a 0.3 MPa load.^{228–230}

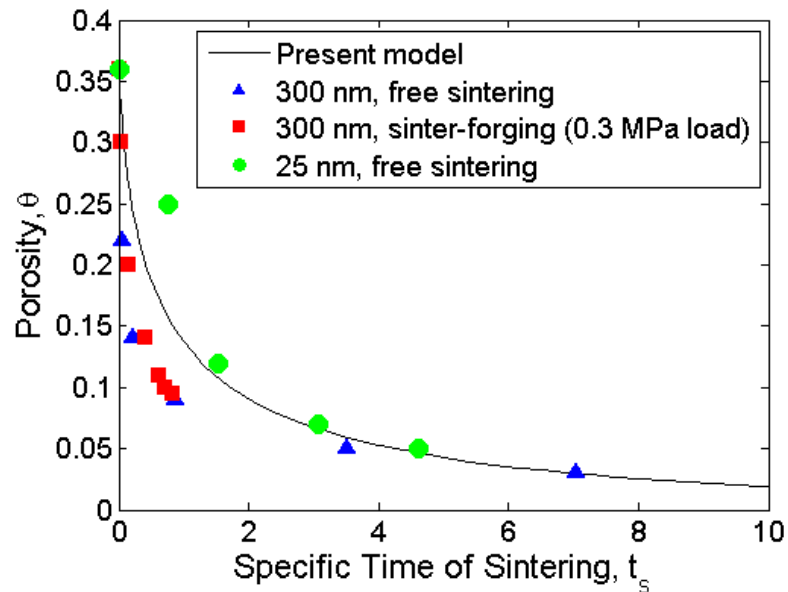


Figure 3.14 - Comparison of the densification kinetics model with experiments for alumina powder of different sizes.

By plotting the densification curve in function of the normalized time we are allowed to compare different powder sizes and temperature regimes, since their influence is embedded in the specific sintering time definition itself.

The choice of alumina was based on the large availability of sintering data in the literature, and on its consequent well-known material properties, even though often such values are not assessed.

Equation (3.84) results to be a useful tool in this sense, most interestingly for the individuation of a first estimation of the strain-rate sensitivity parameter. By comparing equation (3.84) with experimental data obtained by means of procedures which fall into the field of applicability of the present study, one can thus infer the mechanism underlying the densification process, case by case, by simply looking at the value of the strain-rate sensitivity parameter that provides the best fit.

The proposed iterative procedure is a useful and practical substitution of homogeneization techniques for the study of average mechanical properties of non-uniform materials.

Expressions (3.81) and (3.83) can be used instead of (3.76) and (3.63) for bulk modulus and sintering stress of materials with significant amounts of initial small-size intra-agglomerate porosity. Such an alteration is usually not necessary for the large inter-agglomerate pores, since the sample's volume fractions that they occupy is typically less than 10%, thus allowing assuming them to be isolated from each other.

3.1.5 Shear modulus of homogeneous and hierarchical porous structures with nonlinear viscous constitutive behavior

The shear modulus of a material expresses its resistance to any change of shape attempt. As for the bulk modulus case, when the material presents internal voids, the shear modulus will become dependent on porosity, together with the intrinsic properties of the material constituting the skeleton.

A treatment of the shear modulus analysis with a procedure that follows similar steps to what employed for sintering stress and bulk modulus, namely the individuation of a suitable simple domain and the application of opportune loading conditions, does not apply as smoothly to the present case. The reason for this is individuated in the definition of the equivalent strain rate W , here repeated for convenience of exposition.

For the analysis of a non-agglomerated domain (monoporous) we need to utilize the expression involving only the small size porosity

$$W_{monopor} = \sqrt{\frac{\psi \dot{\epsilon}^2 + \varphi \dot{\gamma}^2}{1 - \theta_s}} \quad (3.11)$$

For a medium containing hierarchical porous structures, we have to consider the overall porosity and the corresponding invariants, in this form

$$W_{bipor} = \sqrt{\frac{\Psi \dot{E}^2 + \Phi \dot{\Gamma}^2}{1 - \theta}} \quad (3.85)$$

In both cases, a “macroscopic” point of view has to be adopted. This means that the equivalent strain rate would be calculated for the entire domain, inclusive of the central void, which in the first case represents the small size porosity, while in the second case is the schematic of the large size one.

The advantage of this type of problem formulation in the sintering stress and bulk modulus contexts lied into the loading conditions that we imposed. By choosing an hydrostatic compression of a sphere, we were automatically eliminating the change of shape term ($\dot{\gamma}$ or $\dot{\Gamma}$), and consequently decoupling the bulk modulus derivation from the shear modulus one.

This is not possible here, and this limitation does not only render the problem more complex to solve. It also raises another issue due to the “macroscopic” viewpoint that we need to adopt when using a single-pore domain to reproduce the behavior of a medium endowed with an abundance of these pores and treat it as a continuum. The issue we refer to is the macroscopic expression of the second strain rate invariant. For the first strain rate invariant, we have the indissolubility equation (or conservation of mass) – (3.33) and (3.64) – that offers the possibility of immediately obtaining an expression that does not only apply to the dense material, but includes the pores too. An analogous resource is not available for the second invariant. This can be made clearer by considering the now well-known domain utilized for the determination of the properties of a monoporous material: a fully dense spherical layer surrounding a concentric hole (Figure 3.9). For this same domain, two perspectives have been adopted. We have solved the boundary value problem relative to the bulk material only (following Finnie and Ashby),^{148, 152} focusing in particular on the radial velocity and the radial and tangential strain rates. The shell is in itself incompressible, which implies that the strain rate tensor trace for the sole shell is equal to zero. At the same time, the second strain rate invariant is of immediate individuation by plugging the calculated strain rates in its definition. On the other hand, we have also looked at the hollow sphere as a whole. In this latter situation, the first strain rate invariant is not zero anymore, since it is defined by the indissolubility equation as a function of the porosity, with this porosity being the internal void. A global definition of the second strain rate invariant consists in noting that in these hydrostatic loading conditions it is equal to zero. One needs to understand that mixing the two perspectives would

mean basing our derivations on contradictory premises and obviously leads to erroneous results.

Some possible alternative options can be proposed. One needs first of all to change the study domain. A good alternative is identified in a hollow cylinder, even if such choice implies that we are shifting our attention from closed porosity to open porosity. This distinction goes back to the initial developments in the science of sintering, and refers to the voids interconnections within a powder specimen. As mentioned before, by open porosity we indicate the interconnected network of voids typical of green compacts and of the sample during the first stages of sintering. By closed porosity we mean the isolated pores, with no outlet on the external surface, that are inside the specimen during the final stages of densification, typically after 92% relative density has been reached. In the entirety of this work, the SPS optimization efficiency is based on this latter type of porosity (we will also see in Chapter 4 how we will focus our attention on the holding time step of the SPS route even when analyzing spatial temperature distributions). This is because in the stages in which open porosity is predominant, the main phenomenon associated with the sintering process is a material rearrangement that leads to the formation of necks and consequently to a global strengthening of the specimen. The shrinkage, on the other hand, occurs during the final stages, which is when closed porosity is the major component of the voids fraction in the sample.

However, even hypothesizing that using an open porosity schematic is an acceptable approximation for the individuation of the normalized shear modulus, the hollow cylinder domain presents further issues. In order to explain these additional aspects, let us consider the simpler fully dense cylindrical shell with an internal concentric cavity, instead of a biporous medium. We have pointed out how an optimal choice of the loading schematics plays a crucial role in the following derivations. For a fully dense cylindrical shell, as in the bulk spherical

layer case, the first step of the analysis consists in solving the associated boundary value problem in order to get velocities and strain rates. The solution of a power-law creep problem is not immediate for any system. The ones that can be obtained analytically are generally present in the literature, for instance in the same Finnie's publication that we cited for the sphere.¹⁴⁸ For a hollow cylinder, solutions have been reported for a radially loaded thin shell, not applicable here, or for a thick shell that is infinitely long in the axial direction (alternatively, a hollow cylinder constrained in the axial direction, since the advantageous condition here is the absence of axial strain), still radially loaded. This second one is not suitable to our study either, because in the case of infinitely long cylinder we are essentially simulating an absence of shape change again. Even with the axial constraint option, which leads to an aspect ratio change, once we have eliminated the central hole by means of radial compression, no further change of shape is allowed anymore, while in the general case a fully dense material can still be deformed as long as such deformation does not require a volume change. We have therefore implemented a specific case which fails to be generalized to more complex or realistic cases. The proof of that is found in the fact that such a solution provides a φ that tends to infinity when θ_S goes towards zero (as in the bulk modulus case), while one of the limit conditions that the shear modulus has to satisfy is being equal to one for a fully dense material:

$$\varphi(\theta_S = 0) = 1 \quad (3.86)$$

$$\Phi(\theta = 0) = 1 \quad (3.87)$$

The limit condition for porosity tending to 100% is, and in the bulk modulus case, φ and Φ approaching zero. We would therefore need to solve the power-law creep problem for a non-axially fixed thick and fully dense hollow cylinder, either loaded with a radial or a uniaxial pressure, but this case is not of immediate analytical solution and needs to be addressed numerically. Employing a numerical strain rates solution for the subsequent

derivation of our shear modulus fails to satisfy the analytical basis of this part of our study (with the only, smaller, exception of the final steps of the porosities kinetics calculations in 3.1.2), and such option is therefore discarded.

Possible alternatives that are still based on the resolution of an opportunely tuned creep boundary value problem can be suggested. An option is averaging the second strain rate invariant ($\dot{\gamma}$ or \dot{I}') over the entire volume of the domain, including the central hole, and then opportunely multiplying by the volume fraction they refer to, $(1 - \theta_S)$ or $(1 - \theta)$, respectively. Another option can be assuming a pure change of shape, without any shrinkage, deformation, in which both the shell and the internal void change their aspect ratio without causing any change in volume. Both these ideas can be the starting point of future work.

We will temporarily put them on a side for the sake of individuating the normalized shear modulus by using a strategy that requires less elaborated calculations. We will perform a hybrid experimental and analytical derivation.

It consists in the association of the continuum theory of sintering equations with a wide experimental campaign. Such campaign led to the proposal of an expression for the ratio of the yield stresses of a porous and a dense material, which has proven to be applicable to any powder material system constituted by spherical particles behaving visco-plastically.

The experimental results on which this approach relies are reported by Geindreau *et al.*^{159,160} They collected a large amount of data from previous works and added them to their own (relative to a lead powder), in order to obtain relationships that were generic enough to be applied to any spherical powder system. Their work is also aiming at proposing a constitutive model for the sintering of powders with the assistance of an external pressure. They, specifically, focus on the hot forming of metal powders, since at the time field-assisted sintering techniques were not fully developed yet. Even though our study wants to be applicable to both metals and ceramics and focuses on the more innovative spark plasma

sintering technologies, the premises of Geindreau's analysis render their outcomes suitable in the present context too. The section we are interested in for the individuation of the shear modulus is the one in which they analyze all the collected data on the uniaxial hot pressing of a variety of materials, and interpolate them with a suitable expression that gives the ratio between the flow stress of a porous material and its porous counterpart. The selection of a uniaxial compression as loading schematics is in line with what explained above in terms of opportunity of domain and boundary conditions settings when investigating on the shear modulus. Their domain was nonlinear viscous and monoporous.

The experimental fitting of this ratio leads to an expression which is only function of relative density. We here propose a first order approximation of the formula present in their publication, after having assessed that the change ingenerated by this simplification is negligible. We also substitute relative density with porosity, in order to be consistent with the notations used in the rest of our derivations. We call the ratio $s(\theta)$, defined as

$$s(\theta) = \frac{\sigma_{zf}(\theta)}{\sigma_{zf}(\theta = 0)} = 1 - \left[1 + \frac{3}{4}(1 - \theta) \right] \sqrt{\theta} \quad (3.88)$$

where $\sigma_{zf}(\theta)$ is the flow stress of specimen with porosity θ and $\sigma_{zf}(\theta = 0)$ is the flow stress of a fully dense specimen at the same strain rate. Figure 3.15, borrowed from Geindreau's publication, shows the plot of s as a function of relative density. Equation (5) in the figure corresponds to our (3.88).

We now show where the role of s comes into play for the shear modulus derivation.

The first step consists in taking the constitutive equations of the continuum theory of sintering and rewriting them to express strain rates as functions of stresses. We obtain

$$\dot{\varepsilon}_{ij} = A_n \sigma(W)^{\frac{n-1}{2}} \left(\frac{1}{\varphi} \sigma'_{ij} + \frac{1}{\psi} \sigma_{kk} \delta_{ij} \right) \quad (3.89)$$

with σ'_{ij} being the deviatoric part of the stress tensor (Pa). Notice that we have used A_n and n because of clarity of notations. Recall that they can both be immediately connected to their “ m ” counterparts as $A_n = A_m^{-n}$ and $n = 1/m$.

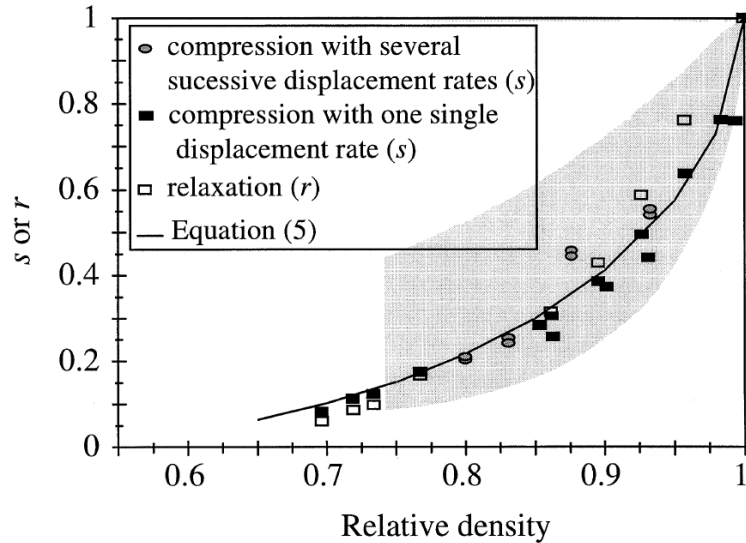


Figure 3.15 – Plot of the function s as a function of relative density with the corresponding experimental data. (Geindreau and Bouvard, *Eur. J. Mech.*, 1998)

The equivalent stress, instead of as a function of W , can also be written as

$$\sigma(W) = \sqrt{\frac{p^2/\psi + \tau^2/\varphi}{1 - \theta}} \quad (3.90)$$

where p and τ are the first and second stress tensor invariants (Pa), respectively, and θ here means a generic porosity, which we will take care of specifying (small size, large size or global) later.

In uniaxial compression we find that the equivalent stress becomes

$$\sigma(W) = \sigma_z \sqrt{\frac{1/\psi + 1/\varphi}{1 - \theta}} \quad (3.91)$$

and the axial strain rate component is given by

$$\dot{\epsilon}_z = A_n \left(\sigma_z \sqrt{\frac{1/\psi + 1/\varphi}{1 - \theta}} \right)^n \sqrt{(1/\psi + 1/\varphi)(1 - \theta)} \quad (3.92)$$

It is here that the function $s(\theta)$ is needed. Considering that the applied load σ_z is the flow stress of our porous specimen, and recalling the definition of $s(\theta)$, the axial strain rate can be expressed in the following form

$$\dot{\epsilon}_z = A_n \left(\frac{\sigma_z}{s} \right)^n \quad (3.93)$$

By equating (3.87) and (3.88), we ultimately obtain

$$\frac{1}{\psi} + \frac{1}{\varphi} = [s^{-2n}(1 - \theta)^{n-1}]^{\frac{1}{n+1}} \quad (3.94)$$

which, in terms of the strain-rate sensitivity m , becomes

$$\frac{1}{\psi} + \frac{1}{\varphi} = \left[\frac{(1 - \theta)^{1-m}}{s^2} \right]^{\frac{1}{1+m}} \quad (3.95)$$

We now restore the distinction between homogeneous and agglomerated porous structures. We also introduce apposite subscripts for the two moduli, remarking that the following outcomes are partially dependent on experimental results.

For a monoporous (homogeneous) domain, recalling that when considering only one size of porosity we are associating it with the small size type, we have

$$\frac{1}{\psi} + \frac{1}{\varphi_{exp}} = \left[\frac{(1 - \theta_S)^{1-m}}{s^2} \right]^{\frac{1}{1+m}} \quad (3.96)$$

from which we derive the normalized shear modulus for a monoporous nonlinear viscous specimen as

$$\varphi_{exp} = \frac{1}{\left\{ \left[\frac{(1 - \theta_S)^{1-m}}{s^2} \right]^{\frac{1}{1+m}} - \frac{1}{\psi} \right\}} \quad (3.97)$$

which becomes

$$\varphi_{exp} = (1 - \theta_s)^{\frac{1-m}{1+m}} \left\{ \left[1 - \frac{\sqrt{\theta_s}}{4} (7 - 3\theta_s) \right]^{\frac{-2}{m+1}} - \frac{9}{4} \left(\frac{m\theta_s^m}{1 - \theta_s^m} \right)^{\frac{2}{m+1}} \right\} \quad (3.98)$$

The graphs in Figure 3.16 compare the semi-experimentally developed formulation of φ with the ones proposed by Skorokhod,¹¹³ Sofronis and McMeeking,¹⁵⁵ and Geindreau and Bouvard.¹⁶⁰ The latter used our same source of experimental data but with a different model for the creep of a porous medium. All the three formulations are given in the following Table 3.4.

Table 3.4 – Expressions of normalized shear modulus of a monoporous material compared in Figure 3.16

	Present Work	Skorokhod
φ	$(1 - \theta_s)^{\frac{1-m}{1+m}} \left\{ \left[1 - \frac{\sqrt{\theta_s}}{4} (7 - 3\theta_s) \right]^{\frac{-2}{m+1}} - \frac{9}{4} \left(\frac{m\theta_s^m}{1 - \theta_s^m} \right)^{\frac{2}{m+1}} \right\}$	$(1 - \theta_s)^2$
	Sofronis and McMeeking	Geindreau and Bouvard
φ	$\left[\frac{1 - \theta_s}{1 + \theta_s} \right]^{\frac{2}{1+m}}$	$\left[1 + 21.5 \left(\frac{\theta_s}{0.43 - \theta_s} \right)^{1.25} \right]^{-1}$

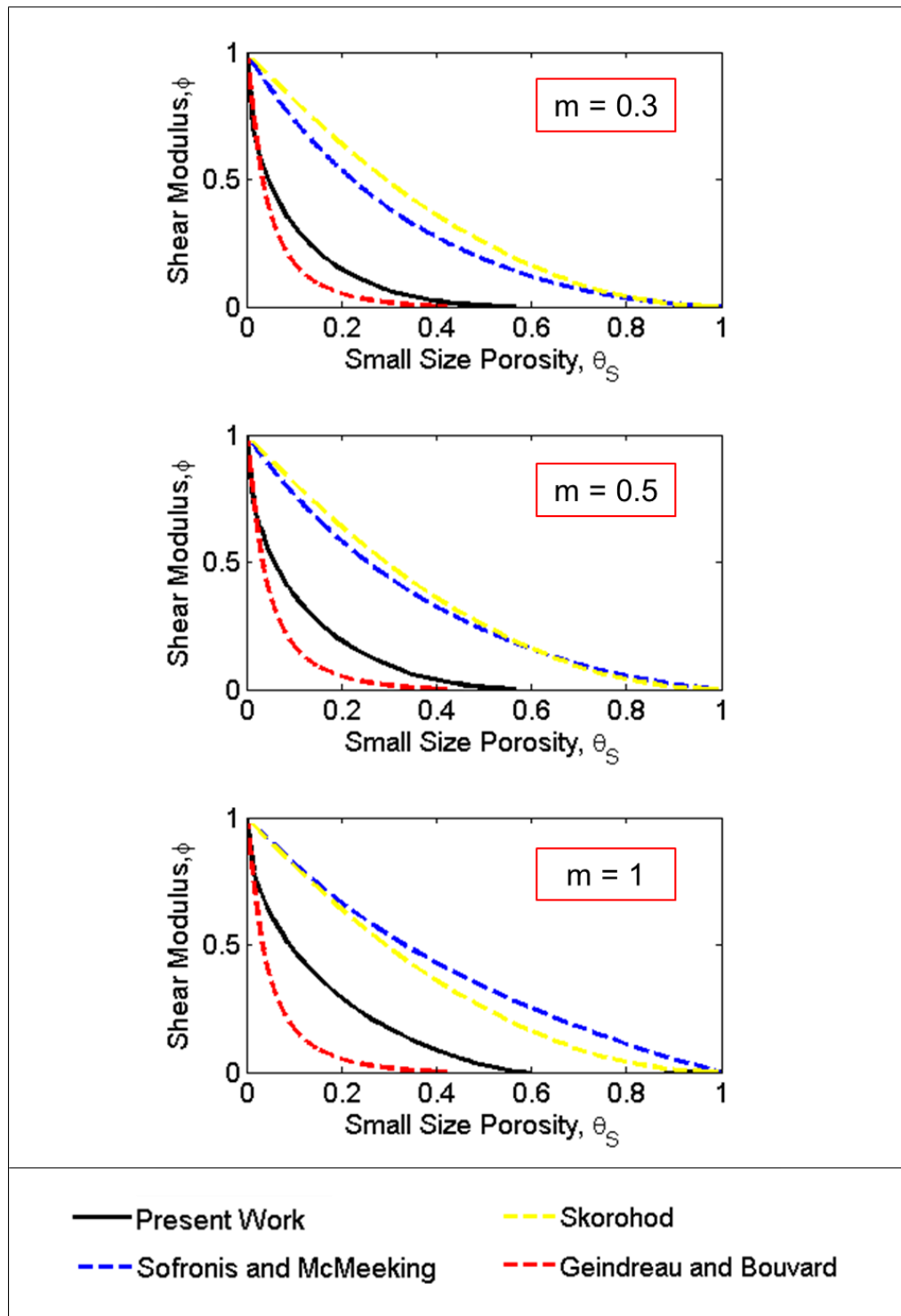


Figure 3.16 – Normalized shear modulus expressions for monoporous materials and different values of the strain-rate sensitivity parameter.

An important verification concerns the limits mentioned above that this function needs to respect when porosity disappears or tends to 100%. For a dense material we have that the shear modulus equals zero, while it asymptotically goes to zero when the voids volume fraction increases towards a value of 1, because of the same reasons explained in the context of the bulk modulus investigation.

It is interesting to notice that here, having used experimental results for the derivation, our shear modulus reaches zero before porosity approaches 100%. This trend also appears in the same Geindreau's study, for both bulk and shear moduli (see Figure 3.12).

Analogously to the monoporous case, for the biporous (hierarchical) one, having the material the same rheology, we obtain

$$\Phi_{exp} = \frac{1}{\left\{ \left[\frac{(1-\theta)^{1-m}}{s^2} \right]^{\frac{1}{1+m}} - \frac{1}{\bar{\psi}} \right\}} \quad (3.99)$$

which can also be expressed as a function of porosities only, but we will keep this more compact formulation for now, so that it is immediate to see that when the large size porosity tends to zero Φ_{exp} reduces to φ_{exp} .

The derivation of the necessary parameters is now complete. Future work will consist in analyzing more in depth the macroscopic expressions, in which for now the dependence on the monoporous parameters has been left explicit in order to verify that the two versions coincide when large size porosity vanishes. The numerical study in the following section will indeed be based on the macroscopic expressions of bulk modulus, shear modulus and sintering stress. A purely analytical derivation of the shear modulus can also be attempted, according to the guidelines suggested at the beginning of this section.

3.2 Optimization of the material structure based on strain-rate sensitivity

3.2.1 Strain-rate sensitivity and temperature

With the completion of the kinetics and mechanical properties analysis, we have concluded the definition of the analytical modeling framework for the study of a nonlinear viscous material presenting a hierarchical porous structure. We can now proceed to the optimization stage.

The proposed optimization strategy relies on the connection between powder material's rheology and temperature. Since all the derived expressions depend on strain-rate sensitivity, we can aim at equating (or regulating) the shrinkage rates of small and large pores by selecting the optimal degree of nonlinearity (strain-rate sensitivity value). The degree of nonlinearity is, in turn, controlled by temperature, and thus an aware choice of SPS thermal routine can lead to improved control of the material structure evolution during processing.

It has been anticipated in the introductory comments that the strain-rate sensitivity is as fundamental as unexplored parameter for the study of powder processing at elevated temperatures. We have also underlined how its value provides an indication of the order of nonlinearity characterizing the constitutive behavior of a material, and therefore of the creep mechanism that the material is undergoing during the hot deformation. The physical meaning of the interconnection between strain-rate sensitivity and thermal conditions lies in the mechanisms underlying plastic deformation at high temperatures. Creep consists in temperature-enhanced permanent material deformation, which, as any plastic strain formation, proceeds through dislocations generation and motion. At high temperatures, diffusion phenomena are present and start interacting with such dislocation movement. Therefore, depending on the temperature level, such interactions will be of different entity and level, and

thus influence mesoscopic and macroscopic deformation in a variety of fashions. A few guidelines have been empirically drawn:^{231, 232}

- For $m = 1$ ($n = 1$) we have Nabarro-Herring creep, a transport of matter by diffusion through the grain lattice, which sometimes specializes into the Coble creep, characterized by diffusion through the grain boundaries;
- For $m = 0.5$ ($n = 2$) we have grain-boundary sliding (GBS)-based creep;
- For $m = 0.3$ ($n = 3$) we have dislocation glide-controlled creep;
- For $m = 0.2 - 0.25$ ($n = 4 - 5$) we have dislocation climb-controlled creep;
- For $m < 0.1$ ($n > 10$) we have the creep characterizing dispersion-strengthened alloys.

The characteristic of strain-rate sensitivity that interests us the most is its dependence on temperature. Such correlation can be found combining analytical considerations with experimental data. The literature lacks a comprehensive analysis of how creep phenomena are altered when applying different temperatures, but there is the exception of the work of Shuji Taira *et al.*,²³³⁻²³⁶ who investigated on the effects of varying temperatures and loads on the high-temperature deformation of steels. Since their considerations are based on the assumption that the equation of state for creep holds, their results can be generalized to other material systems, provided sufficient experimental data. Their studies are particularly valuable as they show how information on creep under varying temperature conditions can be inferred from constant temperature data for the same material, and also how the secondary creep stage (steady-state) is related to the primary one (transient). These features allow the derivation of outcomes on non-constant temperature creep directly from data that are abundant in the literature. Such considerations depend on the applicability of the mechanical equation of state. Since in our case the creep equation of state is precisely the relation that we use to describe the

rheology of the powder materials undergoing consolidation, we can consider Taira's results suitable for our derivations.

It is also worth mentioning that the experimental analyses under varying temperatures were conducted with very high heating rates, a condition which turns out to be particularly suitable for the application to the spark plasma sintering case. Such fast temperature changes even turned out to be responsible for enhanced creep deformation rates, which could at least partially explain the efficiency of SPS in consolidating powder materials.

Our analytical procedure for the derivation of $m(T)$ consists in equating two empirical expressions for the strain rate during the creep steady state (secondary stage), the one proposed by Taira²³³ and the one proposed by Ashby.²¹⁷

Taira shows that the steady-state creep deformation rate can be written as

$$\dot{\epsilon} = \left(\frac{A_{\bar{n}} \bar{n}}{C_2} \right)^{\frac{1}{C_1}} \exp \left(- \frac{\bar{K}}{C_1 T} \right) \quad (3.100)$$

where A_0 (1/s) and \bar{K} (K) are constants that depend on the applied stress, \bar{n} is the exponent of time in the strain-time relation ($\dot{\epsilon} \propto t^{\bar{n}}$), C_1 and C_2 are material constants ($C_1 \cong 0.5$ and $C_2 = 1 \sim 6$).

We equate expression (3.100) to the equation of secondary creep as proposed by Ashby,²¹⁷ resulting in

$$\left(\frac{A_{\bar{n}} \bar{n}}{C_2} \right)^{\frac{1}{C_1}} \exp \left(- \frac{\bar{K}}{C_1 T} \right) = 10^{-6} \exp \left[- \frac{Q_{PLC}}{RT_m} \left(\frac{T_m}{T} - 2 \right) \right] \left(\frac{\sigma}{\sigma_{ref}} \right)^n \quad (3.101)$$

with Q_{PLC} being the activation energy for creep (J/mol), T_m the material's melting point (K), and σ_{ref} (Pa) the stress at which a strain rate of 10^{-6} 1/s is reached when a temperature equal to half the melting point is applied. Note that Ashby's expression is given in a form such that experimental data on the pre-exponential coefficient, A_n – particularly complicated to obtain – are not needed (see paragraph 3.1.1 and expressions (3.2) and (3.29)).

We call $a = \left(\frac{A_0 \bar{n}}{c_2}\right)^{\frac{1}{c_1}}$, $b = \frac{K}{c_1}$, $c = 10^{-6}$ and $d = \frac{Q_{PLC}}{R}$, and we rearrange such that

$$\frac{a}{c} \exp\left(\frac{d-b}{T} - \frac{2d}{T_m}\right) = \left(\frac{\sigma}{\sigma_{ref}}\right)^n \quad (3.102)$$

which, defining $f = \frac{2d}{T_m}$, can be written as

$$\ln\left(\frac{a}{c}\right) - f + \frac{d-b}{T} = n \cdot \ln\left(\frac{\sigma}{\sigma_{ref}}\right) \quad (3.103)$$

Rearranging, we obtain

$$n = \frac{gT + h}{T} \quad (3.104)$$

where we have called $g = \frac{\ln(a/c) - f}{\ln(\sigma/\sigma_{ref})}$ and $h = \frac{d-b}{\ln(\sigma/\sigma_{ref})}$.

Since $n = 1/m$, the strain-rate sensitivity dependence on temperature is then found as

$$m = \frac{T}{gT + h} \quad (3.105)$$

for which the parameters g and h depend on the studied materials' properties and, formally, on the applied stress, and can be calculated from data on conventional creep curves. In the classic theory of creep, the strain-rate sensitivity should not depend on the applied stress. We will show how this still holds, in practice, for expression (3.105).

The data that need to be plugged into (3.105) can be taken from the broad available literature on high-temperature deformation of a variety of materials. More specifically, the data for the right-hand side of expression (3.101) – Q_{PLC} , T_m and σ_{ref} – are given in Ashby's HIP Readings 6.0,²¹⁷ while the values of a and b are easily derived from the interpolation of experimental creep results.

For most materials, creep data are abundant and extremely scattered, because of the wide variety of testing conditions, in terms of loading schematics, surrounding atmosphere, addition of dopants and grain size. We therefore select the necessary experimental data from

sources that operated under testing conditions as close as possible to our SPS cases, namely the application of compressive loads, vacuum or inert atmosphere, and suitable material compositions. The choice of focusing on compressive loads is also due to our interest in ceramic materials, which are complicated to test in tension or bending, and for which the most consistent and repeatable results on the secondary creep stage are attained under compression conditions.

We can now plot how strain-rate sensitivity changes with temperature, specifically in a range that is reasonable for SPS thermal routines. We provide here some examples for three different materials, namely copper, alumina and silicon nitride. Copper and alumina are the typical materials – insulating and conductive, respectively – that one selects for the initial assessment of sintering theories and models, because of the large amount of data available in the literature. Silicon nitride was the object of a comprehensive FEM study of spark plasma sintering that will be described in detail in the following chapter. The temperature intervals considered on the x-axis are calculated to be $0.5T_m - 0.9T_m$, since typical sintering temperatures oscillate around 70% of the processed material's melting point.

Even though the information that one can individuate in the literature to validate the obtained results for $m(T)$ are often unclear and sometimes contradictory, some guidelines can still be individuated. The influence of temperature on m is often taken as negligible, because of the narrow range of temperatures on which each creep study tends to focus (intervals around 50-100°C). Nevertheless, if one compares all the values of strain-rate sensitivity for the same material as presented in certain review articles, some noticeable changes appear.^{146,}

¹⁴⁷ A closer look at the plots of strain rate vs. stress that are typically employed for the determination of the stress exponent generally shows slight differences in slope of the curves when different temperature levels are considered. Ashby and Frost themselves stated that the constant values of n provided in their deformation maps¹⁶⁵ are approximations, and that a

good rule of thumb is considering that the stress exponent becomes $n + 2$ at temperatures lower than half the material's melting point. We, thus, expect to obtain plots in which m ($1/n$) increases with temperature, and spanning a range of values smaller than the entire admissible interval ($0 < m < 1$). This also follows the experimental evidence according to which the Nabarro-Herring type creep ($m = 1$) occurs at very high temperatures.²³⁷ Another immediate check of the reliability of our plots is assessing if our obtained m values are comparable with what available in the literature for certain thermal levels.

Figure 3.17 shows the copper case.²³⁸⁻²⁴⁰ The trend is what expected and the values are consistent with the data of Ashby,²¹⁷ according to which $n = 4.8$, and therefore $m = 0.21$. This value is indicative of dislocation-climb controlled deformation, and indeed dislocation activity is known to play a significant role in the consolidation of ductile powders. Other publications on the creep deformation of copper at low and high temperatures (400-600 K and 800-1100 K, respectively) further confirm that m increases when raising the applied temperature.^{165, 237} The Taira parameters for copper are $A_0 = 6 \times 10^5$ 1/s and $K = 22859$ K, assuming $\bar{n} = 0.5$, an average value for every material.

Figure 3.18 presents the alumina case. This is a material for which the experimental data are extremely scattered,^{147, 241, 242} but with some additional analysis consistency can be reinstated.

Ceramics in general present a dependence of the creep exponent on the tested material's grain size. This phenomenon is particularly evident for certain material systems, such as alumina and silicon nitride themselves,^{241,242} but in any case it is important to distinguish between polycrystalline and monocrystalline materials. Single crystals tend to show a lower value of strain-rate sensitivity. The value of m presented in the HIP Readings (0.33)²¹⁷ is, when inserted in a broader context,¹⁴⁷ the one typical of single crystals, while polycrystalline materials show higher values, approaching 1 at higher temperatures.

Because of our interest in powder consolidation, we obviously focused on experimental data relative to polycrystalline materials, with a grain size of a few microns, to find a and b .¹⁴⁷ From these, we obtained $A_0 = 12 \times 10^5$ 1/s and $K = 35875$ K, with the same assumption of $\bar{n} = 0.5$. All other data were taken from the available literature,²¹⁷ with the only exception of the creep activation energy (Q_{PLC}), for which we had to introduce a correction due to the effect of the magnesia (MgO) doping added for grain size retention.¹⁴⁷ Again, the expected trend of m augmenting with temperature is confirmed, and the range of values spanned in the considered temperature interval includes the one proposed in the relevant paper, $m = 0.83$. The dominating deformation phenomenon is therefore Nabarro-Herring diffusional creep, with minor contributions of grain boundary sliding.

Figure 3.19 shows the result obtained for silicon nitride. As in most ceramics, the value of the stress exponent n oscillates between 1 and 3.¹⁴⁷ For the compressive creep case study from which the values of a and b were inferred (given $A_0 = 6 \times 10^8$ 1/s, $K = 44192$ K and $\bar{n} = 0.5$), relative to a micron-sized powder, n resulted to be ~ 2.3 , corresponding to $m \cong 0.43$.^{243,244} Such values approach grain boundary sliding phenomena, but the case of silicon nitride is particularly complex because of the many phases involved when deforming at elevated temperatures, including the presence of a glassy phase at the grain boundaries.^{244–247}

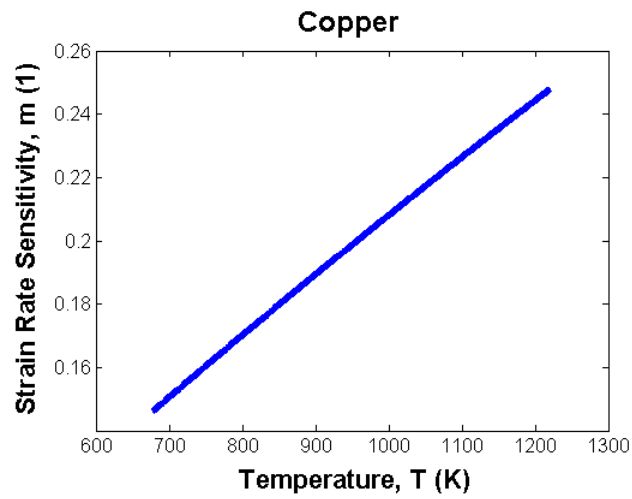


Figure 3.17 – Strain-rate sensitivity evolution with temperature for copper.

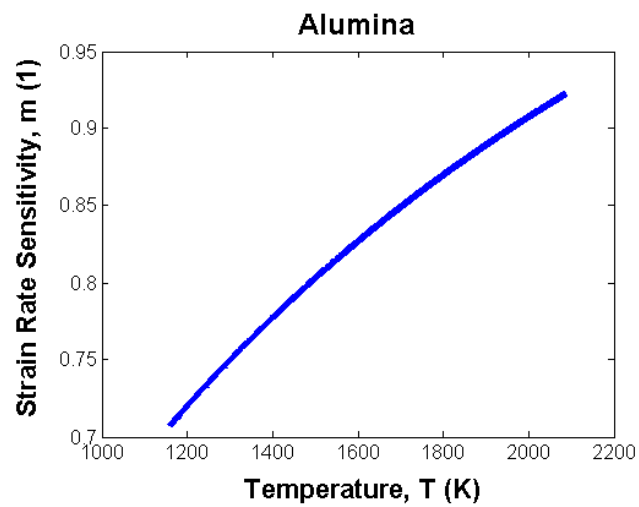


Figure 3.18 – Strain-rate sensitivity evolution with temperature for alumina.

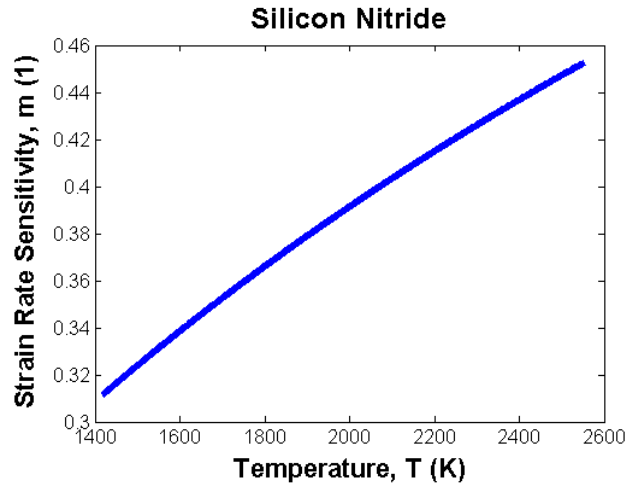


Figure 3.19 – Strain-rate sensitivity evolution with temperature for silicon nitride.

We employed data for silicon nitride also to evaluate the effect of the applied stress on these types of curves, as represented in Figure 3.20. A wide range of values were available for the case of yttria-doped silicon nitride. Because of the different composition, slight discrepancies with respect to the previous plot can be observed. The first interpolation of experimental data, in part (a) of Figure 3.20, actually shows a noticeable change between the different applied stress levels. This happens because we are keeping the activation energy for power-law creep (Q_{PLC}) constant, while it has been shown that its value increases with the imposed pressures.²⁴⁸ In traditional creep studies, as n is estimated from strain rate/stress curves plotted at constant temperature, Q_{PLC} is derived from strain rate/temperature graphics, with each curve relative to a specific stress level. Taking into account such rise in activation energy when shifting from 100 to 150 and 200 MPa, a much better agreement is found, as depicted in part (b) of the same figure. The minor discrepancies that are still present are ascribable to experimental error in the measurement of the data used for our regression procedure.

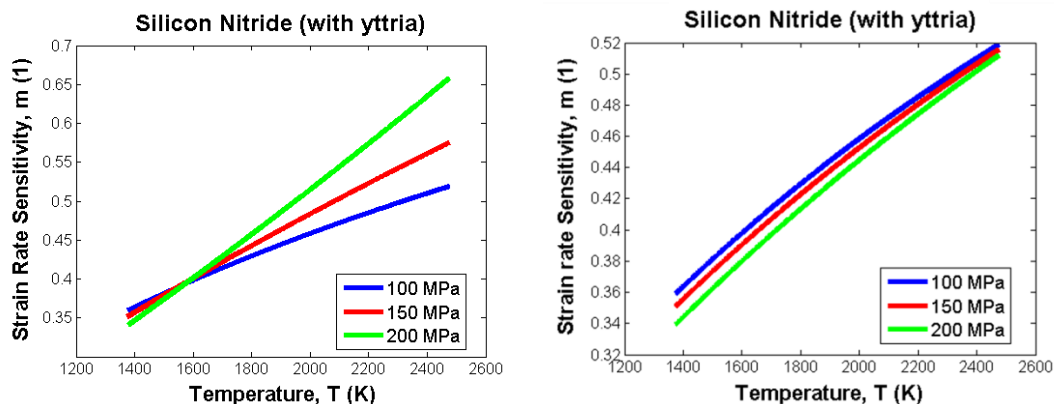


Figure 3.20 – Strain-rate sensitivity dependence on temperature and stress for silicon nitride without (left) and with (right) activation energy correction.

From these examples it will be noticed that the pre-existing experimental results that need to be selected as input for (3.105), and thus the derivation of the $m(T)$ plots, need to be carefully selected to be as adherent as possible to the material of interest, in terms of composition, grain/particle size and surrounding atmosphere. The vast variety of creep data available in the literature could, nevertheless, be easily summarized with the numerical regression and machine learning algorithms available today. In such a way, trends and correlations, together with the weight of each influencing parameter, could be more clearly individuated. This step can be the object of further work, which would fall in the context of the Materials Project (<https://materialsproject.org/>).

3.2.2 Optimization strategies

The optimization of the SPS efficiency based on strain-rate sensitivity coincides with individuating the most suitable dwelling thermal conditions to eliminate agglomeration *in situ*. Now that we have the tools necessary to assess how m depends on temperature, we can correlate such information with the remaining of our optimization procedure. We employ,

therefore, the expressions provided throughout Section 3.1, namely the formulations of the material properties characterizing a hierarchical porous structure in function of m itself.

We report here a summary of the outcomes of the derivations in Section 3.1. Certain substitutions have been operated in order to simplify the obtained formulas. Note that the sintering kinetics are expressed with respect to the specific time of sintering, and that the sintering stress and bulk modulus for monoporous materials are given for the non-dilute case (more general and adherent to experimental spark plasma sintering studies).²¹⁸

Table 3.5 – Summary of sintering kinetics, sintering stress and bulk and shear moduli expressions for monoporous and biporous materials.

<p><i>Small size</i> <i>porosity</i> <i>evolution rate</i></p>	$\frac{d\theta_S}{dt_s} = \left[\frac{\left(1 + \frac{P_{LS}}{P_{ext}}\right) (1 - \theta_S)^{\frac{m+1}{2}} (\theta_S - 1)^{m-1}}{\left(1 + \frac{P_{LOS}}{P_{ext}}\right) \psi} \frac{1}{(2k\theta_L - 1)} \left(6k^2\theta_L^2 \frac{\psi}{\varphi} + 1\right)^{\frac{1-m}{2}} \right]^{\frac{1}{m}}$
<p><i>Large size</i> <i>porosity</i> <i>evolution rate</i></p>	$\frac{d\theta_L}{dt_s} = -3k\theta_L \frac{1 - \theta_L \psi}{1 - \theta_S \varphi} \left[\frac{\left(1 + \frac{P_{LS}}{P_{ext}}\right) (1 - \theta_S)^{\frac{m+1}{2}} (\theta_S - 1)^{m-1}}{\left(1 + \frac{P_{LOS}}{P_{ext}}\right) \psi} \frac{1}{(2k\theta_L - 1)} \left(6k^2\theta_L^2 \frac{\psi}{\varphi} + 1\right)^{\frac{1-m}{2}} \right]^{\frac{1}{m}}$
<p><i>Small-size</i> <i>pores radius</i> <i>evolution rate</i></p>	$\frac{dr_{sp}}{dt_s} = \frac{r_{sp}}{3\theta_S(1 - \theta_S)} \left[\frac{\left(1 + \frac{P_{LS}}{P_{ext}}\right) (1 - \theta_S)^{\frac{m+1}{2}} (\theta_S - 1)^{m-1}}{\left(1 + \frac{P_{LOS}}{P_{ext}}\right) \psi} \frac{1}{2k\theta_L - 1} \left(6k^2\theta_L^2 \frac{\psi}{\varphi} + 1\right)^{\frac{1-m}{2}} \right]^{\frac{1}{m}}$
<p><i>Large-size</i> <i>pores radius</i> <i>evolution rate</i></p>	$\frac{da}{dt_s} = \frac{a}{1 - \theta_S} \left(\frac{1}{3} - k \frac{\psi}{\varphi}\right) \left[\frac{\left(1 + \frac{P_{LS}}{P_{ext}}\right) (1 - \theta_S)^{\frac{m+1}{2}} (\theta_S - 1)^{m-1}}{\left(1 + \frac{P_{LOS}}{P_{ext}}\right) \psi} \frac{1}{2k\theta_L - 1} \left(6k^2\theta_L^2 \frac{\psi}{\varphi} + 1\right)^{\frac{1-m}{2}} \right]^{\frac{1}{m}}$

Table 3.5 – Summary of sintering kinetics, sintering stress and bulk and shear moduli expressions for monoporous and biporous materials (cont.).

<p><i>Sintering stress monoporous materials</i></p>	$P_{L_S} = P_{L_0S} (1 - \theta_S)^{\frac{2}{(m+1)}}$
<p><i>Bulk modulus monoporous materials</i></p>	$\psi = \left[\left(\frac{2}{3} \right)^m \frac{(1 - \theta_S)^{(m+3)/2} (1 - \theta_S^m)}{m \theta_S^m} \right]^{\frac{2}{(m+1)}}$
<p><i>Shear modulus monoporous materials</i></p>	$\varphi = (1 - \theta_S)^{\frac{1-m}{1+m}} \left\{ \left[1 - \frac{\sqrt{\theta_S}}{4} (7 - 3\theta_S) \right]^{\frac{-2}{m+1}} - \frac{9}{4} \left(\frac{m \theta_S^m}{1 - \theta_S^m} \right)^{\frac{2}{m+1}} \right\}$
<p><i>Sintering stress biporous materials</i></p>	$P_L = \frac{P_{L_S}}{1 - 2k\theta_L} \left(6k^2 \theta_L^2 \frac{\psi}{\varphi} + 1 \right)^{\frac{1-m}{2}}$
<p><i>Bulk modulus biporous materials</i></p>	$\Psi = \psi \frac{(1 - \theta_L)^{\frac{m-1}{m+1}}}{\left(1 - 3k\theta_L \frac{\psi}{\varphi} \right)^{\frac{2m}{m+1}}}$
<p><i>Shear modulus biporous materials</i></p>	$\Phi = \left\{ \left[\frac{(1 - \theta)^{1-m}}{\left((1 - \sqrt{\theta} - \frac{3}{4} \sqrt{\theta} (1 - \theta))^2 \right)^{\frac{1}{m+1}}} \right]^{\frac{1}{m+1}} - \frac{\left(1 - 3k\theta_L \frac{\psi}{\varphi} \right)^{\frac{2m}{m+1}}}{\psi (1 - \theta_L)^{\frac{m-1}{m+1}}} \right\}^{-1}$

Because of how we conducted our derivations, two optimization procedures are possible.

The first one is the semi-analytical solution of the kinetics equations (3.36) and (3.41) that we anticipated above. In order to complete the analysis from this perspective, we needed to derive sintering stress, bulk and shear modulus for the small size porosity and for a nonlinear viscous rheology. Now that we have done so, we have achieved our initial aim of obtaining

$$\dot{\theta}_S = f(\theta_S, \theta_L, m)$$

$$\dot{\theta}_L = g(\theta_S, \theta_L, m)$$

as reported in Table 3.5.

This is where numerical methods come into play. The resolution of a set of two coupled ordinary differential equations, which can be operated with the Runge-Kutta methods, is what renders the investigation, purely analytical until now, semi-analytical. We can also include the pores radii shrinkage rates in our computations, and therefore employ the same numerical methods to solve a set of four coupled differential equations. Note that the radii shrinkage rates are functions of the same parameters listed above, namely porosities and strain-rate sensitivity. Material properties, such as creep parameters and surface tension, and externally applied load are embedded in the normalized sintering time. The apparent dependence on surface tension that seems to be still present in the equations in Table 3.5, through the factor k , is actually canceled out if we recall the definition of k and substitute the sintering stresses definitions:

$$k = \frac{P_{L0L}}{P_{L0L} + 3P_{LS}} = \frac{\frac{3\alpha}{a}}{\frac{3\alpha}{a} + \frac{9\alpha(1-\theta_S)^{\frac{2}{m+1}}}{r_{sp}}} = \frac{r_{sp}}{r_{sp} + 3\alpha(1-\theta_S)^{\frac{2}{m+1}}} \quad (3.31)$$

Any SPS (or more general sintering) routine can be reconstructed, provided we plug into the formulas experimental data on material properties and powder compact morphology. Specifically, the inputs needed for the coupled ODE's solution are the initial values of porosities ($\theta_{L,0}$ and $\theta_{S,0}$) and pores radii (a_0 and $r_{sp,0}$).

Some additional information is needed to estimate the normalized SPS time. As expressed by (3.42), we need the same applied load, surface tension and pore size, but also the creep constant A_m . The work of Ashby²¹⁷ provides a useful way of calculating it, in accordance with what shown in Equation (3.101). Because of the difficulties in experimentally determining its value, he proposed to manipulate the creep equation in such way that

$$A_n = \frac{10^{-6}}{(\sigma_{ref})^n} \exp \left[-\frac{Q_{PLC}}{RT_m} \left(\frac{T_m}{T} - 2 \right) \right] \quad (3.106)$$

with the involved parameters already defined in Section 3.2.1. Note that the data required are all easily retrievable with conventional creep tests and are tabulated for a variety of materials in the HIP Readings.²¹⁷

Recalling that $A_m = (A_n)^{-m}$, and considering the typical duration of spark plasma sintering processes to be of the order of a few minutes and up to one hour, we can calculate a reasonable range of normalized SPS time for each material of interest. It results to be between 10 and 100 for most materials.

We can thus study the evolution with time of θ_S and θ_L , together with the radii of small and large pores, r_{sp} and a , and identify the values of m such that the large size porosity can be removed before the shrinkage of the small size ones (or, if in certain cases this is not an achievable objective, the fastest shrinkage of large pores with respect to the small ones). Such an analysis can be simply conducted in MATLAB®, or with similar software.

A first example of the results that can be obtained is given in Figures 3.21 and 3.22. The specific sintering time was estimated for the spark plasma sintering of alumina, with

holding step of 15 minutes at 1850 K and with an applied pressure of 60 MPa. The initial values of small and large size porosity were chosen to be 30% and 10%, respectively, and the small and large pores initial radii were 100 nm and 1 μm . It appears evident how a wide size gap between small and large pores (two orders of magnitude) leads to an almost negligible shrinkage of the inter-agglomerates voids. Both the porosity and radius shrinkage curves are almost flat for the large voids, while for the small pores we can observe very fast shrinkage, due to their small sizes. This leads to the undesired non-uniform final structures, with residual large voids and grain growth within the agglomerates. It can also be observed that an increase in the strain-rate sensitivity value renders the material more sinterable. Indeed, when m approaches zero, the porosity and radius curves show a sharp decrease at the very beginning of the process, followed by a slow densification, which seems to reach an asymptote, even if for porosity values greater than zero. The sudden initial shrinkage is expected when a plastic behavior is considered ($m = 0$).

These same considerations apply if we consider a narrower gap in initial pore sizes, such as what depicted in Figures 3.23 and 3.24. Here small pores have an initial radius of 1 μm , while the large voids are just five times larger. In such a case we choose to use a linear scale instead of a logarithmic one for the radius axis in Figure 3.24. This choice makes it more evident that, as expected, large pores shrink faster than the small ones. Unfortunately, the decrease in densification rate still hampers the de-agglomeration process, so that the two curves, small and large size porosity, do not catch up completely even in this case. Nevertheless, the fast initial shrinkage plays an important role in the reduction of both volume fraction and size of large pores. Since small-size porosity reaches values close to 0% in all cases with $m \geq 0.3$, the amounts of overall residual porosity should not exceed 5%, an acceptable values in many practical situations. These curves become useful not only to select the most suitable strain-rate sensitivity value (and thus holding temperature), but also for the

determination of a dwelling step duration that is sufficient to produce densification without significant grain growth. This translates in not continuing the process for more than a few minutes after the small-size porosity has disappeared. Ideally, we would like the two porosity curves to intersect each other as late as possible, meaning that the large pores have time to shrink and reach the small ones size, while small pores are still present.

Figure 3.25 shows densification curves for the same agglomerated alumina, zoomed in at the beginning of the SPS holding. Also in this case the initial porosities are 30% for the intra-agglomerates voids and 10% for the inter-agglomerates ones. We can observe that a decrease in the value of strain-rate sensitivity leads to the desired delay in the intersection, but, as stated above, it also slows down densification. A compromise solution needs to be found case by case.

Figure 3.26 shows the effects of changing the initial content of small and large size pores, while keeping the overall amount of voids constant. We can observe a shift in the curves, which remain parallel to each other. In the small-size porosity case the initial shrinkage is so fast that the three curves are almost overlapped.

Figure 3.27 presents the evolution of the ratio between small and large pores radii as a function of normalized time and for different values of strain-rate sensitivity. The large pores are 100, 10 and 5 times the size of the small ones in the top, center and bottom plots, respectively. It is interesting to notice how, when reducing the size gap, the radii ratio tends to increase at the beginning of the SPS holding time, especially when approaching a perfectly plastic rheology. Such an effect is the direct consequence of the material's quasi-plastic constitutive behavior. In this regime, the application of a pressure leads to a more intense shrinkage of the large pores with respect to the small ones, and thus to a sudden increase in the ratio between small and large pores sizes. In all cases the applied pressure was 100 MPa. This

leads to longer specific times of sintering with respect to Figures 3.21-3.24, while for Figures 3.25 and 3.26 just the first instants of an SPS process assisted by higher loads are shown.

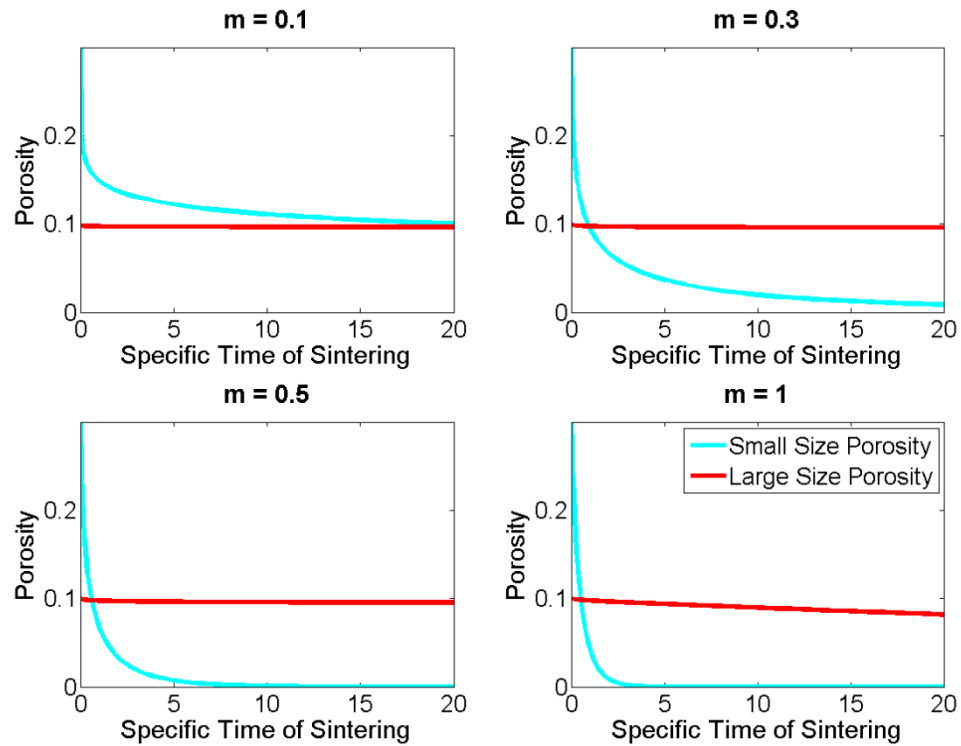


Figure 3.21 – Small and large size porosities evolution for initial small pores radius = 100 nm and initial large pores radius = 10 μm .

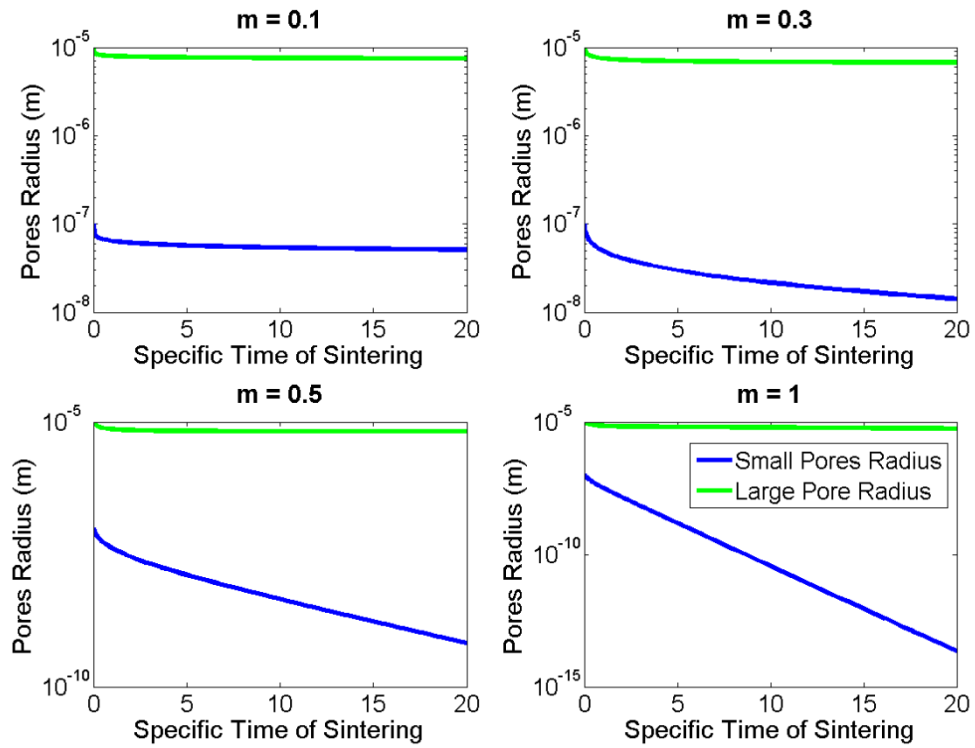


Figure 3.22 – Small and large size pores radii evolution for initial small pores radius = 100 nm and initial large pores radius = 10 μm .

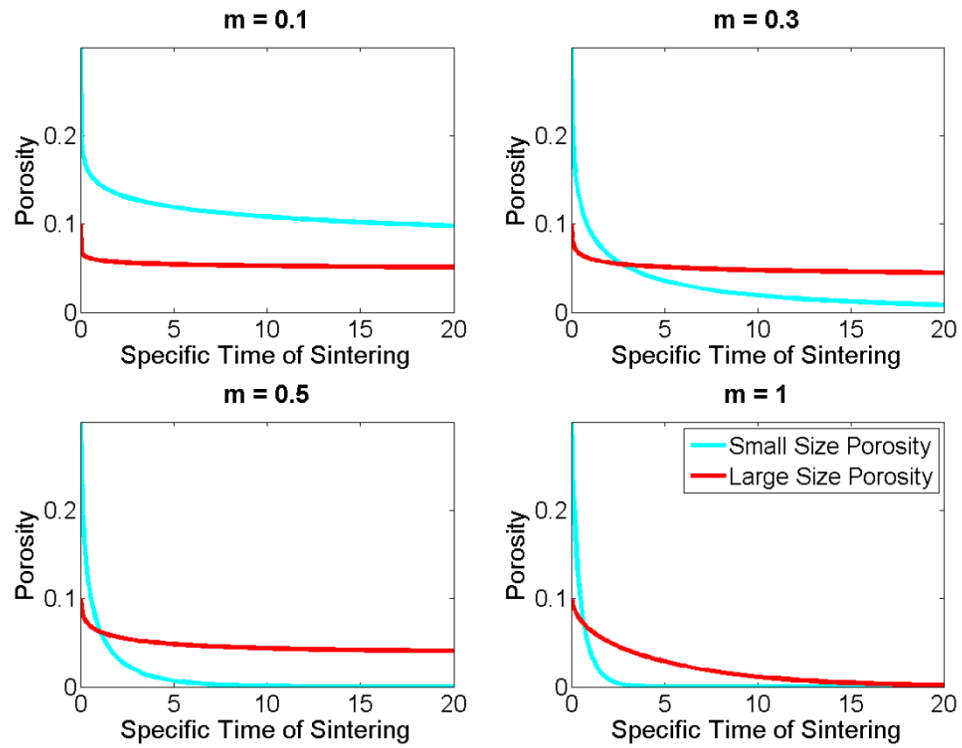


Figure 3.23 – Small and large size porosities evolution for initial small pores radius = $1 \mu\text{m}$ and initial large pores radius = $5 \mu\text{m}$.

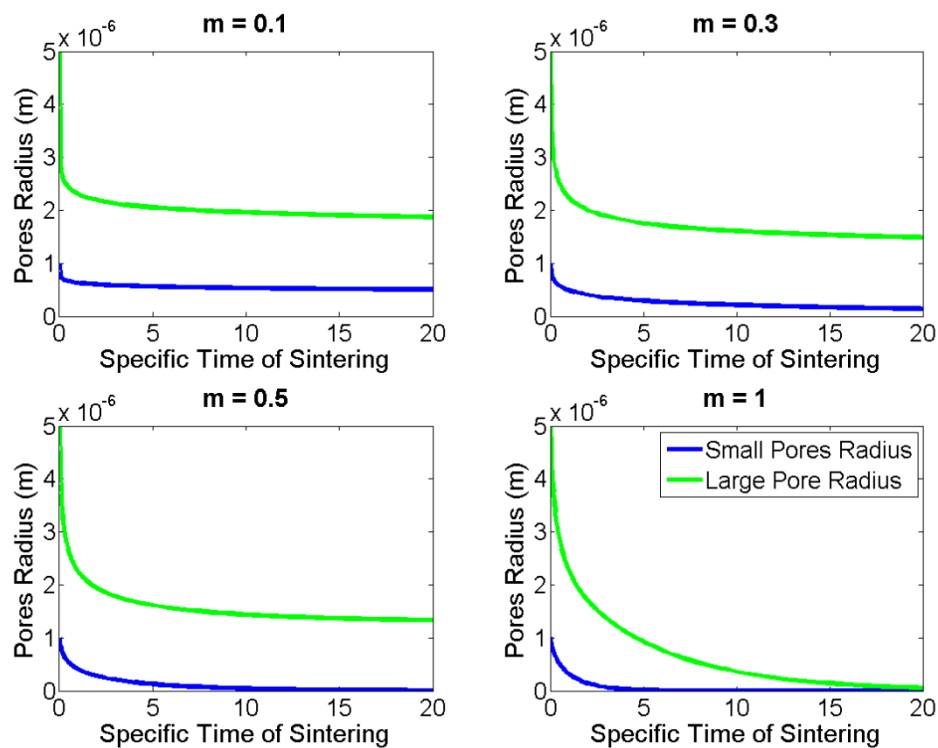


Figure 3.24 – Small and large size porosities evolution for initial small pores radius = $1 \mu\text{m}$ and initial large pores radius = $5 \mu\text{m}$.

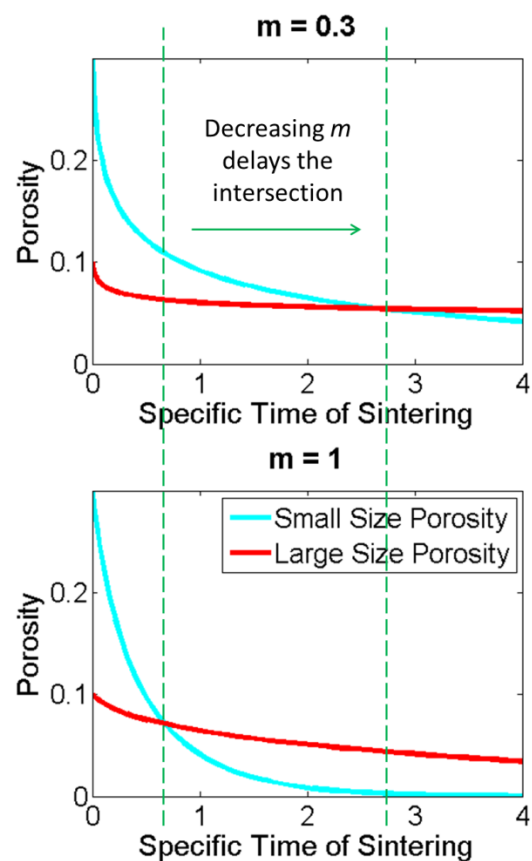


Figure 3.25 – Impact of strain-rate sensitivity on the intersection between large and small-size porosity densification curves.

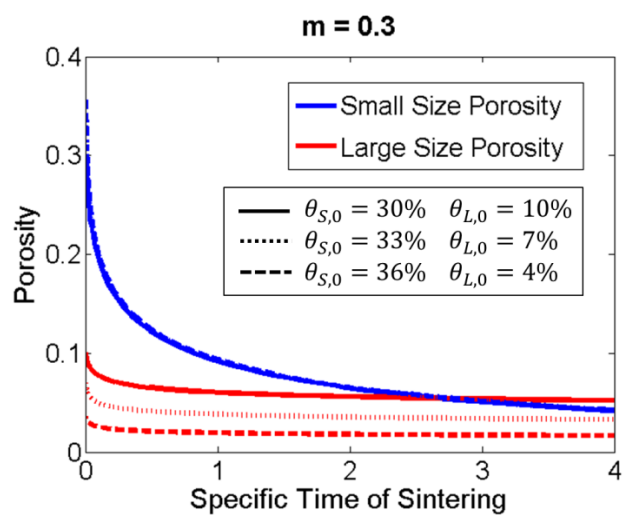


Figure 3.26 – Densification curves for various initial porosities values.

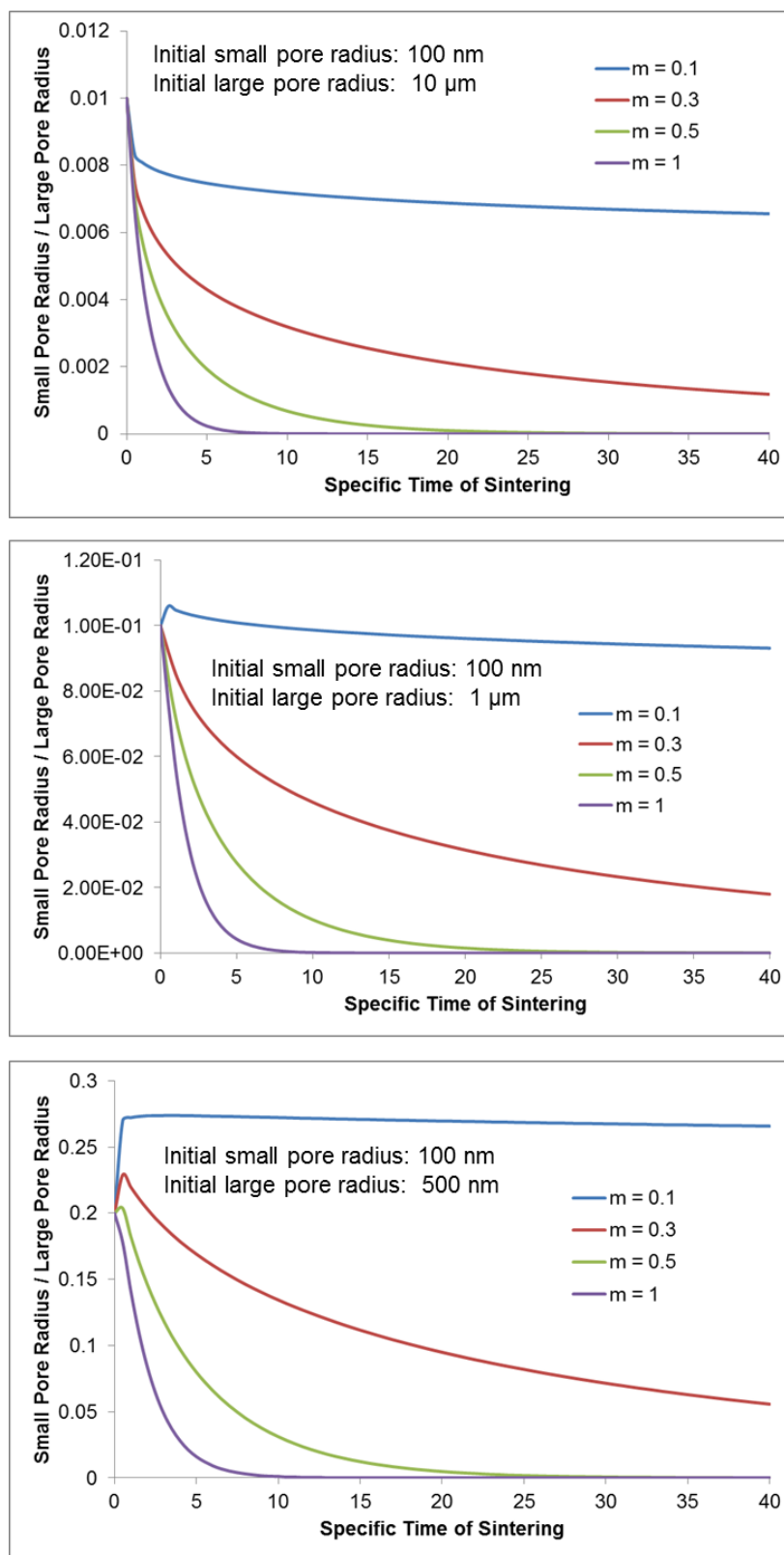


Figure 3.27 – Pores radii ratio evolution for different m values.

At this stage it is also appropriate to compare the proposed kinetics model with experiments. From the solution of the kinetics equations, it is immediate to derive the evolution of the overall porosity. This type of data is used for a comparison with the experimental work by J.-S. Lee and coauthors that inspired this investigation.⁹⁴ They proposed to exploit controlled agglomeration phenomena for the net-shaping of iron nanopowders. They showed how an optimized control on the size of agglomerates leads to a beneficial pore size redistribution which prevents the undesired densification gradients typical of biporous materials. While in the presence of large agglomerates, after a fast initial shrinkage, relative density reached an asymptotic value between 90 and 94% (corresponding to the large inter-agglomerate pores left in the specimen and at this stage very hard to remove), in the case of smaller agglomerates densification was less rapid but kept progressing steadily.

Figure 3.28 shows some of their results, compared with the predictions of our model. Note that the experiments were conducted with conventional free pressure-less sintering, and thus the processing times are longer than the ones typical of SPS. Processing by conventional sintering or spark plasma sintering changes significantly the value of the creep pre-exponential factor A_m , and therefore the proposed model becomes extremely versatile. The fast initial shrinkage even for conventional pressure-less sintering is due to the small size of the powder, which leads to very high values of sintering stress. The values of small and large pores radii were taken from the data of J.-S. Lee *et al.*, who reported 10 nm small pores and large pores of 500 nm for large agglomerates and 30 nm for controlled small agglomerates. The amounts of initial small and large size porosities were estimated accordingly. The model curves were obtained for $m = 0.2$, a reasonable value for iron, and available at the considered processing temperature (648°C).

The agreement between model and experiments is fairly good. The main point of interest - the faster initial shrinkage of the large agglomerates case, followed by a stagnation,

in contrast with the more steady and continuous increase in relative density of the small agglomerates case - is captured by the model, even if it predicts higher density values than what obtained experimentally. The mismatch between experimental and modeling curves can be explained by the uncertainty in a variety of input data, such as the exact proportions of initial small and large size porosities, and the creep properties of this specific powder, which included a percentage of nickel. Indeed, J.-S. Lee and coauthors reported an estimation of apparent activation energy for the mass transfer mechanisms leading to densification, proposing that its value changes from 80 kJ/mol to 280 kJ/mol with increasing density, while in our calculations we kept the constant literature value of 280 kJ/mol. This can explain why the model curves proceed at a slower rate than the experimental ones in the initial stages. More accurate input data for the model can be the object of future work.

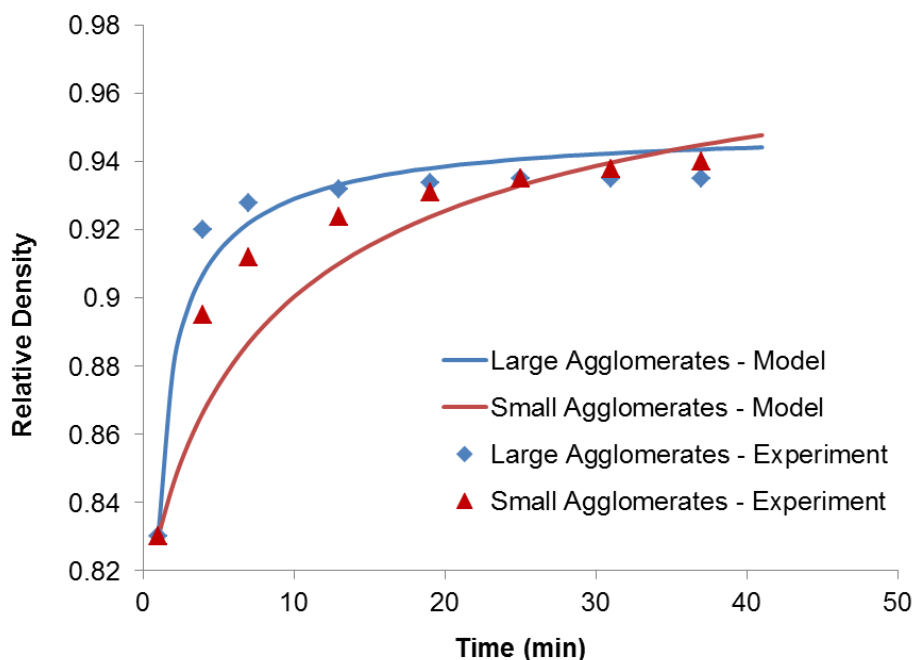


Figure 3.28 – Comparison between the proposed kinetics model and experiments.

Following the considerations above, we can summarize the shrinkage kinetics-based optimization strategy with the scheme given in Figure 3.29. Tools have been developed to produce plots of the evolution of pores amounts and sizes during SPS for varying values of strain-rate sensitivity, and also plots of the dependence of strain-rate sensitivity on temperature. Post-processing of these data leads to the formulation of strategies to obtain the desired porous material structures during the spark plasma sintering process itself.

Given certain easily retrievable material data, graphs of the type shown in Figures 3.21-3.24 can be created. The initial global porosity can be readily obtained with traditional experimental methods, and a good estimation of the large pores volume fraction can be based on the size of the agglomerates in the loose powder. The small-size porosity can subsequently be calculated from the relation between the three. The powder and agglomerates sizes can be estimated at the electronic microscope, and the former is typically provided by the manufacturer too. The required creep data are present in the literature for most materials, and the applied pressure is selected by the SPS operator. The kinetics curves can be plotted with respect to the physical time or with respect the specific SPS time. In the former case, as explained above, the influence of applied pressure and material properties are of more immediate visualization, while the latter possibility is useful to isolate the effects of different powder sizes and draw more general conclusions.

From the kinetics curves the most suitable value of strain-rate sensitivity can be selected. In order to verify if such value is available for the material of interest, and, if so, what temperature it corresponds to, the $m(T)$ plots come into play. The same creep data used as initial input are needed, together with some information on creep strain rates retrievable from experimental creep curves generally present in the literature. If such information is not available, creep tests are needed.

The optimized SPS holding temperature can thus be selected by means of this simple, two-step procedure.

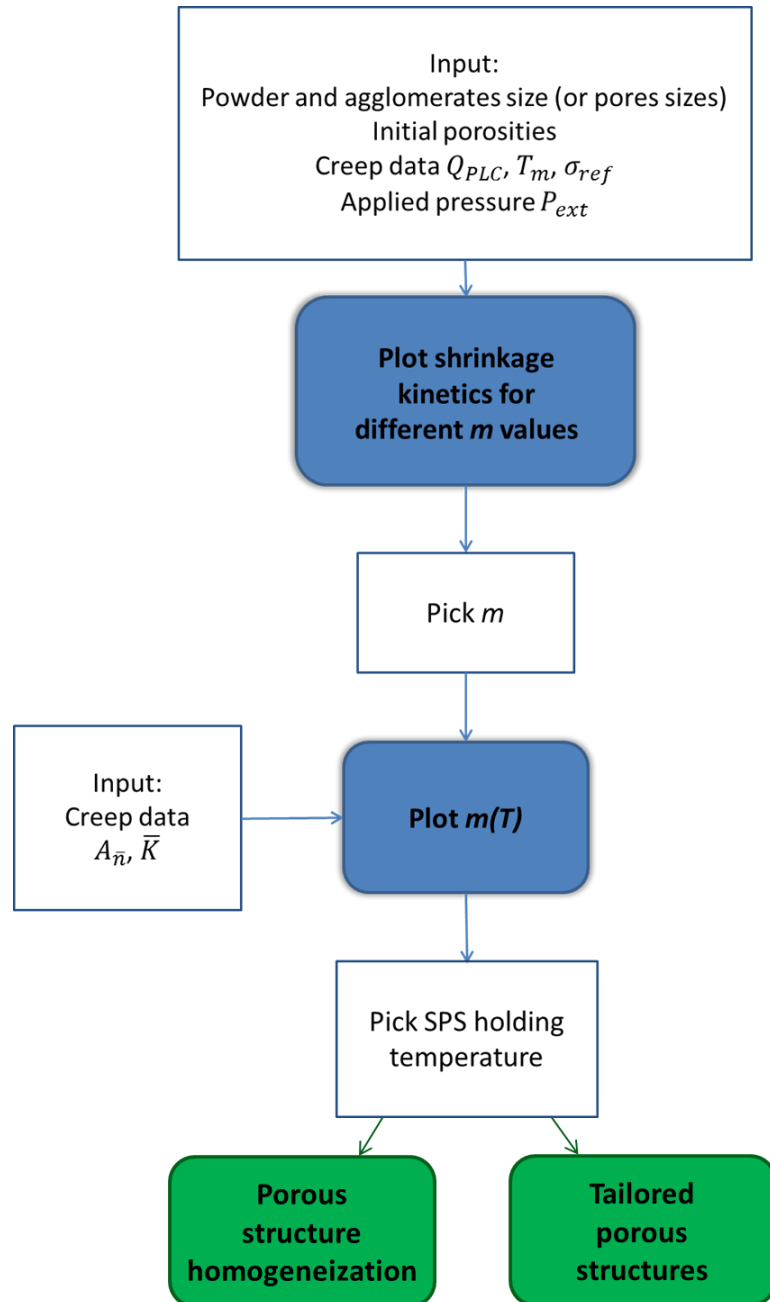


Figure 3.29 – Optimization strategy based on shrinkage kinetics.

The derived expressions are not only useful for practical applications, but also constitute a valuable extension of the continuum theory of sintering, which has been lacking a comprehensive inclusion of nonlinear viscous rheology and agglomeration phenomena. A broader continuum theory of powder materials consolidation has therefore been built, from which the well-known equations for monoporous linear viscous materials can be immediately derived as special cases.

The developed model also sheds some light on the intrinsic limitations of agglomerated powders when it comes to attempting *in situ* de-agglomeration during SPS. It has emerged that large inter-agglomerate pores cannot be completely eliminated, even with the most suitable thermal regime, if the size gap between small and large pores is too wide (2 orders of magnitude or more). Even for smaller size gaps, the densification of nano-sized pores is too fast for the inter-agglomerates ones to catch up before undesired grain growth phenomena start taking place. The issue is likely to be the significant difference in surface sintering stress acting on areas with such different curvature values. *In situ* de-agglomeration strategies thus need to be accompanied by pre-sintering treatments, such as ball milling or the addition of suitable dopants, in order to reduce the initial large pores size, enhance the surface tension effects and hamper grain growth inside fully dense agglomerates.

In order to get the desired homogeneization, we can attempt to increase the applied pressure or to reduce the size-gap between large and small pores. The following plots address such attempts. They are produced with respect to the physical time instead of the specific sintering time, to have a more immediate visualization of the applied load's effects. We also consider a larger powder size (10 μm order of magnitude), to enhance the effect of pressure with respect to the sintering stresses. With such a larger powder size it is also reasonable to assume that agglomeration phenomena are less severe and thus justify considering a narrower gap size between small and large voids.

The linear viscous case ($m = 1$) is the one that shows the highest level of deformability of the porous material. If we keep the large pores size as five times the small pores one (small pores size is $10\ \mu\text{m}$ and the large pores one is $50\ \mu\text{m}$), and we increase the pressure all the way up to $500\ \text{MPa}$, we can obtain shrinkage of both large and small pores in a very short SPS time (less than a minute of holding time, see Figure 3.30). The large pores, as expected, still require a longer time to reach full shrinkage, but in this case this additional time is so short that we can safely assume that grain growth phenomena would be very limited.

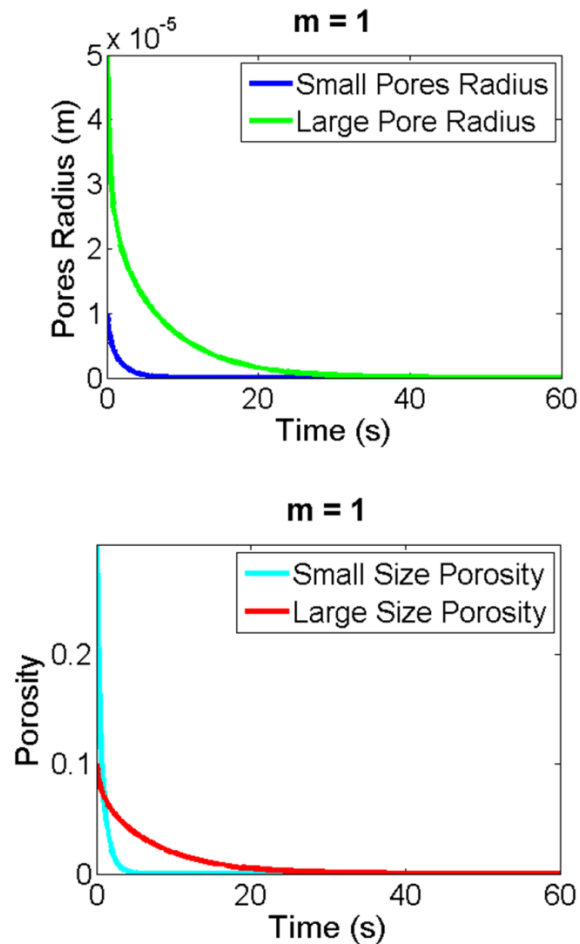


Figure 3.30 – Shrinkage kinetics for the linear viscous case with $500\ \text{MPa}$ applied pressure.

If we consider the same pores sizes and increase the applied pressure to 1 GPa, in the $m = 0.5$ case, we find that large pores can still shrink in a reasonable time for SPS processing, but with a much larger delay with respect to the linear viscous case (Figure 3.31). The small pores, on the other hand, are still densifying very quickly. This leads to a more detrimental situation with respect to the $m = 1$ case scenario, due to the time available for the microstructure to be affected by significant intra-agglomerate grain growth.

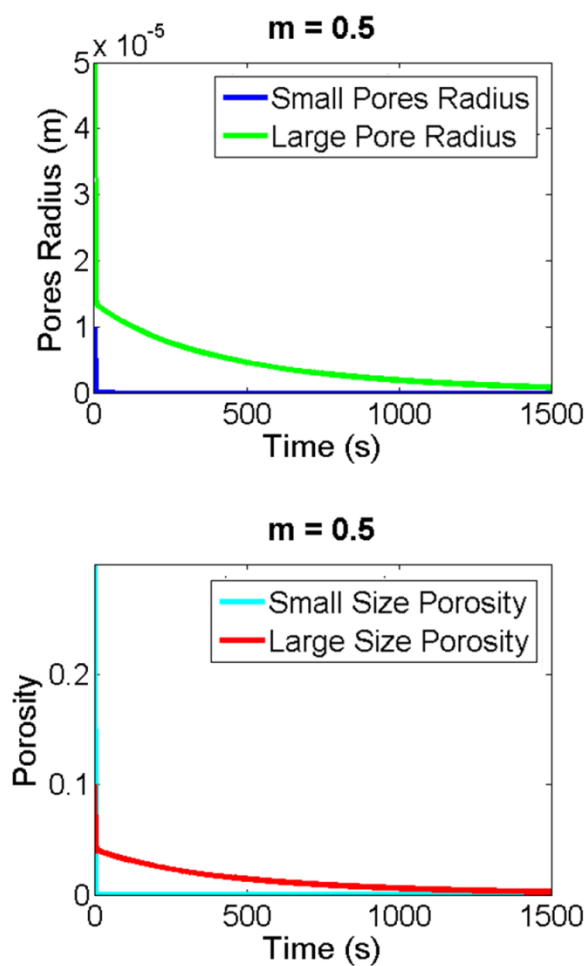


Figure 3.31 – Shrinkage kinetics for the $m = 0.5$ case with 500 MPa applied pressure.

We now shift our attention to the almost perfectly-plastic case ($m = 0.1$), which is where we expect to have the highest initial quasi-instantaneous shrinkage, and thus the highest probability of equating the size of small and large pores in very brief timespans. Recall that this corresponds to significantly lower processing temperatures, rendering such a case almost a cold (or warm) pressing process.

For the same loading conditions of 1 GPa, it turns out that a narrow size gap between the large and small pores radii ($\approx 1 \mu\text{m}$) cannot be eliminated, unless we employ extremely long SPS times. Densification happens during the first instants of the process, and then proceeds at a very slow pace, as presented in Figure 3.32.

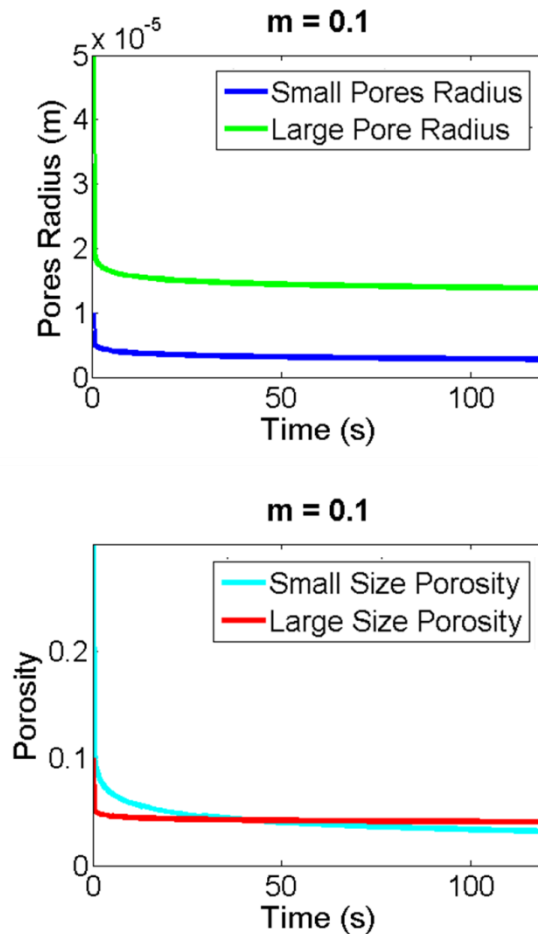


Figure 3.32 – Shrinkage kinetics for the $m = 0.1$ case with 1 GPa applied pressure.

Since the shrinkage curves, after this initial compaction, evolve with a slope that is close to zero, we can consider the residual porosity to be practically non-removable (even if it has values lower than 5% for both small and large size voids).

The size gap between the two radii curves result to be unavoidable even if we apply pressures up to 3 GPa. We are, nevertheless, able to attain an overlapping of the two curves if we reduce the initial size gaps to large pores being 2.5 times the size of the small ones, even with the same 1 GPa applied load, as Figure 3.33 shows. Note that, even though the two radii curves coincide after the initial sudden shrinkage, the pores size (and thus the porosities) does not reach zero. In order to achieve full shrinkage, even higher loads need to be applied.

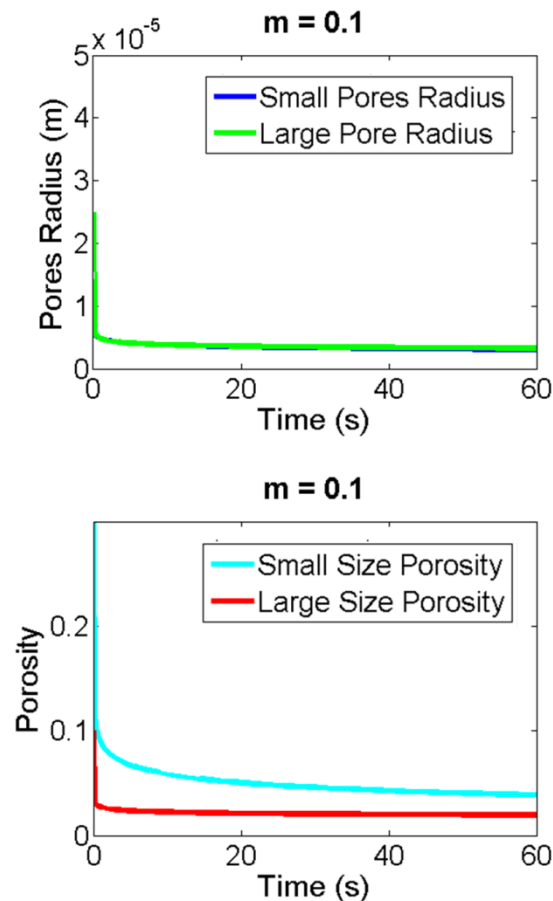


Figure 3.33 – Shrinkage kinetics for the $m = 0.1$ case with 1 GPa applied pressure and a narrow pores size gap.

We have therefore shown that homogenization of agglomerated powder materials can be obtained if high pressures are applied to porous materials with a relatively narrow size-range. For nanopowders, which are particularly prone to form large agglomerates, this will correspond, in most cases, to pre-SPS de-agglomeration treatments. Such conclusions confirm what obtained experimentally by Anselmi-Tamburini, Garay and Munir in the context of nanopowders consolidation.⁹²

An important point to take into account is that the proposed model does not take grain growth into account. Some of the derived conclusions could, thus, change quite significantly when grain growth mechanisms are included in the treatment, since there are well-known interactions between them and pore migration and shrinkage. The present approximation is, nevertheless, perfectly acceptable for levels of relative density up to 92%. For lower amounts of density, pores are still interconnected in an open porosity network, and thus have a pinning effect that hampers grain growth.

The possibility of utilizing non-constant holding temperatures and the role of heating rates should also be explored before turning to such treatments.

Nevertheless, together with providing a thorough theoretical analysis of nanopowders (and micropowders) processing by spark plasma sintering, the proposed model can also find interesting applications when it comes to tailoring hierarchical material structures. There is currently a growing interest in the production of biporous materials with specific characteristics, for example for new generation batteries and fuel cells components. Polymeric pore formers are often used to create hierarchical structures with controlled features. The large and small pores kinetics equations can therefore play an important role in the selection of optimal processing routines (in terms of temperature, pressure and loading schematics) to obtain the desired meso-scale structures. In this context, the macroscopic properties (see same Table 3.5) also become a particularly valuable tool.

This brings us to the second possible optimization strategy, which relies on the derived macroscopic properties expressions: P_L , Ψ and Φ . The baseline of this strategy consists in the replacement of the biporous study domain (hollow sphere made of porous material) with a homogeneous equivalent. The mechanical properties of such a homogeneous equivalent already take into account the fact that both large and small pores are present, together with the nonlinear viscous rheology of the material.

Figures 3.34, 3.35 and 3.36 show their dependencies on the two types of porosities typical of hierarchical porous structures, for a specific value of strain-rate sensitivity (0.5). Again, the expected trends as pores volume fractions increase or decrease are found.

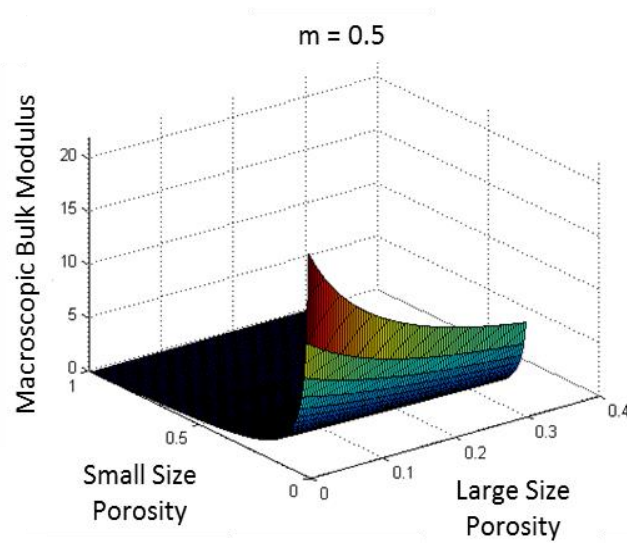


Figure 3.34 – Macroscopic bulk modulus in function of small and large size porosities.

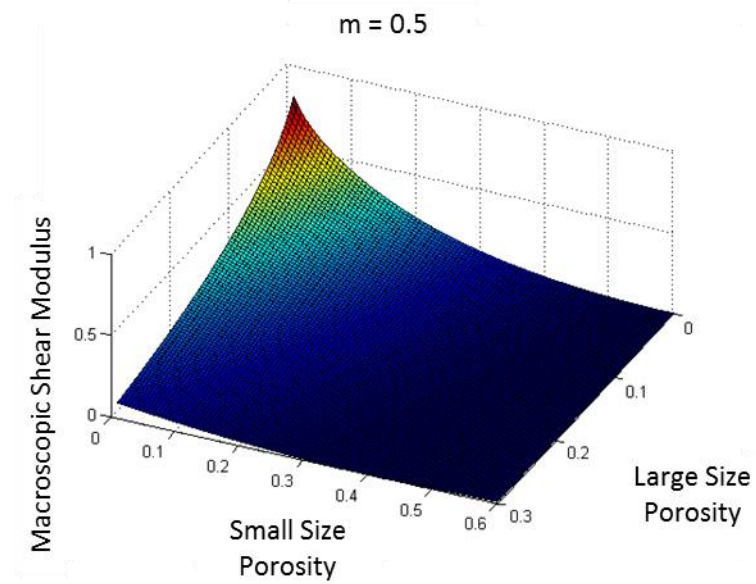


Figure 3.35 – Macroscopic shear modulus in function of small and large size porosities.

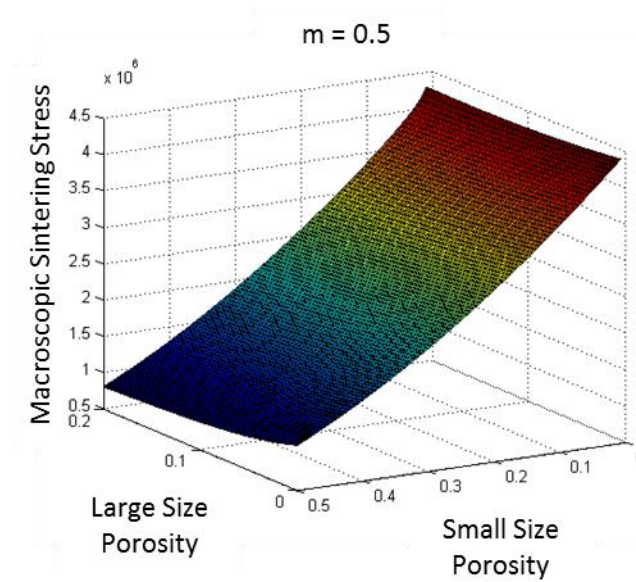


Figure 3.36 – Macroscopic sintering stress in function of small and large size porosities.

To the best of our knowledge, these expressions are the first ones that take into account both biporous material structure and nonlinear viscous rheology. We have already compared the monoporous nonlinear viscous formulations with the main models from the literature (Figures 3.10, 3.12, 3.13, 3.16). Formulations for biporous materials, even for the linear viscous case, are instead scarcely available. There is the exception of the work of Shtern and Kuzmov,¹⁰⁴ who adopted an approach similar to the one presented in Section 3.1 (mechanics-based) to derive shrinkage kinetics and material properties of agglomerated powders presenting a linear viscous constitutive behavior. The following Figure 3.37 presents the comparison between their model and our expression, evaluated for three different values of strain-rate sensitivity. Their outcome and ours for the case $m = 1$ do not overlap, but the latter is still the closest to their expression among the various values of strain-rate sensitivity. The lower the value of m considered, the further we move from the Kuzmov-Shtern result. The present model predicts higher values of normalized bulk modulus and lower values of normalized shear modulus.

Recall that, for the large size porosity influence, we considered the diluted case. Kuzmov and Shtern did the same. Therefore, for all the cases shown in the figures, both bulk and shear moduli are overestimations when we consider large size porosities greater than 10-15%.

This second strategy, enabled by such macroscopic expressions, enriches our analysis with the possibility of evaluating an entire specimen, for which we assume isotropic distributions of small and large pores. The porous hollow sphere that we have been using as study-domain for our derivations can now be replaced with an equivalent homogeneous medium, with properties dependent on both small and large pores.

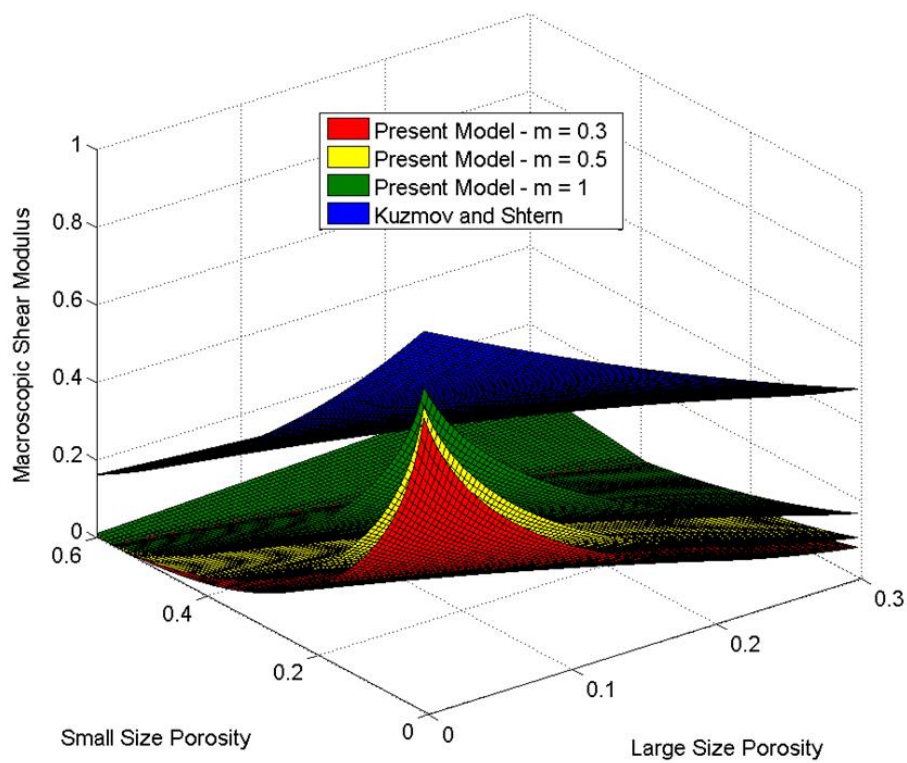
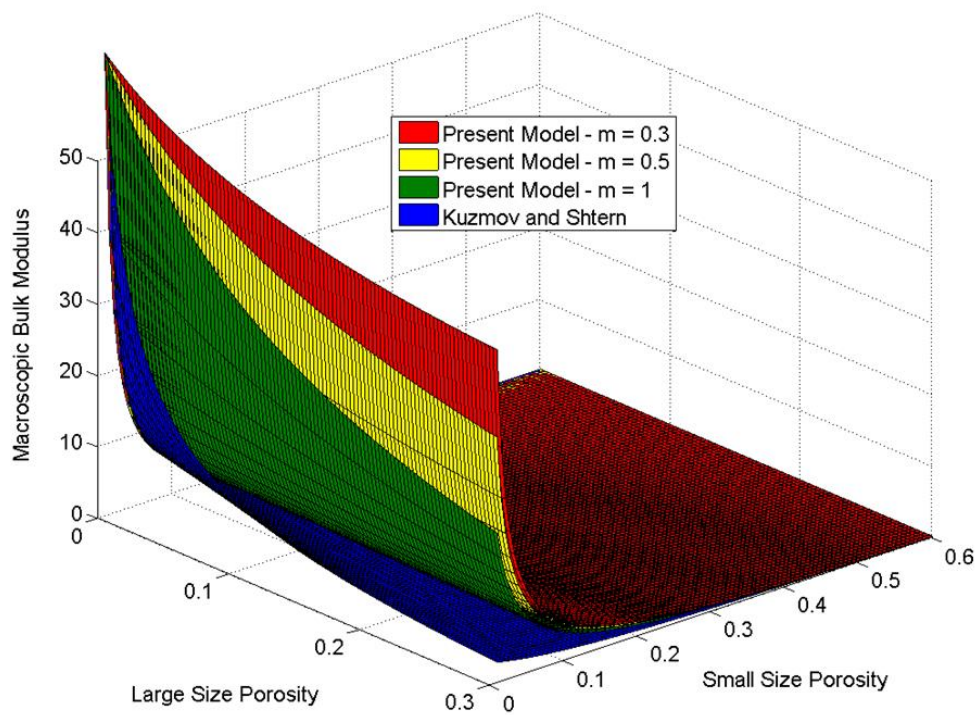


Figure 3.37 – Comparison between the present and Kuzmov-Shtern models for biporous materials.

The macroscopic formulations can be used for both analytical considerations and FEM simulations. In the former case, boundary-value problem for biporous materials can now be easily solved by considering the studied material to be homogeneous and isotropic. In the latter case, the derived macroscopic properties enable the implementation of a multiscale framework. Simulations that reconstruct simultaneously the evolution of the entire specimen and of the single pores can be implemented. The details are given in the following paragraph, with a case study applied to solid oxide fuel cells components.

3.2.3 Multiscale FEM simulations of pore shape evolution during sinter-forging of hierarchical composites

We have anticipated in the previous paragraph that the results of the presented analytical derivations can not only be used for de-agglomeration and uniformization of powder materials during spark plasma sintering, but also for the tailored optimization of hierarchically porous media.

Biporous or multiporous ceramics have raised growing attention in the last years, because of their numerous applications in advanced materials for energy and biomedical applications, such as solid oxide fuel cells, all-solid-state batteries, gas absorbers, thermal insulation, artificial tissues and bio-implants, to name a few.

Sintering is still one of the main techniques employed for the production of tailored porous ceramics, even though at the current state of the art it is not possible to monitor the evolution of the meso-scale structure that characterizes and controls the performance hierarchical materials. Specifically, for the synthesis of cathodes for solid oxide fuel cells (SOFC), polymeric pore-formers are often introduced in the green specimen. These pore-formers are subsequently burnt out during the firing process, leaving large voids of the desired

size. Such a technique has been applied by Bordia *et al.* to the production of SOFC cathodes starting from LSM-YSZ powders (mixing of 40 vol% $\text{La}_{0.8}\text{Sr}_{0.2}\text{MnO}_3$ and 60 vol% Y_2O_3 -stabilized ZrO_2).^{90, 91} In each sample they have both small-size pores between the powder particles (which they call “intrinsic” porosity) and large pores left by the pore-formers above 400 °C (addressed as “extrinsic”). Note that the employed powder size is of the order of micrometers, and thus agglomeration phenomena play a minor role in this case, also thanks to suitable pre-sintering treatments and the polymeric spheres’ presence.

During free pressure-less sintering, the biporous specimens behave as expected, with both large and small pores progressively assuming a spherical shape and starting to shrink. When, on the other hand, sinter-forging is performed, a peculiar phenomenon can be observed. Sinter-forging consists in sintering with an applied uniaxial load, while leaving the lateral surface of the specimen free to move radially. What Bordia and coauthors observed after their experiments was that the pores assumed different preferred orientations depending on their size: the large extrinsic pores tended to be flattened perpendicularly to the applied load, while the small intrinsic ones aligned along the uniaxial load direction. This can be explained with the concurring phenomena responsible for densification. Diffusion-driven mass transfer, particularly relevant at the grain boundaries, will be the prevalent one for small pores. Such a type of transfer is enhanced in the planes perpendicular to the applied load, and thus the small pores will be filled by material in the radial direction more than in the axial one, leading to a shape preferentially elongated in the axial direction.²⁴⁹ Large pores, instead, are much bigger than the powder particles themselves, and thus can be easily filled up by visco-plastic shifting of entire particles inside the voids themselves, which leads to final shapes that are horizontally oriented.

By means of experimental procedures, it is only possible to access information on the initial and final shape and volume fraction of the two porosities, while it would be useful to be

able to follow the entirety of the process at the pores scale in order to develop strategies for the production of tailored hierarchical ceramics. Multi-scale finite-element modeling then becomes a useful tool to monitor the evolution of these kinds of porous structures during sintering. The important role of modeling for a better understanding of the mechanisms lying behind densification anisotropy during sintering has indeed been underlined in a variety of cases, for both metals and ceramics.^{249–251}

We employed the commercial software COMSOL Multiphysics™ to implement FEM simulations of the densification of biporous materials. This FEM framework enables us to simultaneously follow the evolution of the processed material at the local pores' level and at the entire specimen's scale. Specifically, we were interested in reconstructing the shape and size evolution of large pores, while monitoring the consolidation of the specimens. We simulated both sintering and sinter-forging experiments, analogous to the ones reported in the corresponding experimental works.^{89–91}

Our numerical framework involved two scales: macroscale, relative to the whole specimen, and mesoscale, referring to a unit cell representative of the biporous material. The latter was selected in accordance with the previous analytical derivations, with the only difference of selecting a cylinder with a spherical void instead of a hollow sphere. This choice was based on the work of the same Bordia and coauthors, who in parallel conducted modeling of their hierarchical ceramics with non-numerical approaches.

Figure 3.38 shows a schematic representation of the multi-scale study domains. The specimen had initial dimensions analogous to the experimental case (12 mm height and 12.75 mm diameter). The cylindrical unit cell presented a central spherical cavity, representative of a large extrinsic pore. The diameter of this void was 7.5 μm , corresponding to the dimensions of the polymeric (PMMA) pore formers employed during experiments. The diameter and height of the unit cell were equivalent, with dimensions imposed by the value of large pores volume

fraction. For the present study, the extrinsic porosity was selected to be 30% of the entire specimen's volume, because of the wide availability of experimental data,^{90, 91} and because such a value resulted to be the highest amount of large pores allowing to neglect the interactions among them (and thus the determination of macroscopic mechanical properties from the unit cell's behavior).⁹⁰ In reference to the same Figure 3.38, the value of the cell edge (2L) resulted thus to be 9.79 μm .

The large porosity evolution was therefore studied from a kinetics viewpoint (displacements and velocities of the large void boundary). The small intrinsic pores were, instead, addressed again by means of the continuum theory of sintering.¹¹³ This implies that small pores were assumed to be homogeneously and isotropically distributed in the medium surrounding the large pore in the unit cell. The continuum theory of sintering was also utilized at the macroscopic scale, with the specimen presenting a uniform isotropic distribution of pores, both extrinsic and intrinsic. The mechanical properties of the specimen are individuated at the mesoscale and thus take into consideration the effects of the co-presence of small and large pores. The total porosity is expressed based on the small and large size porosities as in (3.7), here reported:

$$\theta = \theta_L + (1 - \theta_L)\theta_S \quad (3.7)$$

The initial total porosity was chosen, in accordance to experimental values, to be 50%. Initial small-size porosity was therefore equal to 28.57%.

The bottom part of Figure 3.38 shows the two domains as implemented in COMSOL. Thanks to the problem symmetries, it was sufficient to implement 1/4 of each domain (2-D axisymmetric), at both the macroscale and the mesoscale. We selected a "free triangular" mesh, with "normal" size for the specimen and "fine" size for the unit cell, in accordance with the software denominations.

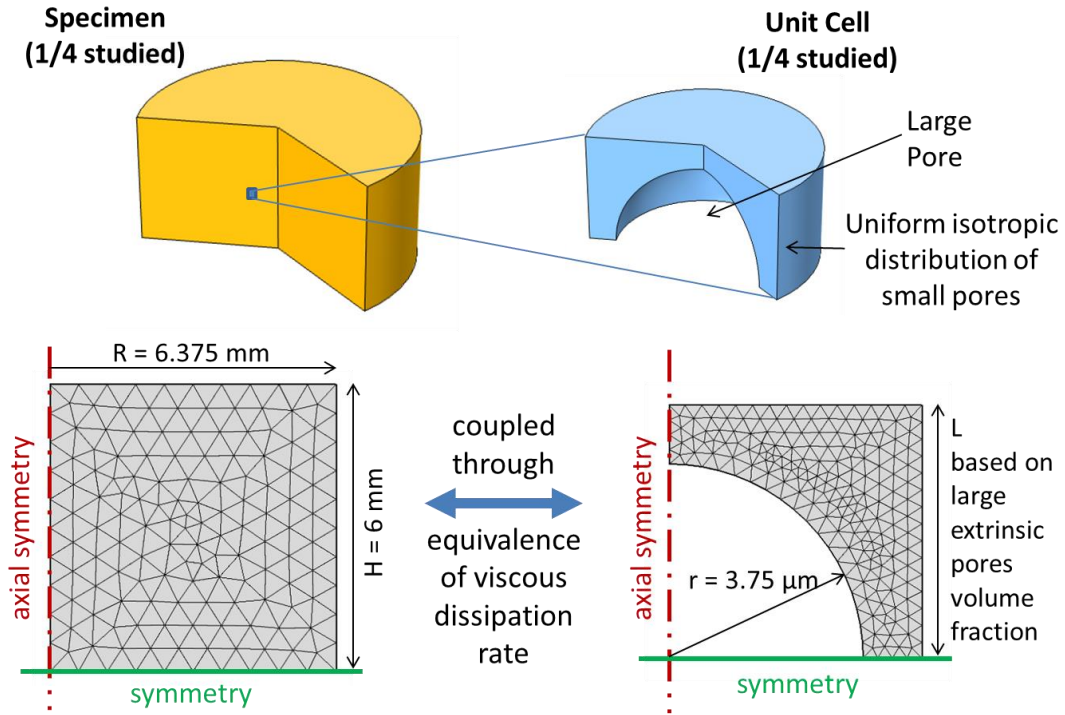


Figure 3.38 – Multiscale FEM domains definition.

The coupling of the two scales was done by imposing equivalence of the viscous dissipation rate.²¹⁴ More details are given in Figure 3.39. At both scales we solved a mechanics problem for materials presenting linear viscous constitutive behavior. The constitutive equation for linear viscous materials is written as

$$\sigma_{ij} = 2\eta_0(\varphi\dot{\varepsilon}'_{ij} + \psi\dot{\varepsilon}\delta_{ij}) + P_L\delta_{ij} \quad (3.107)$$

in which, as described in Section 3.1, σ_{ij} denotes the stresses, $\dot{\varepsilon}_{ij}$ the strain rates, $\dot{\varepsilon}$ the strain rate tensor trace, $\dot{\varepsilon}'_{ij}$ the deviatoric strain rates, ψ the normalized bulk modulus (function of porosity), φ the normalized shear modulus (function of porosity), P_L the sintering stress and η_0 the viscosity of the solid phase. This type of constitutive equation is adopted at both the

mesoscale and the macroscale, for the effects of small size porosity and global porosity, respectively.

A linear viscous rheology of the powder material is a reasonable assumption in the present case because of the low pressures applied (0-5 MPa) and the utilization of micrometer-sized powders. The viscosity of the solid phase, η_0 , was selected to be equal to $E/3$, where E is the elastic modulus. This assumption follows the linear viscous analogy with solutions of elasticity problems.^{95, 252} In our study, the powder material was composed by 40 vol% of LSM and 60 vol% of YSZ. The overall Young's modulus was therefore calculated as

$$E = 0.4 E_{LSM} + 0.6 E_{YSZ} \quad (3.108)$$

with E_{LSM} and E_{YSZ} depending on both temperature and porosity. The porosity dependence was expressed as^{113, 140}

$$E = E_0(1 - 1.9\theta) \quad (3.109)$$

while the temperature influence was based on data taken from the literature, since the mechanical properties of materials traditionally used for the production of fuel cells have been thoroughly studied.²⁵³

The boundary conditions imposed on the macroscopic specimen reflect the sinter-forging procedure: a uniaxial load applied on the top surface, the consequent friction between powder-specimen and punches, and free lateral surface. As for the unit cell, we imposed the axial velocity of the top boundary and the radial velocity of the lateral surfaces. These values were calculated by averaging the respective values in the volume of the specimen at each time-step of the computation. On the boundary of the large pore, the action of the surface tension tending to close the pore was imposed by applying a boundary load proportional to the material's surface tension and to the local curvature of the void (with a proportionality factor equal to 3, characteristic of spherical pores).

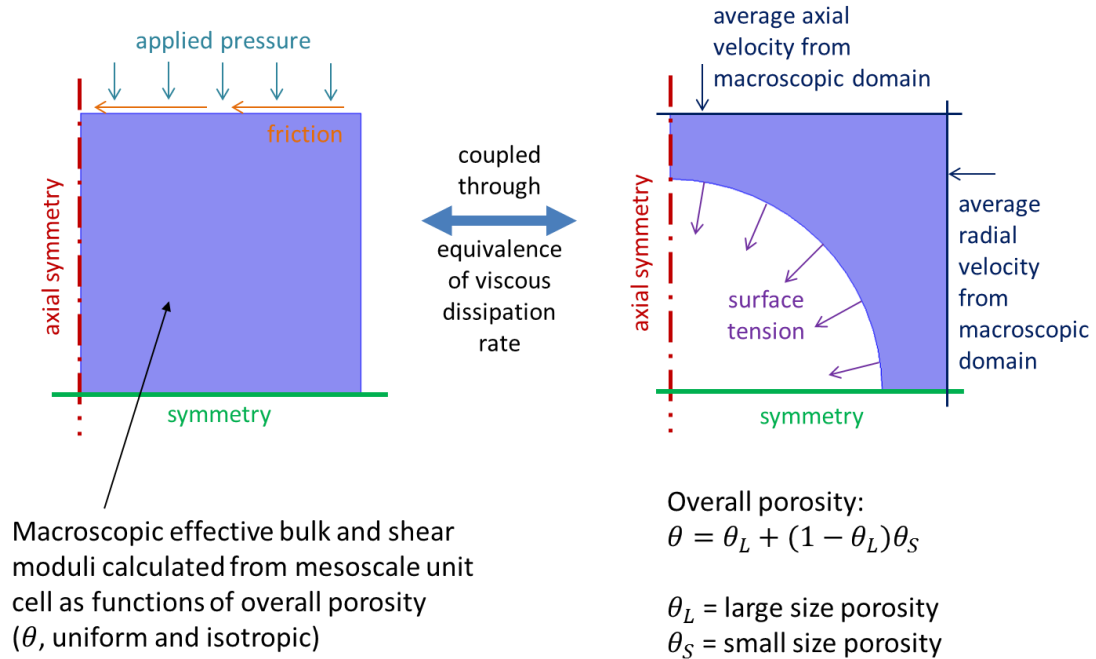


Figure 3.39 – FEM boundary value problem definition.

Among the several routines that had previously been implemented experimentally, we chose to simulate a sintering regime consisting of a 10 K/min heating ramp, followed by a 90 min holding at 1523 K. Specifically, to shorten the computation time, we started the simulations from a temperature of 1373 K, as no densification was observed before this value during experiments.⁹⁰ We studied the 0, 3 and 5 MPa-applied pressure cases. In accordance with the experimental routes, these external loads were applied when 1473 K was reached.⁹¹

Figure 3.40 shows the kinds of results that we aimed at obtaining with our FEM framework. The mesoscale relative to the unit cell allowed us to monitor the evolution of the large pores size and shape throughout the entire sintering process. The small size porosity was instead studied in terms of volume fraction, such that we could obtain its spatial distribution at

every time-step. The densification of the macroscale specimen could be followed simultaneously.

Figure 3.41 shows the porosity distributions and deformations of specimen and unit cell at the end of the isothermal holding stage. A uniform distribution of both total porosity at the macroscale and small size porosity at the mesoscale is obtained for the free sintering case, together with the large pores retaining their initial spherical shape while decreasing in size, as expected. Inhomogeneities appear when an external pressure is applied, accompanied by a barreling of the specimen due to the friction contribution, and a progressive flattening of the large pores. The deformations shown are based on the displacements calculated by the software and are presented with a scale factor equal to 1.

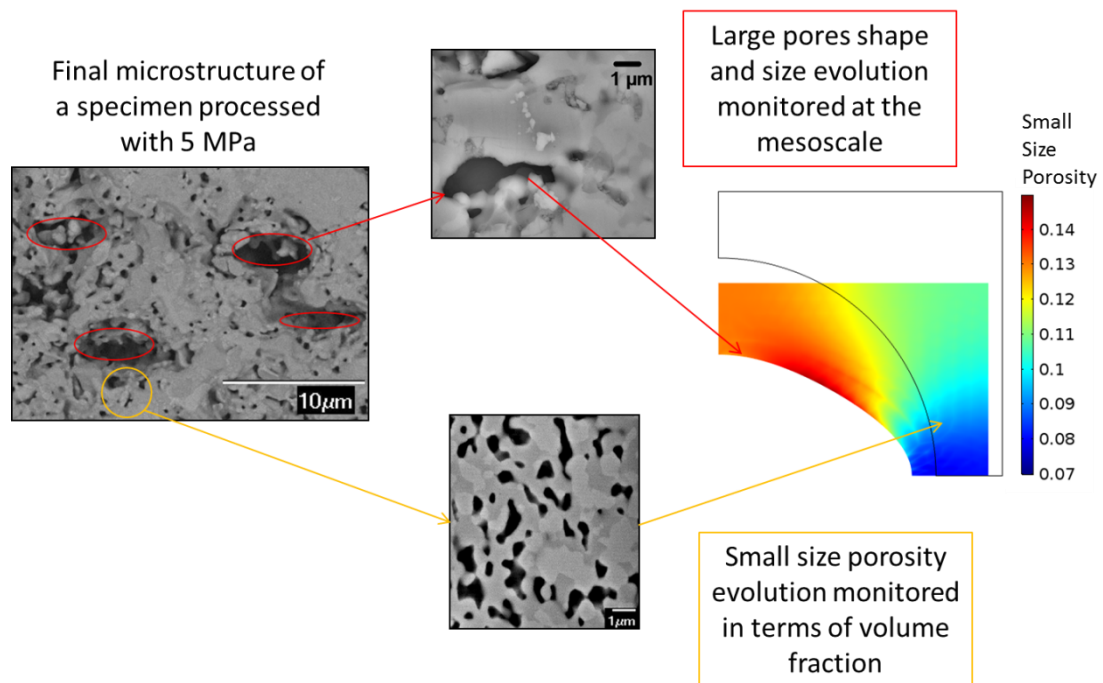


Figure 3.40 – Correlations between FEM-implemented unit cell and experimental results.

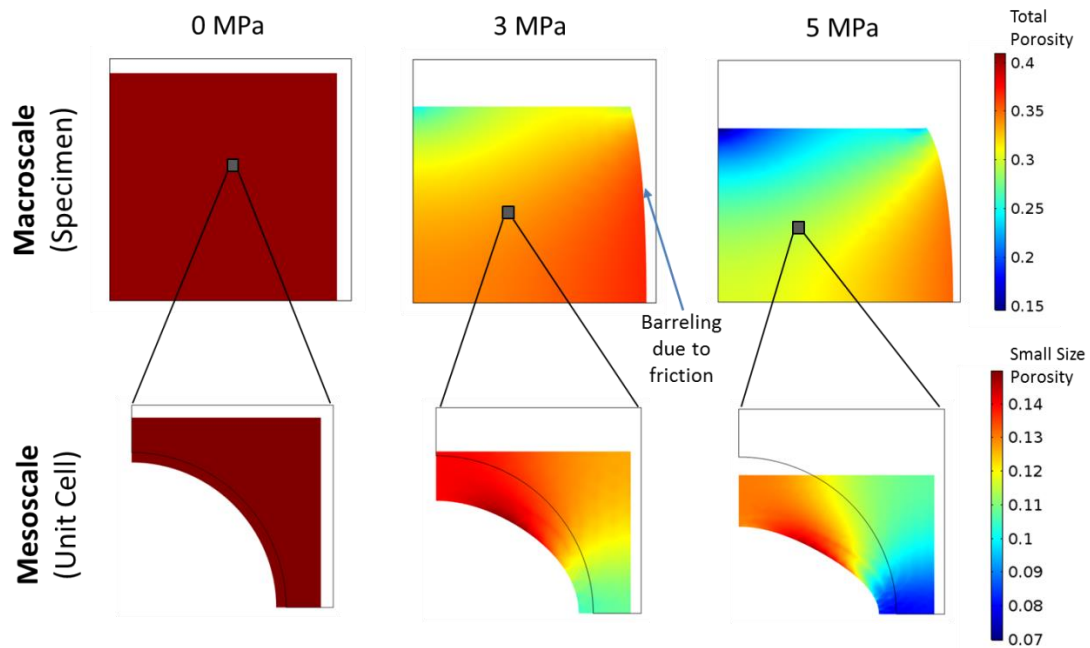


Figure 3.41 – FEM-derived deformation and porosity distributions of specimen and unit cell at the end of the isothermal holding.

Figure 3.42 shows the evolution of overall porosity, large pore size (average diameter) and aspect ratio (major axis/minor axis, approximating the void as an ellipse) with respect to time for the different applied pressures. As predicted, increasing external loads lead to faster densification and increasing elongation of the large pores. Note how the curves suddenly start diverging when the load is applied. 3-D representations of both specimen and unit cell for different time instants and applied pressures are also depicted at sample times.

Figure 3.43 compares numerical and experimental results, the latter taken from the work of Shang *et al.*^{90, 91} A good agreement is found, with the largest mismatch showing in the aspect ratio context. The discrepancies with experiments might be due to the uncertain values of surface tension of the composite powder material and of initial size of small pores, estimated to be 1 μm , which in turn influences the sintering stress of the powder compact.

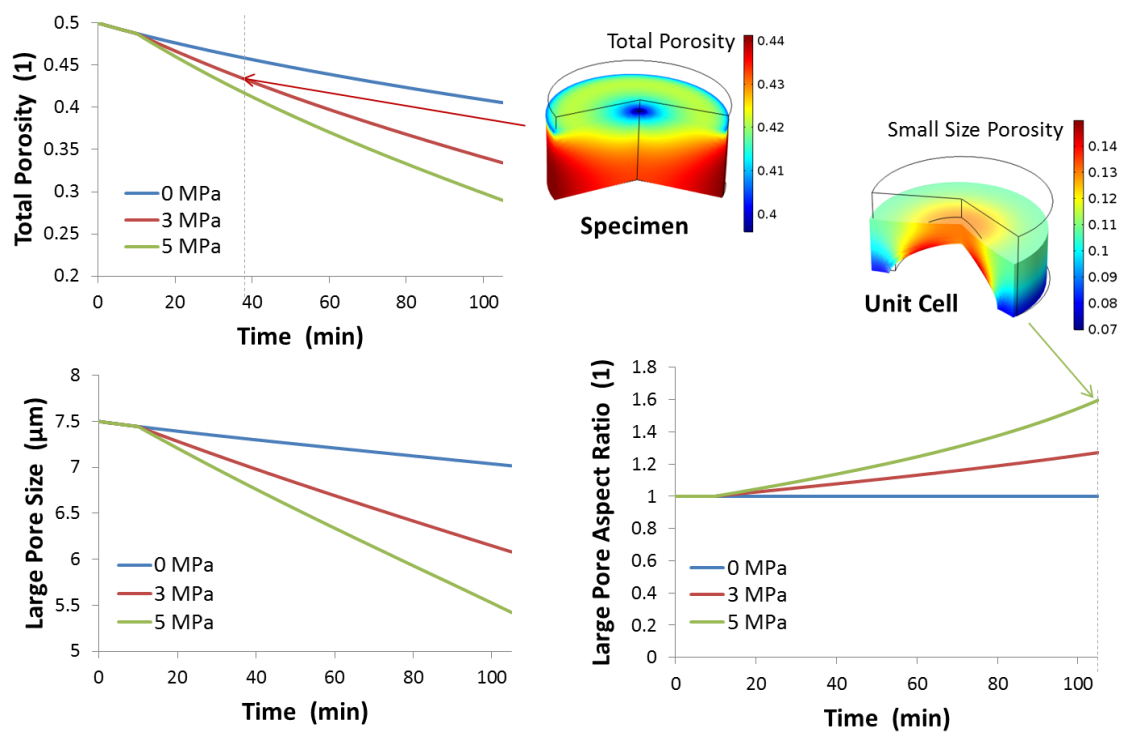


Figure 3.42 – FEM-derived evolutions of global porosity, large pores' size and aspect ratio for the 0, 3 and 5 MPa-applied pressure cases.

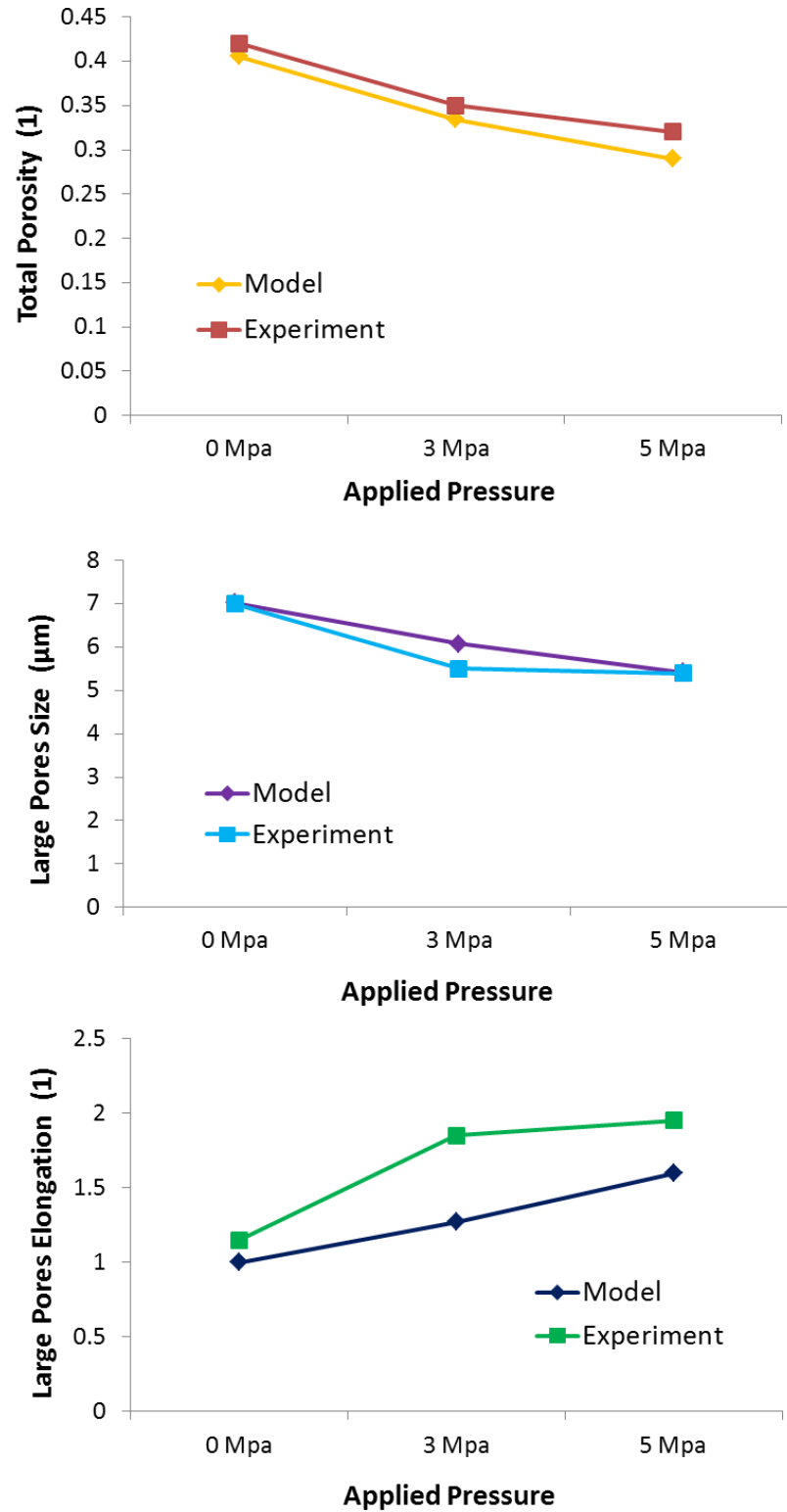


Figure 3.43 – Comparison between experimental and FEM results.

Our multiscale FEM framework for the simulation of sintering and sinter-forging thus allows us to monitor the evolution of size and shape of large pores, small size-porosity distribution and overall specimen shrinkage, with a good degree of accuracy. Further work is needed in order to implement the application of higher loads and larger amounts of voids without encountering numerical problems, and to include grain growth and locally-enhanced grain boundary diffusion phenomena. These types of simulations can also be applied to nonlinear viscous cases, even though with some additional difficulties for the numerical software, due to the nonlinearity of the process itself. Once such obstacles are overcome, de-agglomeration and tailored hierarchical structures can be directly optimized in the FEM context, which allows the direct monitoring of a variety of extra details with respect to the approach based on densification kinetics.

Some guidelines for the usage of these distinct (but interconnected) strategies can be drawn. The solution of the kinetics equations (evolution of porosity and pores' radii with time) can be obtained much more rapidly than the FEM-based outcomes. If one wants to choose the optimal SPS routine in order to obtain de-agglomeration or a certain ratio of small and large pores, with well-determined average sizes, the use of densification equations is recommended, especially thanks to built-in differential equations solvers available in MatLab® or analogous software (here MatLab®'s ode45 was utilized). Macroscopic properties can both provide immediate solutions to boundary value problems and serve as input for multiscale finite-element simulations. The former can be utilized for overall predictions of the SPS processing of specimens containing agglomerates, while the latter can give detailed information on distributions of porosity, stresses and strains, together with pores shape and size evolution, at every time-step.

A schematic summary of the above-mentioned options is given in the following figure, which is a zoomed-in detail of the research objectives tree (Chapter 2).

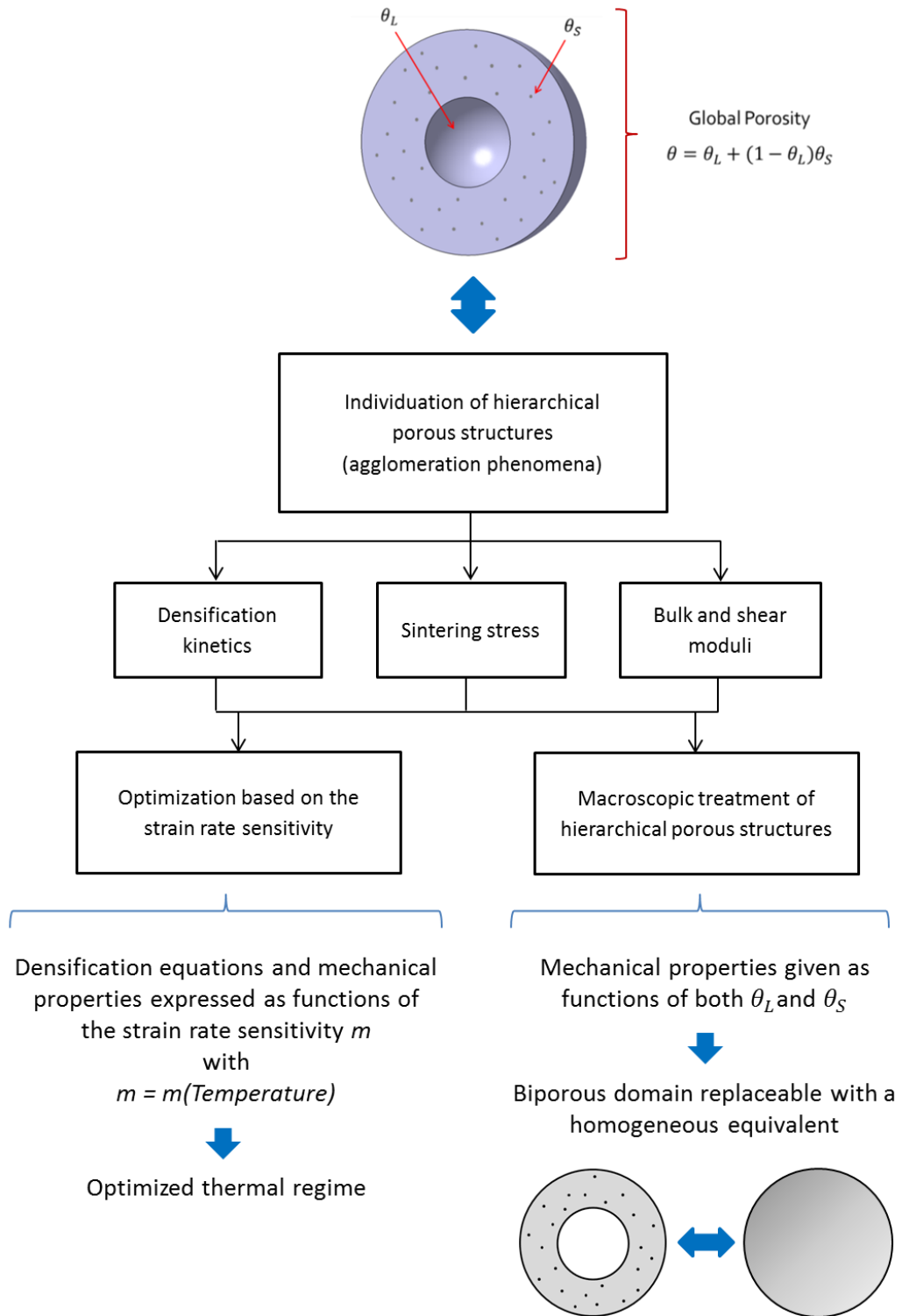


Figure 3.44 – Schematics of the material structure optimization strategies.

Now that we have completed the material structure's optimization based on spark plasma sintering thermal regimes, we need to ensure that such optimized temperatures are experienced by the entirety of the specimen. Samples subjected to sintering, and especially to SPS, are, nevertheless, typically exposed to significant temperature gradients, due to how the heat is provided. In the case of ceramics, the heat is provided via conduction by the surrounding electrically conductive tooling, leading to temperatures decreasing with the distance from the area in contact with the tooling itself. Even in the case of conductive powders, in which heat is directly produced via Joule effect inside the powder specimen, the electric current distribution is usually non-uniform, and temperatures follow accordingly.

The thermal gradients issue is the object of the next chapter. We have anticipated in the introduction that the uniformity of the final result in spark plasma sintering is strongly dependent on the tooling setup in which the specimen is located. A complete optimization of the SPS efficiency has to take this factor into account. Chapter 4 is dedicated to the role of the tooling geometry in the temperature uniformization during SPS. The FEM analyses that will be performed here will, therefore, be further expanded in the following chapter, by simulating the whole tooling-specimen assembly and therefore finalizing the optimization study.

Parts of Chapter 3 have been published in the *International Journal of Refractory Metals and Hard Materials* (D. Giuntini, X. Wei, A.L. Maximenko, L. Wei, A.M. Ilyina, and E.A. Olevsky, "Initial Stage of Free Pressureless Spark-Plasma Sintering of Vanadium Carbide: Determination of Surface Diffusion Parameters," *Int. J. Refract. Met. Hard Mater.*, 41, 2013). Other parts of Chapter 3 are in press in the *Journal of the American Ceramic Society* (D. Giuntini and E.A. Olevsky, "Sintering Stress for Materials with Nonlinear Viscous Rheology," *Rapid Comm. J. Am. Ceram. Soc.*, accepted for publication) and prepared for publication in *Acta Materialia* (D. Giuntini and E.A. Olevsky, "Sintering Kinetics of

Agglomerated Powders with Nonlinear Viscous Rheology,” *Acta Mater.*, prepared for publication). The dissertation author is the primary author of these publications. The results in the last paragraph of the same Chapter 3 are part of a work prepared for publication in *Acta Materialia* (H. Shang, D. Giuntini, E.A. Olevsky, and R.K. Bordia, “Pore Shape Evolution during Sinter-Forging of LSM-YSZ Composites”, *Acta Mater.*, prepared for publication).

Chapter 4

Optimization of Spark Plasma Sintering

Based on Improved Tooling Setup

4.1 The role of the spark plasma sintering tooling design

We have pointed out before that the optimization of spark plasma sintering efficiency can be conducted on a variety of levels. The complexity of this field-assisted sintering technology arises from the combination of several physical mechanisms, ranging from electric currents, to heat transfer, solid mechanics and densification kinetics. A main difference with respect to traditional sintering techniques consists in the fact that in SPS the powder compact needs to be placed in a quite elaborated tooling setup, typically made of graphite, even though other materials with appropriate values of electrical and thermal conductivities can also be considered. In conventional sintering, instead, the green specimen (as the pre-compacted powder sample, ready to be sintered, is usually denominated) is directly located in the apposite location inside the sintering furnace. It is currently well agreed that the presence of such tooling has drastic effects on the densification process itself. SPS tooling setups are available in a variety of schematics, dimensions and materials, but we will provide here a general description in order for the reader to be able to grasp a first basic idea of its components, function and morphology, while more specific details will be given in the following sections. Figure 4.1 will serve as graphical reference.

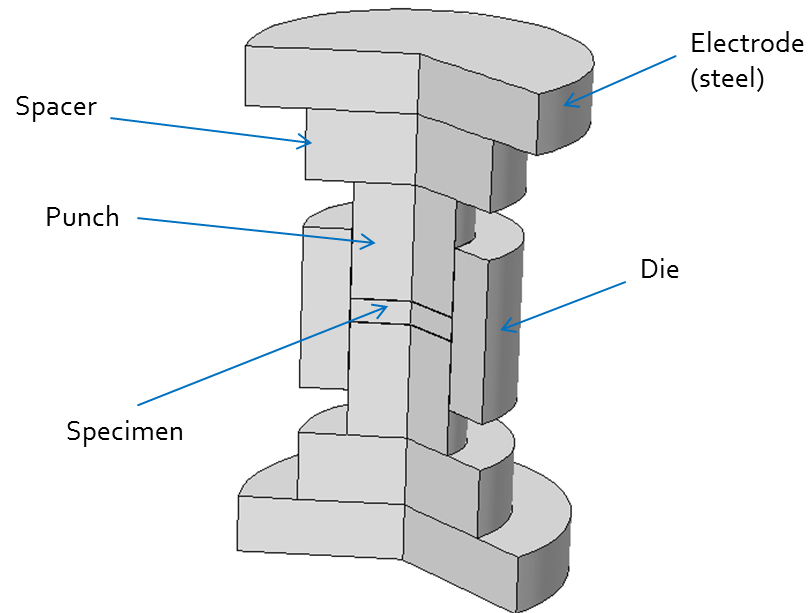


Figure 4.1 – Spark plasma sintering tooling setup.

The powder compact is located into a cylindrical cavity formed by a die and two punches. The die is a hollow cylinder that radially confines the specimen, while the two punches constrain it axially by being inserted into the hole of the die. Since a voltage has to be applied for the current to flow along the axial direction and allow the sintering process to happen, a transition between the narrow punches extremities and the wide steel electrodes is usually added. This transition is generally called spacer, and provides a smooth gradient in the cross-section area from the punches, which have the same cross-section area as the sample, to the electrodes, that are much larger, in order to accommodate a variety of tooling sizes. A graphite felt is often wrapped around the die in order to provide thermal insulation and increase the SPS efficiency. Between the powder and the adjacent tooling components a graphite foil is located to prevent adhesion due to the high temperatures reached during sintering. Once the specimen-tooling setup has been assembled, it is inserted in the spark

plasma sintering machine chamber, vacuum conditions are applied, and the sintering route can be started.

Even from this brief description it is evident that the complexity introduced by the presence of such assembly cannot be neglected. One can look at this important role of the tooling as a valuable SPS optimization resource, instead of an uncontrollable limitation of our control over the process. This is the aim of the second part of our study. In the previous chapter we have focused on the specimen only, by looking at the material structure from both a meso-scale and a macro-scale viewpoint. Now we shift to an even larger scale and we involve process the entire SPS setup in our efficiency optimization. Notice that the main optimization parameter is still temperature. While previously we have started to study the most suitable thermal regimes, namely the route that one needs to impose on the SPS machine in order to gain the best outcomes, here we will make sure that such regime is followed within the entire specimen, and not only locally. Spatial temperature gradients, indeed, can be extremely intense during spark plasma sintering, and therefore cause inhomogeneous thermal conditions, and render vain our efforts of the previous chapter.

The presetting of a temperature regime on the SPS machine's control panel, typically a heating ramp ranging from 100 to even 1000 °C/min, followed by a holding time step at the optimal densification temperature for the material under consideration, does not guarantee that the entire specimen is experiencing those same conditions. The adherence to the imposed temperature profile is certain for one specific point only, the location on which the thermal probe is located. The probes utilized are thermocouples or pyrometers; therefore the measurement happens by direct contact or optically. In any of these cases, it is difficult to reach the specimen itself. Most often, the measurement location is in its proximities, or, even if it is possible to reach the specimen, at the current state of technology we cannot go further than the surface. Thus, while the PID controller embedded in the spark plasma sintering

device operates by keeping the temperature at this specific location coincident with the settings, we do not have any information about what is happening in the surroundings. It is well known that the bigger the size of the setup,^{184, 185} the larger the gradients, but very little quantitative data are available to support this statement. This difficulty is due to the configuration and the operative modalities of the SPS machine, since the specimen and tooling are put in an inaccessible closed chamber under vacuum conditions.

The relevance of this study has, therefore, multiple aspects. It naturally arose from the previous part of the work, and specifically from the demand of homogenizing the conditions experienced by the SPS samples in order for our thermal route optimization results to be applicable in the real world. But it also provides an important insight of the conditions experienced by a specimen during the entirety of any field-assisted sintering process, by being able, thanks to finite-element simulations, to reconstruct data that are experimentally unavailable. It is also connected to the solution of actual issues of significant thermal gradients hampering SPS outcomes during experimental procedures operated at various institutions. In addition, it is important to underline that temperature gradients cause localized overheating at certain specific locations in the SPS setup, therefore they do not limit to damage the quality of the densified products, they endanger the tooling too.

For all the listed reasons, a combined numerical and experimental investigation has been conducted, with the aim of optimizing the SPS efficiency by creating an innovative, improved, tooling design. Such design has the purpose of rendering the temperature within the powder specimen, and possibly the entire setup, homogeneous and adherent to the optimal value for each processed material system.

The present chapter will address these issues for both the radial and the axial direction. Setups that are different for dimensions and morphology will be analyzed, and distinct powder specimen materials will also be considered, depending on the availability of

the experimental data or on the specific real world problem to be solved. Particular attention will be devoted to ceramics, being these insulating materials, and therefore more prone to the intensification of thermal non-uniformities. Another reason to prefer electrical insulators over conductors for a temperature-based optimization study of SPS is found in the fact that with insulators we are certain to be capable of isolating the thermal phenomena, while, being an electric current at the basis of SPS techniques, conductors still raise many interrogatives in terms of the internal consolidation mechanisms. For a ceramic powder, instead, it is reasonable to assume that all the thermal input is a direct consequence of Joule heating, since the current cannot flow through the compact, but inside the graphite tooling only. It is worth mentioning explicitly that our definition of conductive and insulating is relative to the electrical conductivity of the tooling constitutive material. Nevertheless, the outcomes that we will derive will be valid for metal powder systems too, provided some necessary, slight, modifications, which will be explicitly pointed out throughout the chapter.

4.2 Optimization of the radial temperature distributions by improved punch design

4.2.1 The radial thermal gradients issue

Because of the typical aspect ratio of a spark plasma sintering sample, characterized by a diameter larger than the height, the radial thermal gradients are the most significant. We will conduct this analysis for an insulating material, and ultimately explain how the conclusions we reach can be immediately adapted to a conductive sample.^{174, 175}

When the powder inside the die-punches assembly has higher electrical resistivity with respect to the tooling material, the path that the current can follow has certain restrictions put in place by the specimen itself. Let us look at Figure 4.1 again and imagine the electric current flow once the voltage has been applied. The bottom electrode is grounded, so we will have a flow from the top to the bottom of the tooling setup. Knowing that the specimen is not accessible to the current, once its path approaches the lower end of the upper punch, a sharp deviation of the flow will happen, in order for it to avoid the insulating component. This deviation leads to a strong current concentration inside the die wall, in correspondence of the specimen axial position. The thinner the die wall, the more significant such concentration will be. Because of the Joule effect, this zone of the die will undergo a strong heat generation. Thus, the lateral surface of the specimen, separated by the die wall only by means of thin graphite foil, will be overheated, while its center will be relatively “cold”. It is now easy to imagine that only a small portion of the specimen will be subjected to the optimal temperature of the preset route, while the remaining areas will be exposed to lower or higher thermal conditions, depending on their position with respect to the recording probe focus point. These thermal disparities will reflect in inhomogeneities of both density and microstructure of the final product. The areas in the proximity of the edge will densify faster, while the central ones might show non-negligible amounts of residual porosity once the process is complete. Alternatively, even if almost full density is reached everywhere in the sample, thanks to a sufficiently long dwelling time at the highest temperatures grain growth phenomena will be present in the lateral zones, creating important non-uniformities in the mechanical properties of the sintered material. Other possible consequences are the generation of residual stresses and localized phase transformations, together with the combination of many of these phenomena.

When interested in assessing the presence and entity of the radial thermal gradients experimentally, a possibility lies in the employment of a double measurement probe setup. Ceramics usually require higher sintering temperatures with respect of metals, even if switching from conventional sintering to SPS can help in lowering them. Still, the typical sintering temperature corresponds to 70% of the melting point, which for ceramics is generally very elevated. The type of probe used for measuring the temperature in a spark plasma sintering setup depends on the levels of temperature reached during the process. As a rule of thumb, in many devices thermocouples are utilized for regimes that are maintained below 1000°C, and beyond this point pyrometers take over (thermocouples resistant to higher temperatures are nevertheless available on the market).

We applied our study to a silicon nitride powder, with which green specimens 6 cm in diameter were produced and spark plasma sintered in a machine endowed with two pyrometers.^{174, 175} The choice of silicon nitride arose from a collaboration with the Dresden Fraunhofer Institute for Ceramic Technologies and Systems IKTS, and also pushed by the growing interest in such material from a variety of fields, from biomaterials to aerospace applications. SPS offer unique possibilities for the consolidation of this material, which is otherwise extremely hard to process.^{254–257}

Note the dimensions of the specimen: a diameter of 6 cm exceeds the typical laboratories size, which range between 1 and 2 cm. This explains why the radial thermal gradients issues had become so significant. The initial height of the specimens was around 1 cm, allowing us to focus on the radial direction only.

The powder was processed in a FCT HPD25 device (FCT, Germany), developed for the production of medium size samples like the ones considered here. The tooling setup was composed by the parts listed in Table 4.1 and made of R7710 graphite (SGL Carbon SE, Germany), whose properties are listed in Table 4.2. Together with the components mentioned

in Table 4.1, graphite foil (Sigraflex, SGL Carbon SE, Germany) and a graphite felt (Sigratherm GFA10, SGL Carbon SE, Germany) were present. The former was inserted in a double layer, each 0.25 mm thick, at the contact interfaces between specimen, die and punches, to ensure the stability of the electro-thermal and mechanical contacts, to prevent adhesion among the parts and minimize the reactions of the powder compact with the graphite of the tooling.

The impact of this graphite foil layer is not negligible and will therefore be taken into account in the FEM framework too. The importance of its role is explained by the characterizing strong anisotropy, induced by the flake-like structure of the raw material employed for the calendaring of the thin foil. The paper's in-plane electrical conductivity is two orders of magnitude higher than the through-plane one, and its properties are dependent on the applied pressure. The graphite felt is a foam-like, 10 mm thick and 80 mm long, layer of soft material wrapped all around the external surface of the die in order to minimize the heat loss by radiation. Figure 4.2 presents a schematic representation of the assembled tooling setup, comprehensive of specimen.

Even if not properly part of the tooling, the figure includes also an indication of the two pyrometers' focus points, since it is thanks to this double-probe setup that we were able to experimentally determine the presence of radial thermal gradients. As shown, Pyrometer A is axially mounted and focuses on the bottom of the 30 mm deep hole in the top punch, while Pyrometer B is radially adjusted and monitors the temperature at a point on the die wall whose axial position corresponds to the central radial cross-section of the specimen.

For this purpose, in the thermal insulation felt a 7 mm through hole had been realized. Hence, Pyrometer A provides an indication of the temperatures experienced by the center of the specimen, while Pyrometer B gives an estimation of the overheating of the edge. The

leading Pyrometer was A, where by leading we mean that it was the one connected to the machine's PID for the control of the temperature regime.

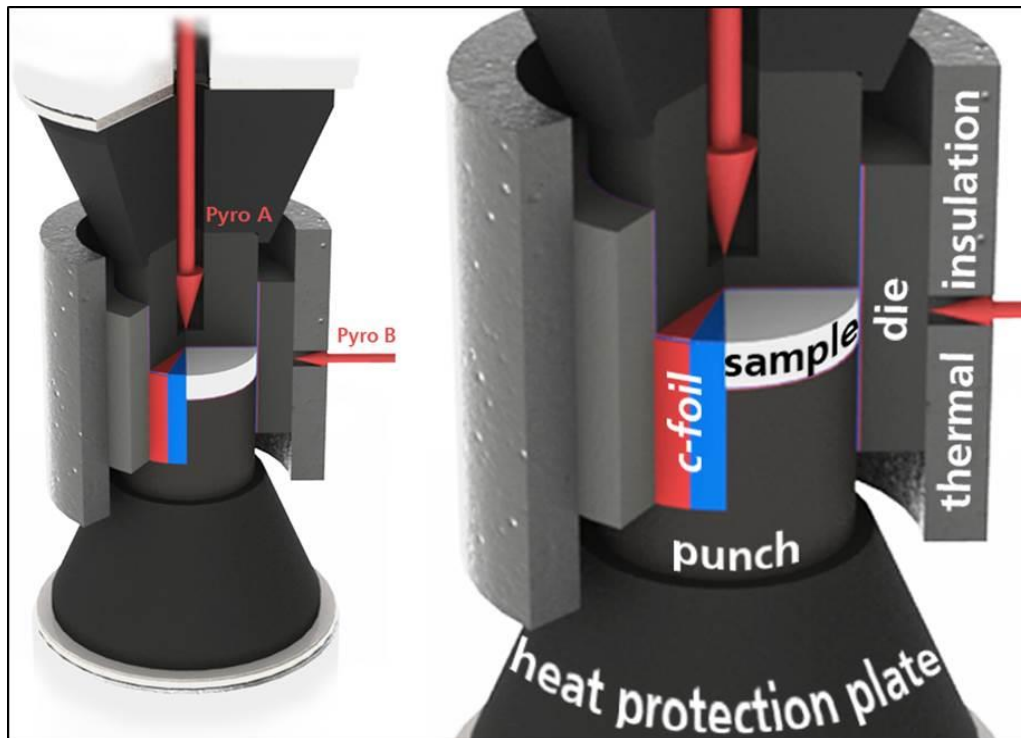
This implies that the preset thermal profile was respected in the proximities of the center of the specimen, but at a location that did not even belong to it, a point of the top punch 5 mm away from the upper sample's surface. Such a discrepancy evidences again the important role of numerical simulations for the retrieval of data that are experimentally unavailable.

Table 4.1 – Tooling setup components for the radial gradients study.

Component (number)	Dimensions
Punches (2)	Height: 35 mm Diameter: 62 mm Hole diameter: 10 mm Hole Depth: 30 mm
Die (1)	Height: 48 mm Thickness: 10 mm
Conical spacers (2)	Height: 45 mm Diameter 1: 80 mm Diameter 2: 62 mm Through hole diameter: 10 mm

Table 4.2 – R7710 graphite properties.

Theoretical density, ρ_{th}	1900 $\left[\frac{kg}{m^3}\right]$
Electrical conductivity, σ_{el}	$\frac{1}{2775 - 2.86T + 0.0027T^2 - 1.04 \times 10^{-6}T^3}$ $\left[\frac{\mu S}{cm}\right]$
Heat capacity, C_p	$1023 + 0.6285T$ $\left[\frac{J}{kg \cdot ^\circ C}\right]$
Thermal conductivity, k_T	$104.7643 - 0.1359T + 1.4921 \times 10^{-4}T^2 - 8.3859 \times 10^{-8}T^3 + 1.7368 \times 10^{-11}T^4$ $\left[\frac{W}{m \cdot ^\circ C}\right]$
Emissivity, ν_{rad}	0.8
Compression strength, S_{comp}	250 [MPa]
Bending strength, S_{flex}	80 [MPa]

**Figure 4.2** – SPS tooling presenting the radial thermal gradients issue. The various components and the two pyrometers positions are marked.

The powder material utilized was a silicon nitride-based composite of 96 wt% alpha- Si_3N_4 (Silzot HQ, AlzChem AG, Germany), with 2 wt% of Al_2O_3 (AKP50, Sumitomo Coal Mining Ltd., Japan) and Y_2O_3 (Grade C, Treibacher, Austria), ground in isopropanol (planetary ball mill, 3 hours, 300 rpm, Achat furniture). As in the case of the R7710 graphite, the material properties were experimentally assessed and interpolated to find the corresponding expressions as functions of temperature, with the only exception of the power-law creep parameters, taken from Ashby's HIP Readings 6.0.²¹⁷ We consider here constant values for the main creep parameters, as tabulated in the literature, to temporarily isolate the addressing of the tooling optimization problem from the material structure one. We will ultimately connect the results in order to implement a combined material structure and tooling geometry optimization, but before doing so we need to make sure that both parts of the study are reliable and robust.

The material properties of silicon nitride are reported in Table 4.3. The addition of oxides enhances the consolidation of silicon nitride by a dissolution-diffusion-precipitation mechanism, leading to a transformation from low-temperature alpha to high-temperature beta phase. Such phase transformation is regulated by the time and intensity of the exposure to high temperatures, and can be therefore utilized to estimate the local temperature distribution within the composite during consolidation.²⁰¹ This, together with the topology of density and grain size distributions, were used as complementary sources of qualitative information about the temperature distribution within the specimen. The combination of microstructural observations and analysis with the two pyrometers data, well correlating with each other, provided a reliable set of data confirming the significance of radial temperature gradients during the SPS of ceramics.

For each experiment 50 grams of silicon nitride composite powder were utilized, loosely poured into the cavity of the SPS tooling. The optimal SPS route for this material

system consisted in a heating ramp of 100 °C/min from 400 up to 1750 °C, followed by an isothermal dwell time (holding time step) of 5 min at 1750 °C. A uniaxial pressure was also applied, with an initial value of 8 MPa, then increased to 50 MPa between 900 to 1000 °C and kept constant until the end of holding time. The sample was finally freely cooled down to room temperature and cleaned by sand blasting in order to remove the adhering graphite foil.

From the SPS experimental procedure a variety of data can be obtained on the evolution of the densification process. We will first give a brief description of the axial displacements data, and then move to the central issue of this section, the thermal disparities along the radial direction.

Table 4.3 – Silicon nitride properties.

Theoretical density, ρ_{th}	3178 $\left[\frac{kg}{m^3}\right]$
Electrical conductivity, σ_{el}	$\frac{1}{1.2647 \times 10^{20} \exp(-0.0117T)}$ $\left[\frac{\mu S}{cm}\right]$
Heat capacity, C_p	
Thermal conductivity, k_T	$32 - 0.0136T$ $\left[\frac{W}{m \cdot ^\circ C}\right]$
Strain-rate sensitivity, m	0.33
Activation energy, Q_{PLC}	636 $\left[\frac{kJ}{mol}\right]$
Surface tension, α	0.5 $\left[\frac{J}{m^2}\right]$
Porosity size, r_0	1.5 $[\mu m]$

Every spark plasma sintering device automatically collects data about axial displacements of the top punch, temperature, electric power, voltage and current. The latter three ones will be indispensable for the reliable reconstruction of the problem in the modeling context. From the displacement readings, instead, the shrinkage of the silicon nitride sample under the applied uniaxial force could be derived. Several distinct stages can be identified, each one explainable by a specific underlying physical phenomenon. From 400 to 900 °C the specimen height increased, because of a thermal expansion not accompanied by any relevant densification phenomena, which translated into a slight negative increase of the axial displacement value (defined as positive in the shrinkage direction). We have had a chance to point out earlier that the initial stages of sintering see mainly a rearrangement of the matter by surface diffusion, which tends to make the pores spherical and favors the formation of necks among the particles, but is accompanied by little or no shrinkage. Between 900 and 1000 °C the applied pressure was increased from 8 to 50 MPa, leading to a mechanically-induced densification, indicated by a displacement's positive increase of approximately 2 mm, which then stayed constant until a 1300 °C temperature was reached. At 1300 °C volume shrinkage started occurring, subsequently stabilized during the holding time-step, and not complete until the sample had reached room temperature.

The most fundamental set of data for the purpose of this study is the one pictured in Figure 4.3. The plot summarizes the preset temperature profile (Pyrometer A) and a parameter that we will call temperature disparity, ΔT , which is calculated by subtracting $T(A)$ from $T(B)$, since the latter revealed to be notably higher.

The values of ΔT are significant. Because of its definition, a positive ΔT is therefore a signal of that strong localized overheating of the sample's outer surface that we had anticipated in the previous paragraphs. A negative value would imply that the radial temperature pattern is reversed, and thus that this same outer surface is experiencing lower

temperatures with respect to the specimen's center, a phenomenon typically occurring when considering conductive powders.

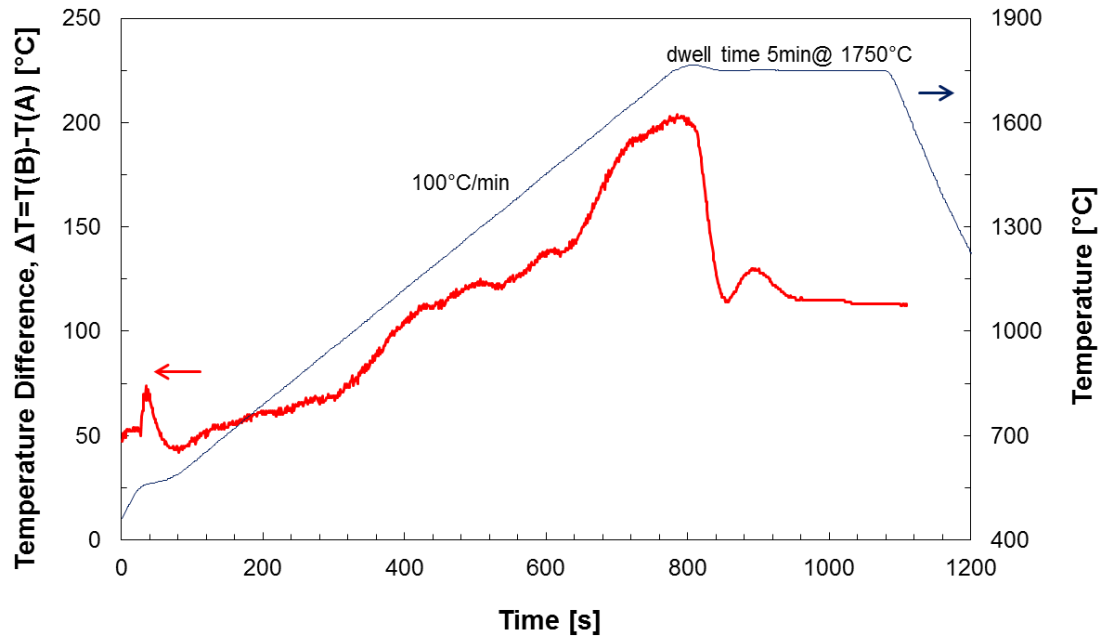


Figure 4.3 – Temperature regime and temperature disparity among the two pyrometers in the conventional SPS setup.

This important result will be later combined and confirmed with a series of microstructural evidences, based on various experimental techniques. The need for a method to lower these non-uniformities was consequently felt, and a promising approach was identified in an optimization of the tooling geometry.

4.2.2 FEM reconstruction of the spark plasma sintering tooling setup

The problem of reconstructing a complete spark-plasma sintering problem with the finite element methods is complex. We have anticipated at the beginning of this chapter that field-assisted sintering techniques simultaneously involve a variety of physical phenomena:

electric currents, heat transfer, solid mechanics and densification kinetics. A fundamental initial requirement is, thus, the availability of a FEM software that allows the combination of a number of “physics” (as they are called in the software interface itself) within a single model. A suitable solution was found in COMSOL Multiphysics®, whose distinguishing capability of coupling several physics at the same time is making it gain growing attention in the SPS modeling area.

While in Chapter 3 the optimization process was based on the temperature versus time profile and therefore considering the specimen’s meso-scale evolution was sufficient, here we are aiming at improving the temperature spatial distribution, which is strictly dependent on the tooling containing the specimen. This imposes to model the entire SPS tooling setup by FEM. Every component – punches, die, spacers and specimen – was reconstructed in its geometric details in SolidWorks® and consequently imported in the COMSOL® environment. As for the graphite foil and thermal insulation, we chose not to complicate the model further by inserting other components, and simulated their effects with the appropriate boundary and contact conditions, which we will explicitly state later. Thus, in the FEM software we created a three-dimensional, time dependent, fully coupled model of the SPS system. The choice of a three dimensional simulation, instead of exploiting the axial symmetry of the setup and therefore reducing the computational costs, lied in the fact that we were planning to simulate also alternative geometries of the tooling, which would not have been necessarily axisymmetric. The time dependency allows us to simulate a typical SPS regime, inclusive of heating ramp and isothermal holding time step. By fully coupled we indicate the simultaneous combination of the various physics involved, that are interconnected by means of the opportune software options and the addition of the necessary dependences of the materials’ properties. The FEM simulation of spark-plasma sintering procedures therefore requires the implementation of an electrical module, describing the current flowing through the SPS setup,

together with a thermal one, responsible for the consequent heat transfer by Joule heating phenomena, a mechanical section, allowing the application of external loads, the description of the interactions between components and the introduction of the powder compact constitutive behavior, and finally a mathematical section, reconstructing the densification kinetics. The required equations are presented here.

For the DC current distribution we use

$$\mathbf{J} = \sigma_{el}(-\nabla V) \quad (4.1)$$

where \mathbf{J} (A/m²) is the current density, σ_{el} (S/m) the electrical conductivity and V (V) the voltage.

The consequent heat transfer by joule heating is given by the Fourier equation with the appropriate source term, as follows

$$\rho_{eff} C_p \frac{dT}{dt} = \nabla \cdot (k_T \nabla T) + \nabla \cdot \mathbf{J} \quad (4.2)$$

in which C_p is the heat capacity (J/kg/°C), T (°C) the temperature, k_T (W/m/°C) the thermal conductivity, and the density ρ_{eff} (kg/m³) is expressed as a function of the theoretical density of the bulk material ρ_{th} (kg/m³) and the porosity θ , in the following form

$$\rho_{eff} = \rho_{th} \rho = \rho_{th} (1 - \theta) \quad (4.3)$$

Notice again that we conducted this study for a specimen in which we assumed absence of hierarchical porous structures. We wanted to decouple the two sides of the temperature-based SPS optimization study, by not considering the tooling when analyzing the material structure and not embedding agglomeration when working on the tooling design. Once the two aspects have been assessed, we will finally combine them. As for now, we will only be dealing with a homogeneous size of porosity, which we will simply address as θ .

The last equation to be added is the sintering constitutive equation. Since we are operating SPS of a crystalline material with the aid of an external pressure, we will apply it to a power-law creep rheology of the skeleton. We repeat here the equation of interest:

$$\sigma_{ij} = A_m W^{m-1} \left[\varphi \dot{\varepsilon}_{ij} + \left(\psi - \frac{\varphi}{3} \right) \dot{\varepsilon} \delta_{ij} \right] + P_L \delta_{ij} \quad (3.13)$$

The various terms have been defined elsewhere. In line with the simplification choices made for porosity and the power-law creep parameters, we also chose to lighten the model by expressing the sintering stress and the normalized bulk and shear moduli in their classic formulation, due to Skorokhod,^{111, 113} which poses them as independent from the strain-rate sensitivity m , therefore preventing the possibility of computational problems. At this stage of the tooling geometry optimization study, an extremely accurate reproduction of the kinetics and mechanics of the sample is not required, since we are focusing our attention on the electro-thermal phenomena within the whole SPS setup. This is why such initial approximation is justified.

Accuracy is nevertheless strictly required in imposing initial, boundary and contact conditions. This series of parameters will guarantee the adherence to the experimental procedures, and their definition is a crucial step in the modeling validation process. We list them here according to the physics to which they refer.

Let us start with the electrical currents module. The initial voltage was set to zero. The lower surface of the bottom spacer was grounded, while the current input (extracted from the SPS machine readings during the experimental process) was applied to the top surface of the upper spacer. All the outer tooling surfaces were electrically isolated. Finally, the electrical contact resistance was imbedded at the interfaces between the tooling components as a function of temperature and pressure, in the following manner²⁵⁸

$$\mathbf{n} \cdot \mathbf{J} = \frac{\Delta V}{r_{el,c}} \quad (4.4)$$

$$r_{el,c}^h = (4.15 - 0.21 \ln T) \left(\frac{19}{P_{ext}} \right) \quad [m\Omega \cdot cm^2] \quad (4.5)$$

$$r_{el,c}^v = (-0.006 \cdot T + 19) \cdot (-0.008 \cdot P_{ext} + 1.14) [m\Omega \cdot cm^2] \quad (4.6)$$

where \mathbf{n} is the outward unit vector normal to the interface surface, ΔV the voltage drop across the interface (V), $r_{el,c}$ the interface contact resistance ($m\Omega \cdot cm^2$), P_{ext} the externally applied pressure (MPa).

The first equation tells the software that in correspondence of a certain, preselected, surface an electrical resistance is present, in the form given by the second equation or the third equation. The denomination $r_{el,c}^h$ refers to the horizontal contacts and $r_{el,c}^v$ to the vertical ones. By horizontal contact surfaces we denote the ones that lie perpendicularly to the current flow, while the vertical interfaces are the ones parallel to it. In the first category we include the punch-specimen and punch-spacer interfaces, while in the second case we are considering the die-punch and the die-specimen contacts.

These two last equations are the result of a broad experimental study, which we will here briefly summarize.²⁵⁸

The presence of a thermal and electrical contact resistance at the interfaces between the many components of a spark-plasma sintering tooling has been theorized by many studies, by seldom addressed quantitatively.^{47, 196, 259} A few exceptions concerned the formulation of an expression that was giving the electrical contact resistance as a function of temperature,¹⁸⁶ but no such studies included pressure too.

Contact resistance is due the microscopic imperfections characterizing every real world surface. Impurities, roughness, inclusions, wear are among the causes of the imperfect planarity of a theoretically flat surface. When two of such surfaces are put in contact, they will be touching each other in correspondence of the tips of these roughness peaks, and not on the entirety of the contact area. Being this the reason why a contact resistance exists, it is

immediate to infer that both temperature and pressure are parameters to be taken into account, since they directly affect the morphology of the surface roughness. After having shown that the thermal contact resistance plays only a negligible role during SPS processes, we focused our attention on the electrical one.

We opted for a wide series of experiments performed in the absence of powder, so that our results could be applied to the SPS of every material. Apposite design of the tooling components were tailored and produced for the individuation of a single type and layer of resistance at a time. Specifically, to obtain the horizontal resistance we run experiments with a conventional setup first, and then we substituted the two punches with a single one, with the exact same dimensions of the previous two assembled together. For the vertical one we utilized this single punch with a regular die first, and later a special dummy die, namely a whole piece reproducing the shape and dimensions of the die-punch assembly. Figure 4.4 shows both experimental configurations for the two parameters investigated. In such way, we have isolated the effect of a single horizontal contact resistance layer in the former case, and of a single vertical one in the latter.

Since the spark plasma sintering machine automatically provides the readings of the voltage and current at each second of the conducted experiment, by applying the Ohm's law the corresponding electrical resistance could be calculated. By subtracting the one-punch values from the two-punches ones in the horizontal study, and the dummy-die from punch-die values in the vertical one, the resistance associated with the aforementioned single layers was obtained. Experiments were run multiple times for each level of applied temperature (between 600 and 1600 K) and pressure (20, 30, 40 or 50 MPa, since for higher values the effect of pressure was not varying anymore).

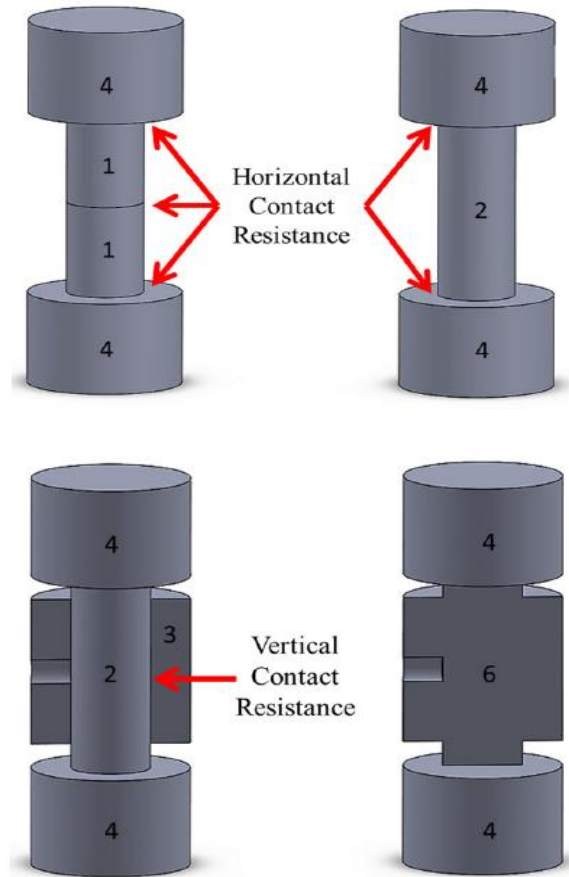


Figure 4.4 – Schematics of the setups utilized to study SPS contact resistance.
 (a) Horizontal resistance layers, (b) Vertical resistance layer.

The outcomes were opportunely averaged and normalized with respect to the contact area, in order to be generalizable. Finally, by numerical regression, equations (4.5) and (4.6) were developed. By looking at the dependencies on temperature and pressure, the physical phenomena underlying these changes in the contact resistance could be identified. The nonlinear decrease of the horizontal resistance with increasing temperature and pressure corresponds to the creeping of the graphite, combined with the progressive crashing of the surface roughness peaks and the consequent improvements in the interface quality. The linear decrease of vertical contact resistance, still with augmenting temperature and pressure, can be

explained by considering Poisson deformation and thermal expansion of the tooling components, both linear phenomena with the applied load and the thermal increase, respectively.

It is important to notice that this electrical contact resistance study was conducted in our laboratory at San Diego State University, while the silicon nitride experiments that provide the data for this work were run at the Dresden institution. The two facilities employ different types of graphite. This does not imply that the contact resistance results cease to be valid. The physical phenomena causing such relationships between electrical resistance, temperature and pressure are analogous, no matter what type of graphite is being used, and such are the dependencies expressed by equations (4.5) and (4.6). The only distinction will appear in the coefficients multiplying the temperature and pressure functions, which are indeed slightly different in the two situations. The formulations reported above are the ones referring to the graphite R7710, the constituent of the tooling setup that we are aiming at optimizing.

Now we consider the boundary and contact conditions associated with the heat transfer module. The initial temperature was set to be 25 °C. The same constant temperature of 25 °C was imposed at the bottom surface of the lower spacer and at the top surface of the upper one, corresponding to the cooling effect of the circulating water in the SPS machine. The outer surface of the die was thermally insulated, as the presence of the graphite felt imposes. Ideal thermal contacts between layers were implemented, since the role of thermal contact resistance was proven to be negligible.²⁵⁸ The external surfaces were endowed with a heat radiation boundary condition, according to the Stefan-Boltzmann formulation, with a value of 0.8 for graphite emissivity. Remember that SPS is operated in vacuum.

Such equation is preexisting in the FEM software and is expressed as

$$\mathbf{n} \cdot (k_T \nabla T) = v_{rad} \epsilon (T_{amb}^4 - T_{wall}^4) \quad (4.6)$$

where ν_{rad} is the graphite thermal emissivity (1), ϵ the Stefan-Boltzmann constant, $5.6704 \cdot 10^{-8}$ W/m²/K⁴, T_{amb} is the room temperature (25 °C) and T_{wall} the temperature of the radiating surfaces (°C), in this case all the outer surfaces of the tooling except for the die wall and the top and bottom surfaces.

Lastly, we consider the conditions that concern mechanics and densification kinetics. The entire setup was obviously initially in static equilibrium, and an initial porosity of 30% was introduced. The bottom surface of the lower spacer was fixed, while the top surface of the upper spacer was subjected to an externally applied pressure equal to the load utilized in the experiments. The contact between the different tooling components was ensured.

Once inserted in the model variables section the set of material properties reported in Table 4.2 and Table 4.3, and having defined the thermal route as a function of time in the software's time-dependent settings, the FEM implementation of the spark plasma sintering of silicon nitride was complete. At this point, a validation of the model is of fundamental importance to allow the prosecution of the study. In the absence of a substantial validation step, the application of this same framework to alternative tooling geometries would not be justified.

Because of the focus of this study on temperature distributions, the thermal variable will be at the center of our attention. This is made possible by the availability of two sets of experimental data for temperature, one from Pyrometer A and one from Pyrometer B, which is an unusual and convenient circumstance when checking on the adherence of the numerical reconstruction to the actual experiments. Thus, the model validation consisted in providing the software with the experimental current profile as input, and subsequently assessing that the temperatures observed at the two pyrometers locations coincided between experiments and modeling. Other possible approaches rely on a PID controller to guarantee the adherence to

experiments.²⁰⁸ It is worth spending a few words here on why we preferred not to proceed in that direction.

An introduction must be given on the possible operational modes of a SPS device. Two options are available: temperature control mode or current control mode. In the first case, the most commonly employed, the desired temperature regime is set on the machine's control panel, and the same machine's PID controller will take care of guaranteeing the this profile is respected, at least at the location in which temperature is measured. In the latter situation, the user imposes a current profile directly on the control panel, and the temperature follows depending on all the other conditions involved. Since, in the SPS modeling by finite elements context, the usual practice is to attempt a reproduction of a certain thermal route, certain authors decide to build a numerical PID controller in their simulations and let it take care of following the thermal profile that they have chosen. It is a legitimate procedure, but we have reasons to believe that not imbedding this PID in the FEM environment helps ensuring that every parameter in the simulations is following what previously performed experimentally.

Our choice of not adding a PID controller was motivated as follows. First, in order to guarantee that the simulations reproduce the machine's processes, we have to guarantee that the experimental and numerical PID's are analogous. Therefore we need to have information on the details of the PID functioning in the SPS machine. Since such data were not available for the machine that we employed, we would have been forced to implement a generic PID equation relating current and temperature, and the adherence to experiments would not have been guaranteed. Therefore, a numerical reconstruction of SPS procedures that includes a PID controller needs its own validation. Namely one needs to ensure that the current profiles obtained experimentally and numerically coincide. On the contrary, one often can find examples of PID-inclusive model validations based on analogous thermal profiles for simulations and experiments. But this is rather obvious if the PID equation is properly defined.

The temperature profile will be the preset one, but the same cannot be assumed for the current profile, which is why this is the parameter that needs to be checked in this case. A non-verified PID controller could even compensate for other errors, such as inexact material and contact properties, by adopting a different current profile with respect to the experiments, which nevertheless leads to the same temperatures, thanks to the mismatch between real and simulated material and interface features. In addition to this, it is important to remember that a numerical simulation will unfailingly introduce an error in the process reconstruction. The PID controller simulation will introduce an error, as well as the SPS process simulation itself. This implies that, when operating numerical simulations of SPS with a PID controller, we are introducing two errors in our model. Thus, instead of inserting such two errors, and moreover having to assess the coherence of the numerical PID-produced current profile with the experimental data, we chose to employ directly the experimental current data as input. An objection that could be arisen consists in noticing that our simulations were reproducing a SPS machine operating in current-control mode, while the experiments were conducted in temperature-control mode. We believe, nevertheless, that the reliability of a modeling framework lies in guaranteeing the best possible matching with experiments as far as the conditions experienced by the SPS tooling and powder are concerned. The operational mode of the machine ceases to be relevant once such matching has been reached (unless one wants to simulate the entire SPS device, which is not the case here). By using the experimental current profile as an input, together with a whole set of experimental data for material and contact properties, we are ensuring the maximum possible adherence to reality. Once two separate sets of temperature data (profiles of pyrometers A and B) are found to be coincident between experiments and simulations, we can be confident that our modeling framework is reliable. Figure 4.5 shows the temperature profiles at point A and B for the experiments and the simulations. Very good adherence is evident for the holding time step, while a more

inexact matching characterizes the heating ramp. We will, nevertheless, consider this outcome to be satisfactory for our purposes, since the holding time is more relevant in the present work. It is during this isothermal dwelling that most of the densification process occurs and it is therefore at this stage that thermal gradients play a more important role. Such confidence was further confirmed by the second set of experiments, posterior to the initial model validation operated with the conventional punch geometry, and by additional experiments conducted in the broadening of this study, as we will report in the following sections.

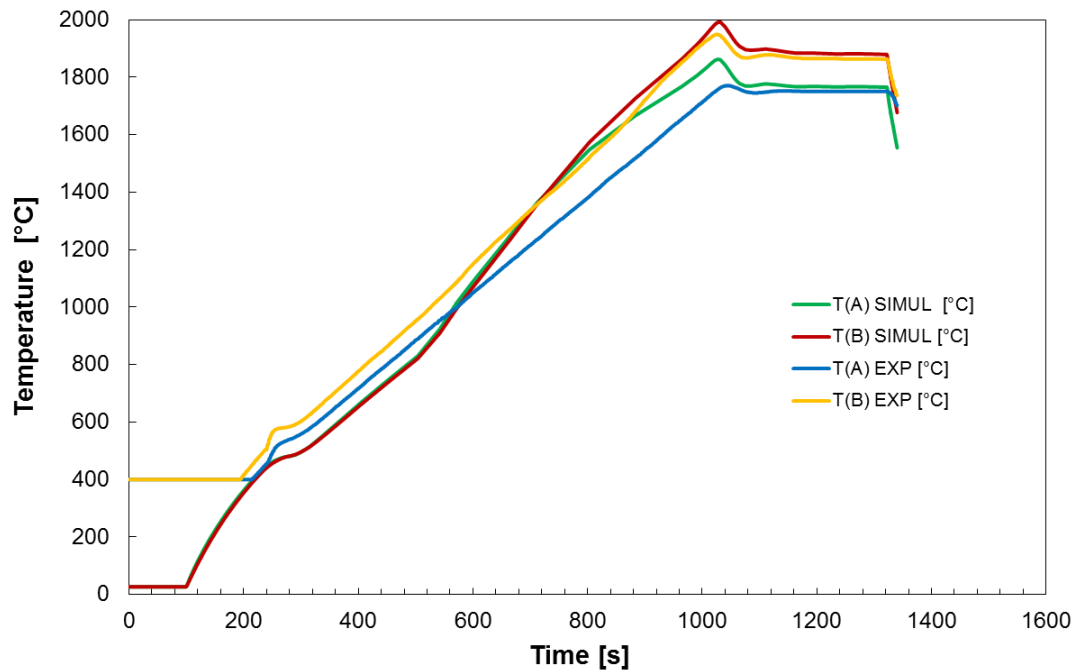


Figure 4.5 – Fitting between experimental and numerical temperature profiles of pyrometers A and B.

At this point, the FEM model is complete and validated, therefore ready to be run, once the study domain has been opportunely meshed. Several meshing attempts have been performed in order to stabilize the simulations' outcomes. A free tetrahedral mesh was finally selected, with a number of “normal”- or “fine”-sized elements ranging between 12,000 and

25,000, automatically generated by the software. Such definitions of the mesh sizes are reported as denominated in the software itself, which uses a qualitative indication of the mesh refinement grade that spans from “extra-coarse” to “extra-fine”.

4.2.3 FEM and experimental implementation of the novel punch design

Now that we have built a reliable finite element modeling framework for our analysis, we proceed to the core of the study: the optimization of the tooling in order to minimize the radial thermal gradients within a ceramic SPS specimen.

First of all we need to focus our attention on a specific component, to which the redesign attempts can be applied with the maximum efficiency. The choice immediately falls on the punch. The punch is the component that ensures the axial confinement of the specimen, by being put in two copies, one above and one below the powder compact. It therefore shares the cross-section area of the sample, and it is also the piece through which the current flows when it is sharply deviated because of the presence of an insulating obstacle. The idea that we decide to implement consists in drilling holes in this same punch, so that the flow of current, and its consequent Joule heating effects, will be altered. Notice that this type of modification is allowed by the graphite’s compressive strength, as simulations will confirm. The holes’ drilling is designed according to specific patterns, represented in Figure 4.6.

Two main families of novel punch geometries are identified, one endowed with an annular array of circular holes, the other with a variable number of concentric ring-shaped holes, both represented in the same Figure 4.6. From this point on, we will refer to this first modified configuration as “Holes”, to the second as “Rings”, while the conventional one will be addressed as “Full”.

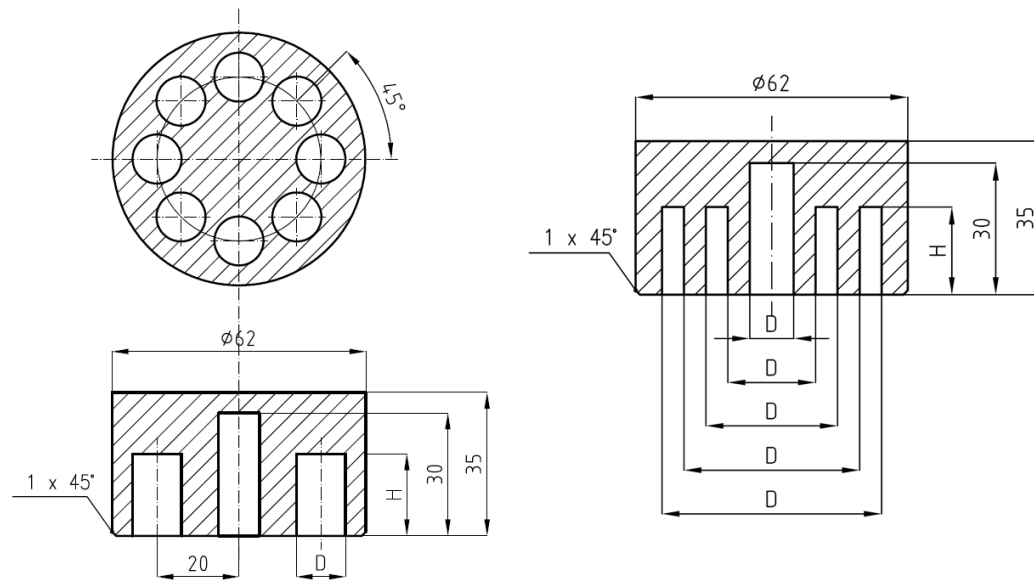


Figure 4.6 – Alternative punch designs: Holes (left) and Rings (right).

For both the Holes and Rings cases, several combinations of the main geometrical parameters are investigated. Several variations are created, by changing the values of the dimensions marked as D and H in the figure. H is the height of the holes, while D is their diameter in the Holes configuration, and the series of concentric rings' diameters in the Rings case. In this first stage of the geometrical optimization study, we choose to minimize the number of variables coming into play by keeping the characteristic dimensions of the holes and the distance among them constant in each attempted configuration. Once we have got the first results and gained an insight in how to regulate radial temperature distributions by altering the punch's morphology, we will investigate on more refined and detailed designs.

Thus, we started the simulations campaign on the altered geometries by selecting a pair of values for D and H for every setup. The following values were applied, in all their possible combinations, for a total of 24 case-studies.

Holes:

D: 8, 10, 12, 14 mm

H: 10, 20, 30 mm

Rings:**1 Ring**

D: 24 – 45 mm

H: 10, 20, 30 mm

2 Rings

D: 20 – 30 – 40 – 50 mm, 18 – 32 – 38 – 52 mm

H: 10, 20, 30 mm

3 Rings

D: 18 – 25 – 32 – 39 – 46 – 53 mm

H: 10, 20, 30 mm

Figure 4.6 refers to a generic Holes case and a 2 Rings one. In the latter one, notice that the smallest hole is the one which was present in the Full configuration to, because it is the one necessary for Pyrometer A to measure the temperature in the proximity of the specimen's center. Therefore such hole will always have $D = 10$ mm. The same holds for the central hole of the Holes configuration.

For each simulation, the sintering route followed exactly what has been applied in the experimental framework. The new outer surfaces resulting from the presence of the holes in the punch were endowed with the same surface radiation boundary condition introduced in the thermal module for the external surfaces of the whole tooling setup.

As a first step, we run a simulation for each of the two categories, namely one Holes and one Rings example. Specifically, we considered the Holes case with $D = 12$ mm and $H =$

20 mm, and the 2 Rings geometry with $D = 20 - 30 - 40 - 50$ mm and $H = 20$ mm. Both models showed promising results. In contrast to the 120 °C of average temperature disparity (ΔT) during the holding for the Full punch case, we were here obtaining average values of 70 °C for the Holes and even 15 °C for the Rings, still during the dwelling time step.



Figure 4.7 – Photographs of the experimentally-implemented Holes (left) and Rings (right) setups.

We therefore decided to implement these two configurations experimentally, in order to further confirm the successfulness of our optimization strategy before widening the numerical part of the study. A picture of the two novel punches is shown in Figure 4.7, Holes on the left and Rings of the right.

The conventional Full punch was replaced by these two optimized geometries and a spark plasma sintering experimental procedure analogous to the one conducted for the conventional setup was conducted. The FEM results were confirmed, as Figure 4.8 shows. Here, similarly to Figure 4.3, the ΔT evolution with time for the three cases experimentally implemented is plotted together with the temperature profile corresponding to the imposed sintering regime.

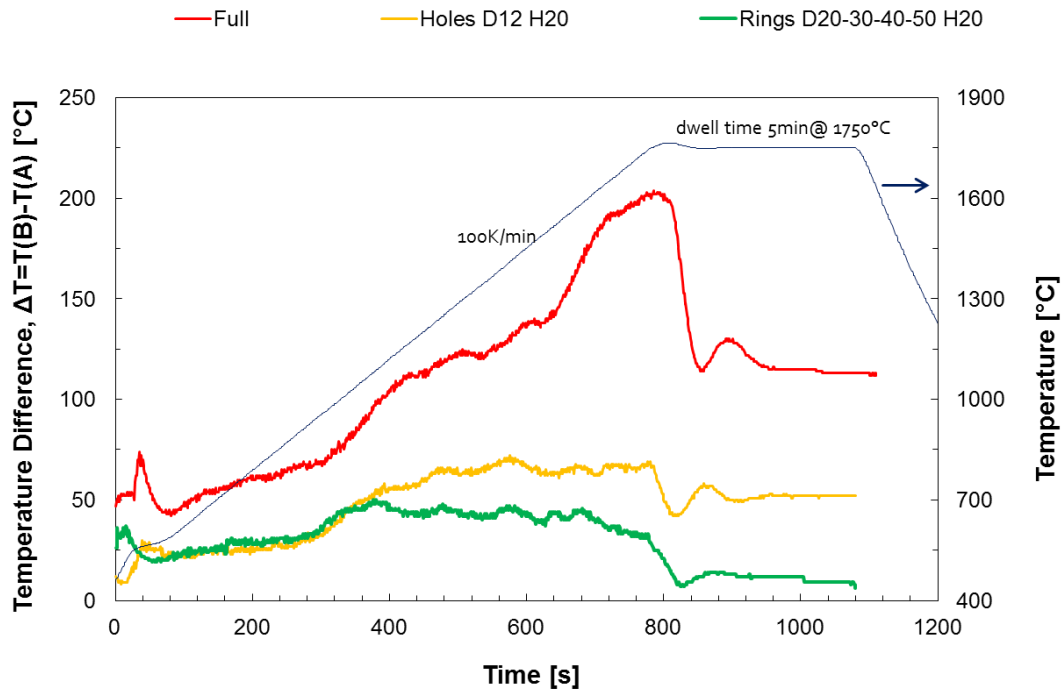


Figure 4.8 – Temperature disparity among the two pyrometers for the conventional Full configuration and the experimentally-implemented Holes and Rings ones.

From this second set of experiments one can see that during the heating ramp ΔT slowly increases with time, nevertheless staying into a relatively low range of 25-35 °C (corresponding to $T(A)=600$ and 900 °C, respectively), but that it suddenly raises when the applied pressure reaches its maximum value of 50 MPa. This is a particular tricky aspect to be reproduced in the FEM model. The most interesting time step, though, is the isothermal dwelling, at the beginning of which the peak of 200 °C temperature disparity for the conventional Full case is successfully lowered down to 64 °C in the Holes configuration and 32 °C for the Rings one. This beneficial tendency appears stabilized with time, since after 2 minutes of holding a ΔT of 115, 51 and 13 °C is seen in the Full, Holes and Rings setup, respectively. Such values are in good agreement with the simulations outcomes, and even lower in the Holes case, meaning that the FEM had underestimated the effectiveness of this redesign in lowering the disparity between $T(A)$ and $T(B)$. We would like to underline here

that it is not only ΔT to be coincident among simulations and experiments, but the two separate temperature profiles at A and B themselves.

It is worth noticing that the punch geometry results do not have any impact on the monitored densification of the sample, whereas the electrical power shows some slight differences among the Full, Holes and Rings configurations experimentally analyzed, as expectable when changing the cross-sectional area through which the current can flow. Table 4.4 compares the cross-section surface values, absolute and relative, for the three considered setups, together with the corresponding final density of the specimen. The relative surface area A_{rel} is normalized with respect to the conventional full-punch case.

The samples' density values reported in Table 4.4 were obtained through the Archimedes' method. The specimens were then cut to analyze the alpha silicon nitride content by means of XRD ($CuK\alpha$) measurements (Figure 4.9), and determine the local density distribution (Figure 4.10). We had anticipated that experimental techniques offer further possibilities of analyzing the topology and intensity of the radial thermal gradients. Since higher temperatures enhance densification, grain growth and transformation from alpha to beta phase, at least in the present material system, by observing the trends of these three parameters along the radial direction we can gain additional information to support our thesis.

Table 4.4 – Cross-section areas and final densities of the experimentally-implemented alternative punch configurations.

Configuration	A (cm²)	A_{rel} (%)	Density, ρ_{eff} (g/cm³)
Full	29,11	100,00	3,06
Holes	20,07	68,92	2,91
Rings	18,12	62,23	2,89

The alpha content quantitative analysis was performed with Autoquan (GE Inspection Technologies, USA) and according to the Rietveld's method. For all the three experimentally studied configurations the alpha content, acting as an indicator for the lower temperatures locations history (the lower the alpha amount, the longer the exposure to local overheating was), is in the range of 40% at specimen center, which is consistent with the temperature data retrieved from the controlling Pyrometer A, located very close to this position. With increasing distance from the sample central area, the values of alpha Si_3N_4 content show a decrease in every configuration, but the most significant reduction is shown in the Full case, evidencing the strong impact of temperature gradients on the final outcome's microstructure and local properties, while the Holes and Rings cases succeeded in lowering these disparities. This tendency is confirmed by the local density measurements results reported in the plot of Figure 4.10.

Together with the XRD technique, the local microstructure evolution was analyzed by Field Emission Scanning Electron Microscopy (FESEM) with a Zeiss Ultra 55, for all the three configurations. FESEM specimens were obtained from the sample's edge and central area. They were subsequently grinded and observed with an energy and angle selective backscattered electrons detector (ESB), which guarantees a good representation of silicon nitride thanks to the selective contrast between the main silicon nitride material and oxide additive phase. The relative images are shown in Figure 4.11.

At a first glance, one notices a non-negligible amount of residual porosity in every specimen. Recall that the quantity of additives was appositely augmented beyond the recommended values in order to hamper consolidation and obtain some extra data on thermal gradients. This also explains why the changes of porosity along the radial direction are less sharp than the ones of alpha phase, as Figure 4.10 shows.

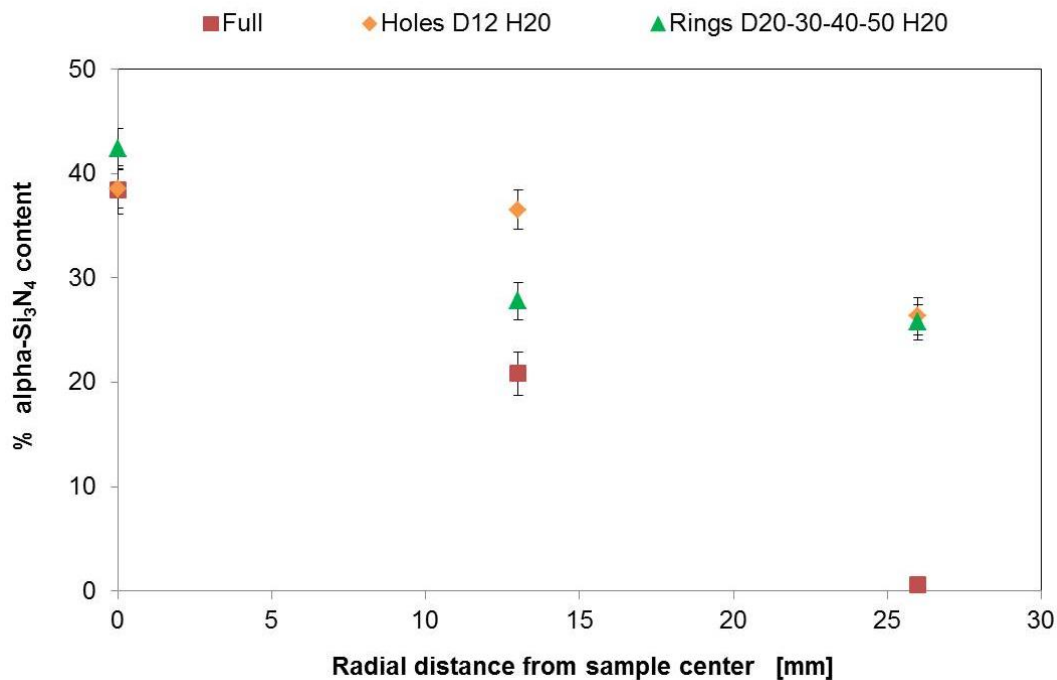


Figure 4.9 – Percentage of alpha-phase content along the radial direction in the silicon nitride specimen for the three experimentally implemented configurations.

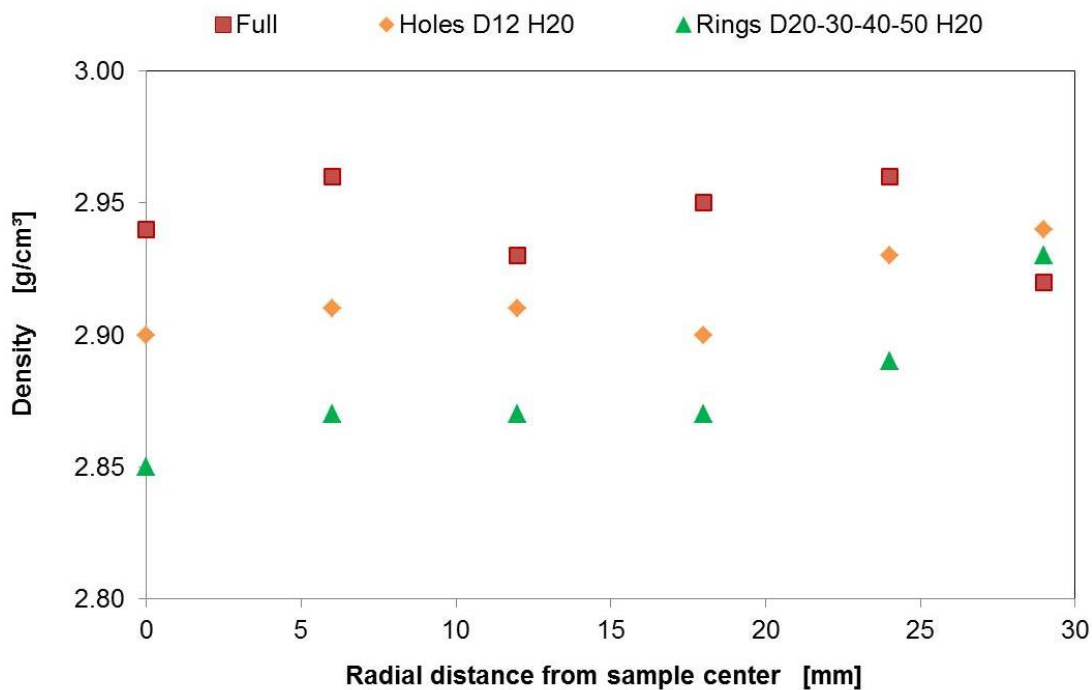


Figure 4.10 – Density along the radial direction in the silicon nitride specimen for the three experimentally implemented configurations.

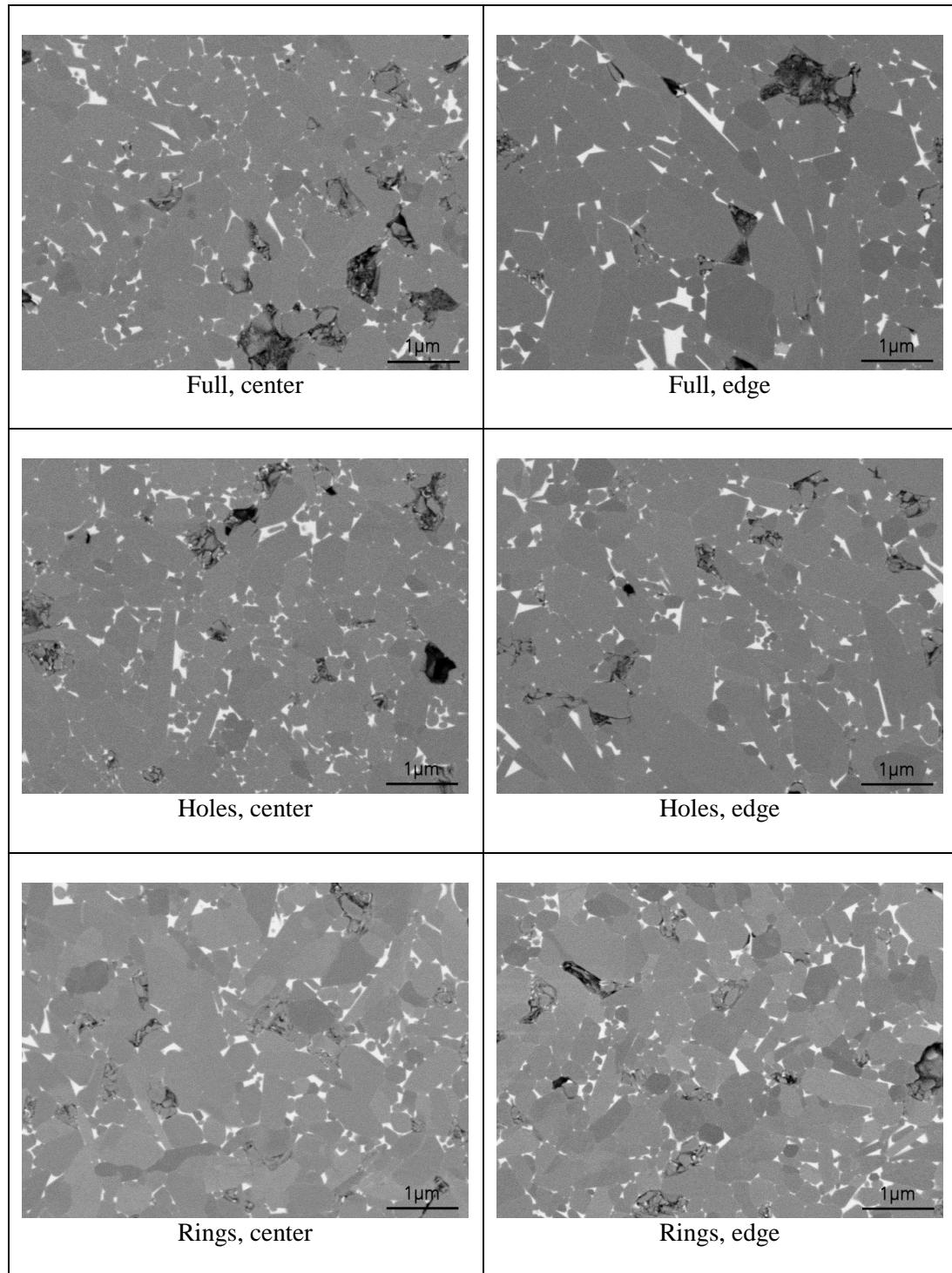


Figure 4.11 – SEM images of the microstructure at the center and at the edge of the specimens obtained with the three experimentally-implemented configurations.

Beside this aspect, for all the three configurations the sample central area shows larger grains, belonging to alpha phase, whereas the smaller elongated or hexagonal-shaped grains were the results of the dissolution-diffusion-precipitation mechanism leading to beta phase formation. The latter are located at oxide-phase rich areas (bright contrast region). The XRD analysis revealed that the amount of beta Si_3N_4 phase located at the sample center was not being altered when changing configuration.

In the Full configuration case, a 100% amount of beta phase was detected in the proximities of the edge, namely the area in which the highest local temperatures were located. Only for this configuration the micrographs reveal that a significant grain growth took place, by means of an Ostwald ripening process, while for the Holes and Rings configuration no significant difference in grain size was detected when moving along the radial direction. These microstructural characterization results are coherent with XRD measurement.

Therefore, from all the characterization techniques performed, the expected trends are confirmed. Overheating happens at the sample's edge, and it is particularly relevant in the Full punch configuration, being made evident by lower porosity values, larger grain sizes and higher amounts of the beta phase typical of elevated temperatures. All these effects are mitigated when repeating the analogous experiments with the newly designed punches.

The obtained combination of effects, namely an improvement in temperature and properties distributions accompanied by negligible modifications of the power output and final overall density when utilizing the modified punches, stimulated the planned broadening of our study. Room appeared to be left for further geometry optimization, aimed at both finding an ideal technological solution to the thermal gradients issue, and answering a series of interrogatives arisen in view of the phenomena described in this section - such as how current density and temperature non-uniformities are correlated, what material characteristics have a

stronger impact on heat transfer, how temperature distributes inside the whole cross-section of the specimen, what are the mechanical strength limitations to the punch geometry alterations.

Thus, we proceeded at running the FEM simulations associated with all the other values of the geometrical parameters D and H listed before. This broader part of the study allowed a refining of the geometry optimization process and a deeper understanding of the phenomena underlying the distribution of temperatures in the SPS tooling setup, together with an assessment of the impact of each of the parameters playing a role in the uniformization of temperatures, focusing in particular on the radial direction.

We analyzed the impact of these other new geometries by first of all looking at the temperature disparity among the two pyrometers during the isothermal holding time step. The results are reported in Figure 4.12 and Figure 4.13.

The denominations for the Holes case are based on the holes diameter D , while the Rings case allows a qualitative classification, based on the number of concentric ring-shaped holes. In the 2 Rings case, two combinations of the D parameter values were attempted, therefore they are distinguished by addressing one as “2 Small Rings” (D : 20-30-40-50 mm) and the other one as “2 Large Rings” (D : 18-32-38-52 mm). Note that this second punch design is the one, in the Rings category, in which most of the material is removed, even more than in the 3 Rings case.

The graphs are given following an order of decreasing cross-section area (larger amount of removed material) for both Holes and Rings, but in the latter case the first two configurations, 1 Ring and 2 Small Rings, present an equal value, meaning that the current density flowing through the interface is the same in the two cases, which therefore differ only for the current distribution inside the punches.

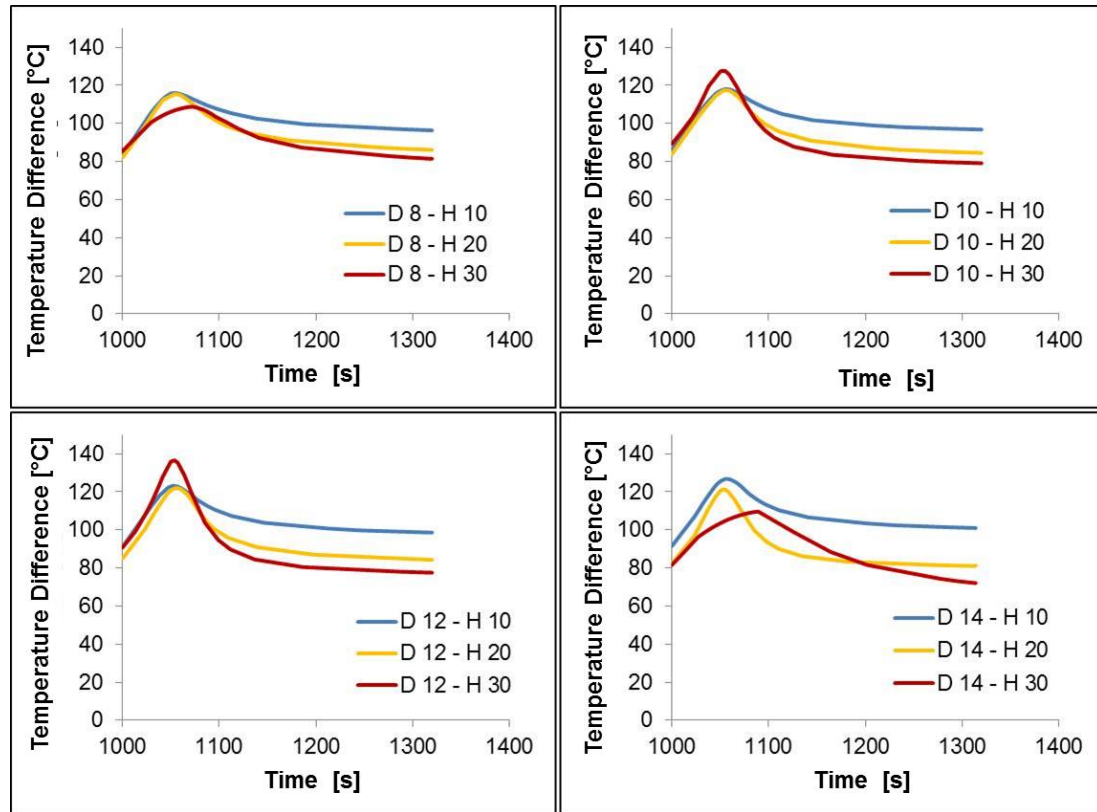


Figure 4.12 – Temperature disparity for the FEM-implemented Holes configurations.

By observing these plots, and in particular this last pointed out aspect, one can immediately infer how a more homogeneous current distribution has a significant beneficial effect on the lowering of the temperature disparities, while current density doesn't seem to play an important role. The first statement is a consequence of the comparison between the two upper plots in the Rings configuration: as mentioned above, 1 Ring and 2 Small Rings present the same cross-section area, but ΔT results to be higher in the former case. The impact of current density deserves a more careful analysis, which will be enounced later. Another immediate observation can be drawn with regards to the effect of a change in the holes' depth, since in all cases an increase in H leads to a decrease in the temperature gradients.

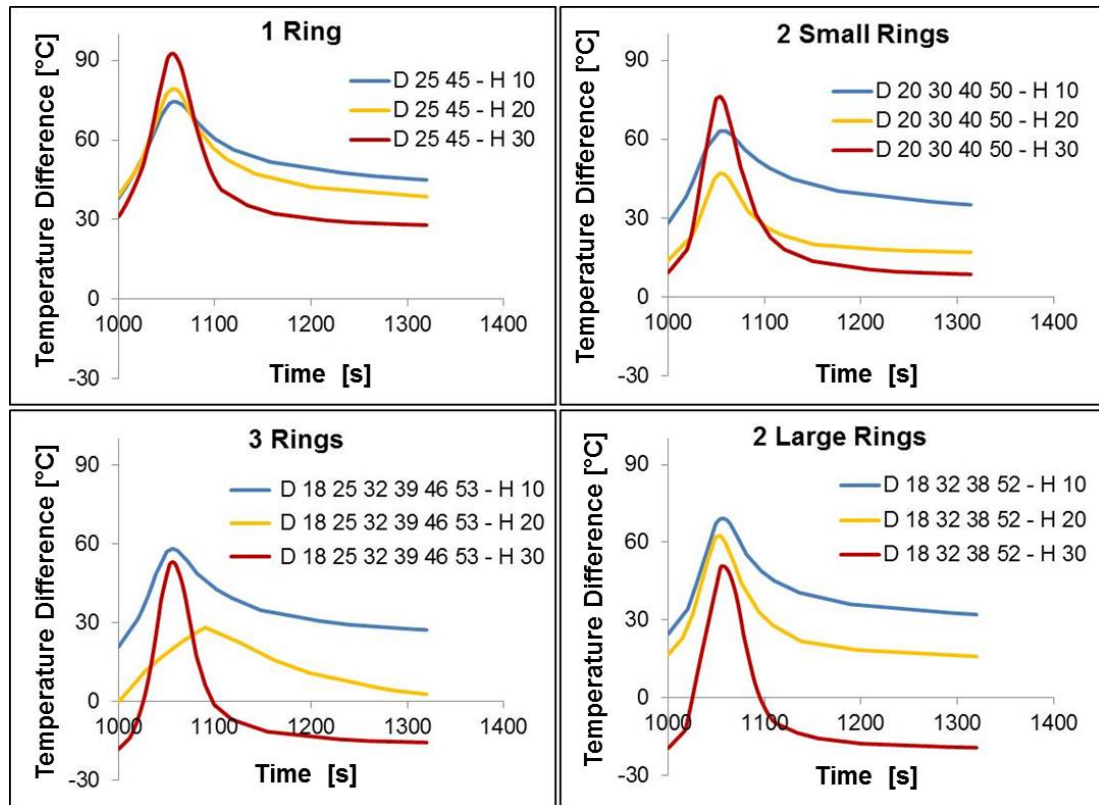


Figure 4.13 – Temperature disparity for the FEM-implemented Rings configurations.

A peak at the beginning of the holding time step appears in each plot. It is due to the current profile, given as an input and presenting the same kind of spike in correspondence to the end of the heating ramp. Such phenomenon is therefore unavoidable, since the reliability and repeatability of our computations required the same experimental electrical current input in every FEM simulation, and also because it was proven, both experimentally and numerically, how this trend was responsible for the preset temperature stabilization during the holding time step. A decreasing of this effect is, however, attainable by lowering the holes depth dimensions: in all the situations considered, an increase in H corresponds to an increase in the initial peak.

Figure 4.14 offers a summarized version of the previous graphs, which renders the optimization strategy individuation easier to identify. A specific time instant was chosen, $t = 1200$ s, corresponding to mid-holding, in order to compare the most significant temperature measurement for every implemented geometry. Here the most successful approach clearly appears to be the Rings, with its temperature disparity levels reaching values of 10 °C, or even negative ones.

This last aspect suggests interesting hints for a further improvement of the punch geometry, eventually able to annihilate ΔT completely. On the other hand, the Holes setup doesn't provide any decrease in ΔT higher than 40 °C with respect to the full-punch case. The impact of current density, current distribution and holes depth described above is thereby confirmed.

From this same figure, we infer how an additional slight change in the drilled holes configuration, in particular of their height, which is the parameter that appears to have the most immediate effect on temperature gradients within the SPS setup, could lead to even better results. By making a direct comparison between the three most promising designs (see Figure 4.15), namely 2 Small Rings with $H = 30$ mm, 2 Large Rings with $H = 20$ mm and 3 Rings with $H = 30$ mm, circled in the upper part of the same figure, one can select the configuration which is more prone to a final refinement of the geometry optimization.

Aiming at decreasing both the initial temperature peak and the current distribution inhomogeneities, the most suitable setup results to be the 3 Rings one, as the lower part of the same Figure 4.15 (ΔT vs. holding time) reveals.

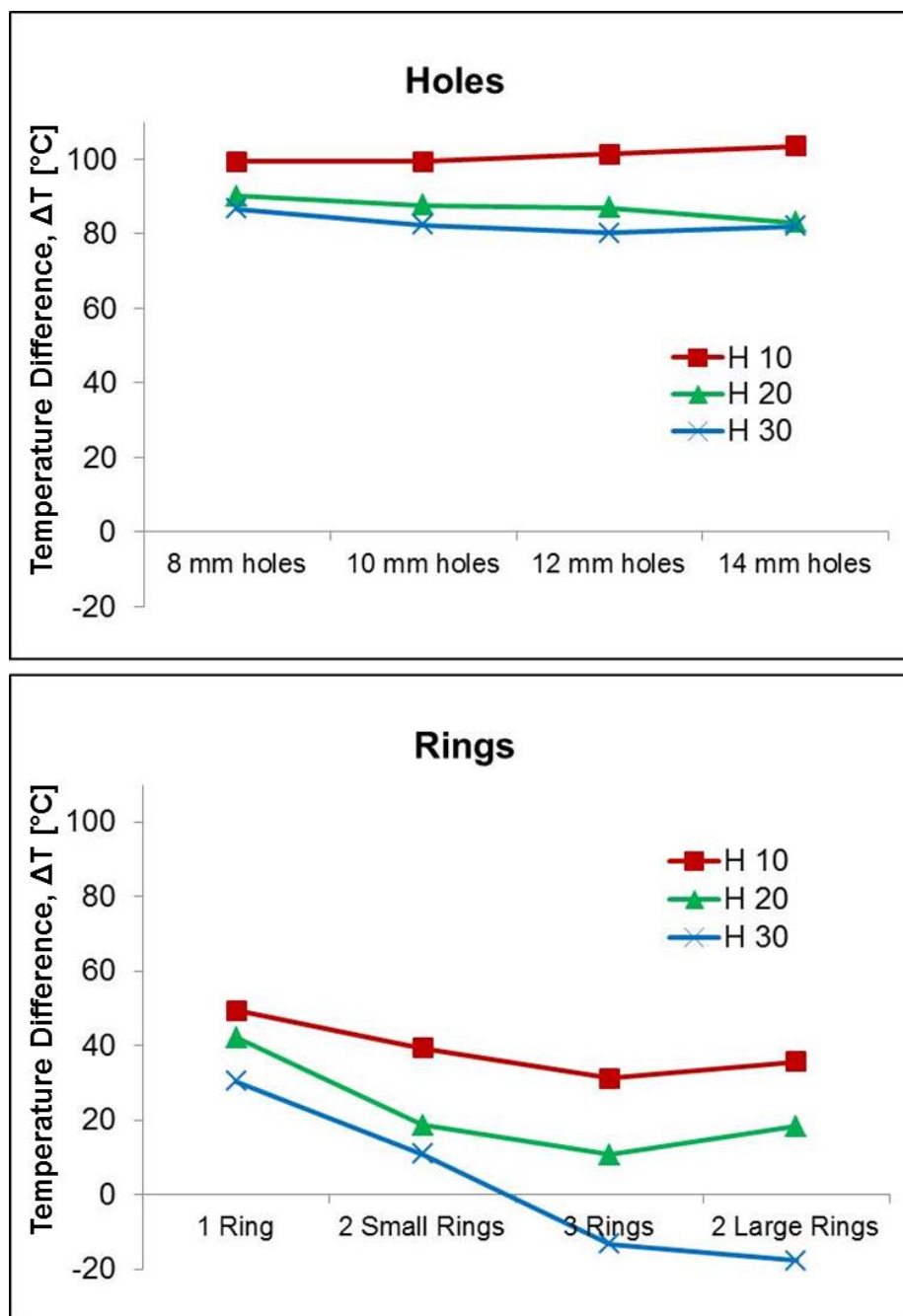


Figure 4.14 – Temperature disparities at mid-holding for the Holes (top) and Rings (bottom) configurations.

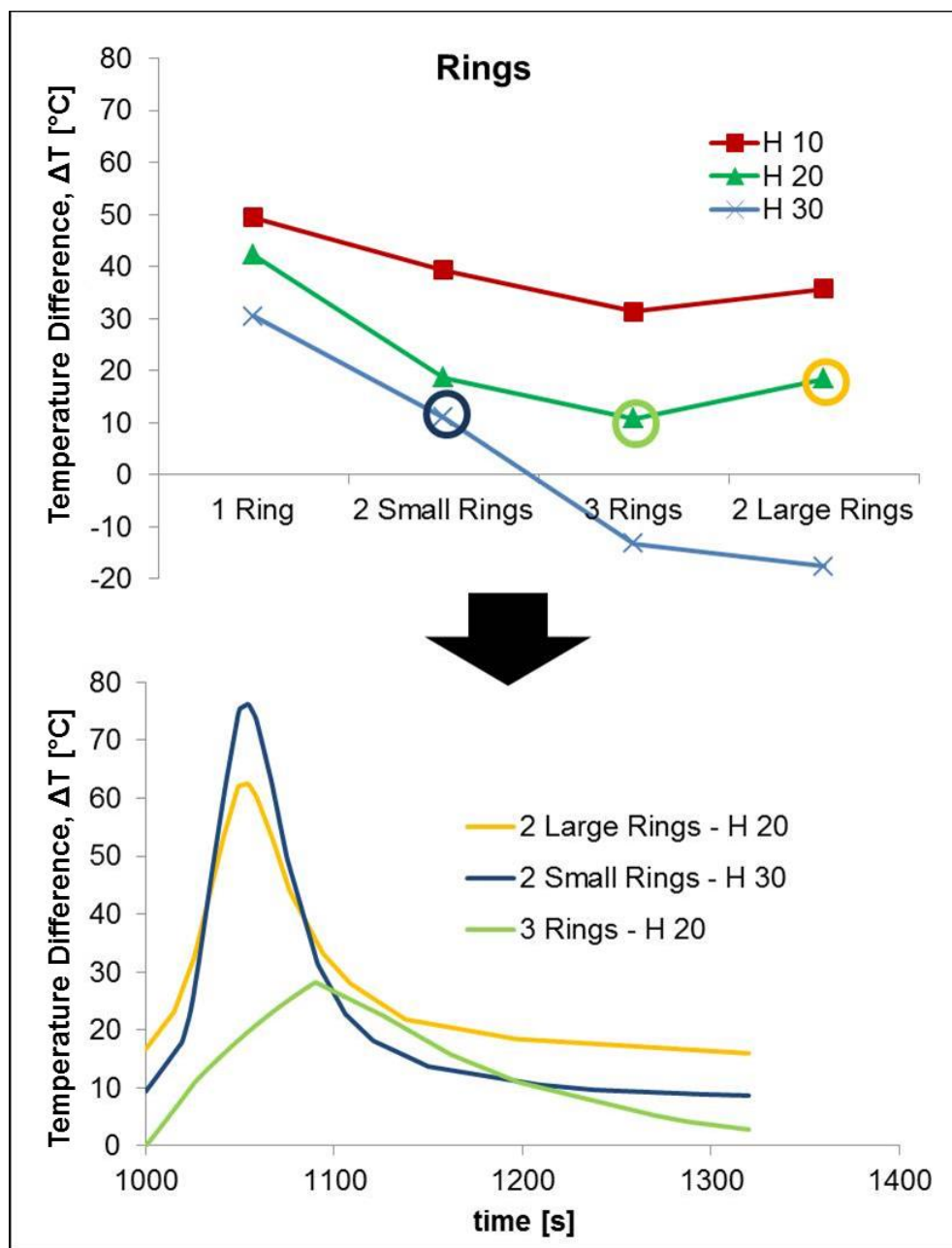


Figure 4.15 – Selection of the Rings configurations to be further investigated.

We therefore selected this 3 Rings case, represented by the green curve in Figure 4.15, and finalized the optimization process. The final stage of the punch redesign consisted in a trial-and-error procedure for calibrating both the H value and the current input. This last aspect, *i.e.* the manual correction of the current input, is due to the effects of a substantial change in the cross-section area available for the current to flow through. As stated before, up to this step of our study, the applied current was imposed to be equal in every case study, for comparison purposes. At this point, once the optimal configuration has been selected and requires only minor adjustments, the verification of the temperature evolution relative to Pyrometer A can show that such parameter doesn't follow the profile imposed by the SPS machine during experimental procedures (since we have not embedded a PID controller, for the reasons explained above). The conclusive outcomes refinement is therefore constituted by slight alterations of H (order of millimeters) and current (order of Amperes), until we obtain a finalized 3 Rings geometry, with $D = 18-25-32-46-53$ mm and $H = 23$ mm.

Figure 4.16 reports both the graph with $T(A)$ and ΔT , and the complete optimized tooling setup, as it looks in the COMSOL® interface. The temperature profile of the leading pyrometer is brought back to the desired value of 1750 °C, and the temperature disparity with respect to Pyrometer B is reduced to approximately zero.

Recall, nevertheless, that neither point A neither B belong to the specimen, they are simply located in its vicinity. This is where the other valuable feature of FEM in spark plasma sintering analysis comes into play, namely the reconstruction of the complete temperature mapping, in any cross-section, or more generic location, and at any time instant of the process. This is valid for any other simulation parameter also, but we will focus on thermal distributions for now, and specifically on the radial temperature map in the central cross-section of the specimen. Figure 4.17 shows this mapping (temperature in °C), which is also an effective representation of the beneficial effect of the novel punch configuration. The plots of

the radial temperatures at this central section are given for the original Full-punch setup and for the present modified 3 Rings case. The graphs refer again to $t = 1200$ s, mid-holding. The use of the same color scale for the legend shows how strong the impact of the tailored holes is.

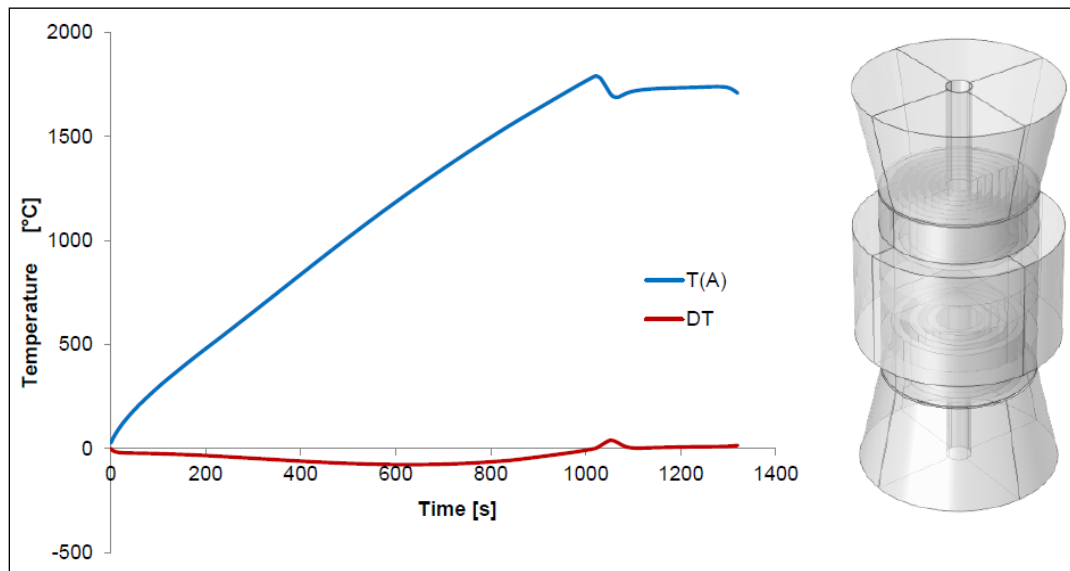


Figure 4.16 – FEM- derived temperature profile and temperature disparity of the optimized 3 Rings configuration.

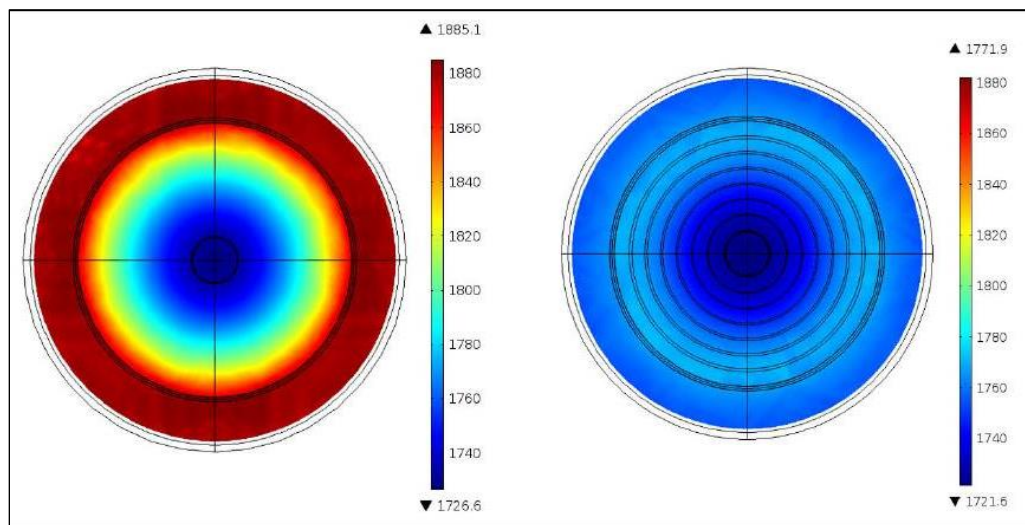


Figure 4.17 – FEM-derived temperature distribution ($^{\circ}\text{C}$) in the central radial cross-section for the Full and optimized 3 Rings configurations.

This final design of the punch was also experimentally implemented. Figure 4.18 shows the complete SPS tooling setup as it looks once the novel punch has been inserted. Figure 4.19 represents two punches geometries, the conventional one on the left, and the optimized 3 Rings one on the right. The central hole for the measurement of temperature by pyrometer A is identical, as all the other geometrical parameters, with the only addition of the three concentric ring-shaped holes. These holes obviously need to be in contact with the spacer and not with the specimen (even with the interposition of graphite paper), in order not to alter the compaction conditions, especially when an external pressure is applied. Notice, thus, that the presence of these rings holes imposes a specific path for the electrical current to follow, which excludes the drilled zones. This translates in a current flow that is obliged to avoid certain areas of the punch adjacent to its edge (external ring-holes) through which it would normally tend to pass, and supposedly be deviated towards the graphite “channels”, as we can define the bulk material between the holes, that are closer to the axis of symmetry. A shift towards the setup’s center of the Joule heating effects is obtained, and therefore the edge overheating is mitigated, by distributing the high temperatures more homogeneously. This positive outcome is obtained even though the holes in the punch are not through cavities, both to preserve the component’s integrity and to leave the contact surface with the sample plain and smooth. Nevertheless, imposing to the current such a preferred path at least for the 23 mm of the holes’ depth still allows a more powerful Joule effect around the center of the specimen, since we are keeping the electrical flow in the vicinity of the axis for a longer distance (counted from top to bottom) than in the conventional case. Such principle of current focus towards the setup center will be further explored in the next section, after we experimentally assess the effectiveness of the present geometry.

The experiments were performed again with analogous conditions and confirmed the beneficial effects of the drilling of three concentric ring-shaped holes in the punches in order

to mitigate the radial thermal gradients throughout the cross-section of the specimen. The same process was conducted three times, in order to ensure the reliability of the results obtained. In this specific phase, certain requirements in the SPS machine's utilization imposed the interruption of the process earlier than in the previous cases, a few minutes after the beginning of the isothermal dwelling time. The previously run campaign ensured that ΔT , $T(B)-T(A)$, maintains a constant value during the isothermal phase (see Figure 4.8), therefore allowing for an extrapolation of the data for the entire duration of the holding time.

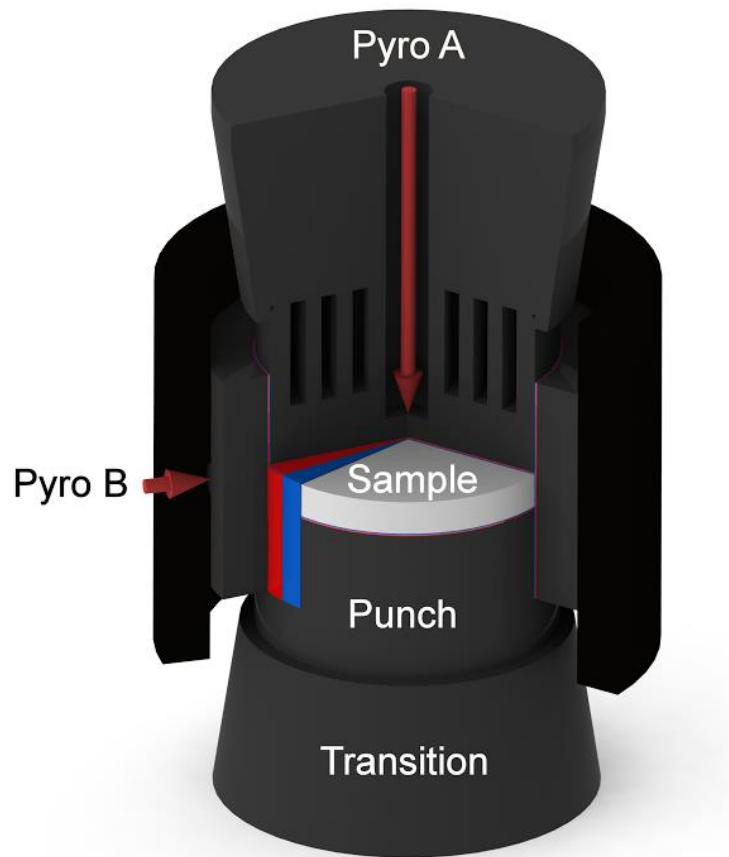


Figure 4.18 – SPS setup with the optimized 3 Rings punch.



Figure 4.19 – Comparison between the Full and optimized 3 Rings punches.

Figure 4.20 shows the extrapolated results for two of the three experiments run with the optimized punch configuration (three rings), compared to the data relative to a conventional Full configuration. It is worth mentioning that the third run results, not explicitly extrapolated in the graph, if shown, would have been located in between the other two curves. The successful application of the three-rings setup is evident in the ΔT values ranging between -5°C and -11°C , compared to the $\Delta T=115^{\circ}\text{C}$ relative to the conventional full-punch case, which in modulus are even lower than the values obtained experimentally for the Holes and the 2 Rings configurations. Such results prove what inferred from the finite-element simulations.

It is interesting to point out in this second set of experiments too that the novel optimized setup does not present any significant difference in terms of the densification behavior with respect to the conventional full punch case, as shown in Figure 4.21. The plot provides densification data during the heating ramp, by means of displacement (in absolute value) of the top punch along the axis of the setup, for the full punch case and the three runs with the optimized tooling, which all appear to have coincident trends.

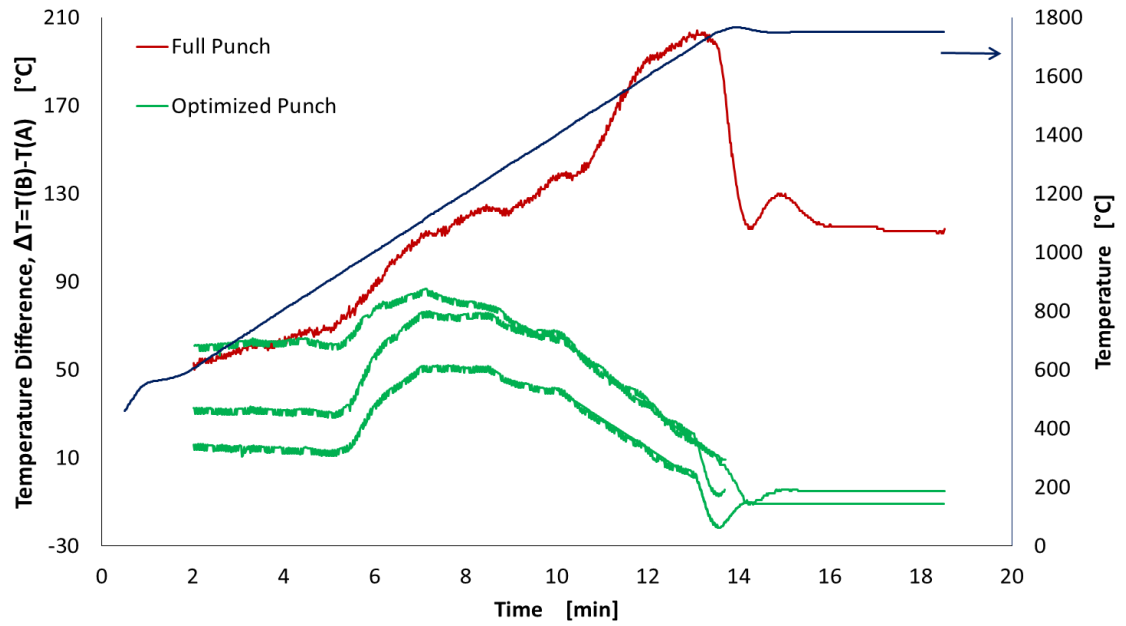


Figure 4.20 – Experimental verification of the temperature disparity with the optimized 3 Rings configuration.

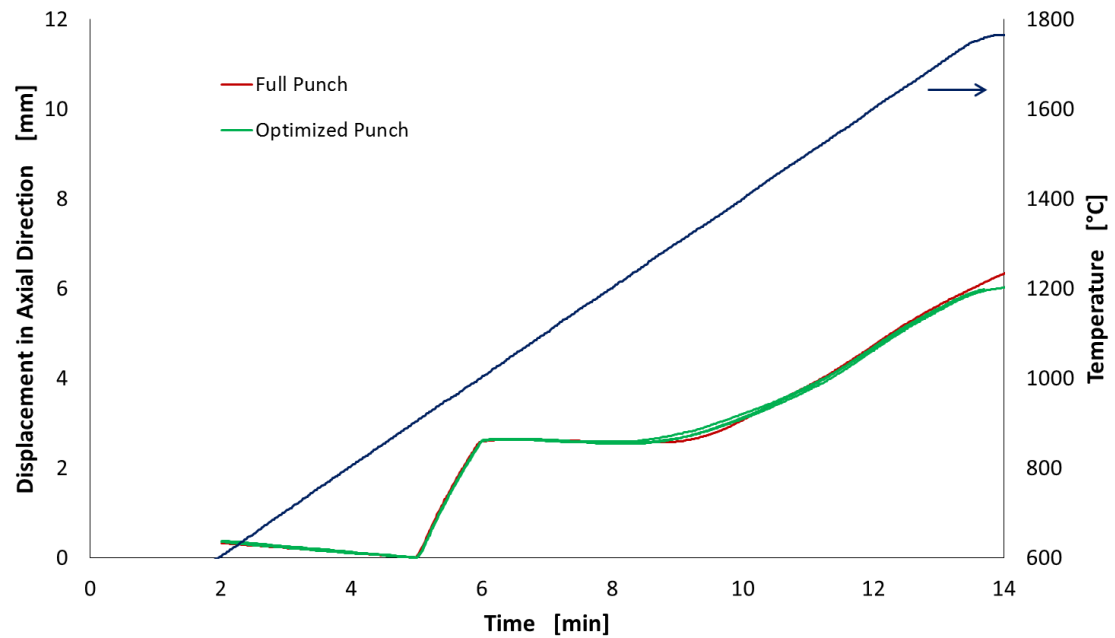


Figure 4.21 – Axial displacement during experimental procedures with the Full and optimized 3 Rings configurations.

On the other hand, while the behavior of the conventional and optimized setups coincides as far as the SPS route is concerned, the same again does not hold for the power input required to reach the pre-set temperature regime. The optimized 3 Rings punch is endowed with a smaller cross-section area, namely 17.53 cm^2 , which corresponds to an A_{rel} value around 60% of the 29.40 cm^2 of the conventional full-punch case. Consequently, current density is automatically increased thanks to the new geometry, and a lower electrical power is sufficient to attain the scheduled $1750 \text{ }^\circ\text{C}$ at the leading pyrometer A. Referring to the dwelling time-step, in which the machine readings can be considered stabilized, the input is reduced from 26 kW (4.7 kA) to 21 kW (4.1 kA), an appreciation factor when considering more extensive productions of components via SPS technologies. Such input power reduction effect implies that the optimized punch configuration, characterized by a set of thin concentric rings with dimensions that can be tailored through numerical modeling, represents a well-balanced combination of current density increase and redistribution along a pattern capable of diminishing temperature differences in the resized cross-section itself.

We have now collected a sufficient amount of experimental and numerical data to discuss the identification and impact of the phenomena influencing temperature non-uniformities within a spark plasma sintering tooling setup. From the obtained results several conclusions can be drawn. The main factors affecting the temperature gradients resulted to be heat capacity, surface radiation, current distribution and current density.

The heat capacity of a certain component can be qualitatively defined as its “thermal mass”, the heating storage capability of such domain, whose diminution revealed to be an efficient method to mitigate the thermal inhomogeneities within the entire tooling.

Surface radiation has proven to act efficiently when temperature peaks manifest during SPS procedures, since an increase in the area of the outer surfaces of the tooling corresponds to a more extensive amount of material exposed to an environment kept at room

temperature. This is quantitatively explained by looking at the Stefan-Boltzmann equation (4.6) relating irradiated heat and temperature disparity between thermal source and destination, in which temperatures appear at the fourth power. By drilling holes inside the punch, we have automatically increased the amount of the tooling setup's external surfaces radiating, and therefore releasing, heat. It is interesting to notice how, even though these holes act as closed cells not in immediate connection with the environment kept at room temperature, they are sufficient to mitigate localized overheating, probably thanks to the emissivity properties of graphite. This conclusion has been assessed by running some simulations with and without the corresponding boundary condition. The temperatures obtained showed variable differences, typically of the order of magnitude of tens of degrees centigrade. Higher temperatures were reached in the case of absence of surface radiation, with consequent changes in the disparities among the two pyrometers. We nevertheless consider such effect not to have an influence as significant as the other factors here listed, because of the abovementioned closed nature of the holes created. A quantification of this result can be the object of further investigation.

Current distribution, as introduced before, influences thermal gradients by lowering the non-uniformities when directed in such a way to result in more spatially homogeneous temperature distributions. Here we strictly refer to the Rings configuration, which, indeed, is also the one that showed the most promising results and a series of possibilities of fine tuning and further optimization. Spatial homogeneity of the current distribution translates in the choice of a pattern of ring-shaped holes consisting of a higher number of thin holes (in the radial direction), instead of a single large one that drastically separates the current flow into two branches running far from each other, one close to the center and one to the edge of the component.

Current density deserves a more careful analysis. In the plots reported in Figure 4.12, Figure 4.13 and Figure 4.14, at a first glance, a change in the current flow density, consequence of an alteration of the cross-section area, seems not to have a significant effect on temperature disparities. Nevertheless, from the considerations listed above, one can notice how a modification of the punch radial cross-section area leads to several simultaneous effects. A reduction of this area, indeed, which is an immediate consequence of the drilling of holes, corresponds to an increase in the overall outer boundary surface area and, more importantly, to a decrease in thermal mass, both beneficial for a lowering of thermal gradients. At the same time, we have a detrimental effect of increased current density, to which localized Joule heating phenomena are proportional. This enhancement of the Joule effects would tend to lead to local peaks of temperatures, but the augmented surface radiation and the diminished heat capacity hamper the verification of such thermal gradients. Therefore it would be incorrect to address radial cross-section area modifications, or, alternatively, current density changes, as ineffective or negligible, since we are instead having a combination of three different effects that end up compensating each other.

Consequently, a comprehensive punch geometry optimization procedure can be operated on different levels, individually or simultaneously implemented. A holes height increase has two advantageous consequences, namely an augment in boundary surface and a diminution of extra thermal mass, without presenting the downside of excessive current density localization. A more homogeneous current flow throughout the punch can be created by providing for the selected material's removal in the form of an increased number of thinner concentric ring-shaped holes. The cross-section area parameter will, on the other side, need to be carefully tuned in order to obtain desirable outcomes. Notice how all the redesign procedures have been based on the Rings configuration, thanks to both its versatility and its distinguishing ability to achieve consistently improved results with respect to the Holes setup,

by removing equivalent quantities of graphite. The Holes configuration, indeed, does not allow a precise control of the current flow path, as instead the Rings case does. In the former, we are simply removing some extra quantity on unneeded mass, while focusing the current towards the center in an imprecise way. In the latter situation, we are sure of where the current is going as long as the holes are present in the cross-section, and we are postponing the current's sharp deviation from the center to the die wall until a zone that is much closer to the specimen itself than it was in the Full and in the Holes cases.

At this point it is also important to point out that our results have been experimentally validated based on temperatures recorded by the two pyrometers, while a prosecution of the study is needed in order to obtain a completely satisfactory correspondence for the porosity distribution. In the experimental procedures section we explained that oxides had been added to the powder specifically to hamper densification and therefore individuate more clearly the radial thermal gradients patterns. The effect of these additives is complex and could not be reproduced in our simulations. Nevertheless, we chose to incorporate porosity and the relative densification equation in the simulations, since we believe that this guarantees a better adherence to reality than considering a bulk compact. Interestingly, experiments revealed that the evidence of thermal gradients lied significantly more in the alpha/beta phases and grain size distributions (Figures 4.9 and 4.11) than in the density distribution (Figure 4.10).

At this point, the successful novel punch design application has been assessed both numerically and experimentally. Principles and qualitative guidelines have been individuated in these last discussion paragraphs. We pointed out earlier that in the just concluded stage of geometry optimization we were minimizing the amount of variables by keeping the two dimensional parameters D and H (diameter and height of the various holes) constant in each setup. At the same time, we have shown how effective the idea of focusing the current flow along the axis is when trying to heat up the sample's center and reduce the edge overheating.

Delaying as much as possible the current passage exclusively inside the die's wall is a convenient method, and thus one can tailor the Rings geometry accordingly.

Having identified the phenomena playing a role in the temperature redistribution, and gained a more complete knowledge on how to control them, room is left for a more refined optimization process. We therefore remove the limitation of keeping D and H constant in the setups, and explore the possibilities of linear change of the holes dimensions along the radial direction.

The following section will describe this and more strategies for improving the effectiveness of the punch design alterations. A second option will be found in the selective coating of the punch's surface with suitable insulating materials. Both the optimization routes described in 4.1.1.4 are purely numerical, since at this stage of the study we can consider the reliability of our FEM framework as broadly confirmed.

4.2.4 FEM analysis of further developments for the novel punch design

We will start by treating the further geometrical optimization first, and only later we will mention the alternative option of not drilling any holes and replicating their effects by coating opportune areas of the punch's surface.

For coherence with the rest of the optimization study, the same silicon nitride powder was considered as starting material. When dealing with an insulating powder compact, we have shown how, since the current flows through the die instead of through the specimen itself, the former tends to reach higher temperatures, while the sample experiences a radial thermal gradient, with temperatures decreasing from the edge towards the center of the powder compact. In order to mitigate this effect, one can design precise strategies aimed at focusing the electric current towards the center of the specimen.

A more refined method to implement this solution consists in tailoring the geometry of the punches along the radial direction, in such a way that the amount of graphite-mass constituting the tooling component goes decreasing with the distance from the axis of symmetry.

Two possibilities arise: a progressive increase in the ring-shaped holes thickness along the radial direction, with constant distance among them, or a gradual decrease in the distance among the holes, while keeping their radial thickness constant. The punch cross-section dimensions (62 mm diameter) do not allow a wide variety of changes in the geometrical parameters, even though an investigation on the two above-mentioned options already provides a set of interesting data. The geometries of the two cases are given in Figure 4.22.

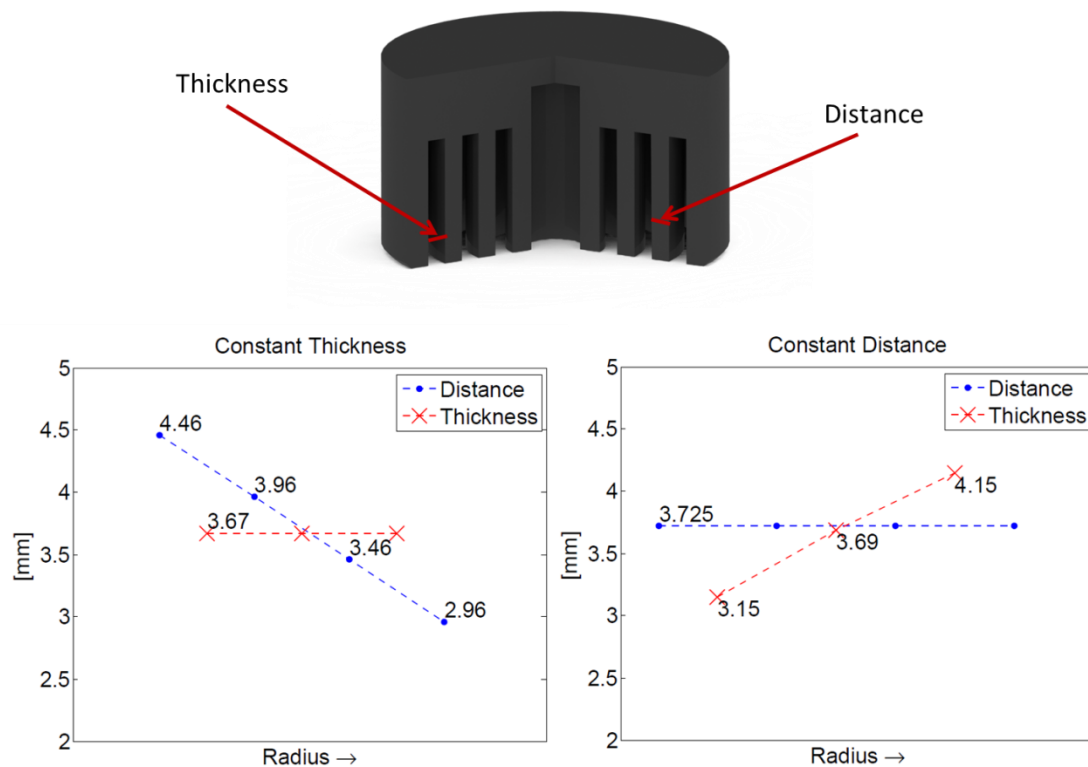


Figure 4.22 – Geometrical parameters along the radial direction for the Constant Thickness and the Constant Distance configurations.

In both cases the holes' depth was set to be 20 mm, the intermediate value of our previous simulations campaign, which resulted to be the best compromise solution between lowering the gradients and preventing the temperatures peak at the end of the heating ramp.

The two options were designed in such a way that the overall cross-section area was kept constant, in order to render the results independent of this geometrical parameter, whose effects resulted to be difficult to regulate. The two punch configurations investigated here will be denominated Constant Thickness and Constant Distance.

In order to maintain coherence with the antecedent part of the work and the experimental results discussed in the previous section, we keep $\Delta T = T(B) - T(A)$ as leading parameter for the optimization procedure. Figure 4.23 provides the plot for the ΔT profile of the two configurations during the holding time-step.

The tailored radial gradient of the geometrical parameters results to be an efficient solution in order to eliminate the heat concentration in the die. The temperature disparity among the two pyrometers switches from the 115°C of the conventional setup to -30°C and -10°C, for the Constant Thickness and Constant Distance configurations, respectively, a significant improvement in both cases. The Constant Distance case, in particular, produces the best outcomes.

Linearly increasing the holes' thickness along the radial direction, thus, results in a beneficial effect of electric current density redistribution tending to uniformize the temperatures. Notice, though, that the attained values of ΔT , in absolute value, are comparable to the ones that we were obtaining when keeping D and H radially constant, especially in certain 2 and 3 Rings applications.

It might seem, then, that such technological effort in linearly changing their values within the same setup is an unnecessary complication. But one has to take into account that what we are trying to obtain here is a series of general guidelines for the optimization of the

SPS tooling geometry in order to remove the undesired thermal gradients, which, it is important to recall, are raised when increasing the size of the specimen that we are sintering. The verification that this linear change of the parameters has beneficial effects in mitigating the disparities is therefore another important result that can be applied to any other case of SPS of large size samples, and will probably gain growing attention when higher values of powder compact diameters are considered.

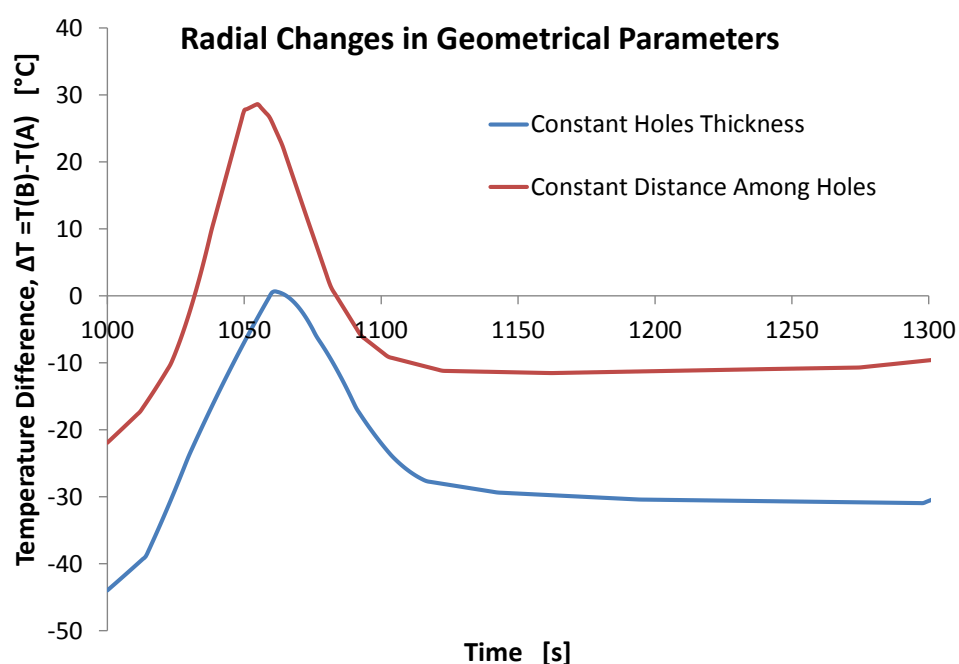


Figure 4.23 – Temperature disparity for the Constant Thickness and Constant Distance configurations.

Another possible objection to the optimization procedure described in this section could lie in the high grade of precision required to practically implement the geometries described above, since the dimensions selected impose very narrow tolerance ranges. But again, the focus of the present study consists in developing a better understanding of the phenomena underlying temperature inhomogeneities in SPS tooling, specifically of the role

played by the electric current flowing through the setup during the process. Manufacturing feasibility is temporarily sacrificed to the intent of individuating some general principles, which would subsequently draw guidelines for the design of optimal punch configurations on even larger scales, in which more room is allowed for the delineation of solutions both appropriately tuned and technologically inexpensive.

With this we can consider our “holes-drilling” optimization strategy satisfactory, and consider a different possibility of tooling improvement. We have mentioned earlier that the production of such tailored cavities in the punches was tolerable from the component’s strength viewpoint, as both experiments and simulations confirmed. The loads for which this outcome was obtained, though, were only the ones that had been initially chosen for this specific sintering route and for silicon nitride, namely ranging between 8 and 50 MPa. One can thus wonder if there are temperature uniformization strategies that would guarantee the integrity and absence of deformation of the punch even when higher loads are applied.

An interesting option was individuated in the tailored selective coating of the top surface of the punches with an insulating material. By top surface we denote the one in contact with the spacer and not with the specimen, since we conventionally refer to the top punch in the tooling assembly. Obviously, as in the previous cases, both punches need to be identical and symmetrically mounted with respect to the central cross-section, in order to guarantee the homogeneity of the results. This procedure, provided the coating itself can resist to the applied pressures, does not require any mechanical weakening of the punches, since there is no graphite removal involved.

Such conclusions were reached during the progress of the work and not ahead of it. This motivates the investigation procedure that is about to be exposed, in which the usage of the coating is first applied to the Rings cases instead of a bulk full punch. Being the outcomes of the coated Rings configurations particularly striking, we choose to report them in detail too,

together with a complete exposition of how the study evolved based on the simulations results reached at every step.

The material to be utilized for the coating has to be endowed with a series of thermal, electrical and mechanical specific properties. It has to be insulating with respect to the tooling constitutive graphite, both electrically and thermally, be able to form a continuous resistant coating layer, do not react with the adjacent material and preserve all these characteristics until the elevated temperatures typical of spark plasma sintering. A promising solution was found in hexagonal boron nitride (hBN).

Boron nitride owns a graphite-type, hexagonal structure of 2-dimensional strong covalent bonding of boron and nitride atoms (sp^2 hybridization) but shows weak bonding in between two planes. High electrical resistivity even at elevated temperature combined with good thermal conductivity ($\sim 30\text{W/mK}$) as well as low density ($2,27\text{g/cm}^3$), a low coefficient of thermal expansion and good thermal shock resistance, are among the reasons for which this material is extensively used for high temperature applications. Its characteristics of good machinability and low values of compressive and bending strength, due to its lamellar structure, render it comparable to graphite. Hexagonal boron nitride is available as coating, which is the form utilized in the present study.^{260, 261}

As a natural continuation of the previous outcomes, we thought of applying the hBN coating to the all Rings cases (1 Ring, 2 Small Rings, 2 Large Rings, 3 Rings) with $H = 20$ mm, in order to see how the thermal disparities obtained in those cases were altered if we isolated the most external ring, still with the purpose of focusing the electric current towards the center of the setup. The coated punches implemented in the simulations are shown in Figure 4.24, where the hBN layer is highlighted in red. Be reminded that setups (a) and (b) of this same figure, 1 Ring and 2 Small Rings, share the value of overall cross-section area, only

differently distributed. Thus they have the same current density, but the flow is organized along a distinct path.

The thickness of the coating layer was $100\mu\text{m}$. It is important to mention the fact that boron nitride can also be deposited in thicker layers. When we reach the order of magnitude of some millimeters, in order to avoid the presence of a little step, namely a ring longer than the others in the axial direction, it is possible to remove the necessary amount of graphite with some machinery and then replace it with the desired thickness of hBN. In our case, with a the maximum applied pressure of 50 MPa, this would be a pointless technological complication, but it is an important consideration for cases in which higher loads need to be applied, which could crash the thin layer and render vain its own presence.

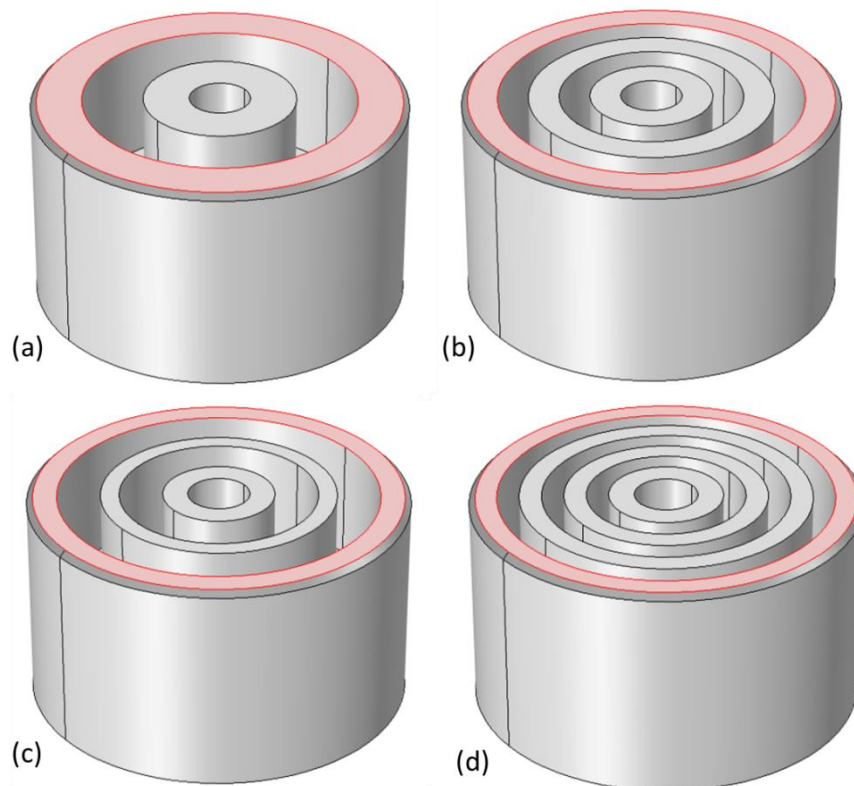


Figure 4.24 – FEM-implemented Rings configurations with boron nitride coating deposited on the external ring.

In our SPS route context, the effects of the deposition of a thin layer on such external ring have been analyzed for a variety of cases, changing the number and dimensions of rings.

The same modeling approach was utilized, namely a set of FEM simulations with the same coupling of electric currents, Joule heating, sintering mechanics and densification mechanisms. Initial, contact and boundary conditions are coincident with what described in the geometry optimization section, with the only addition of a contact boundary condition aimed at reproducing the effect of the hBN coating. The boron nitride properties needed to describe the behavior of such coating were derived through numerical regression from experimental data^{262, 263} and are reported in Table 4.5.

Table 4.5 – Hexagonal boron nitride properties.

Theoretical density, ρ_{th}	2280 $\left[\frac{kg}{m^3}\right]$
Electrical resistivity, r_{el}	$1.53 \times 10^{15} - 7.29 \times 10^{12} T + 1.42$ $\times 10^{10} T^2 - 1.42 \times 10^7 T^3$ $+ 7.69 \times 10^3 T^4 - 2.15 T^5$ $+ 2.43$ $\times 10^{-4} T^6 \quad [\Omega \cdot cm]$
Heat capacity, C_p	$-362.41 + 4.21 T - 0.01 T^2 + 1.69$ $\times 10^{-6} T^3 - 3.25$ $\times 10^{-10} T^4 + 1.89$ $\times 10^{-14} T^5 \quad \left[\frac{J}{kg \cdot K}\right]$
Thermal conductivity, k_T	80 $\left[\frac{W}{m \cdot K}\right]$
Emissivity, ν_{rad}	0.85

Figure 4.25 depicts the evolution of the temperature difference ΔT during the holding time for the four cases investigated. The results show a surprisingly strong effectiveness of the hBN coating in redistributing temperatures in the radial direction. The aim of increasing the Joule heating effects at the center of the sample while lowering the peaks at the outer edge is reached and widely overcome, since ΔT is now negative, but very high in modulus. The absolute value of ΔT augments as the coated area is increased, reaching a peak of -400°C for the 1 Ring case. Even though the 1 Ring and 2 Small rings cases share the same cross-section area value, the latter presents a lower disparity, confirming that allowing the current to flow through two thinner rings instead of through a larger central one plays an important thermal homogenization role. The 2 Large Rings case has a lower cross-section surface area and this is why the disparity between point A and point B is so relevant, together with the previous considerations on the consequences of the uneven distribution of the current flow.

In general, significantly negative ΔT translates in an overheating of the specimen's center, which is obviously an undesired effect. Values of the order of magnitude of several hundred degrees imply that the outer area of the powder compact does not even undergo sintering phenomena.

The abrupt shifting of the radial thermal non-uniformities from highly positive values for the conventional Full punch configuration to highly negative ones in the present cases provides some indications for the design of an intermediate solution.

It appears clear how by covering the entire extension of the external ring, whichever the selected number of rings is, creates a current-insulated area which ends up being too wide, since one has to take into account that the adjacent area, moving inward in the radial direction, constitutes one of drilled holes and is therefore itself insulated too. Such phenomenon provides an even stronger evidence of what discovered in the antecedent part of the study, *i.e.* the beneficial effects of a more homogeneous current distribution throughout the entire

punch's volume, preferable to a sharp channeling of the current flow along paths separated by a larger distance.

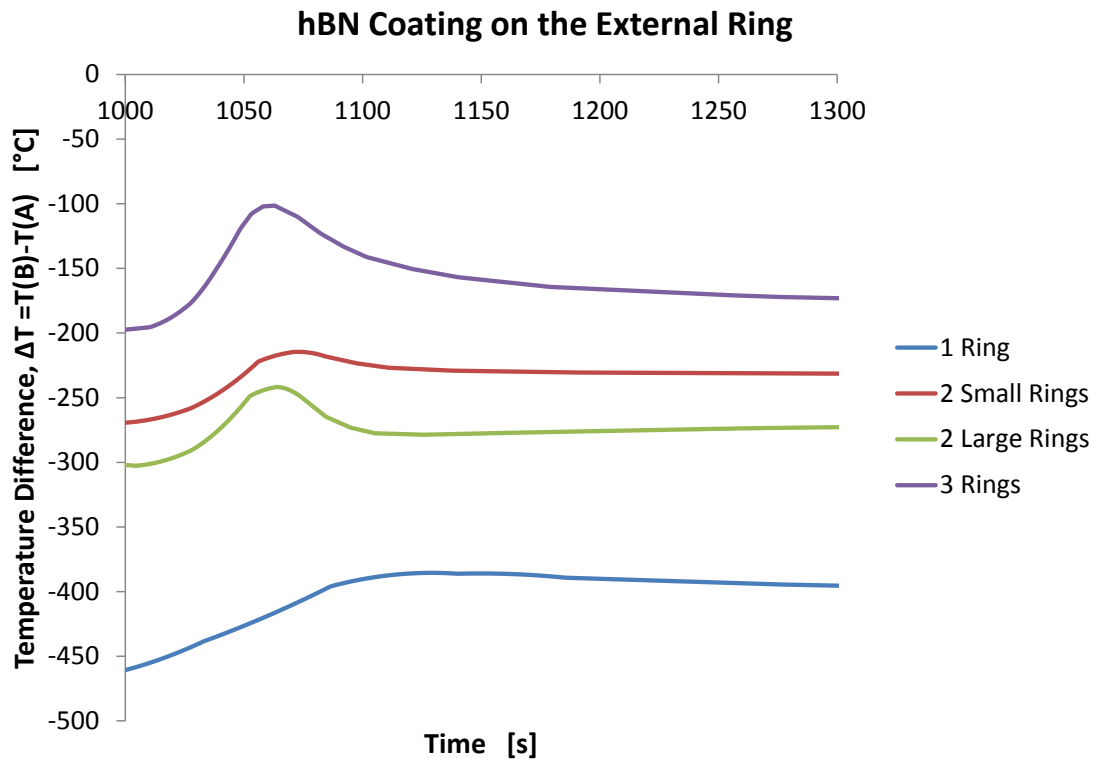


Figure 4.25 – FEM-derived temperature disparity for the BN-coated Rings configurations.

An improved approach was then associated with the idea of only partially covering the outer ring with the hBN layer. The first attempted simulation, applied to the 3 Rings case (as the one presenting the least extreme results) by coating half of the external ring, presented only a slight gradient mitigation, with a ΔT decreased, in absolute value, of around 30°C , with respect to the complete external ring coating of the same geometry.

As a consequence, a more radical strategy was applied: the 1 Ring case was considered, this time for being the setup showing the strongest temperature disparity, with a reduced holes depth (10 mm), in order to lower the beneficial effects of surface radiation and

thermal mass reduction, while at the same time increasing the overall compression strength of the punch, a factor of appreciation when applying higher loads during the SPS procedure. Such configuration did present an improved temperature distribution, with a $\Delta T = -27^{\circ}\text{C}$, although still not completely satisfactory.

From this second set of finite-element modeling-derived data the extremely high impact of hBN coating on the Joule heating effect distribution was confirmed. Some difficulties in controlling the temperature evolution and distribution by means of the combination of boron nitride coating and drilling of ring-shaped holes arose. This manipulation complexity lies in the coexistence of numerous factors playing contrasting roles. Geometry modifications create alterations in the extent of surface radiation, heat capacity, current density and distribution, while the hBN coating's peculiar properties are temperature-dependent, rendering the punch design process to be non-intuitive.

Excluding for the purposes of this study the possibility of investigating on alternative materials to be employed for the coating, an optimal solution could be found in the isolation of the boron nitride influence, by applying it to the conventional full-punch tooling setup.

The results obtained for the coated rings cases, characterized by high thermal gradients with an opposite trend along the radial direction even when only a thin portion of the external ring was covered by a layer of hBN, inspired the idea of utilizing this same boron nitride coating on the conventional full-punch configuration, which had shown a ΔT above 100°C during the holding time-step.

The depth of the coating was kept at the previous level of $100\ \mu\text{m}$, while the extent of the cross-section area covered by hBN was optimized by means of a parametric study in the FEM framework. A suitable solution was individuated in a ring-shaped coated area starting from the outer edge of the punch and extending for 6 mm in the radial direction, as depicted in Figure 4.26.

A significant improvement is detected in ΔT during the isothermal dwelling time: the temperature disparity among the two pyrometers is reduced to 5 °C. The beneficial effects of this partially-coated, Full punch setup are confirmed in Figure 4.27, where a complete map of the radial temperature distribution (in °C) in the central cross-section of the setup is given for the present configuration and the conventional Full one. The plot refers again to 1200 s, mid-holding time, and utilizes the same color scale for both cases, providing a comprehensive overview of the smooth transition between sample's edge and center, provided by the influence of the partial hBN coating. Such a novel design results to be a technologically feasible optimized solution for the uniformization of temperatures along the radial direction of a non-conductive powder specimen.

This concludes our investigation on how to optimize the spark plasma sintering tooling geometry in order to annihilate the strong thermal gradients characterizing the procedure. Various solutions have been proposed and refined, some suggesting the tailored drilling of ring-shaped holes, others the application of a selective coating of boron nitride.

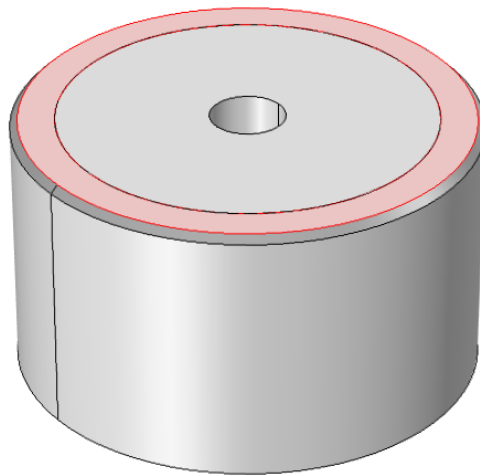


Figure 4.26 – Optimized BN-coated Full punch configuration.

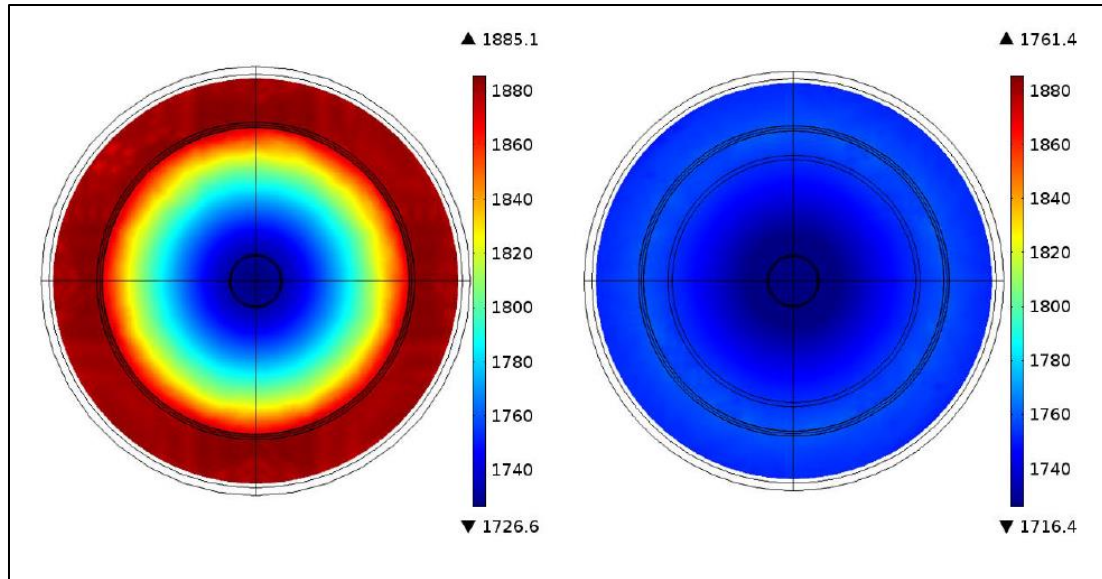


Figure 4.27 – FEM-derived temperature distribution (°C) in the central radial cross-section for the conventional and optimized BN-coated Full configurations.

It is important to evidence that, even if our investigation was focused on the SPS of silicon nitride under specific conditions because of the availability of experimental data, the applications of the analysis do not limit to this context. The individuated optimization strategies can be qualitatively generalized to any setup size, and from silicon nitride to any other insulating material. Furthermore, analogous considerations hold when dealing with conductive powders, in whose context the principles applied here can be simply reversed, such that the aim would be focusing the current towards the edge of the specimen. The quantitative information reported for this specific case helped solving actual issues of tooling overheating and specimen non-uniformities, encountered in the Dresden IKTS laboratories, but the deriving qualitative guidelines are suitable in any other situation.

Room for further work is also left. Once can notice that for the entirety of this section of the study we have used always the same optimization parameter, the disparity of temperatures recorded at two specific locations. This was necessary for coherence with the experiments first, when our numerical models were still undergoing validation, and then for

consistency with the initial plots. None of these locations, though, as we have pointed out elsewhere, belongs to the specimen itself, and in any case such parameter is rather limiting for a thorough redesign analysis. By looking at the two temperature maps in the radial cross-sections (Figures 4.17 and 4.27), indeed, one can see how, even when the disparity was almost reduced to zero, within the specimen the temperature range variations can still reach several tens of degrees. A more exact simulations campaign could, instead, involve the temperatures of the specimen itself, now made available by a FEM framework that we have assessed as reliable.

The reflection of the temperature distributions on the density of the specimens can also be analyzed, and this will be the object of section 4.2.

Before proceeding to focusing our attention on densification and connecting this type of optimization with the results of Chapter 3, we proceed to analyze the thermal gradients in the axial cross-sections of the setup, and the consequent improvements to the geometry of the other tooling components.

4.3 Optimization of the axial temperature distributions by improved spacers design

Analogously to the radial direction, axial planes present problems of thermal gradients. They hamper the specimen's conditions more indirectly, since they tend to create the overheating peaks in areas that are further from the powder compact. Such overheating is a consequence of the progressive heat dissipation as the current flows from the top to the bottom of the setup, combined with the presence of abrupt changes in the cross-section area available for the current to pass through. The highest dissipation happens at the first maximum cross-

section restriction encountered by the electrical current, namely at the interface between upper spacer and punch. Localized overheating at the top punch has been evidenced, during many spark plasma sintering experiments and with a variety of setups, by noticing that this component was becoming red and white hot during the procedure. In certain cases the top punch even sublimated.

It is interesting to already point out that a relatively unexpected result emerges from this study, at least at a first glance. The component responsible for this overheating behavior resulted to be the spacer, which we recall being the transition component that creates the interface between the punch and the respective electrode. A significant improvement in the temperature distributions is found in switching for this tooling component from a tapered (conical) configuration to a stack of disks. The peculiarity of this result lies in the fact that one would expect the inverse trend, since this translates in both an increase of the number of contact resistance layers and a very abrupt cross-section area change at the interface between the smallest disk and the top punch. What this section of the tooling optimization study reveals, instead, is that the increase in free surface area radiating towards the environment and the opportune decrease in graphite mass constituting the spacer assembly play a more efficient role in the overheating peaks mitigation.

Although the location of the overheating peaks seems not to have an influence of the specimen conditions, it is important to point out why the lowering of this type of gradients is still essential for the improvement of the SPS processes efficiency, also from the specimen's viewpoint.

The previous part of the work, focused on the radial gradients within the specimen and the adjacent die, allowed to neglect the axial differences because of the powder compact's aspect ratio, which was 6:1 before starting the process and even more as shrinkage progressed. Sometimes samples have lower values of aspect ratio, therefore rendering the axial thermal

gradients within the specimen not negligible anymore. The presence of very high temperatures at the top punch can only worsen such issue, by making the overall temperature distribution in the axial direction extremely uneven.

There is also an aspect of energy efficiency of the SPS procedure. Overheating at the top punch is an index of the maximum Joule heating effect happening at that location, instead of in correspondence of the specimen as desired.

When attempting to lower the axial temperature disparities, therefore, we are simultaneously homogenizing the thermal conditions experienced by the sample, protecting the tooling from overheating damages, and improving the energetic efficiency of the process.

4.3.1 The top punch overheating issue

Also in this case the study was mainly numerical but supported by experimental evidence.¹⁷³ The tooling setup presenting the issue was made of a different type of graphite, Isocarb 85 (Electrodes Inc., Milford, CT, USA), and slightly smaller in size with respect to the radial study, being the specimen diameter equal to 40 mm.

Figure 4.28 shows the tooling setup employed in the experiments and therefore reconstructed in the simulations. The various components are marked. The two inserts to be located between specimen and punches are optional but were embedded in our study.

Table 4.5 provides the details of the tooling components, while Table 4.6 reports the material properties of the graphite. Note that, together with the tapered transition, there was another cylindrical spacer in the assembly, to be located between the transition and the steel electrode of the machine.

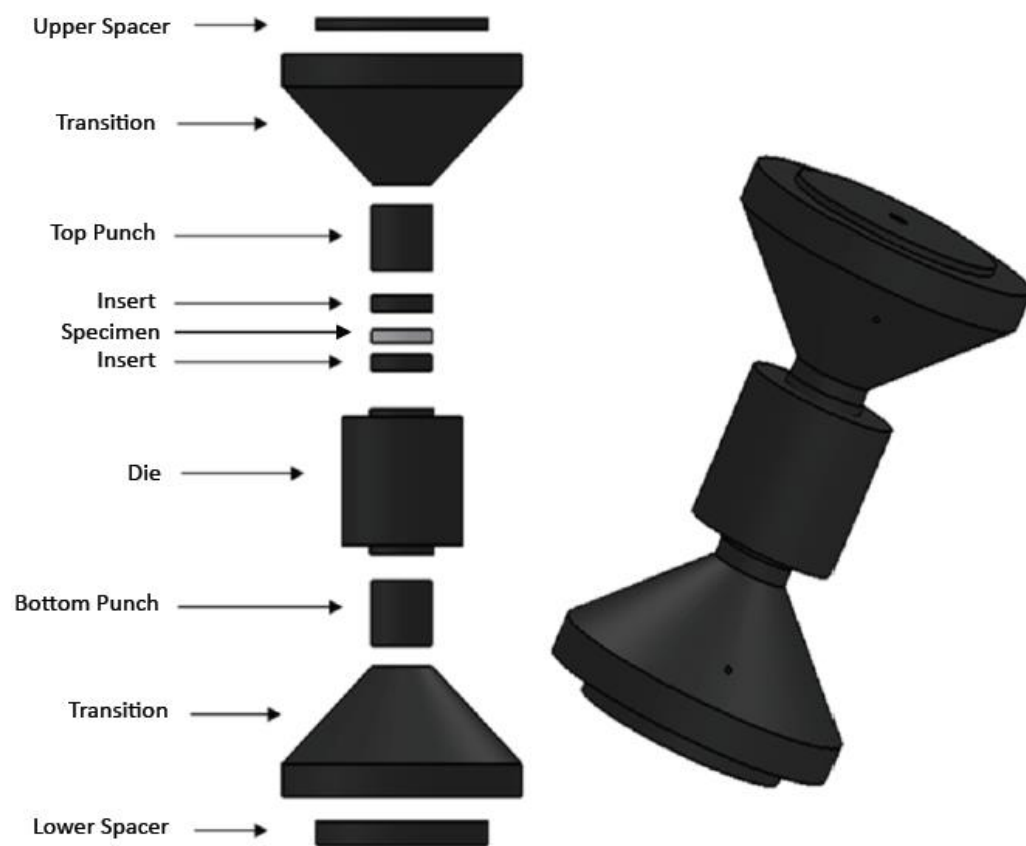


Figure 4.28 - Spark Plasma Sintering (SPS) tooling manifesting the overheating problem.

Table 4.6 – Tooling setup components for the axial gradients study.

Component (number)	Dimensions
Punches (2)	Height: 40 mm Diameter: 40 mm
Die (1)	Height: 80 mm Thickness: 40 mm
Conical spacers (2)	Height: 80 mm Diameter 1: 40 mm Diameter 2: 160 mm
Cylindrical spacers (2)	Height: 20 mm Diameter: 160 mm

Table 4.7 – Isocarb 85 graphite properties.

Theoretical density, ρ_{th}	1850 $\left[\frac{kg}{m^3}\right]$
Electrical conductivity, σ_{el}	$\frac{3}{6.083 \times 10^{-6} + 1.4585 \times 10^{-9}T}$ $\left[\frac{S}{m}\right]$
Heat capacity, C_p	$4(T - 280) + 709.12$ $T < 2000 K$ $\left[\frac{J}{kg \cdot K}\right]$
	8000 $T \geq 2000 K$
Thermal conductivity, k_T	$-0.026(T - 250) + 60$ $T < 1500 K$ $\left[\frac{W}{m \cdot K}\right]$
	27.5 $T \geq 1500 K$
Emissivity, ν_{rad}	0.8
Compression strength, S_{comp}	250 [MPa]

The treated material changes, even though still an insulator, since the overheating problem arose during the SPS of alumina, Al_2O_3 , whose properties are given in Table 4.7. All the listed material properties, for both graphite and alumina, were derived by means of experimental measurements and subsequent numerical regression. The alumina properties include dependencies on porosity.

The experimental procedure applied to the alumina samples consisted in subjecting an alumina powder specimen, with initial density $\rho_0 = 65\%$, to a temperature regime composed by a sequence of 3.3 minutes of 400 K/min heating rate, followed by 10 minutes of holding at 1600 K, for a total of 810 seconds of the simulated time. The temperature measurement was operated by a pyrometer focused on an apposite hole on the die surface. The processing was conducted in temperature-control mode (not current-control), which, again, means that the temperature profile is imposed by setting it on the SPS machine control panel. The FEM reconstruction of the process was done on the same premises used for the radial gradients analysis.

The initial stage of the numerical campaign consisted in the simulation of the conventional tapered setup, which served as calibration of the modeling framework. The equations to be combined in the FEM software were analogous as what explained in the previous section and will not be repeated. We will limit to reiterate the fact that this model of SPS, inclusive of the tooling setup, enables the calculation of the evolution of voltage (V), temperature (T), stress (σ) and porosity (θ). Analogous considerations hold for the functions and parameters selected for the continuum theory of sintering equations. In order to preserve the focus on the problem purely on the thermal aspects and to avoid computational issues, the Skorokhod's formulations for sintering stress, bulk modulus and shear modulus are selected.

Table 4.8 – Alumina properties.

Theoretical density, ρ_{th}	3970 $\left[\frac{kg}{m^3}\right]$
Electrical conductivity, σ_{el}	$\frac{(1 - \theta) \times 10^{-8}}{1 + 2\theta} \left[\frac{S}{m}\right]$
Heat capacity, C_p	$\left(\frac{777.025T}{249.40 + T} + 0.008T\right)(1 - \theta) \left[\frac{J}{kg \cdot K}\right]$
Thermal conductivity, k_T	$\frac{6.5181 \times 10^7 + T}{-6.6963 \times 10^5 + 8.1758 \times 10^2 T} (1 - 1.5\theta - 0.5\theta^2) \left[\frac{W}{m \cdot K}\right]$
Activation energy, Q_{PLC}	520 $\left[\frac{kJ}{mol}\right]$
Strain-rate sensitivity, m	0.33

Initial and boundary conditions are also the same as in the radial study, although a difference is present in the contact conditions. The axial temperatures optimization was conducted while the electrical contact resistance study was still ongoing. This obliged us to follow a more generic approach, consisting in considering contact resistance as a constant. The value of the electric conductance associated with an interface among two components was retrieved from the literature²⁰⁴ and is reported in Table 4.8. Different values are chosen depending on the materials in contact at such interfaces and on their orientation with the current flow. The conductance for graphite-alumina contacts are arbitrarily chosen to be one order of magnitude lower than for the graphite-graphite ones. Vertical contacts present a higher resistivity than the horizontal ones, where vertical and horizontal are defined as before, with vertical meaning parallel to the axis and horizontal denoting the interfaces that are perpendicular to the current flux.

Table 4.9 – Electric contact conductances.

Graphite-Graphite		Graphite-Specimen	
Contact Conductance, $\left[\frac{S}{m^2}\right]$		Contact Conductance, $\left[\frac{S}{m^2}\right]$	
Horizontal	$\sigma_{el,gg}^h = 1.25 \times 10^5$	Horizontal	$\sigma_{el,gs}^h = 1.25 \times 10^4$
Vertical	$\sigma_{el,gg}^v = 7.5 \times 10^4$	Vertical	$\sigma_{el,gs}^v = 7.5 \times 10^3$

In the conducted computations the set of contact resistances is simulated as before, with thin layer of arbitrary thickness between the two contact surfaces, implemented in COMSOL® by means of a distributed impedance in between the disks composing the transition. We chose to study the influence of the electric contact resistance by running all our simulations both in presence and in absence of this thin impedance layer. Interesting results arose in terms of temperatures values and distributions, as we will show in the following paragraphs.

Regarding the finite-element mesh, in this context too various attempts have been performed in order to obtain reliable and stable numerically converging results. The free tetrahedral mesh with the number of elements varying for different considered cases in the range 16,000–22,000 generated by the software, with a size classified as “normal”, “fine”, or smaller, revealed to be the most effective in conducting the 3D-FE calculations.

As an input to the model, we provided the electrical input. The information on electrical input and external pressure was taken from the available experimental data.¹⁸⁴ By imposing the applied voltage in the FEM implementation, the temperature profiles obtained with the SPS equipment were reproduced, with minor discrepancies, negligible in the present

part of the study, and due to the usage of a still unrefined contact resistance formulation. The comparison between the experimental pyrometer measurement and the temperature profile obtained at the same location in the FEM context is provided in Figure 4.29. Notice that the high discrepancy individuated at the very beginning of the process is due to the fact that, in the SPS device utilized for this part of the study, the pyrometer starts measuring the temperature only after a value 400 °C is reached. This preliminary model validation step also served to provide a reference set of data for the optimization study. This time, as suggested at the end of the radial section, as a main parameter we will employ the overall temperature distribution within the axial planes, in contrast with single point measurements. In this case we only have one experimental temperature probe, which is obviously not sufficient to give an indication of the disparities entity.

Figure 4.30 represents this study parameter for the conventional tapered setup, for both ideal and resistive contact. We find that the peak in temperatures occurs after 90 s from the beginning of the process, which is in agreement with the experimental results and also with previous works utilizing FE methods, even if conducted with a different software.¹⁹⁹

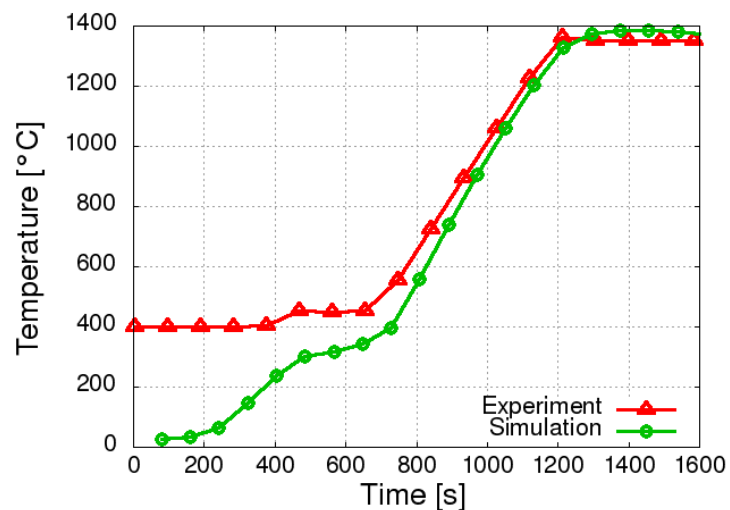


Figure 4.29 – Comparison between experimental and numerical temperature profiles.

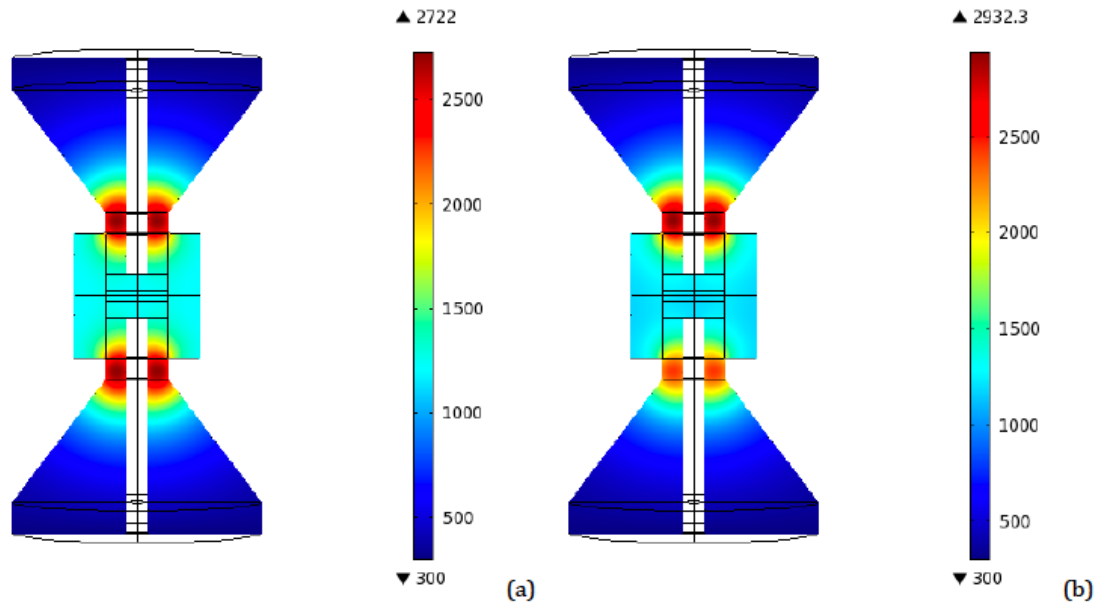


Figure 4.30 – Axial peak temperatures distribution (K) for the conventional tapered setup, with ideal (a) and resistive (b) contacts.

4.3.2 FEM-based optimization of the spark plasma sintering spacers design

In order to decrease the temperatures reached during the SPS processes, the tapered configuration was replaced by a variable number of “steps”, namely disks with different radii and thicknesses. This configuration based on a simple disk-like shape of the spacers also lowers the cost of tooling manufacturing. Several disks’ configurations have been designed, by varying their dimensions and number, for a total of 17 different setups (see Figure 4.31).

The following configurations have been modeled:

- Transition replaced by two disks:
 - Radii: 50 mm and 25 mm. Heights: 40 mm each.
 - Radii: 60 mm and 30 mm. Heights: 40 mm each.
 - Radii: 65 mm and 35 mm. Heights: 40 mm each.

- Radii: 70 mm and 40 mm;
 - Heights: 40 mm and 40 mm.
 - Heights: 30 mm and 50 mm.
- Transition replaced by three disks:
 - Radii: 65 mm, 45 mm and 25 mm;
 - Heights: 20 mm, 30 mm, and 30 mm.
 - Heights: 30 mm, 20 mm, and 30 mm.
 - Heights: 30 mm, 30 mm, and 20 mm.
 - Radii: 70 mm, 50 mm, and 30 mm;
 - Heights: 20 mm, 30 mm, and 30 mm.
 - Heights: 30 mm, 20 mm, and 30 mm.
 - Heights: 30 mm, 30 mm, and 20 mm.
- Transition replaced by four disks:
 - Radii: 80 mm, 70 mm, 60 mm, and 50 mm;
 - Heights: 20 mm each.
 - Heights: 10 mm, 20 mm, 20 mm, and 30 mm.
 - Radii: 75 mm, 65 mm, 55 mm, and 45 mm. Heights: 20 mm each.
 - Radii: 70 mm, 60 mm, 50 mm, and 40 mm. Heights: 20 mm each.
 - Radii: 68 mm, 56 mm, 44 mm, and 32 mm. Heights: 20 mm each.
 - Radii: 66 mm, 54 mm, 42 mm, and 30 mm. Heights: 20 mm each.

The axial temperature distribution in the vertical central plane was considered for all the two, three and four spacer-disks configurations. For brevity, we will address them as 2 Disks, 3 Disks and 4 Disks, respectively. This same distribution was considered for both the temperatures peak moment and the end of the process.

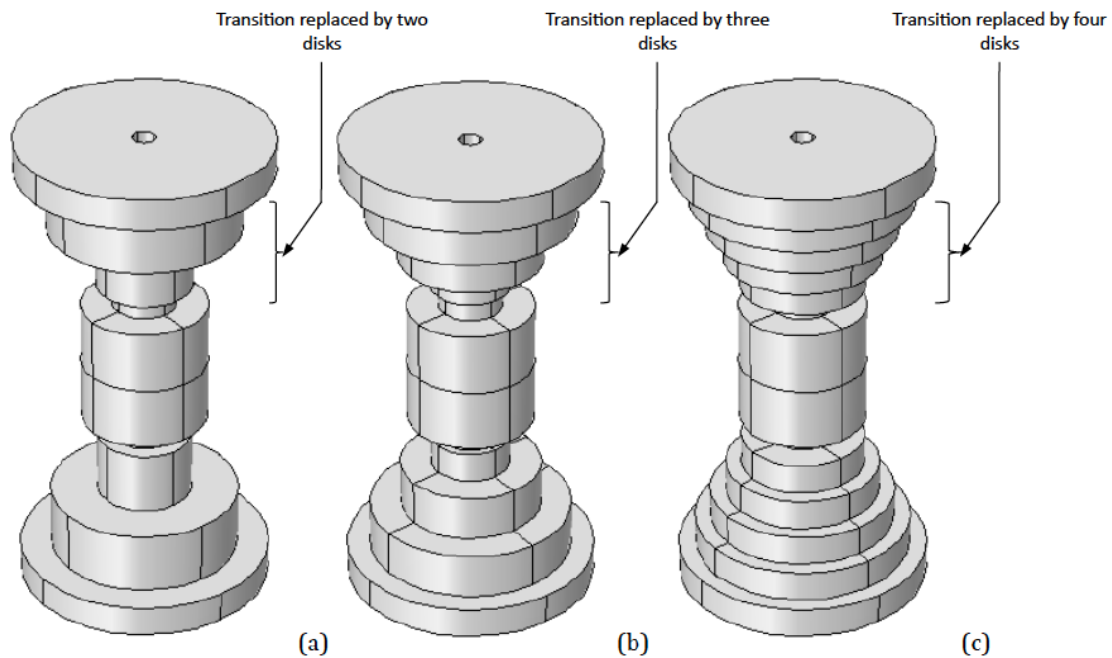


Figure 4.31 – Conical transition replaced by 2 Disks (a), 3 Disks (b) and 4 Disks (c) configurations.

The peak was always reached between 90 and 100 seconds, depending on the particular configuration, from the beginning of the SPS procedure, in accordance with what obtained for the tapered case. Such analogy was respected for its location too, namely the upper zone of the top punch, which, as expected, corresponded to the most narrow cross-section area encountered by the current flow.

Figures 4.32 and 4.33 provide the plots of the peak vertical temperature distributions for four of the most significant implemented geometries, namely the two 2 Disks with smaller and larger dimensions of the disks, and the same two cases for the 4 Disks configuration. All

temperatures are given in K, coherently with the unit utilized during this set of experiments. From these graphs the identification of the precise point of the top punch in which the peak is attained is made possible, a result impossible to derive in the experimental procedures.

From all the collected data, it also emerged that for both the peak and final time instants, the highest value of temperatures is obtained in the 4 Disks case with the largest disks radii, with a 2999 K peak value and a 1992 K final one. This is particularly interesting because such values overcome the tapered configuration ones (2722 K and 1872 K, respectively). More generally, the final and peak temperatures are greater than the conventional tool ones for all the 4 Disks configurations with radii greater or equal to the 70, 60, 50 and 40 mm combination. Thus, the replacement of the tapered configuration with a stack of disks of large size, at least relatively to the size of the previous conical spacer, is not a successful strategy for minimizing the axial thermal gradients.

Another important point made immediately by observing the plots is the asymmetrical distributions of the temperatures with respect to the central radial cross-section of the specimen. This is explained with the presence of electrical contact resistance at the various interfaces among tooling components.

Once the first layers have been overcome, the energy available for dissipation is reduced, and therefore the peak in Joule heating at the second cross-section area restriction (bottom punch) is lower than the top punch one. A confirmation of these conclusions will be found shortly in the analysis of the ideal contacts (absence of electrical resistance) simulations. Recall that thermal contact resistance has been proven to have a negligible effect on temperatures in SPS and is therefore not included in our investigation.

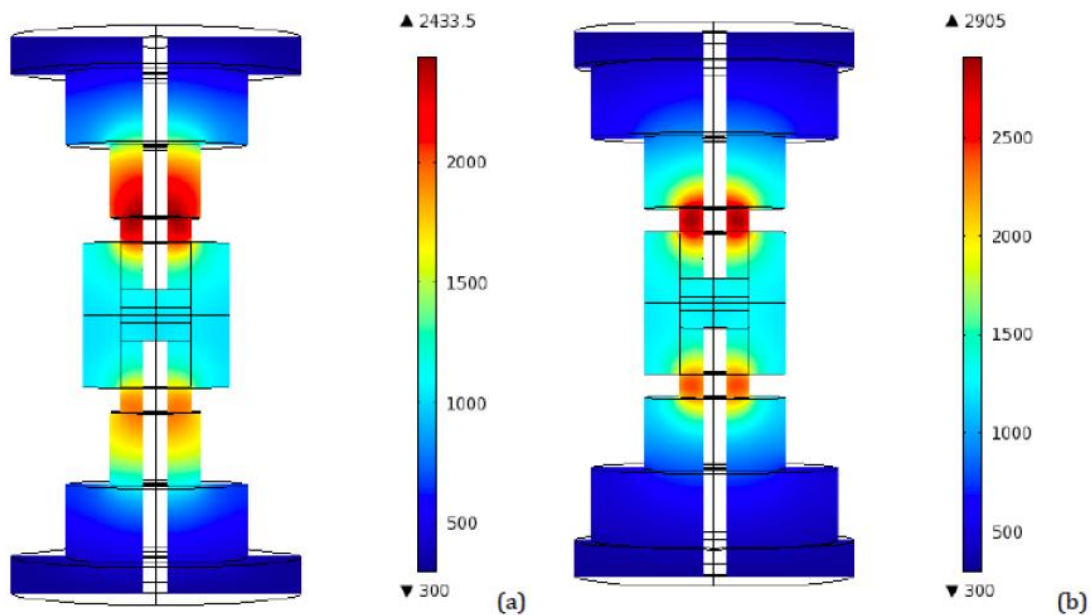


Figure 4.32 – Peak temperature distributions (K) for two of the 2 Disks configurations. (a) Radii: 50 and 25 mm—Heights: 40 mm each; (b) Radii: 70 and 40 mm—Heights: 40 mm each.

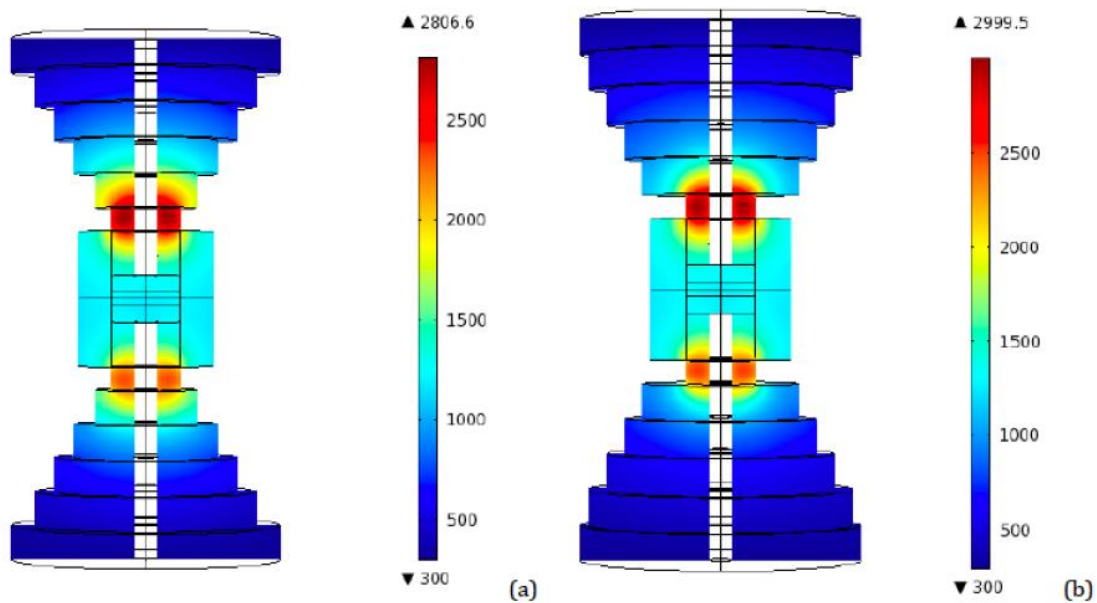


Figure 4.33 – Peak temperature distributions (K) for two of the 4 Disks configurations. (a) Radii: 66, 54, 42, and 30 mm—Heights: 20 mm each; (b) Radii: 75, 65, 55, and 45 mm—Heights: 20 mm each.

The configuration in which the heat penetrates more in depth from the transitional disks towards the specimen is the 2 Disks setup, where a temperature of 1200 K is found at 20 mm from the punch. In this same area the temperatures in the other configurations are approximately 1000 K for the 4 Disks configuration and 1100 K for the 3 Disks configuration. This is again a consequence of the number of electrical contact resistance layers introduced in the tooling assembly when building a transition by means of a stack of disks.

If adherence to the tapered configuration is not a strict requirement, the 2 Disks geometry seems to be the optimal solution in order to increase the efficiency of the SPS thermal process. By efficiency we mean the localizing of the Joule heating in correspondence of the specimen, instead of having large dissipations in areas that are far from it, leading to energy wastes.

As anticipated previously, simulations in absence of electrical contact resistances were also run. We denominate them as ideal contacts cases. For comparison purposes, the same boundary conditions applied in the resistive contact case are employed. Specifically, the voltage utilized to produce the above-mentioned heating regime for the resistive contact case is used in this context too.

We provide the axial peak temperatures distributions for the same four cases that we chose as most representative in the resistive contacts context: two 2 Disks and two 4 Disks configurations, specifically the ones with smallest and largest sizes of the spacer disks (Figures 4.34 and 4.35).

Analogous considerations to the resistive contacts cases can be drawn with respect to the highest temperatures attained. Again these are found in the 4 Disks configuration with the largest disks radii, for both the peak and final time steps of the process. The values shown in the simulations result to be 2917 K at the peak and 1922 K in the last instants. This is a remarkable outcome, since in this case too temperatures are higher than the ones reached in

the tapered geometry. Therefore, the increase in temperatures in setups with increasing number of disks is, as stated before, a consequence of the selected sizes, and not only of the electrical contact resistances. These layers certainly play an important role, since the temperatures obtained here are globally lower than the ones of the resistive contacts cases, but the relevance of the disks dimensions needs to be taken into account for the optimization of the tooling design.

The main difference with the resistive contacts configurations consists in the perfectly symmetrical distribution of temperatures obtained here. This confirms the conclusions stated above on the role of contact resistances in the progressive Joule heating dissipation as current is flowing throughout the tooling. In absence of electrical resistance layers at the components interfaces, the exact same temperatures are reached in the upper and lower parts of the tooling, and the same overheating peaks are present in the top and bottom punches.

We have also noted that ideal contacts render the overall temperatures lower than in the resistive context. We provide in Figure 4.36 plots of the time evolution of temperatures during the entire 810 s simulations. A graph is given for each of the 2, 3 and 4 Disks cases. In each graphs all the simulated geometries are depicted. On the left (a, c, e) we have the ideal contacts, on the right (b, d, f) the resistive ones. The temperatures shown are a volume average in the top punch. The volume average is calculated as the integral over the volume, divided by the volume itself.

From these graphs the increase in temperatures when contact resistances are present is made clear. The time step corresponding to the peak can be inferred, and the range in between 90 and 100 s is confirmed. For all the configurations considered, in terms of number of disks, a decrease in the radii values leads to a decrease in the overall temperatures.

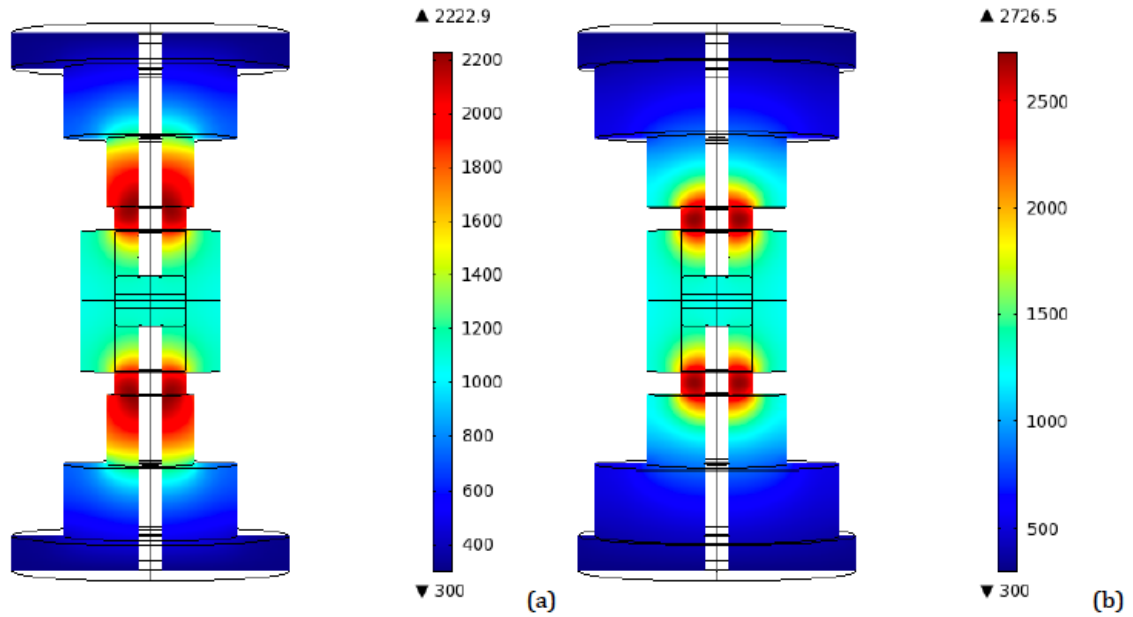


Figure 4.34 – Peak temperature distributions (K) for two of the 2 Disks configurations with ideal contacts. (a) Radii: 50 and 25 mm—Heights: 40 mm each; (b) Radii: 70 and 40 mm—Heights: 40 mm each.

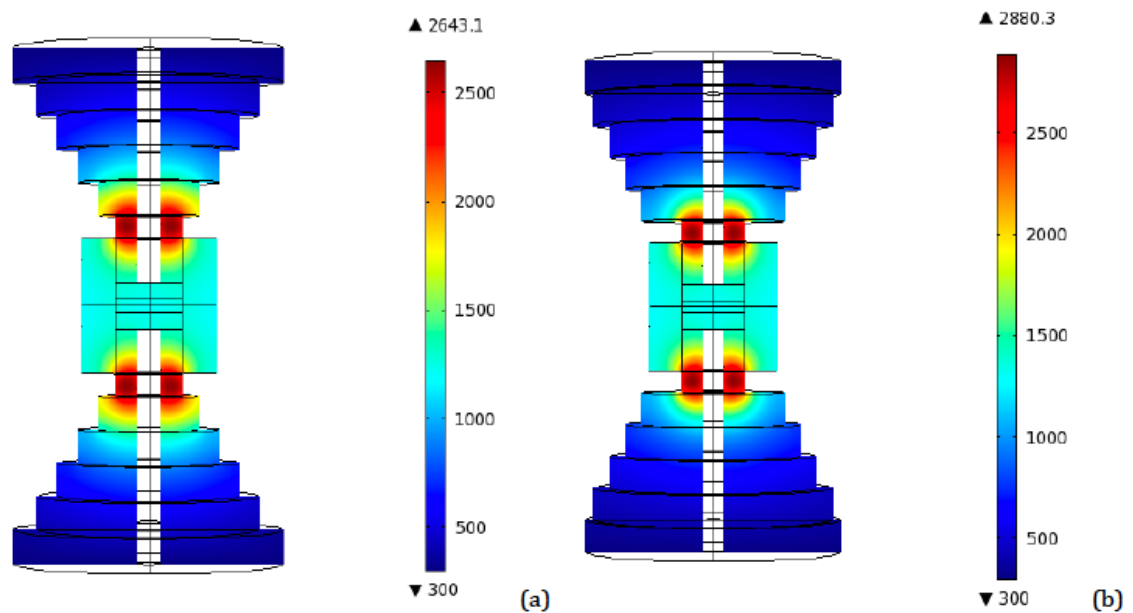


Figure 4.35 – Peak temperature distributions (K) for two of the 4 Disks configurations with ideal contacts. (a) Radii: 66, 54, 42, and 30 mm—Heights: 20 mm each; (b) Radii: 75, 65, 55, and 45 mm—Heights: 20 mm each.

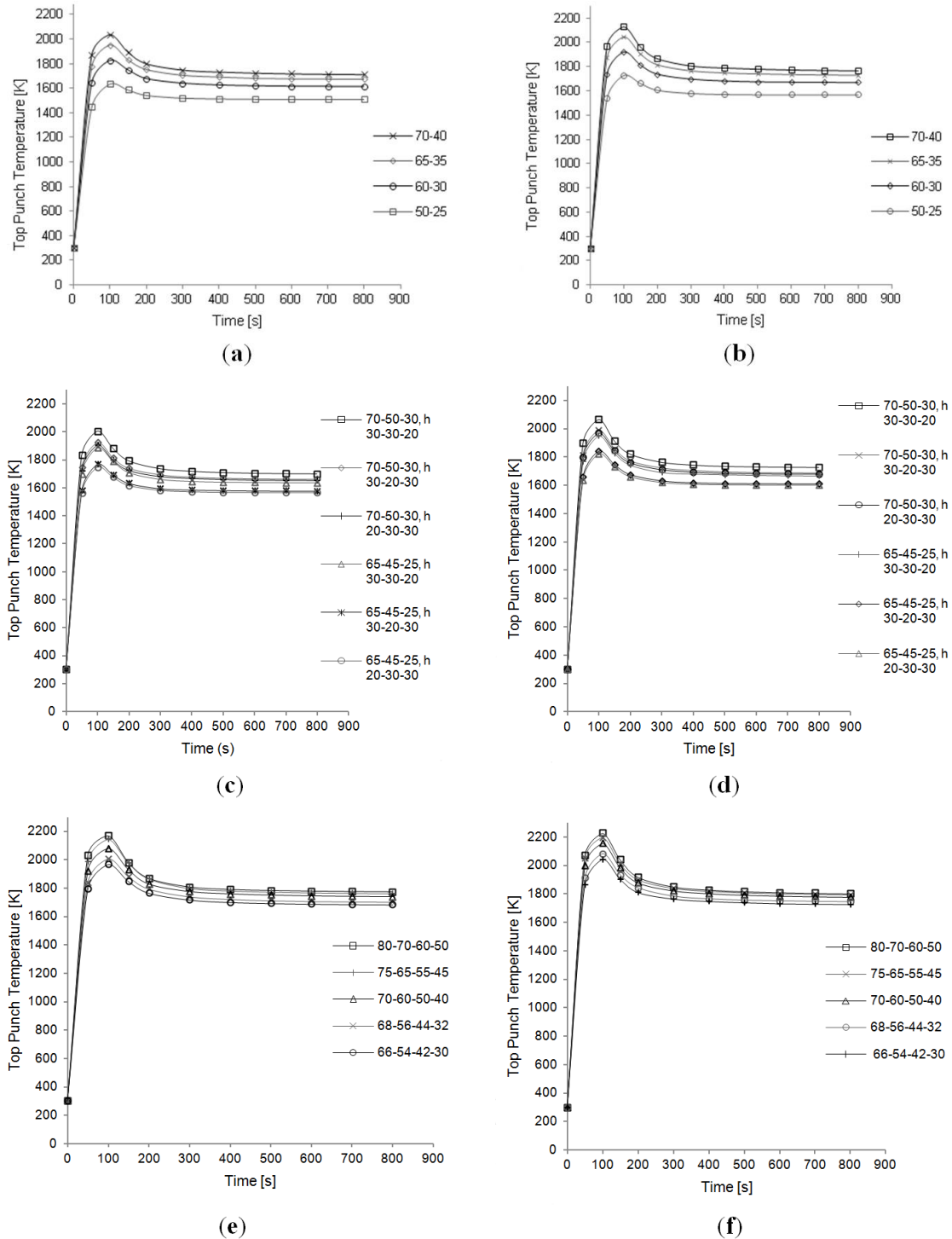


Figure 4.36 - Temperature evolution in the top punch. (a) 2 Disks setup—Ideal contact; (b) 2 Disks setup—Resistive contact; (c) 3 Disks setup—Ideal contact; (d) 3 Disks setup—Resistive contact; (e) 4 Disks setup—Ideal contact; (f) 4 Disks setup—Resistive contact. Dimensions of the setup are listed in the legend.

Moreover, to verify the impact that changes in electric contact resistance can have in the temperature distribution, a different arrangement of contact conductivities has been simulated in a specific case, i.e., the two disks setup (radii: 60 and 30 mm, heights 40 mm each). Here, only horizontal electric contact resistances were considered and the configuration of the graphite-specimen contact is changed to obtain a larger resistivity; these modifications lead to a considerable increase in the top punch temperature (2020 K, instead of 1853 K).

Note that the 3 Disks cases, being the transition overall length equal to 80 mm, imposed an uneven distribution of the disks height. We chose to have two 30 mm high disks and one 20 mm high. All the possible combinations were investigated (see list at the beginning of the paragraph). Figure 4.37 reports the two opposed cases of thinner disk (20 mm height) adjacent to the spacer or to the top punch.

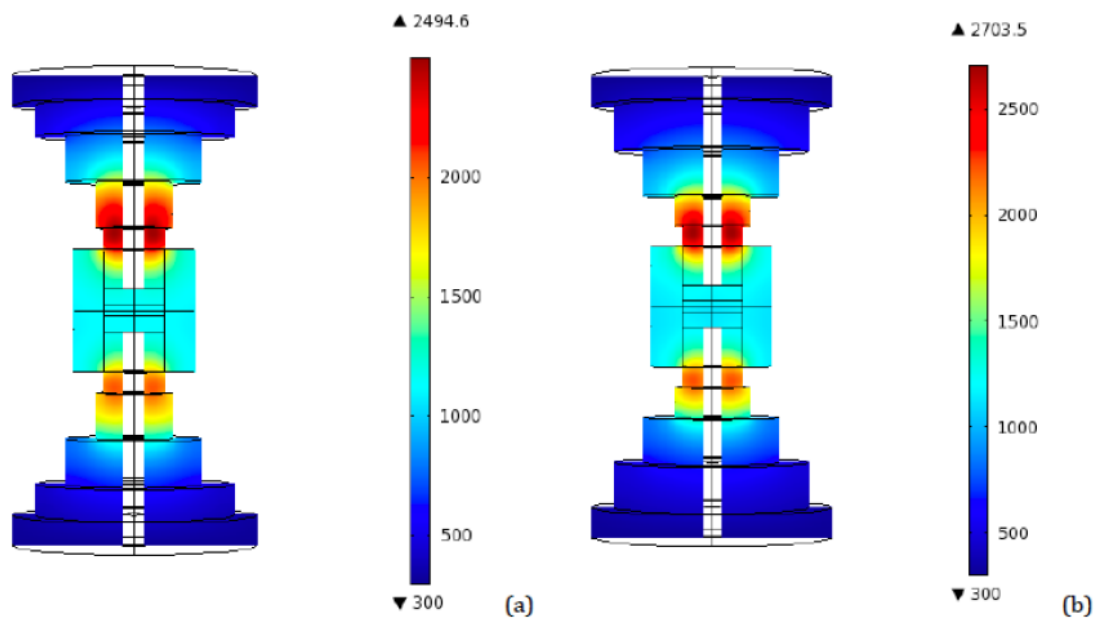


Figure 4.37 – Peak temperature distribution—Height influence comparison for a 3 Disks configuration (Radii: 65, 45, and 25 mm). (a) Heights: 20, 30, and 30 mm from the top; (b) Heights: 30, 30, and 20 mm from the top.

From the temperatures obtained for the 3 Disks cases (see plots in Figure 4.36 and 4.37), we saw that an increase of the height of the disk adjacent to the top punch, while decreasing accordingly the height of the top disk (the one with the largest radius), causes a diminution of the global temperature. A reason for this behavior can be attributed to the larger surface area exposed to the environment, kept at room temperature, close to the hottest zone, which allows for a more efficient surface radiation (see boundary conditions for the thermal module).

With this result in mind, the same procedure was attempted for the two disks and four disks configurations. In both cases, the setups with the largest radii were chosen. These cases are included in the initial geometries list too. In the two disks case, ideal contact was simulated, while for the four disks configuration the resistive contact model was run.

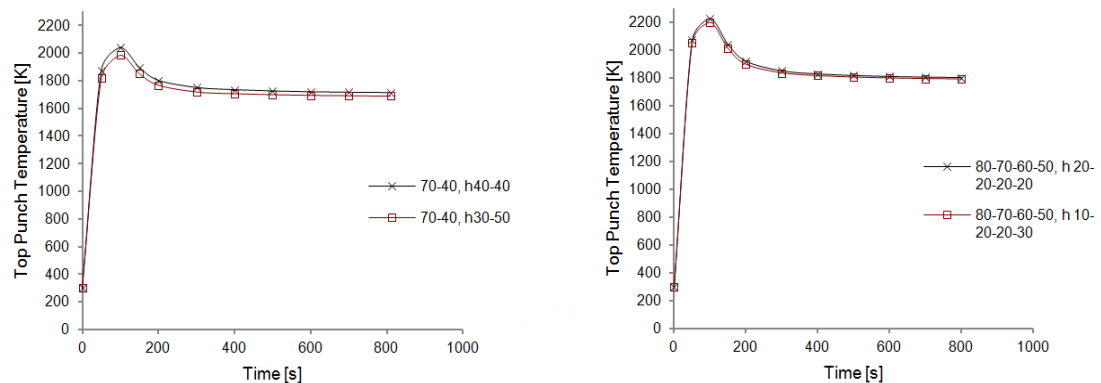


Figure 4.38 - Temperature evolution—Effect of height variation. (left) 2 Disks—Ideal contact—Radii 70 and 40 mm—Height 40 mm each compared with 30 and 50 mm; (right) 4 Disks—Resistive contact—Radii 80, 70, 60, and 50 mm—Height 20 mm each compared with 10, 20, 20, and 30 mm.

As represented in Figure 4.38, again, an increase in the bottom disk height, at the expenses of the top disk one, leads to a decrease in temperatures, even if not substantial. The effect of this geometrical modification appears to be more significant in the ideal contact case than in the resistive contact one. This is therefore a modification that does not have a

significant influence in real world SPS experiments, but still provides further information on the physical phenomena underlying the development of axial thermal gradients, and specifically the role played by surface radiation.

Some remarkable data are obtained from the comparison of the temperatures of the “hot point” of the top punch with the temperatures attained in the specimen, for which a volume average is computed. The key point in the presently applied approach for the analysis of the overheating problem is based exactly on these derived data, distinct from previous works,¹⁹⁶ in which the calculated temperature difference was, instead, the one between the specimen and the external surface of the die, that is at the point where SPS temperatures are usually measured.

Figure 4.39 compares these two temperatures for the 2 and 4 Disks cases. The plots are given with the different radii combinations along the x-axis and the peak and specimen temperatures difference along the y-axis. In both cases all the disks had the same height. The maximum temperature difference corresponds to the peak of the transient temperature and is inferred from the maximum temperature distribution plots. In all the cases, the temperature of the punch for the resistive contact case is higher than the temperature of the punch for the ideal contact.

An opposite situation is seen at the specimen, where a slightly higher temperature is obtained in the ideal contact case, since the Joule heating finds less obstacles on its way to the powder sample. Although the presence of the resistive contact reduces the efficiency of the system, the temperature difference obtained in the specimen between the ideal contact case and the resistive case is relatively small.

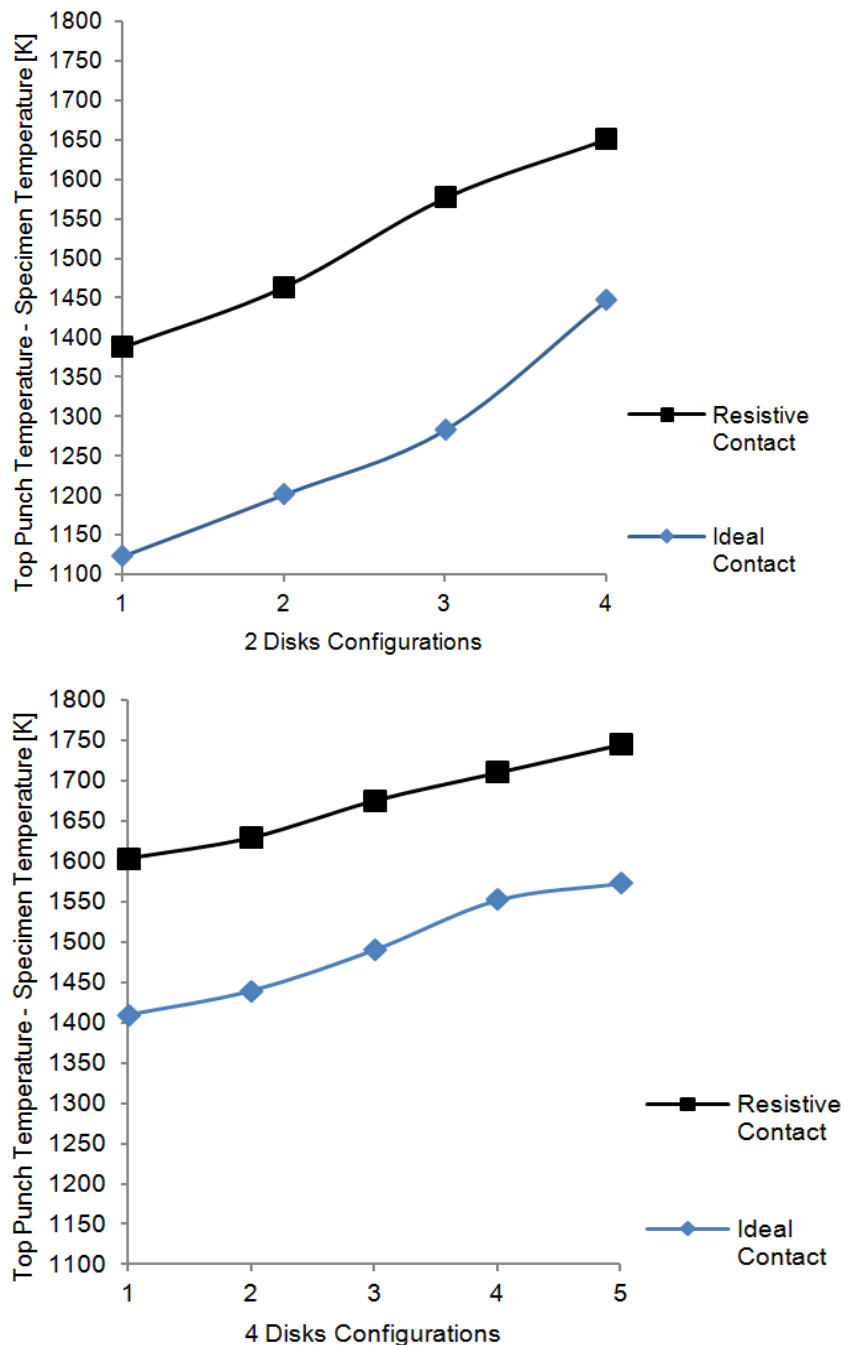


Figure 4.39 - Comparison of maximum (transient) temperature difference between top punch and specimen. (top) 2 Disks configurations. Radii: (1) 50 and 25 mm; (2) 60 and 30 mm; (3) 65 and 35 mm; (4) 70 and 40 mm; (bottom) 4 Disks configurations—Radii: (1) 66, 54, 42, and 30 mm, (2) 68, 56, 44, and 32 mm, (3) 70, 60, 50 and 40 mm, (4) 75, 65, 55, and 45 mm; (5) 80, 70, 60, and 50 mm.

The case where the difference is the largest (4 Disks configuration), which seems to suggest a less efficient system, is precisely the one that is able to heat the specimen more (~1600 K). Therefore, this confirms that the energy losses on the setups depend more on the configuration of the disks than on the actual characteristics of the contacts, at least for the combination of material and electrical contact resistance properties used in the simulations.

In a similar way, the final temperature difference between the top punch and the specimen for the four configurations, with ideal as well as resistive contacts, was investigated. Again, higher differences were obtained for the electric resistive contact case. In this stationary configuration, the differences in temperature vary with the radius of disks in an inversely proportional fashion and stay almost constant with height variations.

Once all the previous outcomes have been examined, it is evident that, in order to choose the most advisable setup, separate considerations can be made for every configuration investigated, categorized in terms of the number of disks.

One of the best choices is certainly the 2 Disks configuration, since here the contact resistance is minimized to only one extra “resistive layer” with respect to the tapered setup. The lower the radii and the higher the bottom disk, the better results we get in terms of temperatures. For instance, radii of 50 and 25 mm can be chosen, or, if these values are too small, since the bottom disk is almost as large as the punches, 60 and 30 mm, preferably with heights of 30 and 50 mm, respectively. In this case a peak temperature decrease of 500 K can be attained.

If the main interest is, instead, in having a configuration as similar as possible to the original conical (tapered) one, the 4 Disks setup can be chosen. Again, the lower the radii and the higher the bottom disks, the better results are attained. Concerning our simulations, the best combination appears to be the one with radii 66, 54, 42, and 30 mm with heights equal to 10, 20, 20, and 30 mm, respectively. Lower values of the radii can be attempted to get even

better results. It should be noted that in this case the most significant decreases in peak temperatures that can be obtained are in a range of 150–250 K.

A compromise solution between the minimum contact resistance and the tapered configuration is the 3 Disks setup. The same considerations concerning radii and heights need to be applied. From our data, the configuration with radii 65, 45, and 25 mm, and respective heights of 20, 30, and 30 mm, appears to be a good option. The diameter of the top disk could be further decreased. The temperatures can be lowered by about 350 K.

It is important to notice that the efficiency of all the suggested configurations needs to be verified in terms of the specimen densification. The lowest peak temperatures correspond to lower temperatures inside the specimen, especially when the contact resistance is imbedded. Simulations and experiments need to be conducted in order to be sure that the specimen's porosity decreases significantly in reasonable time intervals.

Differently from the radial temperatures optimization study, here the conclusions drawn are of even more immediate generalization. The axial gradients have revealed to be a consequence of the localized dissipation of heat at the tooling cross-section area restrictions and in correspondence of contact interfaces among the various components. This is a phenomenon common to both insulating and conductive materials. It is therefore reasonable to assume that, even if an insulating powder specimen will constitute a more substantial obstacle to the current flow, the highest temperatures will still be reached at the top punch, being this the narrowest point on the electrical current path. Since the experiments and simulations conducted here concerned alumina, an insulator, and the die wall in correspondence of the punch was less overheated than the top punch, we can infer that the same would hold for a conductor, in which current can cross the specimen too. We have, nevertheless, already considered what happens when increasing the radial dimension of the specimen, and developed suitable tooling optimization strategies. By combining the punch redesign, and the

consequent radial thermal gradients mitigation, with the spacer-transition redesign, and its lowered overheating at the top punch itself, we obtain a comprehensive tooling optimization, capable to address any thermal non-uniformity issue.

The combination of efforts in Section 4.1 guarantees a globally more uniform temperature distribution in any plane of the whole spark plasma sintering setup, for every size and material involved. We have obtained that the setup, and in particular the specimen, experiences fairly homogeneous temperatures, adherent to what imposed by the sintering route. The sintering regime, on its side, is the object of the optimization in the previous chapter of this study, based on the homogeneity of the material structure (elimination of agglomerates). In order for this improved sintering route to be efficiently applied, we needed to ensure uniform temperatures throughout the whole sample; otherwise our efforts in removing the undesired hierarchical porous structures would have been vain. This is what the present chapter has taken care of. The various aspects of a temperature-based optimization of spark plasma sintering efficiency can thus be considered complete.

Parts of Chapter 4 have been published in *Materials* (D. Giuntini, E.A. Olevsky, C. Garcia-Cardona, A.L. Maximenko, M.S. Yurlova, C.D. Haines, D.G. Martin, and D. Kapoor, “Localized Overheating Phenomena and Optimization of Spark-Plasma Sintering Tooling Design,” *Materials*, 6, 2013), in the *Journal of the Ceramic Society of Japan* (D. Giuntini, J. Raethel, M. Herrmann, A. Michaelis, C.D. Haines, and E.A. Olevsky, “Spark Plasma Sintering Novel Tooling Design: Temperature Uniformization during Consolidation of Silicon Nitride Powder,” *J. Ceram. Soc. Jpn.*, 124, 2016), and in the *Journal of the American Ceramic Society* (D. Giuntini, J. Raethel, M. Herrmann, A. Michaelis, and E.A. Olevsky, “Advancement of Tooling for Spark Plasma Sintering,” *J. Am. Ceram. Soc.*, 98, 2015). The dissertation author is the primary author of these publications. A part of the same Chapter 4

refers to work published in the *Journal of the American Ceramic Society*, of which the dissertation author was among the primary contributors (X. Wei, D. Giuntini, A.L. Maximenko, C.D. Haines, and E.A. Olevsky, “Experimental Investigation of Electric Contact Resistance in Spark Plasma Sintering Tooling Setup,” *J. Am. Ceram. Soc.*, 98, 2015).

Chapter 5

Conclusions

5.1 Summary

We have conducted an optimization efficiency study for spark plasma sintering technologies with temperature as the main parameter. We have pointed out the fundamental role played by temperature for the quality of the final densified product, in terms of uniformity of density and microstructure.

We have individuated two main aspects that need to be optimized in order to reach such uniformity: material structure and tooling geometry.

In the introductory chapter we have analyzed the variety of meanings that the denomination “material structure” can assume for a porous material that undergoes sintering, but we have clarified that the most influential ones during densification are the so-called hierarchical porous structures. They consist in the presence of various sizes of pores, and they are the result of the presence of agglomeration phenomena. Because of the significance of such phenomena in nanopowders, which are gaining increasing attention in the SPS field because of their excellent sinterability and functional versatility, we have proposed to proceed to *in situ* de-agglomeration during the consolidation process.

We have developed a semi-analytical modeling framework in which the biporous material properties (sintering stress, bulk modulus and shear modulus) and densification kinetics are given as a function of strain-rate sensitivity. We have also proposed global formulations of these same material properties that take into account the effect of the presence

of two porosity sizes, together with strain-rate sensitivity. We have, therefore, built a semi-analytical framework with a high potential for numerical (FEM) calculations, in which the material structure optimization can be conducted.

This optimization is based on the dependence of strain-rate sensitivity on temperature. The densification kinetics equations and the material properties formulations serve as tools for the individuation of optimal SPS thermal regimes, such that large pores are eliminated before the shrinkage of small pores is complete, or such that tailored hierarchical porous structures for different applications are produced. Additional factors affecting shrinkage kinetics have been examined and the important role played by the initial material structure has been evidenced. We have considered both conductive and insulating materials, combined our analytical expressions with finite-element calculations, and compared the obtained models with others proposed in the literature and experimental results.

We have derived a simple formulation for the dependence of strain-rate sensitivity on temperature by combining well-assessed empirical models for the steady state of power-law creep. The data needed as input to individuate this correlation are widely available in the literature, and thus the strain-rate sensitivity-based material structure optimization strategy is easily applicable to most material systems.

The derived biporous material properties have also paved the way for the implementation of a multi-scale FEM framework, in which the evolution of both single pores and whole specimen can be simultaneously monitored during processing.

We have subsequently evidenced that this temperature regime optimization would be vain if the specimen experienced severe thermal gradients. This is a well-known issue of spark plasma sintering and becomes progressively more intense as the size of the specimen increases. The tooling geometry plays an important role in the temperature distributions in the specimen and in the entirety of the tooling setup.

We have therefore addressed the thermal gradients issue by considering both the axial and the radial directions. We have conducted a broad combined experimental and numerical campaign in order to individuate the underlying phenomena and design opportune solutions.

Finite element methods have allowed access to information otherwise unattainable, and experiments have confirmed that such a numerical framework is a reliable tool for the investigation on the conditions experienced by the SPS sample and tooling during the process.

Novel design strategies of some of the tooling's components have been proposed. Switching from a conical transition to a stack of disks for the spacers has significantly lowered the axial gradients, while drilling a number of tailored holes in the punches has led to the homogenization of the temperatures in the radial direction. These two geometry optimization procedures have led to the solution of actual tooling overheating and specimen non-uniformity problems, while providing a deeper understanding of the dynamics of spark plasma sintering. The new punch design is also the object of a patent application.

After completing the optimization of both thermal regime and temperature distributions, the two frameworks can be integrated. We have therefore derived guidelines for a thorough uniformization of the SPS results, in terms of material structure (density and microscopic features) and tooling conditions, leading to greatly improved control of any spark plasma sintering routine.

The conclusions described above can thus be summarized in the following points:

- Expressions for densification kinetics, sintering stress, bulk and shear moduli of monoporous and biporous nonlinear viscous materials have been derived;
- An expression for the correlation between strain-rate sensitivity and temperature has been inferred from well-assessed empirical models;
- Strategies to improve spark plasma sintering efficiency based on such tools have been proposed;

- The conditions for *in situ* de-agglomeration have been found in a combination of pre-processing agglomerate size reduction and selection of optimal thermal route and externally applied pressure;
- The derived macroscopic mechanical properties of biporous materials can be utilized for the controlled design of tailored hierarchical porous structures;
- A multi-scale FEM framework for the virtual reconstruction of hierarchically porous materials has been implemented, enabling the simultaneous monitoring of the evolution of porosity and large pores' shape and size;
- A multi-physics FEM framework, comprehensive of specimen and tooling, has been implemented for the virtual reconstruction of the entire SPS process;
- Improved tooling geometries have been designed, able to mitigate the radial and axial temperature gradients within the SPS setup.

Both temperature regime and temperature distributions have been optimized for any spark plasma sintering routine.

We report here a flowchart (Figure 5.1) that summarizes the accomplished research objectives and the respective interconnections.

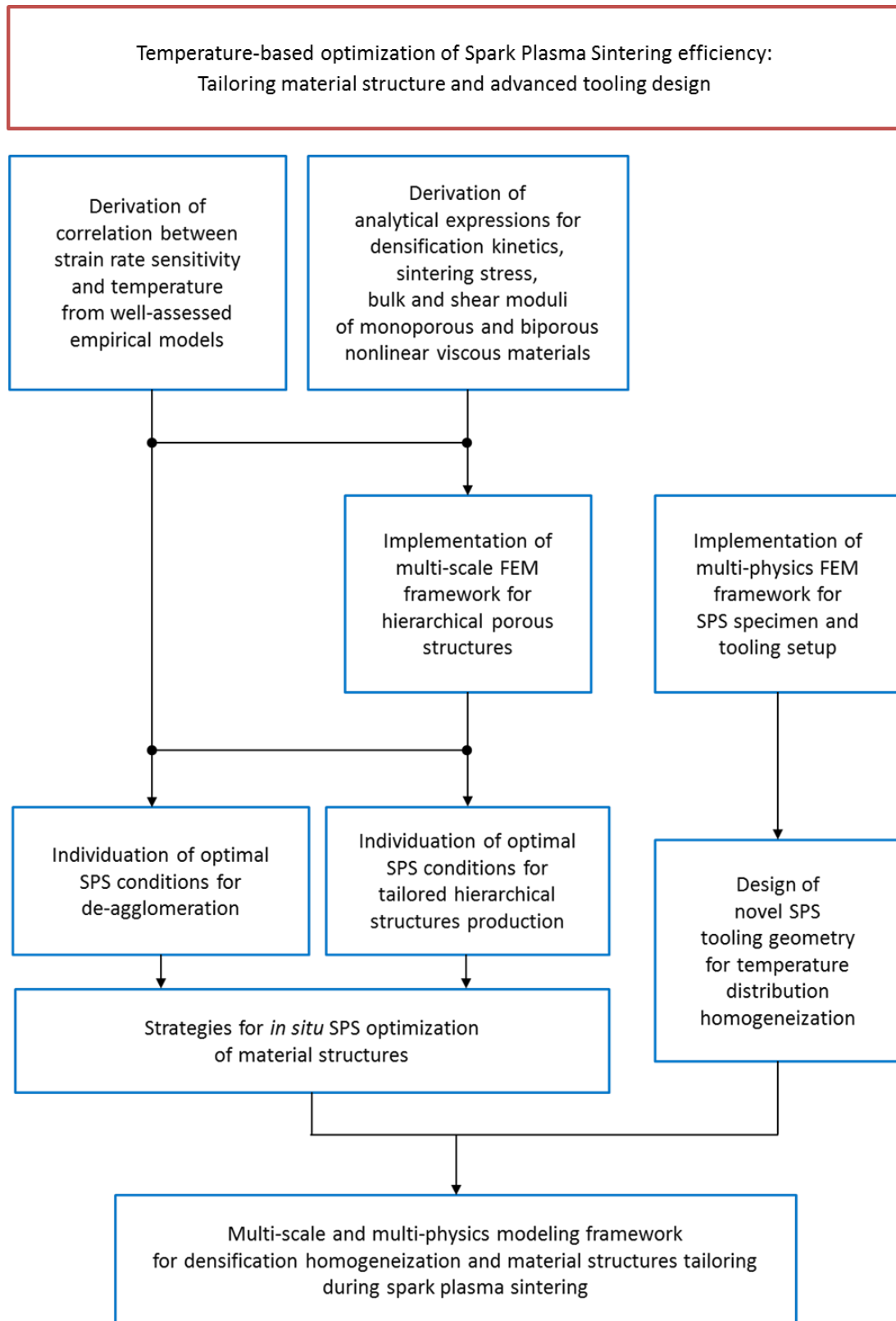


Figure 5.1 – Conclusions summary.

5.2 Scientific and engineering novelty

Significant innovations are proposed at different levels.

The development of an analytical (or semi-analytical) modeling framework for hierarchical porous structures with nonlinear material behavior, to the best of our knowledge, had never been attempted before. The derivation of all the powder compact's properties in function of the strain-rate sensitivity is also an innovative feature, since until now such dependence had only been proposed for monoporosity domains and did not include the sintering stress. The embedding of the effects of both porosities in the formulation of the macroscopic counterparts of these parameters also provides a new tool for the numerical (FEM) modeling of a specimen that contains agglomeration but can be treated as homogeneous, with all the consequent computational advantages.

While the correlation between strain-rate sensitivity with temperature is well agreed on by a variety of authors, literature data on this aspect are rare and fragmentary, and the idea of utilizing such connection in order to optimize SPS holding temperatures – such that *in situ* de-agglomeration is attained – is suggested here for the first time. The explicit formulation of $m(T)$ is also a first-of-a-kind, and immediately applicable to any material.

The outcomes of the proposed model have shed light on the limitations and applicability of in-situ de-agglomeration during SPS, and at the same time have turned out to be a valuable tool to design tailored hierarchical material structures.

The first multi-scale finite-element simulations of the synthesis of cathodes for solid oxide fuel cells have been developed. The macro-scale specimen densification was connected to the large pores shape and size evolution and small size porosity distribution at each time-step.

The utilization of a FEM software for the simulation of SPS procedures is also taken to a more advanced stage by not simply reconstructing experimental procedures, but also individuating and analyzing the main physical phenomena acting within the tooling setup and responsible for temperature spatial distributions. This new insight in the dynamics of thermal effects in SPS leads to the development of novel tooling designs. The most significant tooling optimization advancement consists in a new punch geometry able to mitigate radial thermal gradients, which is currently the object of a patent application.

References

- ¹ D. Jiang, D.M. Hulbert, J.D. Kuntz, U. Anselmi-Tamburini, and A.K. Mukherjee, "Spark plasma sintering: A high strain rate low temperature forming tool for ceramics," *Mater. Sci. Eng. A*, **463** [1–2] 89–93 (2007).
- ² R.L. Roberto Orrù, "Consolidation/Synthesis of Materials by Electric Current Activated/Assisted Sintering," *Mater. Sci. Eng. R Rep.*, **63** [4–6] 127–287 (2009).
- ³ J.E. Garay, "Current-Activated, Pressure-Assisted Densification of Materials," *Annu. Rev. Mater. Res.*, **40** [1] 445–468 (2010).
- ⁴ Z.A. Munir, D.V. Quach, and M. Ohyanagi, "Electric Current Activation of Sintering: A Review of the Pulsed Electric Current Sintering Process," *J. Am. Ceram. Soc.*, **94** [1] 1–19 (2011).
- ⁵ Z.A. Munir, U. Anselmi-Tamburini, and M. Ohyanagi, "The effect of electric field and pressure on the synthesis and consolidation of materials: A review of the spark plasma sintering method," *J. Mater. Sci.*, **41** [3] 763–777 (2006).
- ⁶ E.A. Olevsky, S. Kandukuri, and L. Froyen, "Consolidation enhancement in spark-plasma sintering: Impact of high heating rates," *J. Appl. Phys.*, **102** [11] 114913 (2007).
- ⁷ J. Langer, D.V. Quach, J.R. Groza, and O. Guillon, "A Comparison Between FAST and SPS Apparatuses Based on the Sintering of Oxide Ceramics," *Int. J. Appl. Ceram. Technol.*, **8** [6] 1459–1467 (2011).
- ⁸ L.A. Stanciu, V.Y. Kodash, and J.R. Groza, "Effects of heating rate on densification and grain growth during field-assisted sintering of α -Al₂O₃ and MoSi₂ powders," *Metall. Mater. Trans. A*, **32** [10] 2633–2638 (2001).
- ⁹ L.F. Eugene Olevsky, "Constitutive modeling of spark-plasma sintering of conductive materials," *Scr. Mater.*, **55** [12] 1175–1178 (2006).
- ¹⁰ R. Chaim, "Densification mechanisms in spark plasma sintering of nanocrystalline ceramics," *Mater. Sci. Eng. A*, **443** [1–2] 25–32 (2007).
- ¹¹ E.A. Olevsky, S. Kandukuri, and L. Froyen, "Analysis of Mechanisms of Spark-Plasma Sintering," *Key Eng. Mater.*, **368** 1580–1584 (2008).
- ¹² E.A. Olevsky and L. Froyen, "Impact of Thermal Diffusion on Densification During SPS," *J. Am. Ceram. Soc.*, **92** S122–S132 (2009).

- ¹³ E. Olevsky, I. Bogachev, and A. Maximenko, "Spark-plasma sintering efficiency control by inter-particle contact area growth: A viewpoint," *Scr. Mater.*, **69** [2] 112–116 (2013).
- ¹⁴ J. Langer, M.J. Hoffmann, and O. Guillon, "Direct comparison between hot pressing and electric field-assisted sintering of submicron alumina," *Acta Mater.*, **57** [18] 5454–5465 (2009).
- ¹⁵ J. Langer, M.J. Hoffmann, and O. Guillon, "Electric Field-Assisted Sintering in Comparison with the Hot Pressing of Yttria-Stabilized Zirconia," *J. Am. Ceram. Soc.*, **94** [1] 24–31 (2011).
- ¹⁶ X. Wei, C. Back, O. Izhvanov, C.D. Haines, and E.A. Olevsky, "Zirconium Carbide Produced by Spark Plasma Sintering and Hot Pressing: Densification Kinetics, Grain Growth, and Thermal Properties," *Materials*, **9** [7] 577 (2016).
- ¹⁷ O. Guillon, J. Gonzalez-Julian, B. Dargatz, T. Kessel, G. Schierning, J. Räthel, and M. Herrmann, "Field-Assisted Sintering Technology/Spark Plasma Sintering: Mechanisms, Materials, and Technology Developments," *Adv. Eng. Mater.*, **16** [7] 830–849 (2014).
- ¹⁸ M. Cologna, B. Rashkova, and R. Raj, "Flash Sintering of Nanograin Zirconia in <5 s at 850°C," *J. Am. Ceram. Soc.*, **93** [11] 3556–3559 (2010).
- ¹⁹ M. Cologna, J.S.C. Francis, and R. Raj, "Field assisted and flash sintering of alumina and its relationship to conductivity and MgO-doping," *J. Eur. Ceram. Soc.*, **31** [15] 2827–2837 (2011).
- ²⁰ M. Cologna, A.L.G. Prette, and R. Raj, "Flash-Sintering of Cubic Yttria-Stabilized Zirconia at 750°C for Possible Use in SOFC Manufacturing," *J. Am. Ceram. Soc.*, **94** [2] 316–319 (2011).
- ²¹ J.S.C. Francis, M. Cologna, and R. Raj, "Particle size effects in flash sintering," *J. Eur. Ceram. Soc.*, **32** [12] 3129–3136 (2012).
- ²² R. Raj, "Joule heating during flash-sintering," *J. Eur. Ceram. Soc.*, **32** [10] 2293–2301 (2012).
- ²³ Y. Zhang, J.-I. Jung, and J. Luo, "Thermal runaway, flash sintering and asymmetrical microstructural development of ZnO and ZnO–Bi₂O₃ under direct currents," *Acta Mater.*, **94** 87–100 (2015).
- ²⁴ Y. Zhang and J. Luo, "Promoting the flash sintering of ZnO in reduced atmospheres to achieve nearly full densities at furnace temperatures of <120 °C," *Scr. Mater.*, **106** 26–29 (2015).

- ²⁵ J.G. Pereira da Silva, J.-M. Lebrun, H.A. Al-Qureshi, R. Janssen, and R. Raj, "Temperature Distributions During Flash Sintering of 8% Yttria-Stabilized Zirconia," *J. Am. Ceram. Soc.*, **98** [11] 3525–3528 (2015).
- ²⁶ J.G.P. da Silva, H.A. Al-Qureshi, F. Keil, and R. Janssen, "A dynamic bifurcation criterion for thermal runaway during the flash sintering of ceramics," *J. Eur. Ceram. Soc.*, **36** [5] 1261–1267 (2016).
- ²⁷ R.I. Todd, E. Zapata-Solvas, R.S. Bonilla, T. Sneddon, and P.R. Wilshaw, "Electrical characteristics of flash sintering: thermal runaway of Joule heating," *J. Eur. Ceram. Soc.*, **35** [6] 1865–1877 (2015).
- ²⁸ E. Zapata-Solvas, S. Bonilla, P.R. Wilshaw, and R.I. Todd, "Preliminary investigation of flash sintering of SiC," *J. Eur. Ceram. Soc.*, **33** [13–14] 2811–2816 (2013).
- ²⁹ Y. Dong and I.-W. Chen, "Onset Criterion for Flash Sintering," *J. Am. Ceram. Soc.*, **98** [12] 3624–3627 (2015).
- ³⁰ Y. Dong and I.-W. Chen, "Predicting the Onset of Flash Sintering," *J. Am. Ceram. Soc.*, **98** [8] 2333–2335 (2015).
- ³¹ M.S. Yurlova, V.D. Demenyuk, L.Y. Lebedeva, D.V. Dudina, E.G. Grigoryev, and E.A. Olevsky, "Electric pulse consolidation: an alternative to spark plasma sintering," *J. Mater. Sci.*, **49** [3] 952–985 (2013).
- ³² G. Lee, M.S. Yurlova, D. Giuntini, E.G. Grigoryev, O.L. Khasanov, J. McKittrick, and E.A. Olevsky, "Densification of zirconium nitride by spark plasma sintering and high voltage electric discharge consolidation: A comparative analysis," *Ceram. Int.*, **41** [10] 14973–14987 (2015).
- ³³ R. Roy, D. Agrawal, J. Cheng, and S. Gedevisanishvili, "Full sintering of powdered-metal bodies in a microwave field," *Nature*, **399** [6737] 668–670 (1999).
- ³⁴ M. Oghbaei and O. Mirzaee, "Microwave versus conventional sintering: A review of fundamentals, advantages and applications," *J. Alloys Compd.*, **494** [1–2] 175–189 (2010).
- ³⁵ F. Xue, J. Lu, and J. Ma, "Theoretical study of densification of nano-sized 3Y-TZP powder: density-grain growth coupling model," *J. Nanoparticle Res.*, **11** [7] 1719–1727 (2008).
- ³⁶ R. Chaim, R. Marder-Jaeckel, and J.Z. Shen, "Transparent YAG ceramics by surface softening of nanoparticles in spark plasma sintering," *Mater. Sci. Eng. A*, **429** [1–2] 74–78 (2006).

- ³⁷ R. Chaim, Z. Shen, and M. Nygren, "Transparent nanocrystalline MgO by rapid and low-temperature spark plasma sintering," *J. Mater. Res.*, **19** [9] 2527–2531 (2004).
- ³⁸ R. Chaim, A. Shlayer, and C. Estournes, "Densification of nanocrystalline Y2O3 ceramic powder by spark plasma sintering," *J. Eur. Ceram. Soc.*, **29** [1] 91–98 (2009).
- ³⁹ N. Millot, S. Le Gallet, D. Aymes, F. Bernard, and Y. Grin, "Spark plasma sintering of cobalt ferrite nanopowders prepared by coprecipitation and hydrothermal synthesis," *J. Eur. Ceram. Soc.*, **27** [2–3] 921–926 (2007).
- ⁴⁰ M.A. Yar, S. Wahlberg, H. Bergqvist, H.G. Salem, M. Johnsson, and M. Muhammed, "Spark plasma sintering of tungsten–yttrium oxide composites from chemically synthesized nanopowders and microstructural characterization," *J. Nucl. Mater.*, **412** [2] 227–232 (2011).
- ⁴¹ X. Deng, X. Wang, H. Wen, A. Kang, Z. Gui, and L. Li, "Phase Transitions in Nanocrystalline Barium Titanate Ceramics Prepared by Spark Plasma Sintering," *J. Am. Ceram. Soc.*, **89** [3] 1059–1064 (2006).
- ⁴² X. Zhou, D.M. Hulbert, J.D. Kuntz, R.K. Sadangi, V. Shukla, B.H. Kear, and A.K. Mukherjee, "Superplasticity of zirconia–alumina–spinel nanoceramic composite by spark plasma sintering of plasma sprayed powders," *Mater. Sci. Eng. A*, **394** [1–2] 353–359 (2005).
- ⁴³ G. Bonnefont, G. Fantozzi, S. Trombert, and L. Bonneau, "Fine-grained transparent MgAl2O4 spinel obtained by spark plasma sintering of commercially available nanopowders," *Ceram. Int.*, **38** [1] 131–140 (2012).
- ⁴⁴ O.A. Graeve, R. Kanakala, L. Kaufman, K. Sinha, E. Wang, B. Pearson, G. Rojas-George, and J.C. Farmer, "Spark plasma sintering of Fe-based structural amorphous metals (SAM) with Y2O3 nanoparticle additions," *Mater. Lett.*, **62** [17–18] 2988–2991 (2008).
- ⁴⁵ E.H. Penilla, Y. Kodera, and J.E. Garay, "Blue–Green Emission in Terbium-Doped Alumina (Tb:Al2O3) Transparent Ceramics," *Adv. Funct. Mater.*, **23** [48] 6036–6043 (2013).
- ⁴⁶ E.H. Penilla, Y. Kodera, and J.E. Garay, "Simultaneous synthesis and densification of transparent, photoluminescent polycrystalline YAG by current activated pressure assisted densification (CAPAD)," *Mater. Sci. Eng. B*, **177** [14] 1178–1187 (2012).
- ⁴⁷ U. Anselmi-Tamburini, S. Gennari, J.E. Garay, and Z.A. Munir, "Fundamental investigations on the spark plasma sintering/synthesis process: II. Modeling of current and temperature distributions," *Mater. Sci. Eng. A*, **394** [1–2] 139–148 (2005).

- 48 U. Anselmi-Tamburini, J.E. Garay, Z.A. Munir, A. Tacca, F. Maglia, and G. Spinolo, "Spark plasma sintering and characterization of bulk nanostructured fully stabilized zirconia: Part I. Densification studies," *J. Mater. Res.*, **19** [11] 3255–3262 (2004).
- 49 U. Anselmi-Tamburini, J.E. Garay, Z.A. Munir, A. Tacca, F. Maglia, G. Chiodelli, and G. Spinolo, "Spark plasma sintering and characterization of bulk nanostructured fully stabilized zirconia: Part II. Characterization studies," *J. Mater. Res.*, **19** [11] 3263–3269 (2004).
- 50 Y. Kodera, C.L. Hardin, and J.E. Garay, "Transmitting, emitting and controlling light: Processing of transparent ceramics using current-activated pressure-assisted densification," *Scr. Mater.*, **69** [2] 149–154 (2013).
- 51 G.-D. Zhan, J. Kuntz, J. Wan, J. Garay, and A.K. Mukherjee, "Alumina-based nanocomposites consolidated by spark plasma sintering," *Scr. Mater.*, **47** [11] 737–741 (2002).
- 52 G.-D. Zhan, J. Kuntz, J. Wan, J. Garay, and A.K. Mukherjee, "Spark-plasma-sintered BaTiO₃/Al₂O₃ nanocomposites," *Mater. Sci. Eng. A*, **356** [1–2] 443–446 (2003).
- 53 G.-D. Zhan, J. Kuntz, J. Wan, J. Garay, and A.K. Mukherjee, "A Novel Processing Route to Develop a Dense Nanocrystalline Alumina Matrix (<100 nm) Nanocomposite Material," *J. Am. Ceram. Soc.*, **86** [1] 200–2002 (2003).
- 54 E.K.H. Li and P.D. Funkenbusch, "Modeling of the densification rates of monosized and bimodal-sized particle systems during hot isostatic pressing (HIP)," *Acta Metall.*, **37** [6] 1645–1655 (1989).
- 55 R.M. German, "Prediction of sintered density for bimodal powder mixtures," *Metall. Trans. A*, **23** [5] 1455–1465 (1992).
- 56 J. Pan, H. Le, S. Kucherenko, and J.A. Yeomans, "A model for the sintering of spherical particles of different sizes by solid state diffusion," *Acta Mater.*, **46** [13] 4671–4690 (1998).
- 57 H.N. Chng and J. Pan, "Sintering of particles of different sizes," *Acta Mater.*, **55** [3] 813–824 (2007).
- 58 C.L. Martin and D. Bouvard, "Isostatic compaction of bimodal powder mixtures and composites," *Int. J. Mech. Sci.*, **46** [6] 907–927 (2004).
- 59 J. Ma, J. Zhang, W. Liu, and Z. Shen, "Suppressing pore-boundary separation during spark plasma sintering of tungsten," *J. Nucl. Mater.*, **438** [1–3] 199–203 (2013).

- ⁶⁰ G. Petzow and H.E. Exner, "Particle Rearrangement in Solid State Sintering;" pp. 639–655 in *Sinter. Key Pap.* Edited by S. Sōmiya and Y. Moriyoshi. Springer Netherlands, 1990.
- ⁶¹ H.J. Leu, T. Hare, and R.O. Scattergood, "A computer simulation method for particle sintering," *Acta Metall.*, **36** [8] 1977–1987 (1988).
- ⁶² J.C. Kim, D.M. Martin, and C.S. Lim, "Effect of rearrangement on simulated particle packing," *Powder Technol.*, **126** [3] 211–216 (2002).
- ⁶³ C.L. Martin, D. Bouvard, and S. Shima, "Study of particle rearrangement during powder compaction by the Discrete Element Method," *J. Mech. Phys. Solids*, **51** [4] 667–693 (2003).
- ⁶⁴ B. Henrich, A. Wonisch, T. Kraft, M. Moseler, and H. Riedel, "Simulations of the influence of rearrangement during sintering," *Acta Mater.*, **55** [2] 753–762 (2007).
- ⁶⁵ E. Olevsky, H.J. Dudek, and W.A. Kaysser, "HIPing conditions for processing of metal matrix composites using the continuum theory for sintering—I. Theoretical analysis," *Acta Mater.*, **44** [2] 707–713 (1996).
- ⁶⁶ G. Bolzon, E.J. Chiarullo, P. Egizabal, and C. Estournes, "Constitutive modelling and mechanical characterization of aluminium-based metal matrix composites produced by spark plasma sintering," *Mech. Mater.*, **42** [5] 548–558 (2010).
- ⁶⁷ L. Olmos, C.L. Martin, and D. Bouvard, "Sintering of mixtures of powders: Experiments and modelling," *Powder Technol.*, **190** [1–2] 134–140 (2009).
- ⁶⁸ V. Marcadon, E. Roques, and F. Feyel, "Modelling of the Mechanical Behaviour of Regular Metallic Hollow-Sphere Packings under Compressive Loads;" pp. 91–99 in *Mech. Microstruct. Solids*. Edited by J.-F. Ganghoffer and F. Pastrone. Springer Berlin Heidelberg, 2009.
- ⁶⁹ V.V. Skorokhod, E.A. Olevskii, and M.B. Shtern, "Continuum theory of sintering. III. Effect of inhomogeneous distribution of properties in compacts and of pressing conditions on the kinetics of sintering," *Powder Metall. Met. Ceram.*, **32** [3] 208–213 (1993).
- ⁷⁰ W.H. Rhodes, "Agglomerate and Particle Size Effects on Sintering Yttria-Stabilized Zirconia," *J. Am. Ceram. Soc.*, **64** [1] 19–22 (1981).
- ⁷¹ F.F. Lange, "Sinterability of Agglomerated Powders," *J. Am. Ceram. Soc.*, **67** [2] 83–89 (1984).

- ⁷² D. Giuntini, X. Wei, A.L. Maximenko, L. Wei, A.M. Ilyina, and E.A. Olevsky, "Initial stage of Free Pressureless Spark-Plasma Sintering of vanadium carbide: Determination of surface diffusion parameters," *Int. J. Refract. Met. Hard Mater.*, **41** 501–506 (2013).
- ⁷³ A.G. Evans and C.H. Hsueh, "Behavior of Large Pores During Sintering and Hot Isostatic Pressing," *J. Am. Ceram. Soc.*, **69** [6] 444–448 (1986).
- ⁷⁴ C.-H. Hsueh, "Sintering behaviour of powder compacts with multiheterogeneities," *J. Mater. Sci.*, **21** [6] 2067–2072 (1986).
- ⁷⁵ L.C. De Jonghe, M.N. Rahaman, and C.H. Hsueh, "Transient stresses in bimodal compacts during sintering," *Acta Metall.*, **34** [7] 1467–1471 (1986).
- ⁷⁶ B. Kellett and F.F. Lange, "Stresses Induced by Differential Sintering in Powder Compacts," *J. Am. Ceram. Soc.*, **67** [5] 369–371 (1984).
- ⁷⁷ D.-M. Liu, J.-T. Lin, and W.H. Tuan, "Interdependence between green compact property and powder agglomeration and their relation to the sintering behaviour of zirconia powder," *Ceram. Int.*, **25** [6] 551–559 (1999).
- ⁷⁸ C.F. Tang, F. Pan, X.H. Qu, C.C. Jia, B.H. Duan, and X.B. He, "Spark plasma sintering cobalt base superalloy strengthened by Y–Cr–O compound through high-energy milling," *J. Mater. Process. Technol.*, **204** [1–3] 111–116 (2008).
- ⁷⁹ S. Linardos, Q. Zhang, and J.R. Alcock, "An investigation of the parameters effecting the agglomerate size of a PZT ceramic powder prepared with a sol–gel technique," *J. Eur. Ceram. Soc.*, **27** [1] 231–235 (2007).
- ⁸⁰ M. Suárez, A. Fernández, J.L. Menéndez, and R. Torrecillas, "Transparent Yttrium Aluminium Garnet Obtained by Spark Plasma Sintering of Lyophilized Gels," *J Nanomater.*, **2009** 20:1–20:5 (2009).
- ⁸¹ B.Y. Hanbin Chen, "Effect of Precipitations on Microstructures and Mechanical Properties of Nanostructured Al-Zn-Mg-Cu Alloy," *Mater. Trans. - MATER TRANS*, **49** [12] 2912–2915 (2008).
- ⁸² K.B. Zhang, Z.Y. Fu, J.Y. Zhang, W.M. Wang, S.W. Lee, and K. Niihara, "Characterization of nanocrystalline CoCrFeNiTiAl high-entropy solid solution processed by mechanical alloying," *J. Alloys Compd.*, **495** [1] 33–38 (2010).
- ⁸³ M. Muroi, G. Trotter, P.G. McCormick, M. Kawahara, and M. Tokita, "Preparation of nano-grained zirconia ceramics by low-temperature, low-pressure spark plasma sintering," *J. Mater. Sci.*, **43** [19] 6376–6384 (2008).

- ⁸⁴ H.K. Schmid, M. Aslan, S. Assmann, R. Naß, and H. Schmidt, "Microstructural characterization of Al₂O₃-SiC nanocomposites," *J. Eur. Ceram. Soc.*, **18** [1] 39–49 (1998).
- ⁸⁵ X. Liu, C. Jia, X. Chen, and G. Gai, "Fabrication of Nano-Al₂O₃/Cu Composite With Powder Treated by Spherical Process," *J. Iron Steel Res. Int.*, **14** [5] 94–98 (2007).
- ⁸⁶ W.M. Daoush, "Processing and characterization of CNT/Cu nanocomposites by powder technology," *Powder Metall. Met. Ceram.*, **47** [9–10] 531–537 (2009).
- ⁸⁷ F.C. Robles-Hernández and H.A. Calderon, "Nanostructured metal composites reinforced with fullerenes," *JOM*, **62** [2] 63–68 (2010).
- ⁸⁸ G. Cabouro, S. Le Gallet, S. Chevalier, E. Gaffet, Y. Grin, and F. Bernard, "Dense MoSi₂ produced by reactive flash sintering: Control of Mo/Si agglomerates prepared by high-energy ball milling," *Powder Technol.*, **208** [2] 526–531 (2011).
- ⁸⁹ A.Z. Lichtner, D. Jauffrès, C.L. Martin, and R.K. Bordia, "Processing of Hierarchical and Anisotropic Porosity LSM-YSZ Composites," *J. Am. Ceram. Soc.*, **96** [9] 2745–2753 (2013).
- ⁹⁰ H. Shang, A. Mohanram, and R.K. Bordia, "Densification and Microstructural Evolution of Hierarchically Porous Ceramics During Sintering," *J. Am. Ceram. Soc.*, **98** [11] 3424–3430 (2015).
- ⁹¹ H. Shang, A. Mohanram, E. Olevsky, and R.K. Bordia, "Evolution of anisotropy in hierarchical porous ceramics during sinter-forging," *J. Eur. Ceram. Soc.*, **36** [12] 2937–2945 (2016).
- ⁹² U. Anselmi-Tamburini, J.E. Garay, and Z.A. Munir, "Fast low-temperature consolidation of bulk nanometric ceramic materials," *Scr. Mater.*, **54** [5] 823–828 (2006).
- ⁹³ K. Ada, M. Önal, and Y. Sarıkaya, "Investigation of the intra-particle sintering kinetics of a mainly agglomerated alumina powder by using surface area reduction," *Powder Technol.*, **168** [1] 37–41 (2006).
- ⁹⁴ J.-S. Lee, J.-P. Choi, and G.-Y. Lee, "Consolidation of Hierarchy-Structured Nanopowder Agglomerates and Its Application to Net-Shaping Nanopowder," *Materials*, **6** [9] 4046–4063 (2013).
- ⁹⁵ G.W. Scherer, "Viscous Sintering of a Bimodal Pore-Size Distribution," *J. Am. Ceram. Soc.*, **67** [11] 709–715 (1984).

- ⁹⁶ R.M. Kadushnikov, D.M. Alievskii, V.M. Alievskii, and A.R. Beketov, "Computer simulation for microstructure evolution in a polydisperse material on sintering. Part 2. Zoned segregation," *Sov. Powder Metall. Met. Ceram.*, **30** [5] 356–360 (1991).
- ⁹⁷ R.M. Kadushnikov, I.G. Kamenin, and A.R. Beketov, "Computer simulation of the evolution of the microstructure of polydispersed materials. III. Normal grain growth," *Sov. Powder Metall. Met. Ceram.*, **30** [6] 462–465 (1991).
- ⁹⁸ J. Liu and R.M. German, "Distance or Spacing Parameters in Agglomerated Monosized Spherical Particulate Systems," *Part. Part. Syst. Charact.*, **16** [1] 35–38 (1999).
- ⁹⁹ C.M. Kong and J.J. Lannutti, "Effect of Agglomerate Size Distribution on Loose Packing Fraction," *J. Am. Ceram. Soc.*, **83** [9] 2183–2188 (2000).
- ¹⁰⁰ C.L. Martin, D. Bouvard, and G. Delette, "Discrete Element Simulations of the Compaction of Aggregated Ceramic Powders," *J. Am. Ceram. Soc.*, **89** [11] 3379–3387 (2006).
- ¹⁰¹ G. Perrin and J.-B. Leblond, "Accelerated void growth in porous ductile solids containing two populations of cavities," *Int. J. Plast.*, **16** [1] 91–120 (2000).
- ¹⁰² A.L. Gurson, "Continuum Theory of Ductile Rupture by Void Nucleation and Growth: Part I—Yield Criteria and Flow Rules for Porous Ductile Media," *J. Eng. Mater. Technol.*, **99** [1] 2–15 (1977).
- ¹⁰³ E. Olevsky and R. Rein, "Kinetics of sintering for powder systems with bimodal pore-size distribution," pp. 81–90 in *High Temp. High Press.* Pion, 1995.
- ¹⁰⁴ A.V. Kuz'mov and M.B. Shtern, "Mechanics of Sintering Materials with Bimodal Pore Distribution. I. Effective Characteristics of Biporous Materials and Equations for the Evolution of Pores of Different Radii," *Powder Metall. Met. Ceram.*, **44** [9–10] 429–434 (2005).
- ¹⁰⁵ M.B. Shtern, A.V. Kuz'mov, V.V. Skorokhod, and E. Olevskii, "Sintering stability of biporous materials under kinematic constraints," *Powder Metall. Met. Ceram.*, **49** [1–2] 17–23 (2010).
- ¹⁰⁶ M. Shtern, A. Kuzmov, V. Skorokhod, and E. Olevsky, "Influence of external constraints on the stability of sintering of bi-porous materials," *Model. Simul. Mater. Sci. Eng.*, **19** [1] 15001 (2011).
- ¹⁰⁷ V.V. Skorokhod, M.B. Shtern, A.V. Kuz'mov, and A.V. Ragulya, "Mechanics of sintering materials with bimodal pore distribution. III. Kinetics of sintering combined with various forms of loading and adhesion conditions," *Powder Metall. Met. Ceram.*, **45** [5–6] 221–225 (2006).

- ¹⁰⁸ V.V. Skorokhod and M.B. Shtern, "Mechanics of sintering materials with bimodal pore distribution. II. Mean-square strain rate for the solid phase of a biporous body and instability of the monomodal pore structure during constrained sintering," *Powder Metall. Met. Ceram.*, **45** [1–2] 28–34 (2006).
- ¹⁰⁹ V.V. Skorokhod, "Viscous flow and sintering of porous bodies," *Sov. Powder Metall. Met. Ceram.*, **7** [12] 945–948 (1968).
- ¹¹⁰ V.V. Skorokhod, M.B. Shtern, and I.F. Martynova, "Theory of nonlinearly viscous and plastic behavior of porous materials," *Sov. Powder Metall. Met. Ceram.*, **26** [8] 621–626 (1987).
- ¹¹¹ V.V. Skorokhod, E.A. Olevskii, and M.B. Shtern, "Continuum theory of sintering. I. Phenomenological model. Analysis of the effect of external forces on the kinetics of sintering," *Powder Metall. Met. Ceram.*, **32** [1] 21–26 (1993).
- ¹¹² V.V. Skorokhod, E.A. Olevskii, and M.B. Shtern, "Continuum theory of sintering. II. Effect of the rheological properties of the solid phase on the kinetics of sintering," *Powder Metall. Met. Ceram.*, **32** [2] 112–117 (1993).
- ¹¹³ E.A. Olevsky, "Theory of sintering: from discrete to continuum," *Mater. Sci. Eng. R Rep.*, **23** [2] 41–100 (1998).
- ¹¹⁴ J.K. Mackenzie, "The Elastic Constants of a Solid containing Spherical Holes," *Proc. Phys. Soc. Sect. B*, **63** [1] 2 (1950).
- ¹¹⁵ R. Shuttleworth, "The Surface Tension of Solids," *Proc. Phys. Soc. Sect. A*, **63** [5] 444 (1950).
- ¹¹⁶ L.C. De Jonghe and M.L. Rahaman, "Pore Shrinkage and Sintering Stress," *J. Am. Ceram. Soc.*, **67** [10] C-214 (1984).
- ¹¹⁷ L.C. De Jonghe and M.N. Rahaman, "Sintering stress of homogeneous and heterogeneous powder compacts," *Acta Metall.*, **36** [1] 223–229 (1988).
- ¹¹⁸ M.N. Rahaman, L.C. De Jonghe, and M.-Y. Chu, "Effect of Green Density on Densification and Creep During Sintering," *J. Am. Ceram. Soc.*, **74** [3] 514–519 (1991).
- ¹¹⁹ M.N. Rahaman, L.C. De Jonghe, and R.J. Brook, "Effect of Shear Stress on Sintering," *J. Am. Ceram. Soc.*, **69** [1] 53–58 (1986).
- ¹²⁰ T.B. Bhat and V.S. Arunachalam, "Inhomogeneous flow and the effective pressure concept in pressure sintering," *J. Mater. Sci.*, **15** 1614–1618 (1980).

- ¹²¹ R.A. Gregg and F.N. Rhines, "Surface tension and the sintering force in copper," *Metall. Trans.*, **4** [5] 1365–1374 (1973).
- ¹²² C. Herring, "Surface Tension as a Motivation for Sintering;" pp. 33–69 in *Fundam. Contrib. Contin. Theory Evol. Phase Interfaces Solids*. Edited by P.J.M. Ball, P.D. Kinderlehrer, P.P. Podio-Guidugli and P.M. Slemrod. Springer Berlin Heidelberg, 1999.
- ¹²³ R. Raj, "Analysis of the Sintering Pressure," *J. Am. Ceram. Soc.*, **70** [9] C-210 (1987).
- ¹²⁴ S.-J.L. Kang, "Comment on 'Analysis of the Sintering Pressure,'" *J. Am. Ceram. Soc.*, **76** [7] 1902–1902 (1993).
- ¹²⁵ R. Raj, "Reply to 'Comment on 'Analysis of the Sintering Pressure,'" *J. Am. Ceram. Soc.*, **76** [7] 1903–1903 (1993).
- ¹²⁶ C.R. Reid and R.G. Oakberg, "A continuum theory for the mechanical response of materials to the thermodynamic stress of sintering," *Mech. Mater.*, **10** [3] 203–213 (1990).
- ¹²⁷ K. Shinagawa, "Micromechanical modelling of viscous sintering and a constitutive equation with sintering stress," *Comput. Mater. Sci.*, **13** [4] 276–285 (1999).
- ¹²⁸ J. Svoboda and H. Riedel, "Pore-boundary interactions and evolution equations for the porosity and the grain size during sintering," *Acta Metall. Mater.*, **40** [11] 2829–2840 (1992).
- ¹²⁹ J. Svoboda, H. Riedel, and H. Zipse, "Equilibrium pore surfaces, sintering stresses and constitutive equations for the intermediate and late stages of sintering—I. computation of equilibrium surfaces," *Acta Metall. Mater.*, **42** [2] 435–443 (1994).
- ¹³⁰ P.Z. Cai, G.L. Messing, and D.J. Green, "Determination of the Mechanical Response of Sintering Compacts by Cyclic Loading Dilatometry," *J. Am. Ceram. Soc.*, **80** [2] 445–452 (1997).
- ¹³¹ M.-Y. Chu, L.C. De Jonghe, M.K.F. Lin, and F.J.T. Lin, "Precoarsening to Improve Microstructure and Sintering of Powder Compacts," *J. Am. Ceram. Soc.*, **74** [11] 2902–2911 (1991).
- ¹³² O. Gillia and D. Bouvard, "Phenomenological analysis of densification kinetics during sintering: application to WC–Co mixture," *Mater. Sci. Eng. A*, **279** [1–2] 185–191 (2000).

- ¹³³ F. Wakai and O. Guillon, "Evaluation of sintering stress from 3-D visualization of microstructure: Case study of glass films sintered by viscous flow and imaged by X-ray microtomography," *Acta Mater.*, **66** 54–62 (2014).
- ¹³⁴ J. Song, J.C. Gelin, T. Barrière, and B. Liu, "Experiments and numerical modelling of solid state sintering for 316L stainless steel components," *J. Mater. Process. Technol.*, **177** [1–3] 352–355 (2006).
- ¹³⁵ R. Zuo, E. Aulbach, and J. Rödel, "Experimental determination of sintering stresses and sintering viscosities," *Acta Mater.*, **51** [15] 4563–4574 (2003).
- ¹³⁶ M. Gasik and B. Zhang, "A constitutive model and FE simulation for the sintering process of powder compacts," *Comput. Mater. Sci.*, **18** [1] 93–101 (2000).
- ¹³⁷ T. Kraft and H. Riedel, "Numerical simulation of solid state sintering; model and application," *J. Eur. Ceram. Soc.*, **24** [2] 345–361 (2004).
- ¹³⁸ F. Wakai, Y. Shinoda, and T. Akatsu, "Methods to calculate sintering stress of porous materials in equilibrium," *Acta Mater.*, **52** [19] 5621–5631 (2004).
- ¹³⁹ F. Wakai and Y. Shinoda, "Anisotropic sintering stress for sintering of particles arranged in orthotropic symmetry," *Acta Mater.*, **57** [13] 3955–3964 (2009).
- ¹⁴⁰ R.L. Coble and W.D. Kingery, "Effect of Porosity on Physical Properties of Sintered Alumina," *J. Am. Ceram. Soc.*, **39** [11] 377–385 (1956).
- ¹⁴¹ W.D. Kingery and M. Berg, "Study of the Initial Stages of Sintering Solids by Viscous Flow, Evaporation-Condensation, and Self-Diffusion," *J. Appl. Phys.*, **26** [10] 1205–1212 (1955).
- ¹⁴² W.D. Kingery and B. Francois, "The Sintering of Crystalline Oxides. I. Interactions between Grain Boundaries and Pores.," *Sinter. Relat. Phenom. Proc. Int. Conf. Univ Notre Dame*, 471–498 (1968).
- ¹⁴³ R.L. Coble, "Sintering Crystalline Solids. I. Intermediate and Final State Diffusion Models," *J. Appl. Phys.*, **32** [5] 787–792 (1961).
- ¹⁴⁴ J. Besson and M. Abouaf, "Rheology of Porous Alumina and Simulation of Hot Isostatic Pressing," *J. Am. Ceram. Soc.*, **75** [8] 2165–2172 (1992).
- ¹⁴⁵ É.T. Denisenko and V.K. Mai, "Densification kinetics in the hot pressing of metal powders," *Sov. Powder Metall. Met. Ceram.*, **7** [11] 858–862 (1968).

- ¹⁴⁶ W.R. Cannon and T.G. Langdon, “Creep of ceramics,” *J. Mater. Sci.*, **23** [1] 1–20 (1988).
- ¹⁴⁷ W.R. Cannon and T.G. Langdon, “Creep of ceramics,” *J. Mater. Sci.*, **18** [1] 1–50 (1983).
- ¹⁴⁸ I. Finnie and W.R. Heller, *Creep of engineering materials*. McGraw-Hill, 1959.
- ¹⁴⁹ H. Altenbach, Y. Gorash, and K. Naumenko, “Steady-state creep of a pressurized thick cylinder in both the linear and the power law ranges,” *Acta Mech.*, **195** [1–4] 263–274 (2008).
- ¹⁵⁰ S.M. Mkhitarian, “Solution of the first boundary value problem of nonlinear theory of steady-state creep for a half-space in antiplane deformation,” *Mech. Solids*, **47** [6] 646–653 (2013).
- ¹⁵¹ L.T. Kuhn and R.M. McMeeking, “Power-law creep of powder bonded by isolated contacts,” *Int. J. Mech. Sci.*, **34** [7] 563–573 (1992).
- ¹⁵² D.S. Wilkinson and M.F. Ashby, “Pressure sintering by power law creep,” *Acta Metall.*, **23** [11] 1277–1285 (1975).
- ¹⁵³ L. Banks-Sills and B. Budiansky, “On void collapse in viscous solids,” *Mech. Mater.*, **1** [3] 209–218 (1982).
- ¹⁵⁴ M. Abouaf, J.L. Chenot, G. Raison, and P. Bauduin, “Finite element simulation of hot isostatic pressing of metal powders,” *Int. J. Numer. Methods Eng.*, **25** [1] 191–212 (1988).
- ¹⁵⁵ P. Sofronis and R.M. McMeeking, “Creep of Power-Law Material Containing Spherical Voids,” *J. Appl. Mech.*, **59** [2S] S88–S95 (1992).
- ¹⁵⁶ J.M. Duva and P.D. Crow, “The densification of powders by power-law creep during hot isostatic pressing,” *Acta Metall. Mater.*, **40** [1] 31–35 (1992).
- ¹⁵⁷ Y.S. Lee and K.T. Kim, “An Analysis of Void Deformation Caused by Power Law Creep and Diffusion Enhanced by Mechanical Stress in HIP Process,” *J. Manuf. Sci. Eng.*, **114** [3] 277–283 (1992).
- ¹⁵⁸ A.C.F. Cocks, “Overview no. 117 The structure of constitutive laws for the sintering of fine grained materials,” *Acta Metall. Mater.*, **42** [7] 2191–2210 (1994).

- ¹⁵⁹ C. Geindreau, D. Bouvard, and P. Doremus, “Constitutive behaviour of metal powder during hot forming. Part I: Experimental investigation with lead powder as a simulation material,” *Eur. J. Mech. - ASolids*, **18** [4] 581–596 (1999).
- ¹⁶⁰ C. Geindreau, D. Bouvard, and P. Doremus, “Constitutive behaviour of metal powder during hot forming.: Part II: Unified viscoplastic modelling,” *Eur. J. Mech. - ASolids*, **18** [4] 597–615 (1999).
- ¹⁶¹ C.Y. Hsu, B.J. Lee, and M.E. Mear, “Constitutive models for power-law viscous solids containing spherical voids,” *Int. J. Plast.*, **25** [1] 134–160 (2009).
- ¹⁶² M.M. Carroll and A.C. Holt, “Static and Dynamic Pore-Collapse Relations for Ductile Porous Materials,” *J. Appl. Phys.*, **43** [4] 1626–1636 (1972).
- ¹⁶³ B.M. Butcher, M.M. Carroll, and A.C. Holt, “Shock-wave compaction of porous aluminum,” *J. Appl. Phys.*, **45** [9] 3864–3875 (1974).
- ¹⁶⁴ M.M. Carroll, K.T. Kim, and V.F. Nesterenko, “The effect of temperature on viscoplastic pore collapse,” *J. Appl. Phys.*, **59** [6] 1962–1967 (1986).
- ¹⁶⁵ H.J. Frost and M.F. Ashby, *Deformation-Mechanism Maps*. Pergamon, Oxford, 1982.
- ¹⁶⁶ F.H. Norton, *The creep of steel at high temperatures*. McGraw-Hill, New York, 1929.
- ¹⁶⁷ P.S. Follansbee and U.F. Kocks, “A constitutive description of the deformation of copper based on the use of the mechanical threshold stress as an internal state variable,” *Acta Metall.*, **36** [1] 81–93 (1988).
- ¹⁶⁸ I. Schindler, J. Kliber, and J. Bořuta, “Predictive model for deformation resistance in rolling based on torsion parameters,” *Mater. Sci. Technol.*, **4** [4] 354–360 (1988).
- ¹⁶⁹ I. Schindler, M. Strakoš, and L. Šrámek, “Influence of carbon and temperature on the strain rate sensitivity of carbon steels,” *Scr. Metall.*, **23** [10] 1669–1672 (1989).
- ¹⁷⁰ E. Olevsky and A. Molinari, “Instability of sintering of porous bodies,” *Int. J. Plast.*, **16** [1] 1–37 (2000).
- ¹⁷¹ S. Grasso and Y. Sakka, “Electric field in SPS: geometry and pulsed current effects,” *J. Ceram. Soc. Jpn.*, **121** [1414] 524–526 (2013).
- ¹⁷² S. Muñoz and U. Anselmi-Tamburini, “Parametric investigation of temperature distribution in field activated sintering apparatus,” *Int. J. Adv. Manuf. Technol.*, **65** [1–4] 127–140 (2012).

- ¹⁷³ D. Giuntini, E.A. Olevsky, C. Garcia-Cardona, A.L. Maximenko, M.S. Yurlova, C.D. Haines, D.G. Martin, and D. Kapoor, “Localized Overheating Phenomena and Optimization of Spark-Plasma Sintering Tooling Design,” *Materials*, **6** [7] 2612–2632 (2013).
- ¹⁷⁴ D. Giuntini, J. Raethel, M. Herrmann, A. Michaelis, C.D. Haines, and E.A. Olevsky, “Spark plasma sintering novel tooling design: temperature uniformization during consolidation of silicon nitride powder,” *J. Ceram. Soc. Jpn.*, **124** [4] 403–414 (2016).
- ¹⁷⁵ D. Giuntini, J. Raethel, M. Herrmann, A. Michaelis, and E.A. Olevsky, “Advancement of Tooling for Spark Plasma Sintering,” *J. Am. Ceram. Soc.*, **98** [11] 3529–3537 (2015).
- ¹⁷⁶ M. Tokita, “Large-Size-WC/Co Functionally Graded Materials Fabricated by Spark Plasma Sintering (SPS) Method,” *Mater. Sci. Forum*, **423–425** 39–44 (2003).
- ¹⁷⁷ G. Majkic, N. Chennoufi, Y.C. Chen, and K. Salama, “Synthesis of NiTi by Low Electrothermal Loss Spark Plasma Sintering,” *Metall. Mater. Trans. A*, **38** [10] 2523–2530 (2007).
- ¹⁷⁸ N. Chennoufi, G. Majkic, Y.C. Chen, and K. Salama, “Temperature, Current, and Heat Loss Distributions in Reduced Electrothermal Loss Spark Plasma Sintering,” *Metall. Mater. Trans. A*, **40** [10] 2401–2409 (2009).
- ¹⁷⁹ D. Liu, Y. Xiong, Y. Li, T.D. Topping, Y. Zhou, C. Haines, J. Paras, D. Martin, *et al.*, “Spark Plasma Sintering of Nanostructured Aluminum: Influence of Tooling Material on Microstructure,” *Metall. Mater. Trans. A*, **44** [4] 1908–1916 (2012).
- ¹⁸⁰ J. Raethel, J. Hennicke, Y. Dyatlova, M. Herrmann, and V. Romyantsev, “New Developments of FAST/SPS Tool Materials,” *Adv. Sci. Technol.*, **88** 37–42 (2014).
- ¹⁸¹ C. Manière, L. Durand, A. Weibel, G. Chevallier, and C. Estournès, “A sacrificial material approach for spark plasma sintering of complex shapes,” *Scr. Mater.*, **124** 126–128 (2016).
- ¹⁸² S. Paris, E. Gaffet, D. Vrel, D. Thiaudiere, M. Gailhanou, and F. Bernard, “Time-resolved XRD experiments for a fine description of mechanisms induced during reactive sintering,” *Sci. Sinter.*, **37** [1] 27–34 (2005).
- ¹⁸³ R. Muccillo and E.N.S. Muccillo, “An experimental setup for shrinkage evaluation during electric field-assisted flash sintering: Application to yttria-stabilized zirconia,” *J. Eur. Ceram. Soc.*, **33** [3] 515–520 (2013).
- ¹⁸⁴ E.A. Olevsky, W.L. Bradbury, C.D. Haines, D.G. Martin, and D. Kapoor, “Fundamental Aspects of Spark Plasma Sintering: I. Experimental Analysis of Scalability,” *J. Am. Ceram. Soc.*, **95** [8] 2406–2413 (2012).

- ¹⁸⁵ E.A. Olevsky, C. Garcia-Cardona, W.L. Bradbury, C.D. Haines, D.G. Martin, and D. Kapoor, "Fundamental Aspects of Spark Plasma Sintering: II. Finite Element Analysis of Scalability," *J. Am. Ceram. Soc.*, **95** [8] 2414–2422 (2012).
- ¹⁸⁶ K. Vanmeensel, A. Laptev, J. Hennicke, J. Vleugels, and O. Van der Biest, "Modelling of the temperature distribution during field assisted sintering," *Acta Mater.*, **53** [16] 4379–4388 (2005).
- ¹⁸⁷ M. Tokita, "Development of Square-Shaped Large-Size WC/Co/Ni System FGM Fabricated by Spark Plasma Sintering (SPS) Method and Its Industrial Applications," *Mater. Sci. Forum*, **492–493** 711–718 (2005).
- ¹⁸⁸ M. Tokita, "Industrial applications of advanced spark plasma sintering," *Am Ceram Soc Bull*, **85** 2–32 (2006).
- ¹⁸⁹ S. Grasso, Y. Sakka, and G. Maizza, "Electric current activated/assisted sintering (ECAS): a review of patents 1906–2008," *Sci. Technol. Adv. Mater.*, **10** [5] 53001 (2009).
- ¹⁹⁰ E.A. Olevsky, E.V. Aleksandrova, A.M. Ilyina, D.V. Dudina, A.N. Novoselov, K.Y. Pelve, and E.G. Grigoryev, "Outside Mainstream Electronic Databases: Review of Studies Conducted in the USSR and Post-Soviet Countries on Electric Current-Assisted Consolidation of Powder," *Materials*, **6** [10] 4375–4440 (2013).
- ¹⁹¹ J. Schmidt, R. Niewa, M. Schmidt, and Y. Grin, "Spark Plasma Sintering Effect on the Decomposition of MgH₂," *J. Am. Ceram. Soc.*, **88** [7] 1870–1874 (2005).
- ¹⁹² K. Vanmeensel, A. Laptev, O. Van der Biest, and J. Vleugels, "The influence of percolation during pulsed electric current sintering of ZrO₂-TiN powder compacts with varying TiN content," *Acta Mater.*, **55** [5] 1801–1811 (2007).
- ¹⁹³ J. Schmidt, M. Boehling, U. Burkhardt, and Y. Grin, "Preparation of titanium diboride TiB₂ by spark plasma sintering at slow heating rate," *Sci. Technol. Adv. Mater.*, **8** [5] 376–382 (2007).
- ¹⁹⁴ R.S. Dohedoe, G.D. West, and M.H. Lewis, "Spark plasma sintering of ceramics: understanding temperature distribution enables more realistic comparison with conventional processing," *Adv. Appl. Ceram.*, **104** [3] 110–116 (2005).
- ¹⁹⁵ X. Liu, X. Song, and J. Zhang, "Temperature distribution simulation and neck evolution of powder particles during spark plasma sintering," *Chin Shu Hsueh Pao*, **42** [7] 757–762 (2006).
- ¹⁹⁶ A. Zavaliangos, J. Zhang, M. Krammer, and J.R. Groza, "Temperature evolution during field activated sintering," *Mater. Sci. Eng. A*, **379** [1–2] 218–228 (2004).

- ¹⁹⁷ B. McWilliams, A. Zavaliangos, K.C. Cho, and R.J. Dowding, "The modeling of electric-current-assisted sintering to produce bulk nanocrystalline tungsten," *JOM*, **58** [4] 67–71 (2006).
- ¹⁹⁸ K. Vanmeensel, A. Laptev, O. Van der Biest, and J. Vleugels, "Field assisted sintering of electro-conductive ZrO₂-based composites," *J. Eur. Ceram. Soc.*, **27** [2–3] 979–985 (2007).
- ¹⁹⁹ D. Tiwari, B. Basu, and K. Biswas, "Simulation of thermal and electric field evolution during spark plasma sintering," *Ceram. Int.*, **35** [2] 699–708 (2009).
- ²⁰⁰ Y. Cai, D. Zhao, X. Zhao, L. Chen, W. Jiang, and P. Zhai, "Modeling Temperature Gradient Evolution of CoSb₃ Material for Thermoelectric Devices during Spark Plasma Sintering," *Mater. Trans.*, **50** [4] 782–790 (2009).
- ²⁰¹ J. Räthel, M. Herrmann, and W. Beckert, "Temperature distribution for electrically conductive and non-conductive materials during Field Assisted Sintering (FAST)," *J. Eur. Ceram. Soc.*, **29** [8] 1419–1425 (2009).
- ²⁰² A. Cincotti, A.M. Locci, R. Orrù, and G. Cao, "Modeling of SPS apparatus: Temperature, current and strain distribution with no powders," *AIChE J.*, **53** [3] 703–719 (2007).
- ²⁰³ G. Antou, G. Mathieu, G. Trolliard, and A. Maître, "Spark plasma sintering of zirconium carbide and oxycarbide: Finite element modeling of current density, temperature, and stress distributions," *J. Mater. Res.*, **24** [2] 404–412 (2009).
- ²⁰⁴ G. Maizza, S. Grasso, and Y. Sakka, "Moving finite-element mesh model for aiding spark plasma sintering in current control mode of pure ultrafine WC powder," *J. Mater. Sci.*, **44** [5] 1219–1236 (2009).
- ²⁰⁵ S. Grasso, Y. Sakka, and G. Maizza, "Pressure Effects on Temperature Distribution during Spark Plasma Sintering with Graphite Sample," *Mater. Trans.*, **50** [8] 2111–2114 (2009).
- ²⁰⁶ C. Wang, L. Cheng, and Z. Zhao, "FEM analysis of the temperature and stress distribution in spark plasma sintering: Modelling and experimental validation," *Comput. Mater. Sci.*, **49** [2] 351–362 (2010).
- ²⁰⁷ M. Bellet, P. Mondalek, and L. Silva, "Numerical Modelling of SPS Process;" p. Pages 1340-1343 in *Met. Form. 2010*. Edited by J.L. Edited by Ken-ichiro Mori Maciej Pietrzyk, Jan Kusiak, Janusz Majta, Peter Hartley. Toyohashi, Japan, 2010.
- ²⁰⁸ S. Muñoz and U. Anselmi-Tamburini, "Temperature and stress fields evolution during spark plasma sintering processes," *J. Mater. Sci.*, **45** [23] 6528–6539 (2010).

- ²⁰⁹ J. Zhang and A. Zavaliangos, “Discrete Finite-Element Simulation of Thermoelectric Phenomena in Spark Plasma Sintering,” *J. Electron. Mater.*, **40** [5] 873–878 (2011).
- ²¹⁰ P. Mondalek, L. Silva, and M. Bellet, “A Numerical Model for Powder Densification by SPS Technique,” *Adv. Eng. Mater.*, **13** [7] 587–593 (2011).
- ²¹¹ Y. Song, Y. Li, Z. Zhou, Y. Lai, and Y. Ye, “A multi-field coupled FEM model for one-step-forming process of spark plasma sintering considering local densification of powder material,” *J. Mater. Sci.*, **46** [17] 5645–5656 (2011).
- ²¹² S. Wei, Z.-H. Zhang, X.-B. Shen, F.-C. Wang, M.-Y. Sun, R. Yang, and S.-K. Lee, “Simulation of temperature and stress distributions in functionally graded materials synthesized by a spark plasma sintering process,” *Comput. Mater. Sci.*, **60** 168–175 (2012).
- ²¹³ R. Barea Del Cerro, R. Martinez Rodriguez, and N. Candela Vazquez, “Spark Plasma Sintering (SPS) Control by Finite Element Method (FEM),” *DYNA*, **88** [2] 189–196 (2013).
- ²¹⁴ A. Maximenko, A. Kuzmov, E. Grigoryev, and E. Olevsky, “Direct Multi-Scale Modeling of Sintering,” *J. Am. Ceram. Soc.*, **95** [8] 2383–2388 (2012).
- ²¹⁵ E.A. Olevsky, V. Tikare, and T. Garino, “Multi-Scale Study of Sintering: A Review,” *J. Am. Ceram. Soc.*, **89** [6] 1914–1922 (2006).
- ²¹⁶ M.D. Sacks and J.A. Pask, “Sintering of Mullite-Containing Materials: II, Effect of Agglomeration,” *J. Am. Ceram. Soc.*, **65** [2] 70–77 (1982).
- ²¹⁷ M.F. Ashby, *HIP 6.0 Background reading*. University of Cambridge, Cambridge, 1990.
- ²¹⁸ D. Giuntini and E.A. Olevsky, “Sintering Kinetics of Agglomerated Powders with Nonlinear Viscous Rheology,” *Acta Mater.*, prepared for publication (n.d.).
- ²¹⁹ J.J. Frenkel, “Viscous flow of crystalline bodies under the action of surface tension,” *J Phys.*, **IX** [5] 385 (1945).
- ²²⁰ D. Giuntini and E.A. Olevsky, “Sintering stress for materials with nonlinear viscous rheology,” *Rapid Commun. J Am Ceram Soc*, accepted for publication (n.d.).
- ²²¹ R. Hill, “On Constitutive Macro-Variables for Heterogeneous Solids at Finite Strain,” *Proc. R. Soc. Lond. Math. Phys. Eng. Sci.*, **326** [1565] 131–147 (1972).
- ²²² H. Fröhlich and R. Sack, “Theory of the Rheological Properties of Dispersions,” *Proc. R. Soc. Lond. Ser. Math. Phys. Sci.*, **185** [1003] 415–430 (1946).

- 223 P.P. Castaneda and J.R. Willis, "On the Overall Properties of Nonlinearly Viscous Composites," *Proc. R. Soc. Lond. Math. Phys. Eng. Sci.*, **416** [1850] 217–244 (1988).
- 224 A. Molinari and G.R. Canova, "A self consistent approach of the large deformation polycrystal viscoplasticity," *Acta Metall.*, **35** [12] 2983–2994 (1987).
- 225 D.R.S. Talbot and J.R. Willis, "Variational Principles for Inhomogeneous Non-linear Media," *IMA J. Appl. Math.*, **35** [1] 39–54 (1985).
- 226 G.W. Scherer, "Sintering inhomogeneous glasses: Application to optical waveguides," *J. Non-Cryst. Solids*, **34** [2] 239–256 (1979).
- 227 D. Bouvard and R.M. McMeeking, "Deformation of Interparticle Necks by Diffusion-Controlled Creep," *J. Am. Ceram. Soc.*, **79** [3] 666–672 (1996).
- 228 R.M. German, *Sintering Theory and Practice*. 1996.
- 229 G.R. Karagedov and N.Z. Lyakhov, "Preparation and sintering of nanosized α -Al₂O₃ powder," *Nanostructured Mater.*, **11** [5] 559–572 (1999).
- 230 K. Bodišová, P. Šajgalík, D. Galusek, and P. Švančárek, "Two-Stage Sintering of Alumina with Submicrometer Grain Size," *J. Am. Ceram. Soc.*, **90** [1] 330–332 (2007).
- 231 W. Li, E.A. Olevsky, J. McKittrick, A.L. Maximenko, and R.M. German, "Densification mechanisms of spark plasma sintering: multi-step pressure dilatometry," *J. Mater. Sci.*, **47** [20] 7036–7046 (2012).
- 232 R.M. McMeeking and L.T. Kuhn, "A diffusional creep law for powder compacts," *Acta Metall. Mater.*, **40** [5] 961–969 (1992).
- 233 S. Taira, "Lifetime of Structures Subjected to Varying Load and Temperature," *Creep Struct. Colloq. Held Stanf. Univ.*, 96–124 (1960).
- 234 S. Taira and M. Ohnami, "Creep under Rapid Cyclic Temperatures," *Proc 3rd Jpn. Congr Test Mater*, 77–80 (1960).
- 235 S. Taira, K. Tanaka, and M. Ohnami, "Creep of Low Carbon Steel under Combined Variation of Stress and Temperature," *Proc 2nd Jpn. Congr Test Mater*, 50–54 (1959).
- 236 T. Nishihara, S. Taira, K. Tanaka, and M. Ohnami, "Creep of Low Carbon Steel under Varying Temperatures," *Proc 1st Jpn. Congr Test Mater*, 48–51 (1958).

- ²³⁷ M. Rieth, A. Falkenstein, P. Graf, S. Heger, U. Jaentsch, M. Klimiankou, E. Materna-Morris, and H. Zimmermann, *Creep of the Austenitic Steel AISI 316 L(N)*, (n.d.).
- ²³⁸ E.C. Muehleisen, C.R. Barrett, and W.D. Nix, "On the high temperature-low stress creep of copper," *Scr. Metall.*, **4** [12] 995–999 (1970).
- ²³⁹ H.D. Chandler, "Creep of copper in the temperature range 423–623 K," *Mater. Sci. Eng. A*, **169** [1] 27–32 (1993).
- ²⁴⁰ P. Feltham and R. Sinclair, "High-temperature creep of copper," *Acta Metall.*, **20** [9] 1095–1099 (1972).
- ²⁴¹ W.R. Cannon and O.D. Sherby, "Creep Behavior and Grain-Boundary Sliding in Polycrystalline Al₂O₃," *J. Am. Ceram. Soc.*, **60** [1–2] 44–47 (1977).
- ²⁴² J. Chevalier, C. Olagnon, G. Fantozzi, and H. Gros, "Creep behaviour of alumina, zirconia and zirconia-toughened alumina," *J. Eur. Ceram. Soc.*, **17** [6] 859–864 (1997).
- ²⁴³ G. Bernard-Granger, C. Guizard, and R. Duclos, "Compressive creep behavior in air of a slightly porous as-sintered polycrystalline α -alumina material," *J. Mater. Sci.*, **42** [8] 2807–2819 (2007).
- ²⁴⁴ J.J. Melendez-Martinez and A. Domínguez-Rodríguez, "Creep of Silicon Nitride," *Prog. Mater. Sci.*, **49** 19–107 (2004).
- ²⁴⁵ J.M. Birch and B. Wilshire, "The compression creep behaviour of silicon nitride ceramics," *J. Mater. Sci.*, **13** [12] 2627–2636 (n.d.).
- ²⁴⁶ J.M. Birch, B. Wilshire, D.J.R. Owen, and D. Shantaram, "The influence of stress distribution on the deformation and fracture behaviour of ceramic materials under compression creep conditions," *J. Mater. Sci.*, **11** [10] 1817–1825 (n.d.).
- ²⁴⁷ J.A. Todd and Z.Y. Xu, *The High Temperature Creep Deformation of Si₃N₄-6Y₂O₃-2Al₂O₃*, (n.d.).
- ²⁴⁸ G. Grathwohl and F. Thümmeler, "Interaction between creep, oxidation and microporosity in reaction-bonded silicon nitride," *Ceramurg. Int.*, **6** [2] 43–50 (1980).
- ²⁴⁹ E. Torresani, D. Giuntini, C. Zhu, T. Harrington, K. Vecchio, A. Molinari, and E.A. Olevsky, "Anisotropy of Mass Transfer during Sintering of Powder Materials with Pore-Grain Structure Orientation," *Acta Mater.*, prepared for publication (n.d.).

- 250 H. Shang, D. Giuntini, A. Mohanram, E.A. Olevsky, and R.K. Bordia, "Pore Shape Evolution during Sinter-Forging of LSM-YSZ Composites," *Acta Mater.*, prepared for publication (n.d.).
- 251 D. Giuntini, I.-W. Chen, and E.A. Olevsky, "Sintering shape distortions controlled by interface roughness in powder composites," *Scr. Mater.*, **124** 38–41 (2016).
- 252 O. Gillia, C. Josserond, and D. Bouvard, "Viscosity of WC–Co compacts during sintering," *Acta Mater.*, **49** [8] 1413–1420 (2001).
- 253 S. Giraud and J. Canel, "Young's modulus of some SOFCs materials as a function of temperature," *J. Eur. Ceram. Soc.*, **28** [1] 77–83 (2008).
- 254 M. Belmonte, J. González-Julián, P. Miranzo, and M.I. Osendi, "Spark plasma sintering: A powerful tool to develop new silicon nitride-based materials," *J. Eur. Ceram. Soc.*, **30** [14] 2937–2946 (2010).
- 255 M. Belmonte, M.I. Osendi, and P. Miranzo, "Modeling the effect of pulsing on the spark plasma sintering of silicon nitride materials," *Scr. Mater.*, **65** [3] 273–276 (2011).
- 256 T. Nishimura, M. Mitomo, H. Hirotsuru, and M. Kawahara, "Fabrication of silicon nitride nano-ceramics by spark plasma sintering," *J. Mater. Sci. Lett.*, **14** [15] 1046–1047 (1995).
- 257 Z. Shen and M. Nygren, "Kinetic aspects of superfast consolidation of silicon nitride based ceramics by spark plasma sintering," *J. Mater. Chem.*, **11** [1] 204–207 (2001).
- 258 X. Wei, D. Giuntini, A.L. Maximenko, C.D. Haines, and E.A. Olevsky, "Experimental Investigation of Electric Contact Resistance in Spark Plasma Sintering Tooling Setup," *J. Am. Ceram. Soc.*, **98** [11] 3553–3560 (2015).
- 259 G. Maizza, S. Grasso, Y. Sakka, T. Noda, and O. Ohashi, "Relation between microstructure, properties and spark plasma sintering (SPS) parameters of pure ultrafine WC powder," *Sci. Technol. Adv. Mater.*, **8** [7–8] 644–654 (2007).
- 260 W. Gruner, J. Haßler, P. Barth, J. Behm, and J. Sunderkötter, "The precise determination of nitrogen in boron nitride," *J. Eur. Ceram. Soc.*, **29** [10] 2029–2035 (2009).
- 261 M. Engler, C. Lesniak, R. Damasch, B. Ruisinger, and J. Eichler, "Hexagonal Boron Nitride (hBN): Applications from Metallurgy to Cosmetics," *CFI Ceram. Forum Int.*, **84** [12] (2007).

- ²⁶² L.G. Carpenter and P.J. Kirby, "The electrical resistivity of boron nitride over the temperature range 700 degrees C to 1400 degrees C," *J. Phys. Appl. Phys.*, **15** [7] 1143 (1982).
- ²⁶³ V.L. Solozhenko, V.Z. Turkevich, and W.B. Holzapfel, "Refined Phase Diagram of Boron Nitride," *J. Phys. Chem. B*, **103** [15] 2903–2905 (1999).